SEARCHING FOR QUASAR FEEDBACK IN OBSCURED AND RED QUASARS AT THE PEAK OF GALAXY FORMATION

by

Rachael M. Alexandroff

A dissertation submitted to The Johns Hopkins University in conformity with the requirements for the degree of Doctor of Philosophy.

Baltimore, Maryland

July, 2017

Abstract

Though small on the scale of their host galaxy, supermassive black holes likely play a crucial role in galaxy evolution. A galaxy-scale effect driven by supermassive black holes (or "quasar feedback) is necessary to stop the production of too many massive galaxies in semi-analytical simulations and to drive observational correlations between host galaxy and black hole properties. Nevertheless, such a mechanism is not yet well supported by observational evidence, especially at the peak of galaxy formation. This thesis represents an effort to ground every aspect of quasar feedback at the peak of galaxy formation with strong observational evidence. I first define a sample of obscured and actively accreting supermassive black holes ("quasars) at the peak of galaxy formation using the Sloan Digital Sky Survey. Then, using targeted observations of small sub-samples of these objects across a variety of wavelengths, I show that in a sample of the most luminous quasars, we see emerging evidence for quasar feedback. I show that luminous quasars are capable of launching winds by studying their scattering geometry and kinematics using spectropolarimetry. I advance the theory that sensitive, high resolution radio observations allow us to search

ABSTRACT

for the presence of such winds on galaxy scales. Finally, I show that these winds go on to clear their host galaxies of the molecular gas necessary for star formation. All together, this body of work provides a robust observational window into important mechanisms of galaxy growth and quenching at the peak of galaxy formation and evolution.

Primary Reader: Prof. Nadia Zakamska

Secondary Reader: Prof. Timothy Heckman

Acknowledgments

First I would like to acknowledge my gratitude to Prof. Nadia Zakamska, who was the best thesis advisor that anyone could ask for. Thank you for your lengthy and critical discussions of various project ideas and hypotheses and for encouraging me to diligently work to understand the physics behind every observation. Thank you perhaps most of all for giving me the freedom to pursue those questions that interested me the most. Thank you also to the wonderful Zakamska research group (Guilin, Dominika, Kate, Kirsten, Erini, and Hsiang-Chih) for your support and assistance on a variety of topics. Thank you also to Prof. Tim Heckman, for allowing me to pursue my interest in Lyman Break Galaxy analogs and for being an additional source of support and to Prof. Julian Krolik for supporting me as the third member of my thesis committee. Thank you in addition to the department for their financial support during my first year. Thanks also to my fellow graduate students for making my time at JHU some of the best years of my life.

I would also be remiss if I didn't thank my collaborators outside of Johns Hopkins: Prof. Michael Strauss, Prof. Jenny Greene, Dr. Andy Goulding and Dr. Sean

ACKNOWLEDGMENTS

Johnson at Princeton University, Prof. Fred Hamann at the University of California Riverside, Prof. Aaron Bath at the University of California Irvine, Dr. Nic Ross at the University of Edinburgh, Dr. Isabelle Paris at the Laboratoire d'Astrophysique de Marseille, Prof. Niel Brandt at Pennsylvania State University and Dr. Ai-Lei Sun at the Academia Sinica Institute of Astronomy and Astrophysics.

My work has relied on access to a number of telescope facilities around the world. I want to acknowledge the use of data from the Sloan Digital Sky Survey, the Faint Images of the Radio Sky at Twenty-Centimeters, and the Wide-Field Infrared Survey Explorer at the NASA/IPAC Infrared Science Archive. I would also like to acknowledge the facilities through which I obtained data for this thesis including the Apache Point Observatory, the Gemini Observatory, the Keck Observatory, and the Very Large Array. I wish to recognize and acknowledge the very significant cultural role and reverence that the summit of Mauna Kea has always had within the indigenous Hawaiian community; I was fortunate to be able to conduct observations on the mountain using the Keck Telescope.

Thank you to all of my friends and family for your unflagging support as I pursued the dream I have had since I was seven. From Dr. Alan Alexandroff's lectures on graduating to Dr. Carole Cohen's unfailing telephone support and Miriam's text messages I couldn't have done it without you. Also thank you to my boyfriend Ben for spending weekends in Bloomberg and for convincing me to take a break.

Dedication

This thesis is dedicated to my family and friends who have supported me unfailingly even when every day was "quasar day".

Contents

List of Tables

List of Figures

Chapter 1

Introduction

Black holes of masses one million to one billion times that of the sun known as supermassive black holes are now believed to reside at the centers of almost all massive galaxies in the universe, including our own Milky Way. Sometimes, supermassive black holes enter an active or "quasar" state during which they accrete gas and other forms of matter. The quasar unification model (Antonucci, 1993; Urry & Padovani, 1995) posits that all quasars are surrounding by a torus of gas and dust and that all variation in quasar properties can be explained by a difference in viewing angle. In an obscured or "Type 2" quasar where the viewer is seeing the quasar through the dusty torus, the normal quasar continuum emission is blocked as is the light from the broad-line region near the central engine. Yet, some models (Sanders et al., 1988; Hopkins et al., 2006) suggest that obscured quasars also represent a particular phase in quasar evolution.

Quasars are now thought to play a crucial role in the evolution of their host galaxies. In evolutionary scenarios, a major merger or other cataclysmic event shrouds the entire galaxy in gas and dust and produces an enshrouded supermassive black hole in the quasar state. Then, the quasar drives a wind that removes gas from the host galaxy and shuts off star formation in a process called "quasar feedback" (Sanders et al., 1988; Hopkins et al., 2006). Such a process is necessary to account for the relatively small number of very massive galaxies observed in the universe (e.g. Croton et al., 2006) and perhaps to drive observed correlations between black hole and galaxy properties (Magorrian et al., 1998; Gebhardt et al., 2000).

To understand the complicated interplay of these two effects–orientation and evolution, requires a large sample of obscured quasars specifically in the early universe when galaxies and black holes were forming most rapidly (Madau & Dickinson, 2014). Chapter § 2 describes a search for just such an appropriate sample at the peak of galaxy formation. Such a sample is also crucial to properly constrain the total number density of quasars at all redshifts, and their contribution to reionization at very high redshifts as well as to uncover how the number of obscured quasars as a fraction of the total quasar population evolves with time. Though deep X-ray surveys have suggested that around 50% of high redshift ($z > 2$) quasars should be obscured (Treister & Urry, 2012), previous optical surveys have been too shallow or covered too small an area to identify a significant population of luminous obscured quasars at the peak of galaxy formation. Alexandroff et al. (2013) was the first large sample

of optically-selected obscured quasar candidates at the peak of galaxy formation.

While our theories of galaxy evolution have made great progress, details of the quasar feedback mechanism remain unclear. If we want to understand how supermassive black holes affect the galaxies in which they reside, then we must obtain direct observations of quasar feedback in action, clearing their host galaxies. Yet, despite strong theoretical indicators and indirect evidence, direct observations of quasar feedback remain scarce, especially in the early universe.

We have theoretical reasons to believe that quasars can shock heat gas, which in turn drives the galactic wind in the quasar feedback scenario (Zubovas & King, 2012; Nims et al., 2015). There are, however, few observational probes of this particular feedback phenomenon. One relatively unexplored route is to search for the shocked gas in the radio. There is indirect evidence that unresolved, moderate-luminosity radio sources might be correlated with galaxy winds (Mullaney et al., 2013; Zakamska & Greene, 2014) though we must also rule out small radio jets, star formation and nuclear coronae as the possible sources of the observed radio emission. Chapter § 3 describes an observational pilot program to make the case that quasar winds are likely responsible for the observed radio emission in four luminous quasars at $z \sim 0.5$ using a powerful observational combination of radio luminosity, morphology and spectral index. In addition, it presents results that indicate a continuation of the correlation between radio luminosity and galaxy-scale wind indicators at high redshift ($z \sim 2.5$).

To properly understand quasar feedback, we need to study not only the effect of

quasar feedback on the host galaxy but also understand how the wind is launched near the quasar's central engine. Although the direct view to the nucleus is blocked in Type 2 quasars, some of the quasar light escapes along unobscured directions and is scattered off the surrounding medium toward the observer. Therefore, polarized spectra of Type 2 quasars offer not only a traditional test of the Unification Model (Antonucci & Miller, 1985; Miller et al., 1991) but also a detailed understanding of the local scattering geometry and kinematics near the quasar's central engine by providing a direct view as seen in scattered light. Chapter § 4 presents a study of five obscured and red quasars in polarized light using the Keck Low Resolution Imaging Spectrometer (LRIS; Oke et al., 1995) in polarimetry mode (Goodrich et al., 1995). The results suggest a model for the inner region of the quasar where an equatorial, dusty outflow from the accretion disk is supported by radiation pressure (e.g. Wills et al., 1992; Elitzur & Shlosman, 2006; Veilleux et al., 2016; Chan & Krolik, 2016; Elvis, 2017) and driven by near or super-Eddington accretion.

The most compelling evidence for quasar feedback is the presence of galaxy-wide outflows in the multi-phase interstellar medium of the host galaxy as determined by measuring the gas outflow velocities. In order to measure the destructive impact of quasar winds on their hosts, it is essential to probe the state of the molecular gas the fuel for galactic star formation. Such observations are necessary to confirm that quasar winds halt star formation by removing molecular gas from the galaxy. Chapter § 5 describes a search for emission from molecular gas in a sample of high redshift

quasars. While no line emission was detected, the lack of line emission is perhaps a strong indicator that the host galaxies have been cleared of much of their molecular gas reservoir by quasar feedback.

Thus, this body of work represents a study of the quasar feedback mechanism at the peak of galaxy formation– from wind launching to observational signatures of outflows and the ability of these outflows to remove the ingredients of star formation from the host galaxy.

Chapter 2

Candidate Type II Quasars at $2 < z < 4.3$ in the Sloan Digital Sky Survey III

At low redshifts, dust-obscured quasars often have strong yet narrow permitted lines in the rest-frame optical and ultraviolet, excited by the central active nucleus, earning the designation Type II quasars. We present a sample of 145 candidate Type II quasars at redshifts between 2 and 4.3, encompassing the epoch at which quasar activity peaked in the universe. These objects, selected from the quasar sample of the Baryon Oscillation Spectroscopic Survey of the Sloan Digital Sky Survey III, are characterized by weak continuum in the rest-frame ultraviolet (typical continuum magnitude of $i \approx 22$) and strong lines of C IV and Lyα, with Full Width at Half

Maximum less than 2000 $\mathrm{km\,s^{-1}}$. The continuum magnitudes correspond to an absolute magnitude of -23 or brighter at redshift 3, too bright to be due exclusively to the host galaxies of these objects. Roughly one third of the objects are detected in the shorter-wavelength bands of the WISE survey; the spectral energy distributions (SEDs) of these objects appear to be intermediate between classic Type I and Type II quasars seen at lower redshift. Five objects are detected at rest frame 6μm by Spitzer, implying bolometric luminosities of several times 10^{46} erg $\mathrm{s^{-1}}$. We have obtained polarization measurements for two objects; they are roughly 3% polarized. We suggest that these objects are luminous quasars, with modest dust extinction ($A_V \sim 0.5$ mag), whose ultraviolet continuum also includes a substantial scattering contribution. Alternatively, the line of sight to the central engines of these objects may be obscured by optically thick material whose covering fraction is less than unity.

2.1 Introduction

In standard unification models, many of the observed properties of Active Galactic Nuclei (AGN) can be explained by differences in viewing angle Antonucci (1993). In these models, the accretion disk of the supermassive black hole (SMBH) is surrounded by a torus of gas and dust, which, when oriented along the line of sight, obscures emission from the region around the SMBH at optical, ultraviolet and soft X-ray wavelengths. Because this gas and dust does not cover all 4π steradians around the

central engine, gas in the host galaxy above and below the torus is illuminated by the engine, giving rise to strong narrow high-ionization emission lines (Full Width at Half Maximum (FWHM) $< 2000\ \mathrm{km\,s^{-1}}$) and weak continua (Zakamska et al., 2003) in the rest-frame optical spectra. Such objects are classified as Type II based on their optical spectra, in contrast to Type I objects which show strong ultraviolet continua and broad permitted lines (Khachikyan & Weedman, 1971). Type II AGN tend to show a high ratio of IR to optical light, to have hard X-ray spectra, and to be strongly polarized, consistent with the obscuring torus hypothesis (Antonucci & Miller, 1985; Norman et al., 2002; Smith et al., 2002; Zakamska et al., 2003; Brandt & Hasinger, 2005). However, Sanders et al. (1988), Canalizo & Stockton (2001) and Hopkins et al. (2006) argue that Type I and Type II quasars represent different phases in quasar evolution: in their models, all quasars pass through an obscured phase before outflows from the AGN and central star formation expel the obscuring material.

The comoving space density of luminous Type I quasars peaked at redshifts 2-3 (Schmidt et al., 1995; Richards et al., 2006b; Ross et al., 2013), although the demographics of luminous obscured quasars at this epoch are poorly understood. While it is straightforward to identify unobscured quasars as ultraviolet-excess sources in multi-band optical surveys (Sandage, 1965; Green et al., 1986; Richards et al., 2006a), a complete census of AGN is challenging at visible wavelengths alone, given that an appreciable fraction of the quasar population is obscured by dust. Astronomers have used searches in a variety of wavebands to identify obscured quasars (see, for example,

Brandt & Hasinger, 2005; Stern et al., 2005; Hatziminaoglou et al., 2005; Gilli et al., 2007; Treister et al., 2009a; Vasudevan et al., 2010; Ballantyne et al., 2011; Xue et al., 2012; Donley et al., 2012; Assef et al., 2013; Stern et al., 2012; Mignoli et al., 2013).

The integral of the quasar luminosity function, with appropriate efficiency factors, approximately matches the present-day mass function of SMBH (Soltan, 1982; Yu & Tremaine, 2002; Marconi et al., 2004) indicating that black holes accrete much of their mass during a luminous phase as quasars. This argument has profound implications for understanding the growth of black holes and their role in galaxy evolution, but improving this calculation requires good measurements of quasar demographics, including the obscured quasar fraction, as a function of redshift and luminosity. This goal remains elusive: surveys at different wavelengths often find discrepant results (Lawrence & Elvis, 2010). At $z < 0.8$, Reyes et al. (2008) find that the ratio of optically-selected Type II to Type I luminous quasars is at least 1:1, while X-ray studies (for example, Ueda et al., 2003; Hasinger, 2008) place the value at $\sim$ 3:1 for low-luminosity active nuclei, but $< 1:1$ for high-luminosity quasars. Using X-ray data, Mushotzky et al. (2000) and Hickox & Markevitch (2006) suggest that the obscured fraction remains constant or even increases with redshift (see reviews by Ballantyne et al., 2011; Treister & Urry, 2012, for further discussion).

High-redshift radio-loud Type II quasars have been studied for decades (see, for example, the review paper by McCarthy, 1993) but their radio-quiet counterparts in the optical, IR and X-ray have been harder to find. Deep Mid-IR (e.g. Alexander

et al., 2005; Stern et al., 2005; Dey et al., 2008; Coppin et al., 2010; Donley et al., 2012; Stern et al., 2012) and X-ray (e.g. Treister et al., 2009b; Comastri et al., 2011; Lehmer et al., 2012; Vasudevan et al., 2013) surveys tend to cover small solid angles, and are thus not sensitive to rare luminous objects. Moreover, indications of obscuration do not always agree between different wavebands (e.g., Barger et al., 2005; Civano et al., 2012; Jia et al., 2013). For example, about 50% of X-ray identified Compton-thick objects show broad emission lines in their optical spectra (e.g., Vasudevan et al., 2009).

The Sloan Digital Sky Survey (SDSS; York et al. 2000; Eisenstein et al. 2011) has covered almost 1/3 of the Celestial Sphere in both visible-light imaging and spectroscopy to a depth at which significant numbers of high-redshift quasars are found (Richards et al., 2002). Zakamska et al. (2003) and Reyes et al. (2008) selected high-luminosity Type II objects with $z < 0.83$ among SDSS spectra of galaxies (Strauss et al., 2002) and Faint Images of the Radio Sky at Twenty-cm (FIRST) radio sources (Becker et al., 1995). These objects were identified by their strong narrow emission lines (FWHM less than 1000 $\mathrm{km\,s^{-1}}$in most cases) and weak continuum; [O III]λ5007Å was used as a crude proxy for bolometric luminosity (Heckman et al., 2005). Additional observations of these objects, including spectropolarimetry (Zakamska et al., 2005) and mid-infrared photometry and spectroscopy (Zakamska et al., 2008) demonstrated that these objects were indeed highly luminous obscured quasars, with a space density (at least to $z \sim 0.8$) comparable to unobscured quasars (Reyes

et al., 2008).

Searches for counterparts at higher redshift were not successful in the SDSS-I/II data; narrow-line objects typically had strong continua and extensive Fe emission, showing them to be high-redshift analogs of Narrow Line Seyfert I galaxies (NLS1; Osterbrock & Pogge 1985; Williams et al. 2002). However, the Baryon Oscillation Spectroscopic Survey (BOSS; Dawson et al. 2013) of SDSS-III (Eisenstein et al., 2011) targets quasars two magnitudes fainter than SDSS-I/II did (Ross et al., 2012), probing to continuum levels at which Type II quasar candidates at high redshift begin to appear.

In this paper, we describe a class of high-redshift ($z > 2$) Type II quasar candidates identified by their characteristic spectra from BOSS. We have found 452 candidates with redshifts in the range $2.03 < z < 4.23$ in the SDSS-III Data Release 9 (Ahn et al., 2012, hereafter referred to as DR9). We describe the relevant SDSS data in § 2.2 and the selection of our candidates in § 2.3. The properties of these objects in SDSS data are described in § 2.4, and we match against other datasets in § 2.5. We discuss our results in § 4.4, and conclude in § 4.5. We assume a flat ΛCDM cosmology with $\Omega_m = 0.26$, $\Omega_\Lambda = 0.74$ and $h = 0.71$ (Spergel et al., 2007) throughout this paper. We use AB magnitudes consistently in this paper.

2.2 SDSS Observations and Data Processing

The SDSS has been in routine operation since 2000. It uses the dedicated 2.5-meter wide-field Sloan Foundation Telescope at Apache Point Observatory in New Mexico (Gunn et al., 2006), carrying out both imaging (Gunn et al., 1998) and spectroscopy. The two optical spectrographs were upgraded in 2009 for the BOSS survey (Smee et al., 2013); each is fed by 500 optical fibers with 2″ optical diameter, yielding spectrophotometrically calibrated spectra from 3600Å to 10,400Å[1], with resolution $\lambda/\Delta\lambda \approx 1800$. BOSS is designed to measure the baryon oscillation feature in the clustering of galaxies (Anderson et al., 2012) and the Lyα absorption spectra of quasars (Busca et al., 2013).

BOSS data were first made public in the SDSS DR9, containing spectra of 536,000 galaxies and 102,000 quasars over 3275 deg^2. Because of the need to observe the Lyα forest, quasars are targeted in the region of color space where objects with $2.15 < z < 3.5$ are expected to lie (Ross et al., 2012). This is a challenging task, because the broad-band colors of $z \sim 2.7$ quasars are similar to those of much more numerous F and A stars (Fan, 1999). The quasar candidates are selected to a Point

[1]As described in Pâris et al. (2012) and Dawson et al. (2013), fibers for quasar candidates in BOSS were often offset from their fiducial positions to maximize the throughput in the blue given differential chromatic refraction. However, the spectrophotometric standard stars were observed without these offsets, causing systematic errors in the spectrophotometric calibration of quasars of up to 40%.

Source Function magnitude limit of $g \leqslant 22.0$ or $r \leqslant 21.85$ (after correction for Schlegel et al. 1998 extinction). All spectra are processed with a common pipeline (Bolton et al., 2012); Pâris et al. (2012) report that almost 97% of quasar targets have spectra of sufficient signal-to-noise ratio (S/N) to measure a reliable redshift.

At redshifts above $z \sim 1$, the Hα, Hβ and [O III] emission lines commonly used as diagnostics for identifying Type II quasars at optical wavelengths no longer fall within the wavelength coverage of the BOSS spectrograph. Instead, we used the widths of the Lyα (1216Å) and C IV (1549Å) emission lines as diagnostics of candidate Type II objects, cutting at FWHM < 2000 km s^{-1} (see, e.g., Zakamska et al. 2003; Hao et al. 2005; Sulentic et al. 2007). Given the BOSS spectral coverage, we can measure Lyα cleanly at redshifts $z \gtrsim 2.0$. Line widths are measured directly by the BOSS pipeline, from single Gaussian fits to the Lyα and C IV lines.

2.3 Sample Selection Criteria

Heavily dust-obscured quasars are expected to have strong, narrow emission lines atop a relatively weak continuum, which is a combination of the light from the host galaxy and the light from the hidden quasar scattered by the interstellar material in the host. The classical definition of optically selected Type II active nuclei largely focuses on the widths and ratios of emission lines, which is the approach that Reyes et al. (2008) used in selecting ~ 900 Type II quasars at $z < 0.8$ from SDSS-I/II data. But

because obscured quasars are faint at rest-frame optical and ultraviolet wavelengths, previous searches for Type II quasars at higher redshifts using the SDSS-I/II data have been largely unsuccessful. The redshift range between 0.8 and 2.0 is particularly difficult because none of the strong emission lines characteristic of Type II quasars appear at the optical wavelengths. Only one candidate, SDSS J085600.88+371345.5 at $z = 1.02$ was identified in the original SDSS quasar sample as satisfying all our emission line criteria. This object was also identified as an obscured quasar candidate by Gilli et al. (2010). At redshifts > 2.0, a search for narrow-line objects in the SDSS-I/II quasar sample (Schneider et al., 2010) yielded a number of NLS1, but little else.

Table 2.1: Selection of Type II Candidates

Sample	No. of Objects
All BOSS DR9 quasars	102100
BOSS DR9 quasars with Lyα, C IV measured	79505
$\mathrm{FWHM_{C\,IV}} < 2000\,\mathrm{km\,s^{-1}}$	2494
Class A	145
Class B	307

The BOSS survey goes substantially deeper than SDSS-I/II in spectroscopy, allowing us to resume the search for Type II quasars at high redshifts based on rest-frame ultraviolet spectra. In this paper we adopt a composite approach based both on the properties of emission lines and on the properties of the continuum. For our parent sample, we selected all BOSS objects in DR9 with both Lyα and C IV emission line measurements (given the BOSS wavelength coverage, this corresponds to redshifts of

$z \gtrsim 2.0$) and a reliable pipeline fit (i.e., the flag `ZWARNING` = 0; see the discussion in Bolton et al. 2012). A total of 79,505 objects satisfied these criteria. Objects with FWHM< 2000 km s^{-1} are quite rare, representing only 3.7% of the total in the BOSS sample. These numbers are summarized in Table 2.1.

From this sample, we selected only those objects with 5σ detections in both Lyα and C IV (thus we are insensitive to objects that emit only in Lyα; see, for example, Hall et al. 2004), and restricted ourselves to those objects in which both lines have FWHM< 2000 km s^{-1}. The widths of the two lines are correlated, although the correlation is weak, due in part to absorption features (§ 2.4.4) and limited S/N. We then visually inspected the spectra of the 2494 remaining candidates. The best Type II quasar candidates have narrow but strong emission lines and an extremely weak, flat continuum (see Figure 2.1). There were two main astrophysical contaminants in our original sample: high-redshift analogs to NLS1 galaxies, and broad absorption line (BAL) quasars whose emission lines are mostly absorbed away, leaving only a narrow component in emission (Figure 2.2). The rest-frame ultraviolet spectra of NLS1s (Constantin & Shields, 2003) show narrow permitted lines, but possess a strong blue continuum and emission from Fe II complexes that are not seen in obscured quasars; see for example the upper panel of Figure 2.2. An example of a BAL quasar whose emission line widths met our initial criteria is found in the middle panel of Figure 2.2; the C IV line is clearly truncated by the associated absorption.

We classified our Type II quasar candidates, after removing the BAL quasars and

obvious NLS1, in two categories: those that showed all the qualities of an obscured quasar (narrow emission lines, no associated absorption, weak continuum); hereafter Class A, and those with one or more characteristics of unobscured objects (a broad component to an emission line, an absorption feature, or a strong blue continuum); hereafter Class B. Figure 2.1 presents an example of an object from Class A, while the lower panel of Figure 2.2 shows the spectrum of a Class B object. The Class B object has very narrow emission lines and weak continuum, but strong narrow absorption blueward of C IV. These classifications are S/N-dependent and are somewhat subjective, and there are no doubt objects we have placed in each category that belong in the other (see Figure 2.3 and the discussion in § 2.4.2).

Are our Type II candidate objects truly obscured quasars, in the sense of having bolometric luminosities much larger than inferred from the optical data? Our objects have line widths up to 2000 $\mathrm{km\,s^{-1}}$, while low-redshift Seyfert II galaxies typically have line widths less than 1200 $\mathrm{km\,s^{-1}}$ (Hao et al., 2005). However, outflows in the narrow-line region may give significantly larger widths in more luminous objects, with spatial extents as large as 10 kpc (e.g., Greene et al., 2012; Liu et al., 2013). We will see in what follows that the obscured nature of our objects remains unclear, and it is possible that our sample is somewhat heterogeneous, with more than one population contributing. With all this in mind, we consistently refer to our objects as Type II *candidates*.

Figure 2.3 shows the correlation between the rest-frame equivalent width and

FWHM of the C IV line for each sample. The distribution of objects identified as Type II quasar candidates peaks at much smaller values of C IV FWHM than either contaminating sample, but there is significant overlap among the three distributions. An initial cut at a smaller C IV FWHM would have increased our fraction of identified Type II quasar candidates but would have also excluded many strong candidates.

The Bolton et al. (2012) pipeline redshifts are determined by fits to a linear combination of templates that do not include narrow-line quasars. The asymmetries seen in Lyα due to the onset of the Lyα forest, and especially in C IV due to winds (Richards et al., 2011) in broad-line objects are not present for the objects in our sample, meaning that the redshifts based on these templates are often biased high by of order 0.005. The DR9 quasar catalog (Pâris et al., 2012) includes redshifts measured directly from a Gaussian fit to the C IV line, which usually lines up well with the redshift measured from Lyα and fainter lines such as C III in our narrow-line objects. We thus use the C IV redshift when available in the DR9 quasar catalog, and a redshift based on visual inspection in the rare cases where it is not.

2.4 Properties of Type II Quasar Candidates: SDSS Data

Figure 2.4 shows spectra of further examples of objects in our class A sample, including one of the highest redshift objects in the sample, and the objects with the

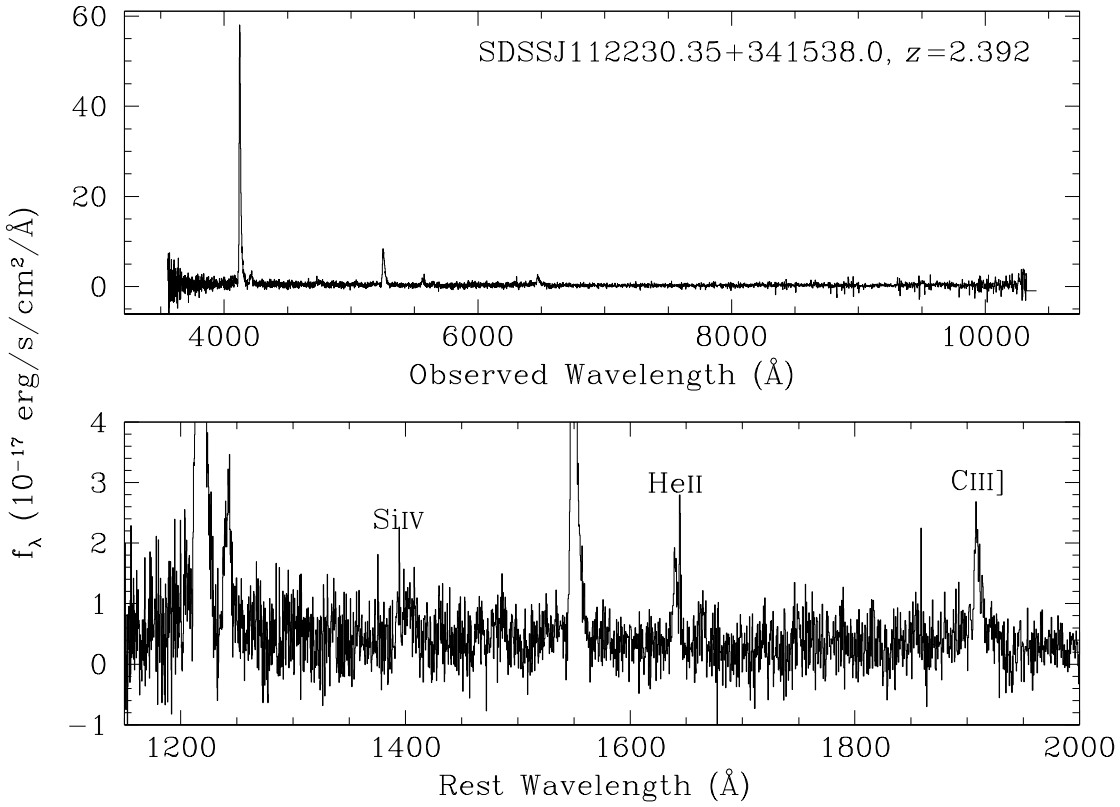

Figure 2.1: BOSS spectrum of a Type II quasar candidate at $z \sim 2.4$; this is a typical object in Class A. Note the strong narrow emission lines (Lyα and C IV have FWHM of 1000 km s^{-1} and 1200 km s^{-1}, respectively) and weak continuum. The upper panel shows the full spectrum in observed wavelengths, while the lower panel expands the horizontal and vertical scales and plots rest-frame wavelengths, with emission lines identified. In this and subsequent figures, the spectra have not been smoothed.

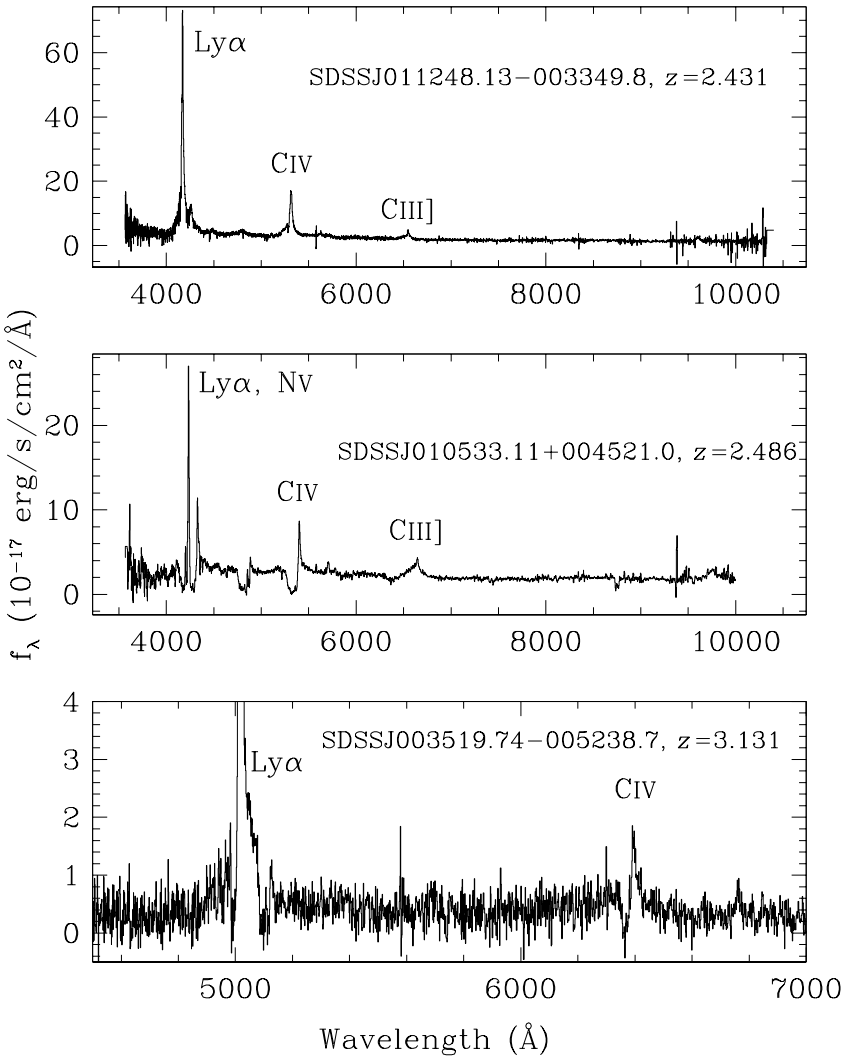

Figure 2.2: **Top**: A narrow-line BOSS object that we classified as a NLS1; note the strong blue continuum. The C IV and Lyα lines have FWHM of 1680 and 1960 km s^{-1}, respectively as measured by the SDSS pipeline. **Middle**: Spectrum of a Broad Absorption Line (BAL) quasar identified in our sample of candidates. The C IV emission line is truncated by the extensive blueward absorption; similar absorption troughs are seen in Si IV, N V, and (to a lesser extent) in C III]. The C IV emission line has a FHWM from the Gaussian fit of 900 km s^{-1}; Lyα is significantly broader, at 1900 km s^{-1}. **Bottom**: An object from our Class B sample; notice the expanded axes. C IV is strongly truncated by narrow absorption.

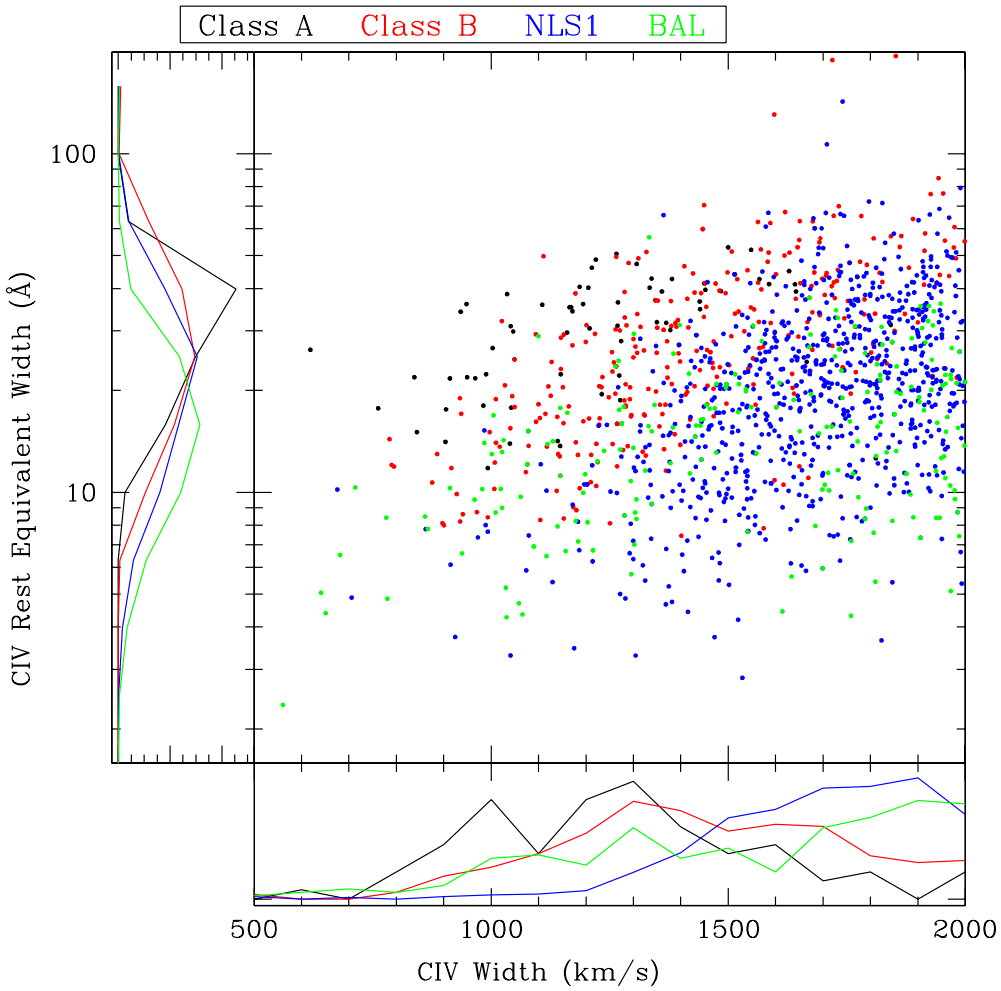

Figure 2.3: The distribution of FWHM and rest-frame equivalent width (EW) of the C IV λ1549Å line for all 2494 objects in SDSS DR9 with FWHM $< 2000\,\mathrm{km\,s^{-1}}$ and 5σ detection of both Lyα and C IV emission lines. Type II quasar candidates are shown with class A objects in black and class B objects in red (see the discussion in § 2.4), NLS1s are shown in blue and BALs in green. The distributions of each quantity (normalized to the same integral) are plotted on the sides. The class A and class B objects tend to have considerably lower FWHM and higher equivalent width than the NLS1 and the BALs.

strongest and narrowest emission lines.

Our sample includes 452 objects that are strong or possible Type II quasars. We list the 145 Class A candidates in Table 2.2 and the 307 Class B candidates in Table 2.3 [2]. Coordinates are given in J2000. The median FWHM of the C IV line among the Class A candidates is 1260 $\mathrm{km\,s^{-1}}$. The line parameters are as measured by the BOSS pipeline (Bolton et al., 2012); null values correspond to problems with the measurement. The mean redshift of these two samples is 2.70, with a redshift range from 2.03 to 4.23 (see Figure 2.6). In what follows, we concentrate on the class A sample.

[2]Full tables are available online at http://vizier.cfa.harvard.edu/viz-bin/VizieR?-source=J/MNRAS/435/3306

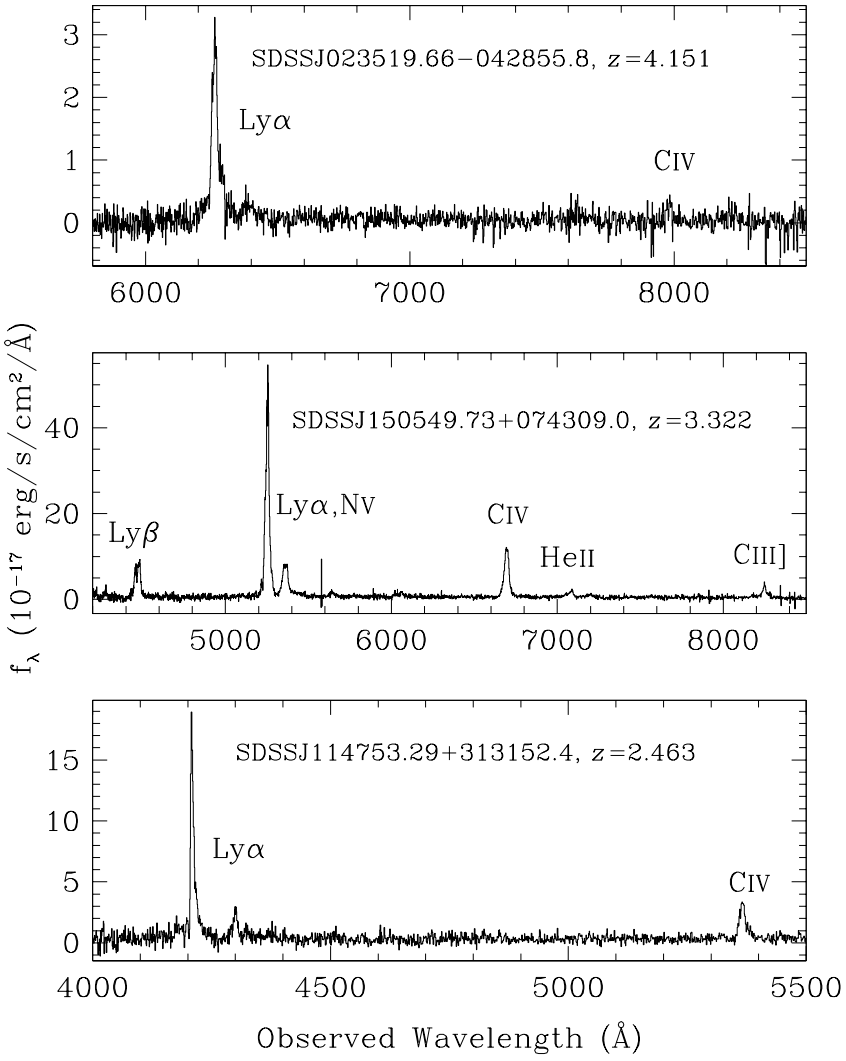

Figure 2.4: The BOSS spectra of some of the notable objects in the Class A sample of Type II quasar candidates. **Top:** One of the highest-redshift objects in our sample. C IV is barely detected. **Middle:** One of the objects with highest emission-line flux. **Bottom:** This object has among the narrowest emission lines in the sample (540 $\mathrm{km\,s^{-1}}$ in Lyα and 950 $\mathrm{km\,s^{-1}}$ in C IV). It also has the reddest continuum in the sample.

Table 2.2: Table of 145 class A candidate Type II quasars. Only a portion of this table is shown here to demonstrate its form and content. A machine-readable version of the full table is available online at http://vizier.cfa.harvard.edu/viz-bin/VizieR?-source=J/MNRAS/435/3306.

SDSS J2000 Name	ra deg	dec deg	redshift	C IV FWHM km s^{-1}	C IV REW Å	C IV flux 10^{-17} erg s^{-1} cm^{-2}	Lyα flux 10^{-17} erg s^{-1} cm^{-2}
SDSSJ001040.82+004550.5	2.67008	0.7640	2.7148	1507±59	43.9±0.0	73.3±2.8	248±2.9
SDSSJ001738.55−011838.7	4.41064	−1.3108	3.2260	768±52	25.2±0.5	21.3±1.4	101.3±2.3
SDSSJ001814.72+023258.8	4.56134	2.5497	2.9024	874±97	19.1±0.8	16.67±1.9	143.6±3.0
SDSSJ003605.26+001618.7	9.02193	0.2719	2.9503	1773±294	12.3±1.5	18.7±3.0	76.2±2.4
SDSSJ004423.20+035715.5	11.09665	3.9543	2.2213	1182±47	null	74.3±3.0	416.8±7.8
SDSSJ004600.48+000543.6	11.50199	0.0955	2.4560	1286±61	28.1±0.5	50.3±2.5	225.2±3.9

Table 2.3: Table of 307 class B candidate Type II quasars. Only a portion of this table is shown here to demonstrate its form and content. A machine-readable version of the full table is available in the online at http://vizier.cfa.harvard.edu/viz-bin/VizieR?-source=J/MNRAS/435/3306.

SDSS J2000 Name	ra deg	dec deg	redshift	C IVFWHM km s^{-1}	C IVREW Å	C IV flux 10^{-17} erg s^{-1} cm^{-2}	Lyα flux 10^{-17} erg s^{-1} cm^{-2}
SDSSJ001008.02+000317.5	2.53341	0.05485	2.2918	1655±21	null	219.4±2.8	477.0±4.7
SDSSJ001142.42−000845.7	2.92675	−0.14602	2.3146	1154±64	11.3±0.4	39.0±2.0	135.5±3.3
SDSSJ001344.04+011456.0	3.43349	1.24889	2.2250	1590±42	null	95.9±2.4	237.2±4.4
SDSSJ001922.82−004938.2	4.84507	−0.82727	3.3060	968±68	8.7±0.4	28.6±2.0	218.3±3.1
SDSSJ003519.74−005238.7	8.83224	−0.87742	3.1290	1086±85	null	25.5±1.9	166.7±2.5
SDSSJ003809.47+031634.1	9.53944	3.27615	2.4644	1173±118	8.8±0.7	34.0±3.5	187.9±5.2
SDSSJ005018.67+050132.5	12.5778	5.02571	2.9370	1149±75	12.8±0.6	46.0±3.2	214.7±3.2

Figure 2.6 shows the continuum ($\lambda = 1450$Å) luminosity density distribution for our candidates, as well as for those objects we identified as NLS1s and BALs. These continuum luminosities, which are measured from the BOSS spectra, are significantly larger than would be expected from the host galaxy of the quasars; the most luminous non-active galaxies at these redshifts have absolute ultraviolet continuum magnitudes -22.5 (Shapley, 2011). For comparison, the Type I quasar luminosity function has been measured down to $M = -25$ at these redshifts from the BOSS survey (Ross et al., 2013). The high luminosities of our objects, together with the quasar-like broad-band colors (see discussion in section 2.4.1 and Figure 2.5), suggest that the quasar continuum of these objects is not completely extincted. These objects may have only a modest dust column, or perhaps the observed continuum is due to light from the central engine that is reflected into our line of sight by dust in the quasar host galaxy, as is found in lower-redshift Type II quasars (Zakamska et al., 2006). A third possibility is that the extinction is patchy, with unextincted light showing through holes in the obscuring dust.

2.4.1 Broadband Colors

Almost all the objects in both Class A and Class B were selected for spectroscopy as quasar candidates, using the algorithms described in Ross et al. (2012). There are four principal algorithms used, but 60% of the objects in our sample were selected using the likelihood algorithm of Kirkpatrick et al. (2011) and the probabilistic al-

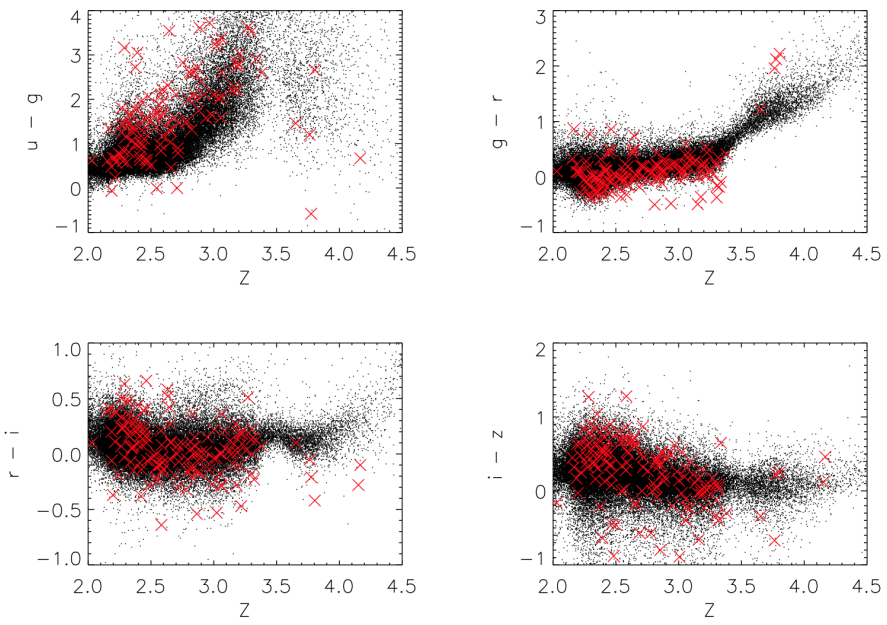

Figure 2.5: SDSS colors as a function of redshift for all BOSS quasars in DR9 (black dots), and the 145 Class A Type II quasar candidates (red crosses). A K-S comparison of the $g - r$ color distribution of the $z < 3.5$ sample with a subsample of Type I quasars matched in i-band magnitude shows that both populations are drawn from the same distribution with 84% confidence. This result suggests that the continuum is more quasar-like than galaxy-like.

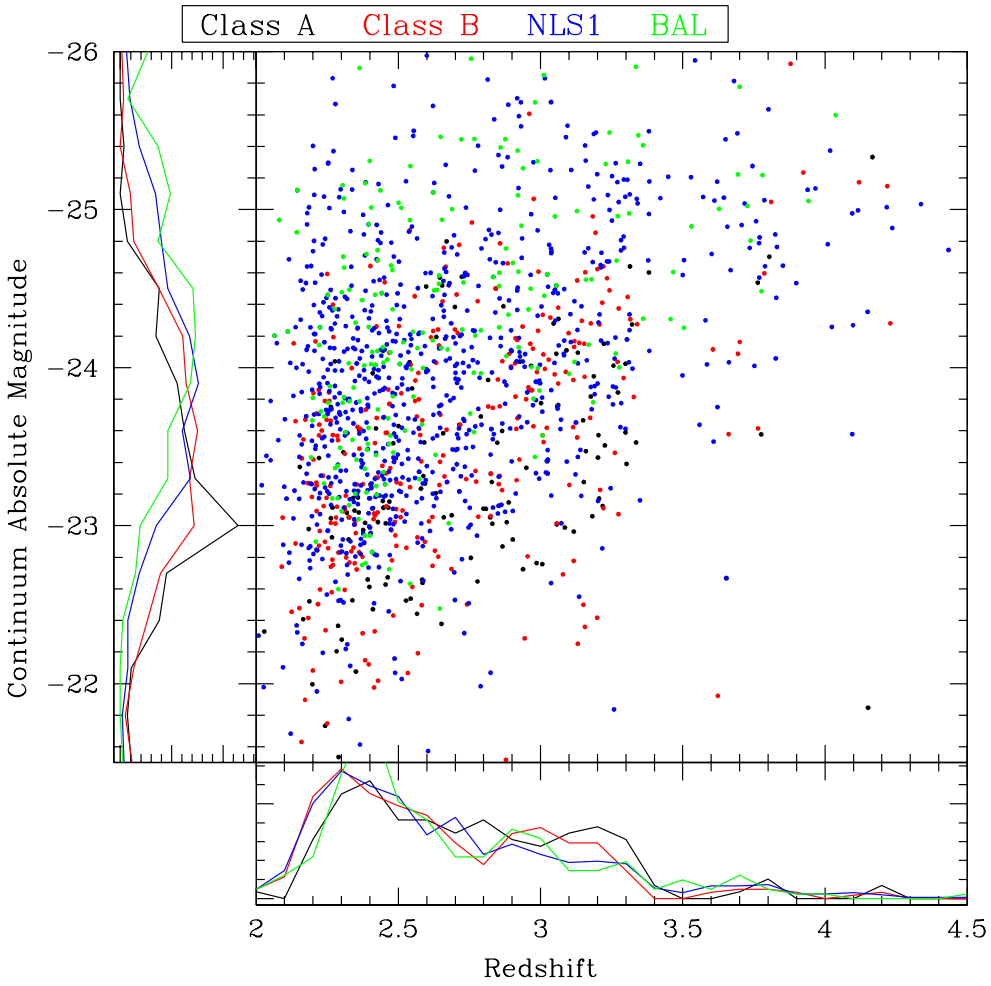

Figure 2.6: Two-dimensional distribution of redshift and continuum absolute magnitude (calculated at a rest wavelength of $\lambda = 1450$ Å) for all Type II quasar candidates in our sample. The color-coding is the same as in Figure 2.3. Normalized distributions of each individual quantity are shown on the side. The continuum luminosities are measured from the spectra; uncertainties in the spectrophotometric calibration are as large as 40%. The Type II quasar candidate continuum absolute magnitude distribution indicates that both the class A objects and the class B objects tend to be fainter than the other two samples, as we would expect for obscured objects. The redshift distributions of the samples are similar to one another, and to the parent DR9 quasar sample overall.

gorithm of Bovy et al. (2011), both of which use the distribution of objects in color space, incorporating information on photometric errors. The broad-band colors of ordinary quasars as a function of redshift are a reflection of the blue continuum, absorption by the Lyα forest and Lyman-limit systems, and, to a lesser extent, emission lines in the various bands (Fan, 1999; Richards et al., 2003). Understanding the demographics of obscured quasars will require quantifying the biases that the target selection algorithms impose on the sample.

SDSS imaging is carried out in five bands, *ugriz* (Fukugita et al., 1996). Figure 2.5 shows the dependence of color on redshift, both for our sample of Type II quasars, and the full sample of DR9 quasars (Pâris et al., 2012). The mean colors of the two groups are roughly the same, suggesting that the continua of objects in our sample are quasar-like. Of course, these objects were selected by their broad-band colors, and it perhaps not surprising that their colors are similar to those of other objects selected in the same way. The rest-frame equivalent widths of Lyα typically the strongest line in these objects, can be as large as 1000Å, at which point the line starts significantly affecting the broad-band colors.

As the Lyα break enters the g band at $z \sim 3.5$, the $g - r$ colors quickly redden with redshift. To quantify the similarity of the colors to unobscured quasars, we selected a subsample of DR9 quasars with similar i-band magnitude distribution as our Type II quasar candidates, so that they have similar photometric errors. Only objects from our sample and the DR9 catalog with a redshift of $z \leq 3.5$ were used

in the comparison, so the color was close to constant over the whole sample. A Kolmogorov-Smirnov (K-S) test of the $g-r$ color for each sample shows that the two distributions are the same at the 84% confidence level, thus the colors of our objects are consistent with having been drawn from the distribution of unobscured quasars.

2.4.2 Composite Spectrum

The upper and middle panels of Figure 2.7 show the arithmetic average spectrum of our 145 Class A Type II quasar candidates. This average is calculated by shifting all spectra to the rest frame, and inverse-variance weighting the spectra at a given wavelength, using errors estimated by the SDSS spectroscopic pipeline.

We used the program `MPFIT` (Markwardt, 2009) in IDL to fit one or two Gaussian components and a local continuum around each emission line in the composite spectra. C IV was fit with two Gaussians corresponding to a broad and narrow line component, after masking any associated absorption blueward of the emission line. Other than Lyα the redshifts and widths of emission lines were constrained to be the same as that of C IV. The Lyα N V, He II and C III lines were also each fit with two Gaussian components, while all other emission lines were fit with only a single Gaussian component. Lyα was fit simultaneously with N V, Si IV was fit simultaneously with O IV], and C III was fit simultaneously with both Si III] and Al III. The resulting fluxes are listed in Table 2.4, and the measured emission line widths are listed in Table 2.5. The continuum level in the composite is constant at about 0.4×10^{-17} erg

s^{-1} cm^{-2} $Å^{-1}$, so rest-frame equivalent widths in Ångstroms are roughly the listed flux value, times 2.5.

Interestingly, the Lyα and C III emission lines in our composite Type II candidate spectrum show a broad base (FWHM > 3000 km s^{-1}; Table 2.5), as does C IV after masking absorption blueward of the line. The flux in this broad component is comparable to the narrow component, as Table 2.4 makes clear. This absorption and broad base were among the qualities that caused us to classify some of our candidates as Class B; at higher S/N, it is likely that many of the individual Class A objects would show broad components or associated C IV absorption. The composite spectrum of our NLS1s shows significantly stronger broad bases on all of the emission lines as well as a significantly higher continuum flux relative to the emission lines. In addition, absorption blueward of C IV is particularly strong.

Table 2.4: Measured emission line fluxes from the composite spectra of our Class A, Class B and NLS1 samples. For strong emission lines where two components were fit we include values for both a narrow and broad component; see Table 2.5).

Emission Line	Wavelength (Å)	Class A Flux (10^{-17} erg s^{-1} cm^{-2})	Class B Flux (10^{-17} erg s^{-1} cm^{-2})	NLS1 Flux (10^{-17} erg s^{-1} cm^{-2})
Lyα (narrow)	1216	35.1	28.5	26.3
Lyα (broad)	1216	37.9	28.6	34.8
N v (narrow)	1240	3.4	3.2	4.4
N v (broad)	1240	9.7	12.3	22.8
[O i]	1305	1.8	1.2	1.3
C ii	1337	0.24	0.22	0.24
Si iv	1397	0.34	0.4	1.0
O iv]	1402	1.9	1.4	1.9
N iv]	1486	0.76	0.25	0.13
C iv (narrow)	1549	10.5	9.3	10.8
C iv (broad)	1549	12.3	13.1	18.5
He ii (narrow)	1638	1.8	1.2	1.4
He ii (broad)	1638	0.8	1.6	2.5
[O iii] + Al ii + Fe ii	1665	0.89	0.66	0.67
Al iii	1857	0.24	0.33	0.60
Si iii] + Fe iii	1892	0.73	0.25	0.49
C iii + Fe iii (narrow)	1906	1.4	1.8	2.1
C iii + Fe iii (broad)	1906	6.7	6.4	9.7

Table 2.5: Measured emission line widths (FWHM) from the composite spectra. We include fits to two Gaussians, a narrow and broad component.

Emission Line	Wavelength (Å)	Class A Width ($km\,s^{-1}$)	Class B Width ($km\,s^{-1}$)	NLS1 Width ($km\,s^{-1}$)
Lyα (narrow)	1216	900	1040	1150
Lyα (broad)	1216	3130	3740	4140
C IV (narrow)	1549	1060	1220	1370
C IV (broad)	1549	3630	6170	7210

The middle panel of Figure 2.7 expands the vertical and horizontal scales to make weaker emission lines visible. We detect features that are usually blended in quasar spectra (Vanden Berk et al. 2001; see also the discussion in Hewett & Wild 2010), such as the Si IVλ1393,1402Å doublet and C IIIλ1909Å, Si III]λ1892Å and Al IIIλ1857Å, are resolved. The N IVλ1486Å line, which is only rarely seen in Type I AGN (Bentz et al., 2004; Jiang et al., 2008), but is seen in high-redshift radio galaxies (Humphrey et al., 2008) and low-luminosity Type II AGN (Hainline et al., 2011) is present. There is little evidence for the Fe II emission complexes blueward of Mg II (Vanden Berk et al., 2001). The mean Type II candidate spectrum is blue in f_λ, although not as blue as in NLS1s. The continuum break due to the Lyα forest is clearly visible.

There are weak absorption features apparent in this composite, but they mostly appear blueward of emission lines, representing outflows from the central engine or the superposition of individual absorption features (Nestor et al., 2008), rather than stellar or interstellar medium lines. At high S/N, the spectra of Lyman-break galaxies (LBG) also show absorption lines in the rest-frame ultraviolet, as is apparent in the composite spectrum of Shapley et al. (2003); high-ionization absorption lines have also been seen in high-redshift Type II AGN (Steidel et al., 2002; Hainline et al., 2011). In LBGs, resonance absorption in the interstellar medium tends to be blueshifted by several hundred km s^{-1}, indicating strong outflows presumably powered by starbursts. In our composite, the only absorption feature that appears to coincide with those in LBGs is Si IVλ1396Å, as shown in the lowest panel of Figure 2.7; the absorption

is considerably blueward of the emission line, corresponding to a blueshift of order 2000 km s^{-1} (the absorption feature blueward of C IV is also offset by $\sim$2000 km s^{-1}). Moreover, it is unclear what is the driving source of these outflows (processes in the host galaxy or the central engine) and whether they are occurring on the galactic or on the circumnuclear scale.

2.4.3 Comparison to Other Samples of Obscured Quasars

We now compare the spectral properties of our objects to those of other obscured AGN samples in the literature. Hainline et al. (2011) have identified 33 AGN selected by their ultraviolet emission-line properties from a spectroscopic survey of star-forming galaxies at $z \sim 2-3$. These objects, all of which show narrow emission lines, are significantly fainter than ours, with typical continuum brightnesses of $R \sim 24$. The ultraviolet/optical SEDs of these galaxies are well-fit by stellar population synthesis models with no AGN component (Hainline et al., 2012). Their composite spectrum is shown in the middle panel of Figure 2.7, arbitrarily normalized to have a similar continuum at 1700Å as our composite, allowing an approximate comparison of the rest-frame equivalent widths of emission lines in the two composites. The emission lines in the Hainline et al. composite show no evidence for a broad base in Lyα or C IV. Unlike our Type II candidates, there is no hint of contamination

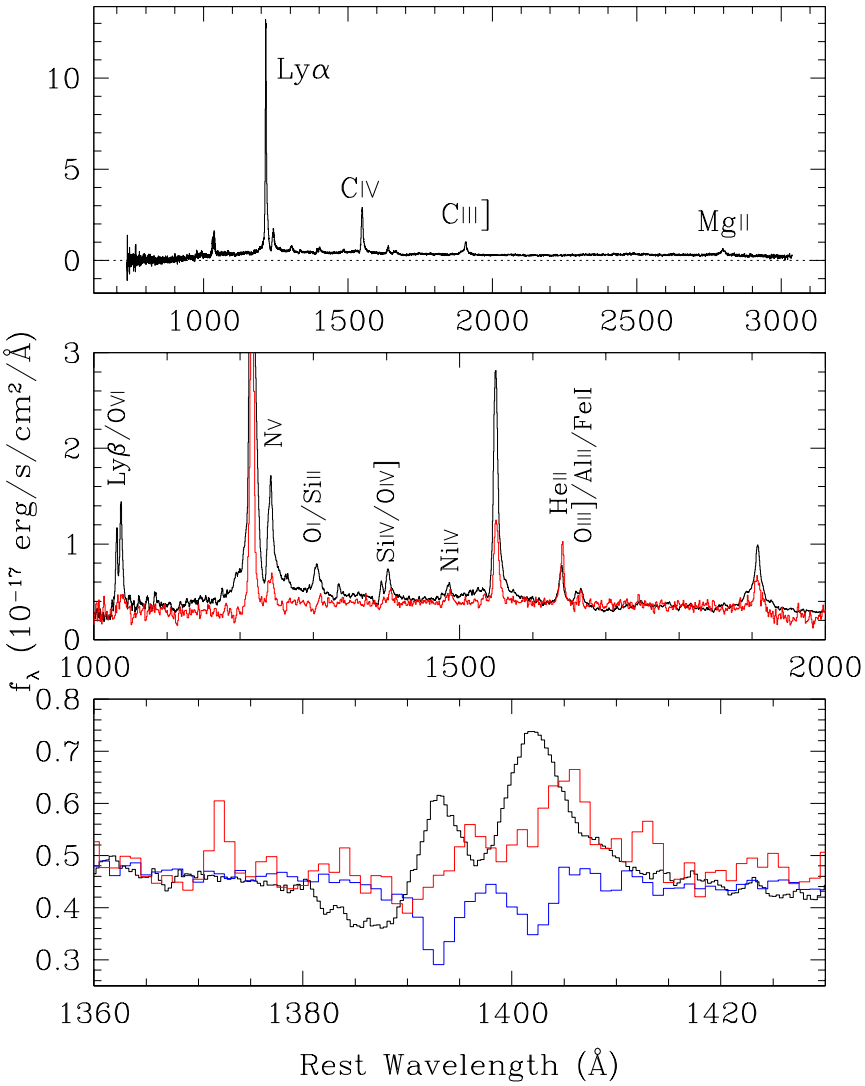

Figure 2.7: Tob: Composite spectrum of all 145 Class A Type II quasar candidates. **Middle:** An expanded view of the composite, to show the weaker emission lines. Superposed in red is the normalized composite of the Hainline et al. (2011) sample of high-redshift AGN, normalized to roughly match the continuum level at 1700Å. The continuum slopes of the two composites are quite similar. The Lyα line in the Hainline et al. (2011) composite peaks at a flux density level half of that in the Class A composite. **Bottom:** An expansion of the composite in the region around the Si IV doublet. The black line is our composite (lightly smoothed). The two emission features are the Si IV doublet at 1393.76 Å and 1402.77 Å, respectively. The blue curve shows the composite LBG spectrum of Shapley et al. (2003, normalized to the same continuum); the absorption features precisely align with the emission lines in our composite. The red curve shows the composite spectrum of Type II objects from Hainline et al. (2011). Intriguingly, the Si IV lines are redshifted relative to rest frame by about 800 km s^{-1}, perhaps due to systematic absorption on their blue wing.

from an unobscured component. However, objects from the Hainline et al. sample have emission line widths comparable to the narrow component of the Class A composite. One is also struck by the significantly greater strength of all emission lines in the Class A composite; Lyα (which goes off-scale in this expanded view) peaks at $\sim 7\times\ 10^{-17}$ erg s^{-1} cm^{-2} Å^{-1} in the normalized Hainline et al. composite, and 14 $\times$ 10^{-17} erg s^{-1} cm^{-2} Å^{-1} in the Class A objects. The one exception is the He II line at 1640Å, which is comparable in strength in the two composites; we'll discuss this line further below.

The peaks of Lyα, C IV, and most weaker lines of our composite align well with those of the Type II composite from Hainline et al., with the interesting exception of the Si IV 1394, 1403λÅ doublet (lower panel of Figure 2.7) which is redshifted in the Hainline et al. composite relative to ours by 800 km s^{-1}. A similar redshift is present in the [O I]/[Si II] 1302Å blend as well. Excess absorption due to outflows in Hainline et al. objects would suppress the blue wings of the emission features and shift them systematically to the red, although the amount of shift seems extreme. Moreover, the composite of our Class A objects also shows absorption, but nevertheless the emission peaks at exactly the expected wavelengths. Indeed, the Si IV lines we see line up well with the Si IV absorption features from the host galaxy in the LBG composite of Shapley et al. (2003).

The Hainline et al. galaxies have continua presumably dominated by their host galaxies, which makes it intriguing that the ultraviolet spectral shape of the composite

is similar to that of the Class A composite. As Figure 2.5 showed, the broad-band colors of our objects are similar to those of unobscured quasars. The continuum of the Shapley et al. (2003) LBG composite is significantly bluer than either of these samples, reflecting on-going star formation in this ultraviolet-selected sample. Similarly, the star-forming galaxy at $z = 2.3$ studied by Erb et al. (2010) is much bluer than our composite. Hainline et al. (2012) point out that AGN spectral lines are strong in LBG spectra in the most luminous objects, which tend to be red; this is why the objects in their sample are redder than typical LBGs. In this interpretation, the similarity in continuum shape between our composite and that of Hainline et al. is fortuitous.

The comparison in the middle panel of Figure 2.7 indicates that the relative strengths of emission lines in our objects and those of Hainline et al. (2011) are quite different. Following the emission-line diagnostic diagram of Villar-Martín et al. (1997), Figure 2.8 compares the ratio of the strengths of C IV and He II to the ratio of C III to C IV for our objects and those of Hainline et al. (2011), the compilation of narrow-line X-ray sources and radio galaxies of Nagao et al. (2006), the radio galaxies of De Breuck et al. (2000), the X-ray-selected Type II quasar of Stern et al. (2002), and ultraviolet observations of the archetypal Seyfert II galaxy NGC 1068 (Kraemer & Crenshaw, 2000). We also show the results for the Class A and Class B composites (red triangles), where we measure both the narrow components of the emission lines, and the sum of narrow and broad components. The collisional excitation of C IV is sensitive to density and to gas temperature and thus metallicity. C IV can appear in

emission in star-forming galaxies, although it is often swallowed by associated absorption in that line. However, the amount of C IV emission relative to other lines is much smaller in starbursts than in active nuclei. C III]/C IV depends on the relative abundance of these two ionization states of carbon, and thus this ratio is sensitive to the ionization parameter. It is about 0.5 in active nuclei (Steidel et al., 2002), whereas it is 3 or greater in even the most extreme starbursts (Erb et al., 2010). Our objects fit squarely in the AGN regime; furthermore, we find that this ratio is considerably smaller for the narrow components of both Class A and B composite spectra than for the full lines (Figure 2.8). Similarly, He II may be produced in Wolf-Rayet stars or in extreme star-formation regions with high ionization parameters, a hard spectrum, and low density, but this line has an equivalent width of no more than 2.7Å in starbursts (Erb et al., 2010), with only a handful of detections known. We detect He II in many individual spectra, and the equivalent width in the composite spectrum is about 6Å.

The ratio of C IV to He II is significantly higher, and the ratio of C III] to C IV lower, than in the other Type II samples we've discussed (with the exception of NGC 1068). Indeed, the narrow-line region photoionization models of Groves et al. (2004) do not predict C IV/He II greater than 3 for any choice of their parameters, while the typical value for our sample is a ratio closer to 10. These high ratios are seen in broad-line regions; for example, the Type I quasar composite spectrum of Vanden Berk et al. (2001) has C IV/He II ~ 50, and the Seyfert I galaxy NGC 5448 (Korista & Goad,

2000) has line ratios which place it in the middle of the cloud of Class A objects in Figure 2.8. So these narrow-line objects have line ratios like that of broad-line objects, but equivalent widths that are significantly higher. Indeed, our composite spectrum is like those of the ultraviolet spectrum of the Seyfert I spectrum NGC 5548 in its low state (Goad & Koratkar, 1998), which shows narrow lines with broad bases, and emission-line ratios similar to our objects. An interesting possibility is that some of our objects may have similarly been observed spectroscopically in a low state; repeat spectroscopy and comparison of the photometry and spectrophotometry can test this hypothesis.

2.4.4 Associated Absorption

The emission line widths have been measured by fitting Gaussian profiles to the spectra. However, the line profiles often differ significantly from Gaussian. A particularly dramatic example is shown in Figure 2.9, where the Lyα and C IV lines show multiple peaks. This is at first glance reminiscent of low-redshift Type II objects possessing emission lines with two or more peaks, interpreted as multiple AGN or biconical outflows (e.g., Liu et al., 2010; Comerford et al., 2012). However, a more likely interpretation of these systems is that they are due to associated absorption within the host galaxy of the AGN; associated C IV absorption is seen in the spectra of quasars with velocity offsets as large as 12,000 $\mathrm{km\,s^{-1}}$ (Nestor et al., 2008). Some of the absorption features in Figure 2.9 match in Lyα and C IV, but inspection of the

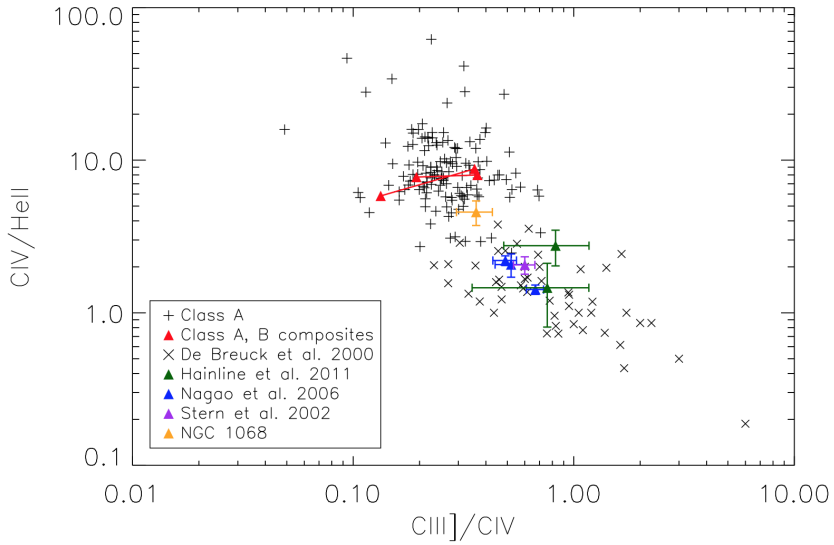

Figure 2.8: Comparison of C IV/He II and C III/C IV for several samples of narrow-line AGN. The plus signs ('+') are our Class A candidates, and the red triangles are from the narrow components of the measured emission lines (left) and the broad+narrow emission lines (right, connected with a line) of our class A and class B composites. The green points are composites from the work of Hainline et al. (2011) where they split their population at a Lyα EW of 63Å. The blue points are composites (X-ray selected narrow line quasars, low-redshift Seyfert IIs and high-redshift radio galaxies) from the compilation of Nagao et al. (2006) while the x's are high-redshift radio galaxies from De Breuck et al. (2000). We also show the Chandra-selected Type II quasar at $z = 3.29$ of Stern et al. (2002), and ultraviolet observations of the low-redshift Seyfert II galaxy NGC 1068 (Kraemer & Crenshaw, 2000).

emission-line profiles of all the objects in our sample shows many more cases in which Lyα displays absorption and C IV does not, as expected in sufficiently low-ionization gas, perhaps from neighboring galaxies. About 12% of our Class A objects possess significant absorption in one or both of these lines; it may be that higher S/N spectra at higher resolution would show more. A handful of objects show absorption in C IV and not Lyα, which may point to hot gas in which all the hydrogen is ionized.

2.5 Sample Properties from Radio to X-Ray

We now turn to the properties of our objects revealed by data beyond the SDSS itself. We match the sample with radio data from the FIRST survey in § 2.5.1 and near-infrared data from the Wide-Field Infrared Survey Explorer (WISE; Wright et al. 2010a) in § 2.5.2. Several sources have also been serendipitously detected at 24μm by the Spitzer Space Telescope (§ 2.5.3). We also used NASA's High Energy Astrophysics Science Archive Research Center (HEASARC[3]) to search for serendipitous X-ray coverage from the XMM-Newton, Chandra and ROSAT facilities (§ 2.5.4). One of our sources is included in the Cosmic Evolution Survey (COSMOS) field (Scoville et al., 2007; Cappelluti et al., 2009) (§ 2.5.5). Finally, we present optical polarization data for two of our sources in § 2.5.6.

[3] `http://heasarc.gsfc.nasa.gov`

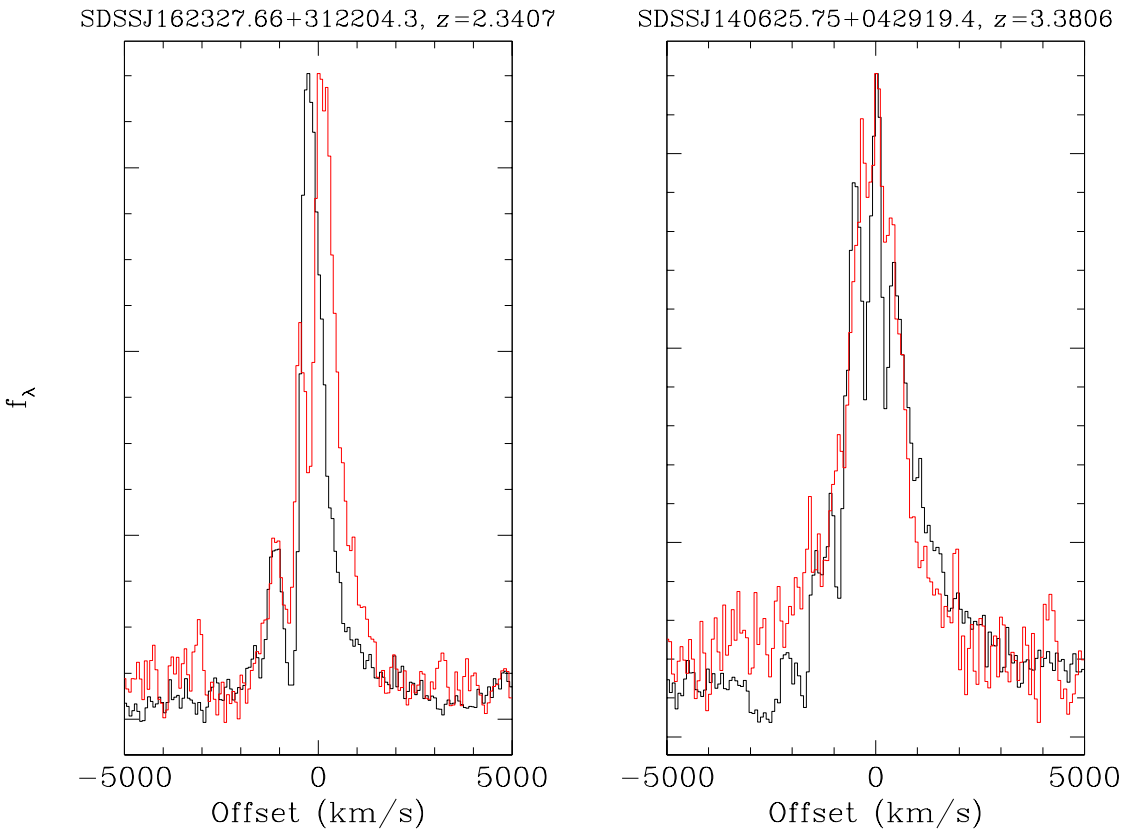

Figure 2.9: Lyα (black) and C IV (red) spectra for two Class A objects, represented in velocity space. The two lines have been scaled to the same maximum. These objects have been chosen for their prominent associated absorption in these two lines. While the profiles of the two lines are similar, Lyα shows additional absorption features, suggestive of low-ionization gas. Some of the structure in the C IV line reflects the fact that it is a doublet. About 12% of our Class A objects show such associated absorption in their BOSS spectra.

2.5.1 Radio: Faint Images of the Radio Sky at 20cm

The FIRST survey (Becker et al., 1995) covers most of the SDSS footprint and was performed using the National Radio Astronomy Observatory (NRAO) Very Large Array (VLA) in its B-configuration in two channels at 1365 and 1435 MHz (∼20 cm). Images were produced covering 1.8″ pixel^{-1} with an rms of 0.15 mJy and a resolution of 5″. Roughly 30% of FIRST sources have optical counterparts in SDSS imaging (Ivezić et al., 2002).

Radio-loud Type II quasars are well-studied at high redshift (McCarthy, 1993); the typical high-redshift radio galaxy shows strong narrow emission lines reminiscent of the objects in our sample. There are only 12 objects in our sample of 452 Class A and B candidates (less than 3%) that match within 3″ of a FIRST source[4]; of these, only three are among the 145 Class A candidates. These are listed in Table 5.2. However, the depth of the FIRST survey is insufficient to designate an undetected object in our sample as radio-quiet (Ivezić et al., 2002). Moreover, this classification depends on the ratio of optical to radio flux, and if the optical flux in our sources is significantly extincted, the optical-to-radio ratio is meaningless. Indeed, while 8-20% of all Type I AGN are radio-loud (Zakamska et al., 2004), only 1.5% of Type I quasars in the DR9 quasar catalog with $21.5 < i < 22$ and redshifts between 2 and 3 are detected in the FIRST catalog. The radio-loud fraction of Type I quasars is lower

[4]using the on-line catalog at `http://sundog.stsci.edu/`

at higher redshift (Jiang et al., 2007); it is possible that this also affects the number of radio detections in our sample.

Of the 12 matches, only one, SDSSJ081257.15+181916.8, appears double-lobed in the FIRST images, with a separation between the lobes of roughly 10″, corresponding to a physical separation of about 80 kpc.

Table 2.6: FIRST Survey radio detections of Class A and Class B candidates.

Name	Peak Flux (mJy/beam)	Integrated Flux (mJy)
Class A		
SDSSJ081257.252+181914.77	2.10	3.31 ± 0.146
SDSSJ112343.182-010315.47	2.09	1.57 ± 0.154
SDSSJ114753.301+3131 2.99	2.04	1.57 ± 0.278
Class B		
SDSSJ005018.623+050132.50	1.28	0.81 ± 0.130
SDSSJ013556.390-001631.83	1.02	0.93 ± 0.104
SDSSJ093323.128-012307.61	1.13	1.13 ± 0.142
SDSSJ133755.789+402150.20	1.15	0.97 ± 0.135
SDSSJ144437.728-013625.50	5.68	5.33 ± 0.146
SDSSJ145924.058+035622.40	3.31	3.07 ± 0.145
SDSSJ160747.246+162123.67	3.43	3.17 ± 0.138
SDSSJ161404.729+042122.83	10.21	9.89 ± 0.154
SDSSJ163414.493+231737.47	3.38	3.40 ± 0.148

2.5.2 Mid-Infrared: Wide-Field Infrared Survey Explorer (WISE)

WISE (Wright et al., 2010a) observed the entire sky twice in four bands centered at 3.4μm, 4.6μm, 12μm and 22μm (W1, W2, W3 and W4) with 5-σ sensitivity of

0.08, 0.11, 1 and 6 mJy and angular resolution 6.1″, 6.4″, 6.5″ and 12.0″ respectively. At the typical redshift ($z = 2.5$) of our sample, the four WISE bands correspond to rest-frame 1μm, 1.3μm, 3.4μm, and 6.3μm, respectively. Quasar SEDs show a break at $\sim 1\mu$m, longwards of which hot dust can dominate the SED (e.g., Richards et al., 2006a), so only the relatively low-sensitivity W3 and W4 bands can tell us about dust emission in our objects.

Obscured quasars are expected to have a high ratio of rest-frame IR-to-optical emission. The IR light is produced by thermal emission of the obscuring material, so it should be present in both obscured and unobscured quasars, whereas the optical light is strongly suppressed in the latter. Unfortunately, the high redshifts of our candidates mean that WISE probes the rest-frame near-IR emission, which is not produced by the obscured material in large amounts and is thus not particularly strong in the SED of unobscured quasars (Figure 2.12). Furthermore, in obscured quasars the rest-frame near-IR may also be affected by extinction. The exception is the 22μm band of WISE, which probes close to the peak of the infrared emission, but in most cases the WISE catalog in this band is not sensitive enough for detecting our sources.

We accessed the WISE Source Catalog using the NASA/IPAC Infrared Science Archive (IRSA)[5] and conducted a search within 2″ of the positions of our class A and class B quasar candidates. Forty of our class A objects (27.6%) and 62 (20.2%) of

[5] `http://irsa.ipac.caltech.edu/cgi-bin/Gator/nph-dd`

our class B objects appeared in the WISE catalog. While Wu et al. (2012) found that more than 85% of optically bright quasars ($i < 19.5$) in DR7 had a WISE match, less than 50% of those with $i > 20.5$ were matched, consistent with our result. While the S/N is typically low in bands W3 and W4 (due to the decreased sensitivity of these bands), 27 class A sources and 29 class B sources have a S/N above 5 in both bands W1 and W2 (only objects that were detected with a S/N > 5 in at least one band are included in the WISE All-Sky Release Catalog). These sources are listed in Tables 2.7 and 2.8 [6]. WISE magnitudes are given on the AB system (Oke & Gunn, 1983). Note that many errors are listed as "null", indicating that the source is undetected in that band; the values listed represent $2\,\sigma$ upper limits on the flux.

There are only nine Class A objects with S/N above 5 in W3, and only two in W4. Ross et al. (in preparation) will discuss the properties of the most extreme W4 detections, with colors approaching those of the dust-obscured galaxy population discovered by Dey et al. (2008), among the SDSS and BOSS quasars. While none of these most extreme sources are among our Type II quasar candidates, several of them show very weak continuum and broad emission lines. While their line widths are above our nominal 2000 $\mathrm{km\,s^{-1}}$ limit, their high IR-to-optical ratios suggests that they are obscured quasars. We will explore relaxing our rigid line-width criterion in future work.

Figure 2.10 shows the WISE $[3.6] - [4.5]$ color of Class A sources as a function of

[6]Full tables are available online at http://vizier.cfa.harvard.edu/viz-bin/VizieR?-source=J/MNRAS/435/3306

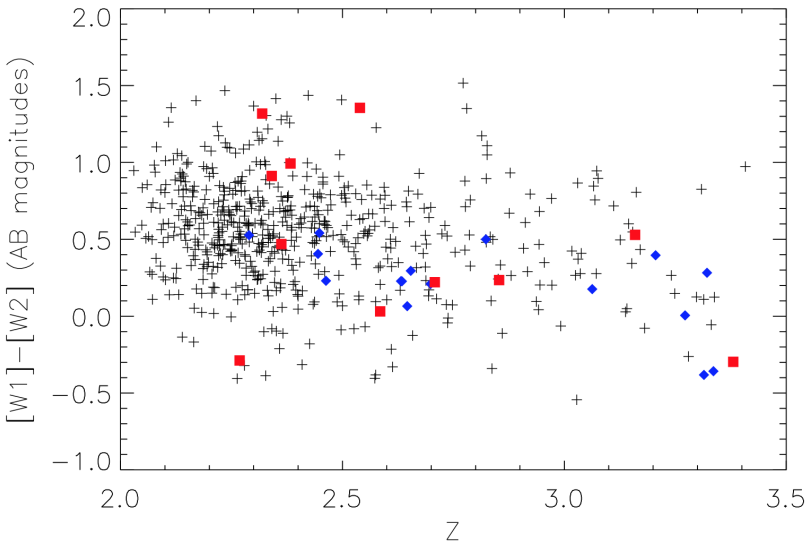

Figure 2.10: WISE color (W1-W2; i.e., [3.4]-[4.6]) as a function of redshift for candidate Type II quasars below redshift 3.5; red squares are those objects detected above 5σ in both bands, while the blue diamonds are sources detected below 5σ in one or both bands. The gray crosses are a sample of Type I quasars from DR9 with a similar distribution of i-band magnitude with WISE detections, and thus similar photometric errors. The distribution of colors is indistinguishable between the two samples with a K-S test.

redshift; a sample of DR9 BOSS quasars with similar i-band magnitudes is included for comparison. The colors of both samples become bluer at redshift $z \sim 3.5$, when Hα enters the W1 band (although this redshift range is not shown in Figure 2.10). A K-S test says the color distributions of the two are the same at the 99.99% level for those objects with redshift less than 3.5; there is no evidence that the Type II objects are redder in this color than unobscured quasars of similar brightness.

Similarly, Figure 2.11 measures a color between the SDSS and WISE bands. A K-S test shows that the color distributions are the same at the 99.9% confidence level. Much of the scatter in this diagram and Figure 2.10 is due to measurement errors both in SDSS and WISE; these detections are often near the flux limit of both surveys.

Table 2.7: All WISE matches in our Class A sample. Values are given in AB magnitudes.Only a portion of this table is shown here to demonstrate its form and content. A machine-readable version of the full table is available online at http://vizier.cfa.harvard.edu/viz-bin/VizieR?-source=J/MNRAS/435/3306.

SDSS Name	W1	W1err	W2	W2err	W3	W3err	W4	W4err
SDSS0046+0005	19.77	0.19	18.92	0.22	16.57	null	14.44	0.25
SDSS0146+1211	19.60	0.12	19.42	0.19	17.24	null	15.28	null
SDSS0154+0157	20.40	0.21	20.44	0.47	18.13	null	15.63	null
SDSS0206+0104	19.61	0.12	19.31	0.18	17.49	0.29	15.83	0.47
SDSS0232+0028	19.49	0.10	18.96	0.12	17.95	0.44	16.07	0.53

Table 2.8: All WISE matches in our Class B sample. Values are given in AB magnitudes.Only a portion of this table is shown here to demonstrate its form and content. A machine-readable version of the full table is available online at http://vizier.cfa.harvard.edu/viz-bin/VizieR?-source=J/MNRAS/435/3306.

SDSS Name	W1	W1err	W2	W2err	W3	W3err	W4	W4err
SDSS0010+0003	19.46	0.15	18.70	0.13	17.38	0.35	15.39	0.51
SDSS0011−0008	19.29	0.12	19.67	0.34	17.51	0.45	15.10	null

SDSS0201+0134	20.16	0.19	20.06	0.36	17.77	null	15.38	null
SDSS0232−0812	18.46	0.05	18.38	0.07	17.17	0.20	16.00	0.50
SDSS0234−0754	20.55	0.23	19.42	0.16	17.62	0.33	16.10	null

2.5.3 Mid-Infrared: Spitzer MIPS-24

Only a handful of objects are detected in the long wavelength filters of WISE. In order to obtain an independent estimate of the bolometric luminosities of our sources, we have searched the Spitzer Space Telescope archive for serendipitous coverage of our Class A and Class B samples. Using the Spitzer Heritage Archive[7], we searched for Multiband Imaging Photometer (MIPS; Rieke et al. 2004) 24μm data covering the positions of our Class A and Class B sources. MIPS-24 is fairly close to the peak of the spectral energy distribution for normal unobscured quasars, whereas serendipitous MIPS observations at longer wavelengths (70 and 160μm) are too shallow to yield any detections of our sources.

We found 13 sources that are covered by MIPS-24 observations. Several objects are covered by multiple exposures, which we coadded to increase the effective exposure time at the positions of our targets. We then conducted aperture photometry at the SDSS positions (accurate to 0.1″; Pier et al. 2003), using a circular aperture with a radius of 12″ and a background annulus between 12″ and 18″.

The photometric measurements are presented in Table 2.9. Five out of 13 sources are detected at the $4\,\sigma$ level or greater; another four sources are marginally detected.

[7] `http://sha.ipac.caltech.edu/applications/Spitzer/SHA/`

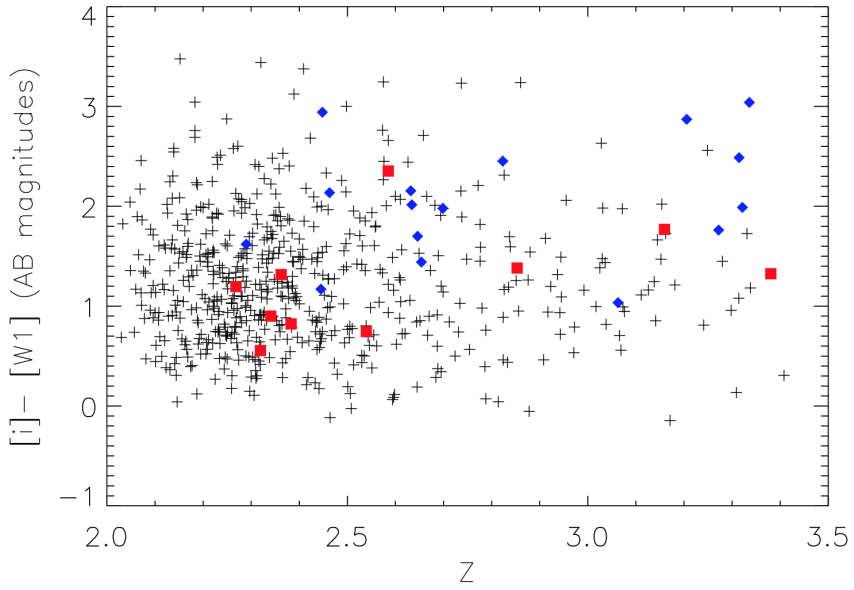

Figure 2.11: The color of Type II candidates between the SDSS i and W1 bands, as a function of redshift; symbols are as in Figure 2.10. The distributions of colors of the Type II and Type I samples are indistinguishable with a K-S test.

We used the observed Spitzer fluxes to calculate the rest-frame monochromatic luminosity at 6μm. At the redshifts of our detected sources, an observed wavelength of 24μm corresponds to rest-frame 5.9−7.3μm; we k-correct to 6μm using $F_\nu \propto \nu^{-1.09}$ from the average Type I spectral energy distribution by Richards et al. (2006a). The bolometric luminosities of our objects can be estimated by multiplying the monochromatic luminosities at 6μm by a factor of 8, again taken from Richards et al. (2006a).

Thus approximately half of the objects covered by the MIPS-24 data are detected at the level 0.5−1 mJy, with detection luminosities in the range $\nu L_\nu[6\mu\mathrm{m}] = 10^{45.4-45.9}$ erg s^{-1} and estimated bolometric luminosities $10^{46.3-46.8}$ erg s^{-1}. Thus these objects are indeed very luminous quasars.

Table 2.9: Spitzer 24μm Data

Object	Flux Density (mJy)	Class	$\log(\nu L_\nu[6\mu\mathrm{m}])$ erg s^{-1}
Detections:			
SDSSJ095819.35+013530.5	0.76 ± 0.10	A	45.89
SDSSJ010554.41+011326.9	0.85 ± 0.16	B	45.94
SDSSJ122353.62+050321.0	1.01 ± 0.12	B	45.77
SDSSJ135136.57+381642.8	0.42 ± 0.11	B	45.39
SDSSJ142610.76+341738.9	1.07 ± 0.12	B	45.72
Marginal detections:			
SDSSJ021834.53-033518.5	0.21 ± 0.06	A	
SDSSJ161447.98+354221.2	-0.11 ± 0.14	A	
SDSSJ020546.33+013907.6	-0.10 ± 0.14	B	
SDSSJ022429.14−024807.7	-0.28 ± 0.08	B	
SDSSJ115840.06+014335.3	0.15 ± 0.06	B	
SDSSJ121326.70+062922.8	0.24 ± 0.07	B	
SDSSJ124219.55+413720.6	0.21 ± 0.08	B	
SDSSJ141649.80+365012.2	0.87 ± 1.04	B	

2.5.4 X-Ray: XMM-Newton, Chandra and ROSAT

Luminous X-ray emission is nearly ubiquitous in unobscured quasars (e.g. Mushotzky, 2004; Gibson et al., 2008), and high-quality X-ray spectra of these Type II quasar candidates could usefully constrain their obscuration levels and/or intrinsic luminosities (e.g. Brandt & Hasinger, 2005; Vignali et al., 2010; Alexander et al., 2011; Comastri et al., 2011; Jia et al., 2013). We therefore have searched the Chandra, ROSAT, and XMM-Newton archives for sensitive X-ray coverage of the sources in our sample. Sources having sensitive X-ray coverage were individually inspected in X-ray and SDSS images to assess critically the reliability of putative X-ray detections and X-ray/SDSS associations. This screening identified five X-ray detected

objects and another that is likely X-ray detected (SDSSJ160554.89+202729.87); the X-ray properties of these sources are listed in Table 2.10. All of these sources were serendipitous detections rather than the targets of their respective observations. In addition, five sources (SDSSJ023337.89+002303.69, SDSSJ023359.27+005925.83, SDSSSJ120355.19+014348.98, SDSSJ144227.31−004725.04, and SDSSJ144441.05−001343.44) are undetected in X-rays in observations of generally comparable sensitivity to those that yielded the detections in Table 2.10.

Table 2.10: X-Ray detections of Type II quasar candidates by Chandra, ROSAT, and XMM-Newton. Three of the sources are included in the second XMM-Newton serendipitous source catalogue (2XMM;Watson et al. 2009). The screened effective exposure time corrects for the effects of vignetting and for time lost to flares.
[1]Two-photon detection; in NDWFS Bootes field,
[2]ROSAT identification likely correct but needs verification.

SDSS Coordinate	Facility	Observation ID	Screened Effective Exposure (ks)	Energy Band (keV)	Observed Flux (10^{-15} erg s^{-1} cm^{-2})	Notes
014841.83+055024.19	XMM-Newton	0112551501	10.6	0.2-12	16	2XMM
082726.58+262803.00	XMM-Newton	0103260601	11.1	0.2-12	23	2XMM
082726.76+214557.08	Chandra	10268	10.0	0.3-8	31	
095819.35+013530.52	XMM-Newton	0302353301	6.3	0.2-12	24	2XMM
142610.77+341738.85	Chandra	7388	4.5	0.5-8	4.8	[1]
160554.89+202729.87	ROSAT	rp600588n00	16.1	0.5-2	8.6	[2]

The sources with X-ray detections in Table 2.10 have 2–99 counts; five of the six sources have 45 or fewer counts. Most also have high backgrounds in the source detection cell owing to large off-axis angles. Thus, unfortunately, none of these sources has sufficient S/N for useful X-ray spectroscopy that could constrain, via X-ray spectral shape, absorption and intrinsic luminosity. Additional X-ray observations are required to perform such spectroscopy. Alternatively, once independent multiwavelength luminosity indicators are available for these sources (e.g., [O III] 5008 Å and far-infrared luminosities), these can be correlated with even basic X-ray emission measurements to assess obscuration levels (e.g. Vignali et al., 2010; Jia et al., 2013).

2.5.5 Cosmic Evolution Survey

The Cosmic Evolution Survey (COSMOS)[8] covered 2 deg^2 with the Hubble Space Telescope (HST) Advanced Camera for Surveys (ACS; Koekemoer et al., 2007), the VLA (Schinnerer et al., 2004), the Spitzer Space Telescope (Sanders et al., 2007), XMM-Newton (Hasinger et al., 2007) and other facilities. One of our sources, SDSSJ095819.35+013530.5 at $z = 3.0554$ (hereafter SDSS0958+0135), lies in the COSMOS field. This object therefore has extensive multi-wavelength coverage and an exquisitely measured SED. The optical and NIR photometry from 15 bands is available via the Infrared Science Archive (IRSA), and so is the Spitzer IRAC (3.6μm-8μm) and MIPS-24μm photometry (as we saw in § 2.5.3). The source is not in the

[8] `http://cosmos.astro.caltech.edu/index.html`

MIPS-70μm catalog of COSMOS. We co-added all 14 available MIPS-70μm exposures, conducted aperture photometry and obtained a tentative detection with a flux of 1.13 ± 0.7 mJy.

In Figure 2.12 we use multi-band data from the COSMOS survey to construct the SED of this object and compare it with those of a Type I quasar template from Richards et al. (2006a) and a Type II (obscured) quasar template derived from Spitzer data (Zakamska et al., 2008) of low-redshift luminous optically-selected obscured quasars (Zakamska et al., 2003). The templates have been arbitrarily normalized to match the observed SED at rest-frame 6μm (as measured by MIPS-24μm).

The SED of SDSS0958+0135 shows several noteworthy features. The ultraviolet to infrared flux ratio is significantly lower than in unobscured quasars (and the high equivalent width of Lyα in emission contributes significantly to the ultraviolet flux). However, the ultraviolet emission in this source is not as suppressed as it is in low-redshift obscured quasars. This feature suggests that SDSS0958+0135 is reddened by moderate amounts of dust, perhaps in its host galaxy. Extinction with $A_V = 0.3-0.6$ mag would suppress the ultraviolet continuum by a factor of 3, but would leave longer wavelengths much less affected. Another possibility is that the object is strongly absorbed, and the observed continuum in the ultraviolet is produced by quasar light that is scattered off the material in the host galaxy and reaches the observer, even though the central engine itself is not visible along our line of sight. However, matching the observed optical SED would require $\sim 10\%$ scattering efficiency, which is quite

extreme. Future polarization measurements of the kind discussed in the next section will help distinguish these two possibilities.

The SED of SDSS0958+0135 appears to peak at relatively short wavelengths – around rest-frame 6μm – declining to longer wavelength, which is similar to the shape of the SED of unobscured quasars, and unlike low-redshift obscured quasars whose SEDs tend to show more cold dust emission. The shape of the mid-infrared SED is consistent with that of a reddened quasar, since modest amounts of reddening applied to a Type I spectrum would not affect mid-infrared wavelengths. Another possibility is a strongly obscured source, but with a compact and hot obscuring region rather than an extended colder one. The observed MIPS-24 flux of 0.76 mJy corresponds to a monochromatic luminosity of $\nu L_\nu[6\mu\mathrm{m}] = 7.7 \times 10^{45}$ erg sec^{-1}, as we saw in § 2.5.3. The similarity of the mid-infrared SED of SDSS J0958+0135 to that of Type I quasars enables us to use bolometric corrections derived by Richards et al. (2006a, a factor of 8 at this wavelength), leading to $L_{\mathrm{bol}} = 6 \times 10^{46}$ erg sec^{-1} in this source. This is clearly a very luminous quasar.

As part of the COSMOS survey, this source was observed in the 0.5-2 keV band by XMM-Newton; the inferred luminosity in the 2-8 keV rest-frame is 9.2×10^{43} erg sec^{-1} (not shown in Figure 2.12). This object was also observed by the Hubble Space Telescope in the ACS/F814W filter, just redward of the Lyα emission, for a full orbit (2028 seconds on-source). The object is unresolved in the HST image; neither the emission from the host galaxy nor extended scattered light are detected. At this

redshift, 0.1″, a reasonable upper limit on the size of the object in the ACS data, corresponds to a physical extent of roughly 1 kpc, suggesting a very compact object indeed. This is not surprising if the light is dominated by the direct (albeit reddened) light from the quasar itself. If, on the other hand, the object is a highly obscured quasar, then the limit on the size of the rest-frame ultraviolet emission suggests that the scattering interstellar medium in the host galaxy is compact. This model would be consistent with recent findings that massive galaxies at high redshifts tend to have small effective sizes (Wuyts et al., 2010).

2.5.6 Optical polarization

Optical polarimetry is a classical test of the obscuration-based unification model of active galactic nuclei (Antonucci & Miller, 1985). Even if the direct line of sight to the nucleus is blocked by obscuration, quasar light can escape along an unobscured direction (or sometimes more than one, Schmidt et al. 2007), scatter off free electrons or dust particles in the interstellar medium of the host galaxy, and reach the observer. Since scattered light is polarized, optical polarimetry and spectropolarimetry are uniquely sensitive to the scattered component.

This process occurs both in obscured and unobscured quasars, but in the latter the scattered component is diluted by the emission from the quasar itself, so the typical levels of polarization in unobscured quasars is 0.5% (Berriman et al., 1990). In obscured or heavily reddened quasars with large enough column density along the

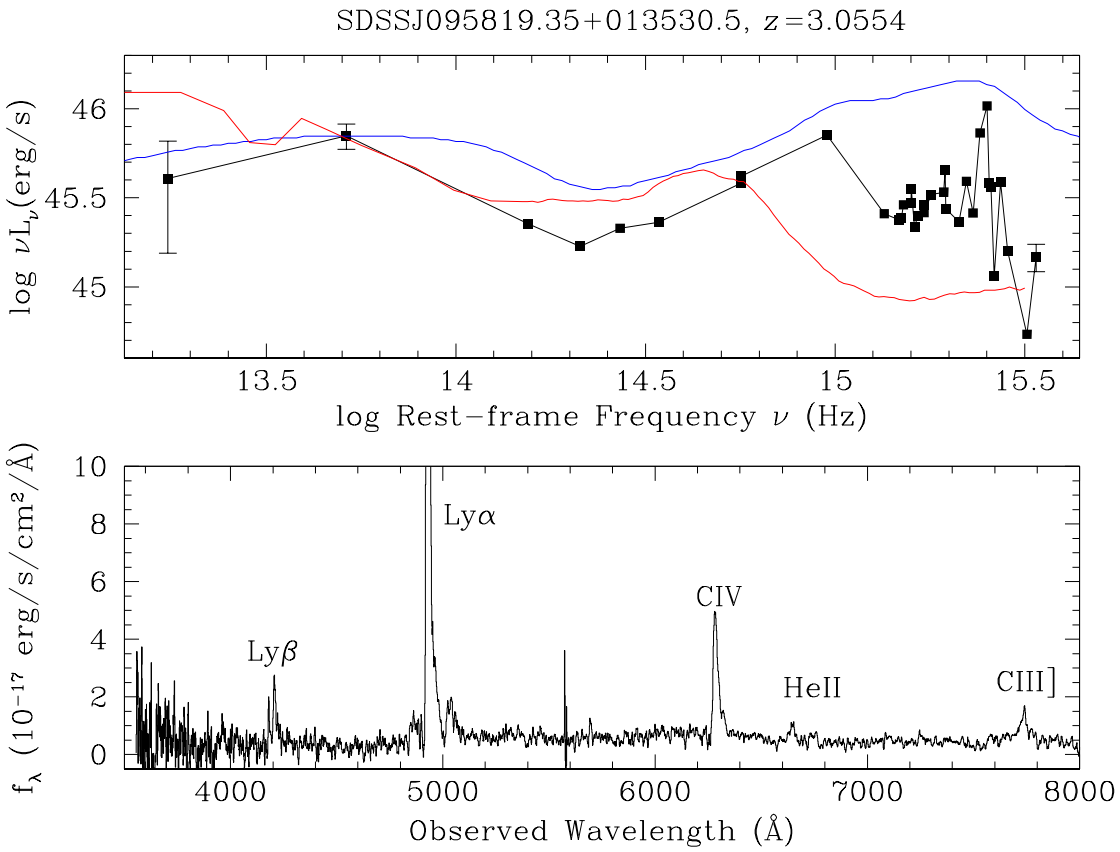

Figure 2.12: Top: The spectral energy distribution (SED) of SDSS0958+0135, which lies in the COSMOS field, including data from the Spitzer Space Telescope and a variety of ground-based facilities. The peak at $\log \nu = 15.4$ is due to Lyα emission. For comparison, the blue line is the composite Type I SED from Richards et al. (2006a) and the red line is the mean low-redshift Type II quasar SED (Zakamska et al., 2008). All curves are normalized to a rest-frame frequency of $10^{13.7}$ Hz (6 μm, corresponding to the 24 μm detection with Spitzer). **Bottom:** The BOSS spectrum of this source with expanded vertical and horizontal axes (the peak of the Lyα line is well off-scale), with emission lines marked. The C IV line is markedly asymmetric, perhaps indicating self-absorption on the blue side.

line of sight, the scattered component dominates over the direct emission, and the typical levels of polarization are much higher – a few per cent (Tran, 1995a; Smith et al., 2002, 2003; Zakamska et al., 2005), reaching $\gtrsim$ 20% in several exceptional cases (Hines et al., 1995; Smith et al., 2000; Zakamska et al., 2005). Thus high levels of polarization are strongly suggestive of an obscured active nucleus. The spectrum of the polarized component can be that of an unobscured quasar, showing a blue continuum and broad permitted emission lines (Antonucci & Miller, 1985; Zakamska et al., 2005).

In 2012 September we observed two high-redshift Type II quasar candidates from our Class A sample with the CCD Spectropolarimeter (SPOL; Schmidt et al. 1992b) on the 6.5m MMT using the National Optical Astronomical Observatory time allocation in sub-optimal weather conditions. SDSSJ220126.11+001231.5 was observed over 4 hours, and SDSSJ004728.77+004020.3 over 2 hours, with a 1.1″ slit and low-resolution grating, resulting in wavelength coverage of 4000-8000 Å and spectral resolution 19 Å. Because the sources are faint ($i = 20.7$ and $i = 21.2$ mag, respectively), we bin the data in wavelength, allocating bins separately for continuum-dominated and emission-line-dominated regions. The combined results of the MMT observations are shown in Figure 2.13. Unfortunately, this binning and the limited S/N mean that we are not able to measure the width of the lines in polarized light.

When averaged over the high S/N continuum region of 5000−7000 Å, SDSS2201+0012 is polarized at a level of $1.9 \pm 0.3\%$, with position angle $176^\circ \pm 4^\circ$ (East of North).

This polarization is significantly higher than the typical polarization of unobscured quasars (0.5%), any instrumental systematics ($\lesssim 0.1\%$), or polarization that can be acquired due to the propagation of light through the dust in the Galaxy ($< 0.8\%$, Berriman et al. 1990). There is no evidence that the narrow emission lines are polarized any less than the surrounding continuum, indicating that the scattering medium is distributed on scales that are larger than the narrow line region. For the COSMOS source (§ 2.5.5), we concluded that the scattering region had to be compact; additional spectrophotometry and high-resolution imaging of the same sources (Zakamska et al., 2006) will be valuable to determine whether there is a contradiction here.

The polarization fraction rises toward the blue part of the spectrum, where it reaches >5%. This change is either indicative of a wavelength-dependent scattering mechanism or of a red unpolarized component that dilutes blue polarized light (Zakamska et al., 2005). Since electrons scatter optical and UV light in a wavelength-independent manner, the first possibility calls for dust particles to be primarily responsible for scattering. This is not an uncommon occurrence, especially in high-luminosity obscured or reddened quasars where scattering occurs over a large fraction of the entire host galaxy (Hines et al., 2001; Zakamska et al., 2005; Schmidt et al., 2007) rather than being confined to the highly ionized circumnuclear material (Antonucci & Miller, 1985). However, the contribution of the unpolarized but reddened quasar continuum can mimic the wavelength dependence of the polarized fraction, and we cannot rule out either of these explanations with the current data. Rest-

frame optical (observed-frame near-infrared) observations will help distinguish these scenarios by allowing us to determine the shape of the continuum and thus the level of quasar obscuration. The high S/N MMT spectrum reveals a hint of a broad shallow absorption feature blueward of C IV, which is thought to come from the central region in AGN, suggesting that the light from the central engine is not completely obscured. In any case, the high level of polarization seen in SDSS2201+0012 strongly suggests that it is either an obscured or a heavily reddened quasar.

SDSS0047+0040 is not as highly polarized as SDSS2201+0012, with a average polarization over 5000 to 7000Å of $0.91 \pm 0.35\%$ (position angle $28^\circ \pm 10^\circ$). The most striking feature in this source is that the mini-absorption trough blueward of the C IV emission line is polarized at a level of $\sim 6\%$, or $> 3\sigma$ higher than the continuum. This feature is similar to that seen in broad absorption line quasars (e.g., DiPompeo et al. 2011). Indeed, in these sources the absorption trough blocks the direct light from the quasar and thus suppresses the quasar continuum contribution relative to the scattered light emission produced on larger spatial scales, increasing the level of polarization seen within the trough relative to that seen at other wavelengths. We conclude that the modest level of polarization of SDSS0047+0040 and the polarization increase within the mini-trough suggest that some of the continuum in this source is direct quasar light. The definitive test whether these two objects are obscured would be broad emission lines in the polarized spectrum. This will require substantially higher S/N spectropolarimetry than we have obtained.

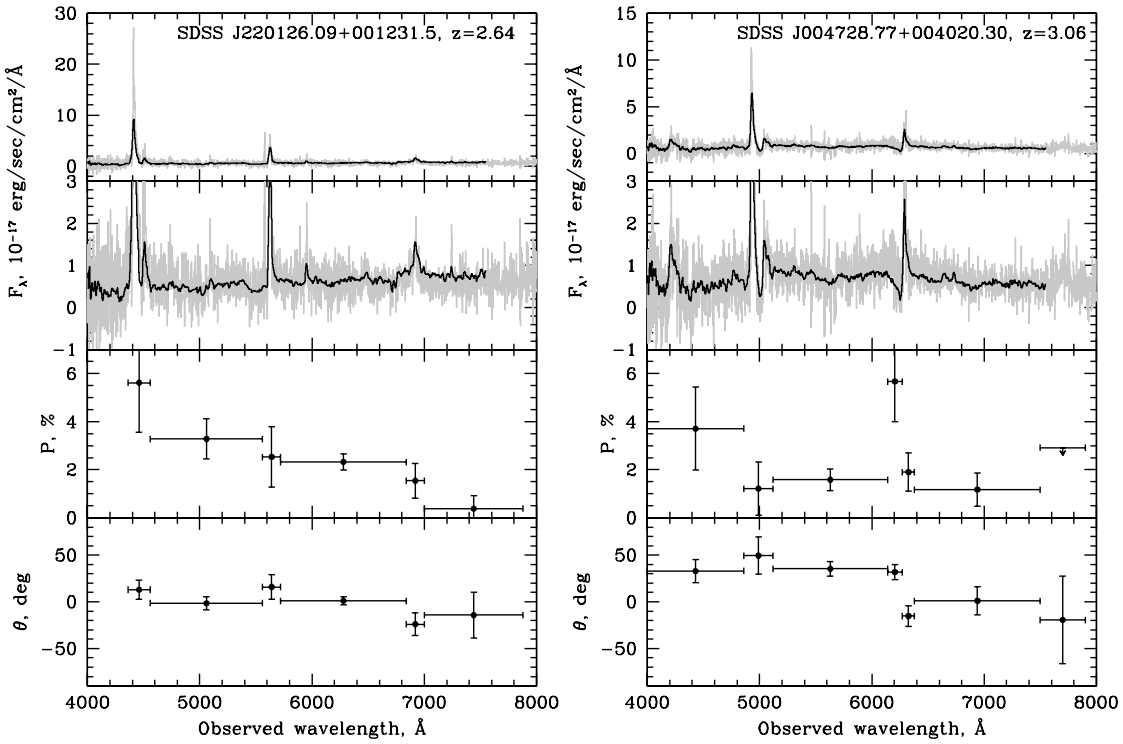

Figure 2.13: Results of spectropolarimetric observations of two candidate obscured quasars with SPOL on MMT. In the top panels, we show the BOSS spectra in gray and MMT spectra in black (both the overall spectra and an expanded view to highlight weak features are shown). The MMT spectra were taken in non-photometric conditions and have been scaled up by a factor ~ 1.5 to line up with the SDSS continuum. In the bottom panels we show the fractional polarization measured using SPOL observations, in percent, and the polarization position angle in degrees E of N. These have been binned over interesting wavelength regions (continuum and lines) to build up S/N.

2.6 Discussion

We consider our objects to be candidate Type II quasars by drawing an analogy with the defining characteristics of Seyfert II galaxies at lower redshift: narrow permitted lines seen in the rest-frame ultraviolet, and a relatively weak continuum, as quantified by high equivalent widths of these lines. The key questions, which we have yet to answer, are: (a) what are the intrinsic luminosities of these objects; and (b) what is the range of the obscuration we probe in this sample. We do know that at least some of these sources are highly luminous ($> 10^{46}$ erg sec^{-1}), given detections in the Spitzer MIPS 24μm band (§ 2.5.3). Although WISE data do not go out to long enough wavelengths to probe the peak of the IR SED, they indicate similarly high luminosities for a few other sources in this sample. X-rays are another probe of unobscured luminosity; observations in the 2-10 keV energy range sample rest-frame energies from 7 to 35 keV, where even moderately Compton-thick sources should be detected. We have serendipitous detections of a handful of sources (§ 2.5.4), but targeted observations with Chandra or XMM-Newton will yield new insights into their true luminosities.

Our objects have continuum absolute magnitudes of -23 and brighter in the ultraviolet (Figure 2.6); this is too luminous to be explained by the stellar continuum of the host galaxy of an obscured quasar. Indeed, the brightest unlensed galaxies known at $z > 2$ are roughly $r = 24$ (Shapley, 2011), two magnitudes fainter than the faintest objects in our sample. Thus the continuum light that we are seeing must

be dominated by the nucleus itself. There are three possible explanations: (a) these sources are only modestly extincted ($A_V \sim 0.5$, corresponding to 1.5 magnitudes of extinction at 1500 Å for an $R = 3.1$ extinction law), (b) substantial amounts of quasar continuum light are scattered by distributed dust or electrons, as is seen in lower-redshift Type II quasars, or (c) the line of sight to the central region is heavily obscured, but the covering fraction is not complete, allowing some amount of unobscured continuum through. The relatively blue continuum and the broad bases seen on the emission lines in the composite spectrum (Figure 2.7) are consistent with all three of these hypotheses, and the rough similarities in the broad-band colors and SEDs of these objects and Type I objects are supportive of the scattering and partial covering hypotheses. We have polarization data on only two objects to date (§ 2.5.6); the fact that both objects are strongly polarized suggests extincted objects with substantial scattering. It may well be that our sample is heterogeneous, with some more extincted than others. With this in mind, it is dangerous to draw conclusions about the whole population from just a few objects.

Lower-redshift obscured quasars have been identified as such by their narrow Balmer emission lines. Near-infrared spectroscopy allows measurement of these lines directly in our high-redshift objects, to determine whether the permitted lines remain narrow at wavelengths where extinction due to dust is significantly smaller. We report observations in the near-infrared in Greene et al. (2014); consistent with the modest extinction hypothesis, many of our sources do show evidence for broad Balmer lines.

The near-infrared data will also allow us to measure the luminosity in the [O III]5008Å emission line, which has been used as a proxy for bolometric luminosity.

If the continua in these objects include a contribution from scattering, we might detect extended scattered emission in high-resolution images, as is seen in lower-redshift Type II quasars (Zakamska et al., 2006). The COSMOS object is unresolved in HST images, but we have an ongoing HST program to image six sources from our survey; the results will be presented in a future paper.

If the continuum we are seeing from these objects is dominated by scattered light on kpc scales, one would not expect to see variability on human timescales. A number of our objects fall on the Equatorial Fall Stripe in the Southern Galactic Cap ("Stripe 82"), which was repeatedly imaged during the SDSS (Abazajian et al., 2009), allowing a search for such variability.

In future work, we hope to use this sample to quantify the relative numbers of obscured and unobscured quasars as a function of redshift and luminosity. This is a challenging task, given the uncertainties we have just discussed about the amount of extinction and the true luminosities of our sources. However, these objects are not extremely rare: the 145 sources in our Class A sample are drawn from SDSS DR9, which represents only the first year of BOSS data taking, or about 1/3 of the final BOSS survey. We can expect the sample to triple in size by the time of the final BOSS data release in late 2014. Future wide-angle spectroscopic surveys on larger telescopes, such as those to be carried out by the Prime Focus Spectrograph being

built for the Subaru Telescope (Takada et al., 2014), may reveal substantially more such objects.

2.7 Conclusions

We have identified a sample of candidate Type II quasars at redshifts between 2.0 and 4.3 from the spectra of the Baryon Oscillation Spectroscopic Survey. They are characterized by strong narrow (FWHM < 2000 km s^{-1}) Lyα and C IV emission lines of high equivalent width. Our sample includes 145 "Class A" objects, plus an additional 307 "Class B" objects whose classification is less certain. Our main conclusions are as follows:

- These objects have continuum absolute magnitudes of -23 and brighter, suggesting that the quasar continuum is only modestly extincted, that the extinction is patchy, or that the quasar continuum is strongly scattered.

- A composite high S/N spectrum shows broad bases (FWHM~ 3500 km s^{-1}) in many emission lines, suggesting modest extinction or substantial scattering of light from the central engine.

- The distribution of broad-band colors of these objects from the rest-frame ultraviolet to 1μm are consistent with those of unobscured quasars at the same redshift.

- The ratios of the strengths of the C IV, He II, and C III emission lines are distinctly different from those of other classes of Type II AGN at high redshift, suggesting a higher ionization parameter and a lower metallicity than these other samples.

- Many of the objects show significant self-absorption in the Lyα and C IV emission lines, often blue-shifted relative to the rest-frame peaks of the lines, suggesting substantial absorbing gas and outflows.

- Serendipitous observations of a dozen objects at 24μm with the Spitzer Space Telescope imply bolometric luminosities above 10^{46} erg s^{-1}.

- Polarization measurements of two objects suggest that there is a significant scattered component to the continuum.

- Further insights into the intrinsic luminosities, obscuration, and physical nature of these sources will require additional X-ray, near- and mid-infrared, and spectropolarimetric observations.

Acknowledgments

We thank Kevin Hainline and Dan Stern for useful discussions and the use of their spectra, and Gordon Richards and Joe Hennawi for useful comments on an early draft of the paper.

Funding for SDSS-III has been provided by the Alfred P. Sloan Foundation, the

Participating Institutions, the National Science Foundation, and the U.S. Department of Energy Office of Science. The SDSS-III web site is `http://www.sdss3.org/`.

SDSS-III is managed by the Astrophysical Research Consortium for the Participating Institutions of the SDSS-III Collaboration including the University of Arizona, the Brazilian Participation Group, Brookhaven National Laboratory, University of Cambridge, Carnegie Mellon University, University of Florida, the French Participation Group, the German Participation Group, Harvard University, the Instituto de Astrofisica de Canarias, the Michigan State/Notre Dame/JINA Participation Group, Johns Hopkins University, Lawrence Berkeley National Laboratory, Max Planck Institute for Astrophysics, Max Planck Institute for Extraterrestrial Physics, New Mexico State University, New York University, Ohio State University, Pennsylvania State University, University of Portsmouth, Princeton University, the Spanish Participation Group, University of Tokyo, University of Utah, Vanderbilt University, University of Virginia, University of Washington, and Yale University. RA and MAS acknowledge the support of NSF grant AST-0707266, and JEG and NZ acknowledge the support of Alfred P. Sloan Foundation Fellowships. NZ is also supported by the Theodore Dunham, Jr., Grant of the Fund for Astrophysical Research. WNB acknowledges the support of NASA ADAP grant NNX10AC99G and NSF grant AST-1108604.

This research has made use of the NASA/IPAC Infrared Science Archive, which is operated by the Jet Propulsion Laboratory, California Institute of Technology, under contract with the National Aeronautics and Space Administration.

Chapter 3

Sensitive radio survey of obscured quasar candidates

We study the radio properties of moderately obscured quasars in samples at both low ($z \sim 0.5$) and high ($z \sim 2.5$) redshift to understand the role of radio activity in accretion, using the Karl G. Jansky Very Large Array (VLA) at 6.0GHz and 1.4GHz. Our $z \sim 2.5$ sample consists of optically-selected obscured quasar candidates, all of which are radio-quiet, with typical radio luminosities of $\nu L_{\nu}[1.4\ \mathrm{GHz}] \lesssim 10^{40}$ erg s^{-1}. Only a single source is individually detected in our deep (rms$\sim$ 10 μJy) exposures. This population would not be identified by radio-based selection methods used for distinguishing dusty star-forming galaxies and obscured active nuclei. In our pilot A-array study of $z \sim 0.5$ radio-quiet quasars, we spatially resolve four of five objects on scales $\sim$ 5 kpc and find they have steep spectral indices with an

average value of $\alpha = -0.75$. Therefore, radio emission in these sources could be due to jet-driven or radiatively driven bubbles interacting with interstellar material on the scale of the host galaxy. Finally, we also study the additional population of $\sim$ 200 faint ($\sim$ 40μJy - 40mJy) field radio sources observed over $\sim$ 120 arcmin^2 of our data. 60% of these detections (excluding our original targets) are matched in the Sloan Digital Sky Survey (SDSS) and/or Wide-Field Infrared Survey Explorer (WISE) and are, in roughly equal shares, active galactic nuclei (AGN) at a broad range of redshifts, passive galaxies with no other signs of nuclear activity and infrared-bright but optically faint sources. Spectroscopically or photometrically confirmed star-forming galaxies constitute only a small minority of the matches. Such sensitive radio surveys allow us to address important questions of AGN evolution and evaluate the AGN contribution to the radio-quiet sky.

3.1 Introduction

The composition of the sub-mJy radio sky, including the active galactic nuclei (AGN) fraction at sub-mJy levels, is still an open question as it is only recently that the capabilities of the expanded Karl G. Jansky Very Large Array (VLA), $5-20\times$ more sensitive than the original VLA, have opened up the realm of sub-mJy radio populations without stacking analysis. A change in the overall slope of differential radio source counts below $\sim$ 1 mJy suggests that a new population of sources be-

gins to contribute below these flux densities. Theoretical predictions (e.g Massardi et al., 2010) and observations by e.g. Bonzini et al. (2013) suggest that at the level of hundreds of μJy the radio sky begins to be dominated by star-forming galaxies. Alternatively, Jarvis & Rawlings (2004) have also suggested, based on X-ray source counts, that type 2 and low luminosity AGN could contribute most of the necessary radio flux below 1 mJy.

Recent deep surveys such as VLA-COSMOS (Schinnerer et al., 2004) and the Extended Chandra Deep Field South (E-CDFS Miller et al., 2013) have differed slightly in their detection fraction of multi-wavelength counterparts (essential for proper source classification), their classification schemes and results. In the E-CDFS, which covered ≈ 0.3 deg^2 down to an average 5σ flux density of ≈ 37 μJy with the VLA at 1.4 GHz, Bonzini et al. (2013) found that AGN made up 43% of their entire sample of 883 sources, being 100% of sources at ~ 10 mJy but only 38% at the survey limit with the remainder of sources being star-forming (SF) galaxies. Meanwhile, Smolčić et al. (2008) find a nearly constant combined fraction of 70% for AGN and quasars in the VLA-COSMOS Survey, covering 2 deg^2 in the COSMOS field down to the survey flux limit of 50 μJy.

At a given bolometric AGN luminosity, the observed radio power varies over many orders of magnitude, with only a small fraction ($\approx 15 - 10\%$) of the most luminous optically-selected sources displaying classical radio-loud jets on kiloparsec scales (Kellermann et al., 1989; Xu et al., 1999; Zakamska et al., 2004). Classically, radio

sources are divided based upon the ratio of their radio luminosity to optical luminosity (or "radio-loudness"), though there is continued disagreement as to whether these two populations, "radio-loud" and "radio-quiet" sources represent a true dichotomy (e.g. Kellermann et al., 1989; Ivezić et al., 2002; Dunlop et al., 2003; White et al., 2007; Bonchi et al., 2013). If there is a break or bimodality in the radio luminosity function of quasars (Kimball et al., 2011; Condon et al., 2013), this might suggest that two different mechanisms may be responsible for the radio emission in the radio-loud and radio-quiet quasar populations.

It is not clear what mechanism would produce the radio emission in radio-quiet quasars. Currently there are four working hypotheses: (i) radio-quiet quasars are simply the scaled-down version of their radio-loud counterparts, implying that the radio emission observed is from a compact jet (Kukula et al., 1998; Ulvestad et al., 2005; Giroletti & Panessa, 2009). (ii) Radio emission could also be due to synchrotron emission in accretion disk corona(Laor & Behar, 2008; Raginski & Laor, 2016). (iii) The presence of a relationship between the kinematics of ionized gas in local Type 2 radio-quiet quasars and their radio luminosity (Mullaney et al., 2013; Zakamska & Greene, 2014) suggests that quasar-driven outflows could be the source of the radio emission in radio-quiet quasars (Stocke et al., 1992; Faucher-Giguère & Quataert, 2012; Zubovas & King, 2012; Zakamska & Greene, 2014; Nims et al., 2015).(iv) Finally, radio emission associated with star formation in the host galaxy may be responsible for most or all of the faint radio luminosity in these sources (e.g. Kimball et al., 2011;

Padovani et al., 2011; Condon et al., 2013).

Differentiating between these scenarios is difficult. Some arguments can be made on the grounds of energetics; for example, star formation rates in host galaxies of quasars at $z < 1$ are inadequate to explain the observed radio emission by about an order of magnitude (Zakamska et al., 2016b), though the same argument might not apply to lower luminosity AGN (Rosario et al., 2013) or quasars at $z > 2$ (Kimball et al., 2011; Condon et al., 2013). As for scenarios (i)−(iii), a detailed analysis of radio spectral indices ($F_\nu \propto \nu^\alpha$) and radio morphology for a large sample of quasars presents the best path for differentiating between these possible explanations for the radio emission in radio-quiet quasars. In particular, coronal emission is expected to be on parsec scales and have flat spectral indices ($\alpha \approx 0$; Laor & Behar 2008; Raginski & Laor 2016), similar to parsec-scale cores of radio jets, whereas radio emission produced on larger scales either in winds or in jet-powered lobes or in star formation is expected to have steep spectra ($\alpha \approx -0.7$) and be partially resolved. The resolution and sensitivity capabilities of the upgraded VLA makes such a dedicated study possible for the first time.

Here we present the results of two separate pilot surveys of the sub-mJy radio sky taken with the VLA in A and B-configurations. The data for this project were intended to study the continuum radio properties of radio-intermediate and radio-quiet predominantly optically-obscured quasars at both low ($z \lesssim 0.8$) and high ($z \sim 2.5$) redshifts using observations that were at least 5× deeper than the Faint Images

of the Radio Sky at Twenty Centimeters (FIRST; Becker et al., 1995) survey. In § 5.2 we describe our various sample selection methods as well as the VLA observations and subsequent data reduction and analysis. We look more closely at our samples of high and low-redshift radio-quiet obscured quasars in § 3.3 and § 3.4. Then § 3.5 explores the sample properties of the sub-mJy radio sources we have identified as well as their optical and mid-infrared (MIR) counterparts and we present some interesting sources in § 3.6. Finally, we discuss the implications of our results and offer our conclusions in § 5.6.

We use a $h = 0.7, \Omega_m = 0.3, \Omega_\Lambda = 0.7$ cosmology throughout the paper. We quote radio luminosities k-corrected to the rest frame 1.4 GHz for ease of comparison with other datasets using equation

$$\nu L_\nu[1.4\mathrm{GHz}] = 4\pi D_L^2 (1+z)^{-1-\alpha} \left(\frac{\nu}{\nu_{\mathrm{obs}}}\right)^{1+\alpha} \nu_{\mathrm{obs}} F_{\nu,\mathrm{obs}}. \tag{3.1}$$

Here, ν and L_ν are at 1.4 GHz, and ν_{obs} and $F_{\nu,\mathrm{obs}}$ are at the frequency of our observations (1.4 or 6 GHz), and for k-corrections we use spectral index $\alpha = -0.7$ when it was not possible to calculate the observed value. We observe objects at $z \sim 2.5$ at 1.4 and 6 GHz, corresponding to rest-frame frequencies 5.3 and 21 GHz, and therefore the mismatch between our reference frequency (1.4 GHz) and the rest-frame frequency probed by our observations is quite significant. If the spectral index is $\alpha = -0.3$ instead of -0.7 for a $z = 2.5$ source whose flux density is measured

at $\nu_{\rm obs}$ = 6 GHz, its true 1.4 GHz intrinsic luminosity is 3 times fainter than that inferred from equation (3.1). In § 5.2−§ 3.4, we use SDSS Jhhmm+ddmm notation for identifying our primary targets (the centers of our fields) and in § 3.5-§ 3.6 we use the full SDSS Jhhmmss.ss+ddmmss.s notation for identifying sources in the field.

3.2 Sample Selection, Observations and Data Reduction

In this section we describe the sample selection, the observations, steps of the data reduction and analysis performed on each field.

3.2.1 Sample Selection and Observations

Our high-redshift program VLA/13B-382 targeted a sample of 11 high-redshift ($2.0 < z < 4.2$) obscured quasar candidates from Alexandroff et al. (2013). These sources were originally selected from the Sloan Digital Sky Survey (SDSS) Baryon Oscillation Spectroscopic Survey (BOSS; Dawson et al., 2013) by their narrow emission line widths with a full-width at half maximum (FWHM)< 2000 km s^{-1} in both C IV and Lyα and weak continuum in the rest-frame UV. Only objects from Data Release 9 (Ahn et al., 2012) or earlier are included in this search due to the timeline of the research. Follow-up spectroscopic observations of a sub-sample of twenty-five

of these objects in the rest-frame optical (Greene et al., 2014) showed that most of them have a broad Hα component and that therefore most of these objects must have intermediate values of extinction ($0 < A_{\rm V} < 2.2$ mag) akin to type 1.8/1.9 quasars. The basic radio properties of this population, based on matching with FIRST, were presented by Alexandroff et al. (2013).

We chose eleven objects for deep observations with the VLA (see Table 3.1), selected to have the greatest possible overlap with other multi-wavelength follow-up of the original Alexandroff et al. (2013) sample; none were detected in FIRST. This sample was observed with the VLA in both L- and C-bands (spanning the frequency range of $\approx 1-2$ GHz and $\approx 4-8$ GHz respectively) in the array's B configuration which provides $\sim 4.3''$ and $\sim 1''$ resolution at the given central frequency respectively. The spatial resolution at ~ 6 GHz corresponds to a physical scale of ~ 8 kpc at $z \sim 2.5$.

Observations were scheduled dynamically in blocks of three objects. We observed one flux/bandpass calibrator at the beginning of each observation set. Targets were observed while nodding between a phase/amplitude calibrator every twenty minutes. Total on-source time was 32.5 minutes in the L-band and 28 minutes in the C-band per object. In the L-band, we recorded in full polarization the total 16 contiguous spectral windows with 64×1 MHz channels each to yield a total instantaneous bandwidth of 1024 MHz centered at 1.4 GHz. In the C-band we had two frequency bands centered at ≈ 5 GHz and ≈ 7 GHz respectively, each with 8 spectral windows of 64×2 MHz

channels to yield a total of 2048 MHz bandwidth.

Our low-redshift program VLA/14A-310 originally targeted 106 type 2 and type 1 radio-quiet quasars at $z \lesssim 0.8$ from Reyes et al. (2008) and Liu et al. (2014), but was scheduled as filler, and as a result only five sources were observed (Table 3.2): four type 2 quasars and one type 1. Of the original sample of 106 objects proposed, 80% were detected with FIRST, at no more than the few mJy level. Of the five objects observed, all but one were previously detected in FIRST and only one of the sources in FIRST (SDSS1123+3105) was clearly resolved.

This sample was observed in the C-band ($\approx 4-8$ GHz) in the VLA's A configuration which provides resolution of $0.33''$, corresponding to ~ 2 kpc at $z \sim 0.5$. All objects were observed on April 14, 2014. Based on our experience with the high-redshift program, we adjusted central frequencies of the two bands to 5.25 and 7.2 GHz, which reduced somewhat the effects of radio frequency interference. Observations included the flux standard 3C286 and were conducted with nodding to an appropriate amplitude and phase calibrator. Total on-source time was 11.5 minutes per source.

3.2.2 Data Reduction and Analysis

We reduced the data using the Common Astronomy Software Applications (CASA) package v4.3.0 (McMullin et al., 2007). Raw visibilities were calibrated using the

VLA Calibration pipeline version 1.3.1[1]. All solutions were inspected and additional flagging, as necessary, was accomplished by hand using CASA's *Plotms* task.

All maps were created in CASA at the band center with a Briggs weighting scheme of ROBUST = 2.0 (natural weighting) to maximize our sensitivity to faint sources. The map size was set to match the primary beam full-width at half power which is approximately 7 arcminutes in the C-band. Certain fields included strong sources far from the image center that left residuals in the images which were difficult to clean. In these cases larger maps were created for the purpose of cleaning but the final images analyzed were cropped to be the same size as the rest of the sample. Finally, we corrected every field for primary beam attenuation using the task *pbcorr*. The typical rms at the field center was $\sim 1.5 \times 10^{-5}$Jy/beam for the C-band and $\sim 8 \times 10^{-5}$Jy/beam in the L-band.

3.2.3 CLEAN bias

CLEAN bias is a loss of flux due to sparse uv-coverage (White et al., 1997; Condon et al., 1998). To measure the CLEAN bias we insert two fake point sources (of flux density 1 mJy and 0.1 mJy) into two of the 6.0GHz B-array fields (SDSS J2233+0249 and SDSS J0046+0005) at the field center. We then clean on the fake source position and measure the total flux density. We find an average CLEAN bias of -12 μJy at 6 GHz, independent of source brightness. At 1.4GHz we insert a fake point source of

[1]https://science.nrao.edu/facilities/vla/data-processing

flux density 10mJy at the field center of SDSS J0046+0005 and measure a CLEAN bias of 1.1mJy. Therefore, CLEAN bias is not important for those of our targets whose flux densitis are known from FIRST to be $\gtrsim$ 1 mJy. We take the CLEAN bias into account when evaluating the quality of spectral indices in the faint radio population (§ 3.5).

3.3 High redshift quasars

In this section, we discuss the VLA observations of eleven moderately obscured quasar candidates at $z = 2-3$ (Table 3.1) and the implications of these data in § 3.3.2. These objects are selected based on their emission line properties from the SDSS spectroscopic database (Alexandroff et al., 2013) and then shown to be moderately obscured ($A_V \lesssim$ a few mag) using follow-up near-infrared spectroscopy (Greene et al., 2014).

Table 3.1: High Redshift Sample Properties. Peak flux density and rms values are in μJy/beam and are measured using *Aegean* to do forced measurements at the optical locations of our sources. SDSS J2201+0012 is the only real radio detection. FWHM[OIII] is the full width at half maximum of the [OIII]λ5007Å emission line where available from the near-infrared follow-up observations, in km s^{-1} (Greene et al., 2014).

Source name SDSS coordinates	z	$F_\nu^{\rm peak}$ 6 GHz	$F_\nu^{\rm rms}$ 6 GHz	FWHM [OIII]
SDSS J004600.48+000543.65	2.458	< 7.07	9.36	
SDSS J004728.77+004020.30	3.063	< 5.41	9.47	
SDSS J013327.23+001959.61	2.723	< 19.2	5.08	
SDSS J090612.64+030900.37	2.503	< 19.9	11.9	
SDSS J091357.87+005530.72	3.206	< 25.8	10.4	
SDSS J091301.33+034207.60	3.006	< 29.3	10.5	390 ± 40

SDSS J095118.93+450432.42	2.451	< 23.8	10.2	401 ± 50
SDSS J103249.55+373649.03	2.354	< 8.85	13.1	840 ± 410
SDSS J220126.09+001231.50	2.635	268.0	7.63	
SDSS J222946.61+005540.51	2.368	< 8.51	4.69	550 ± 50
SDSS J223348.07+024932.80	2.587	< 3.73	5.20	

3.3.1 FIRST and VLA observations of high-redshift obscured quasar candidates

In Alexandroff et al. (2013) we matched our sample of 145 high redshift Type 2 quasar candidates with the FIRST all-sky survey. We found a detection rate of only 2% (3 matches with FIRST within 3″), low by comparison to the radio-loud fraction of quasars, which (depending on the definition of radio-loudness) is estimated at $\sim 10 - 20\%$ (Zakamska et al., 2004; Jiang et al., 2007; Kratzer & Richards, 2015). Of the three sources detected in FIRST, all have measured peak flux densities of only $\sim$ 2 mJy (accounting for CLEAN bias) which corresponds to a k-corrected luminosity of $\nu L_\nu[1.4\ \mathrm{GHz}] = 8.5 \times 10^{41}$ erg s^{-1} at a mean redshift of $\langle z \rangle = 2.34$. At this redshift, such objects may be considered radio-intermediate (Xu et al., 1999). But with typical luminosity sensitivity at this redshift of 10^{42} erg s^{-1}, the FIRST survey is not quite deep enough to probe the transition between the radio-quiet and radio-loud population, and deeper observations were required

We start our analysis of the radio properties of this population with a stack of all 142 non-detected sources from the FIRST survey. We extract 30.6"×30.6″ cutouts

from the FIRST survey[2] at the SDSS position of each quasar that was not detected at the FIRST survey limit of ~ 1 mJy and combine them using both a mean and median stacking (see Figure 3.1). We find no detection in either stack. The standard deviation of the mean image is 11.7 μJy and so we place the upper limit for a detection at 3σ or 35 μJy. While these sources were below the FIRST detection threshold, and thus were not CLEANed during FIRST image processing, we must still account for Snapshot bias in our detection which is also believed to be the result of the non-linear CLEAN processing of images though it is still not well understood (White et al., 2007). We correct for Snapshot bias using equation (1) in White et al. (2007), obtaining a 49 μJy upper limit (3σ) on the mean flux density of our stack. At a redshift of 2.5 our measured upper limit on the flux density corresponds to a k-corrected luminosity of $\nu L_\nu[1.4\ \mathrm{GHz}] < 2.4 \times 10^{40}$ erg s^{-1}.

In our VLA program we targeted eleven high redshift obscured radio-quiet quasar candidates from Alexandroff et al. (2013). Only one, SDSS J2201+0012, is detected in our VLA program, with a flux density of 0.244 mJy corresponding to a radio power of $\nu L_\nu[1.4\ \mathrm{GHz}] = 8.5 \times 10^{40}$ erg s^{-1} at $z = 2.6$. This is above the limit set by our FIRST stacking analysis. We extract cutouts of the same size as the FIRST cutouts from our VLA maps around the SDSS positions of our undetected sources at 6.0 GHz. We see a detection in the mean stack with a flux density of 12.5 μJy at 6 GHz (see Figure 3.2) which, correcting for our measured CLEAN bias, corresponds to an

[2]http://third.ucllnl.org/cgi-bin/firstcutout

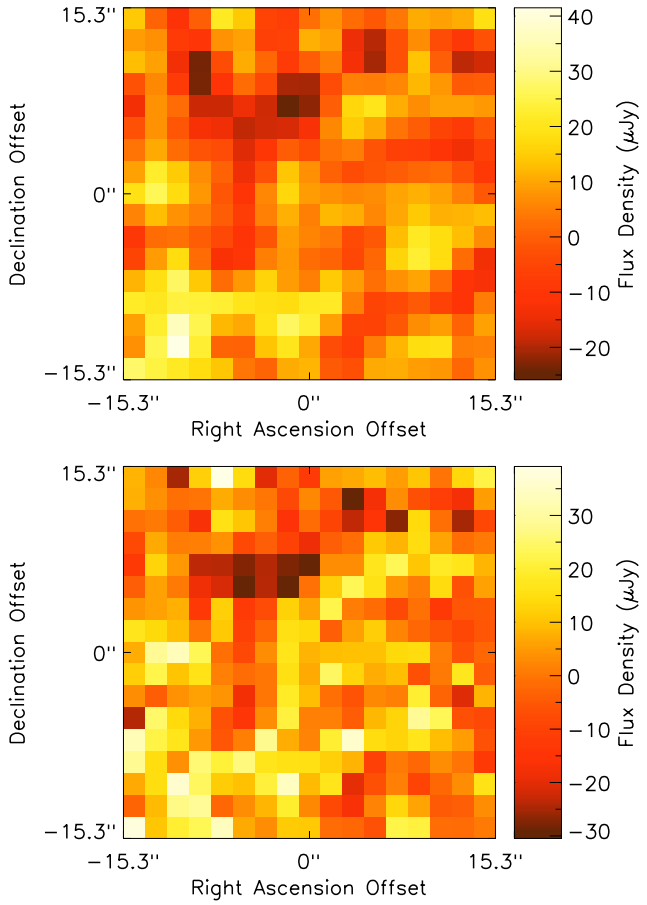

Figure 3.1: Mean (left) and median (right) stacks of FIRST images (20 cm) at the locations of all 142 non-detected Type 2 quasar candidates from Alexandroff et al. (2013) displayed using asinh scaling. Nothing is detected in either stack, allowing us to set an upper limit on the mean flux density of our Type 2 sources at 35 μJy (without Snapshot bias).

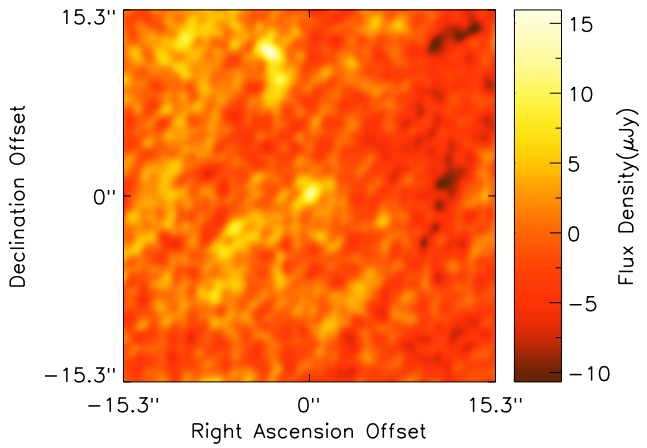

Figure 3.2: Mean stack of VLA images at the locations of all non-detected Type 2 quasar candidates from our VLA program at 6.0GHz. We see a clear detection here with a mean flux density of 12.5 μJy (not accounting for CLEAN bias). This detection is also seen in additional stacks in which we remove a single source at a time, indicating that the radio power is not dominated by a single bright source. The other detection, on the top left of the image, comes from a bright source in the field of SDSS J0818+2237. The patchy structure to the left is residual flux density from the dirty beam of a nearby object in the field of SDSS J0951+4504.

expected real flux density of $\sim$ 24.5 μJy. This corresponds to a radio power using the mean redshift of our sample $\langle z \rangle = 2.67$ median redshift $z = 2.59$) of νL_ν[1.4 GHz]= 9.1($\pm$2.2) $\times 10^{39}$ erg s^{-1} (νL_ν[1.4 GHz]= 8.4($\pm$2.1) $\times 10^{39}$ erg s^{-1}). We make additional stacks, removing one source in each stack, and find that each shows a clear detection, so the radio power in our stack is not predominantly from a single object. The flux density of the stacked detection, if we assume a spectral index of $\alpha = -0.7$, is just below the upper limit set by stacking our FIRST images.

3.3.2 Implications

Obscured quasar candidates at $z = 2 - 3$ remain a challenging population to identify even in deep multi-wavelength surveys, and the full extent of this population remains unknown. Their high infrared-to-optical ratios can be mimicked by those of dusty star-forming galaxies (Martínez-Sansigre et al., 2006). Optical colors alone do not distinguish these objects from various other populations (Alexandroff et al., 2013) because strong narrow emission lines with varying equivalent widths combined with varying degree of extinction can yield a wide range of optical colors. Infrared color selection methods and infrared-to-optical color selection methods recover interesting populations of high-redshift obscured quasars (Assef et al., 2015; Ross et al., 2015), but it is not known whether these methods are complete even at the highest luminosities.

To select a sample of high-redshift obscured quasar candidates, Martínez-Sansigre et al. (2006) used radio flux densities as a distinguishing characteristic to separate quasar candidates from star-forming galaxies. Their minimal radio flux density cut was 0.35 mJy at 1.4 GHz, corresponding to $\nu L_\nu[1.4\ \mathrm{GHz}] = 1.7 \times 10^{41}$ erg s^{-1} at $z = 2.5$. None of our sources would be uncovered with these observations, indicating that radio-based selection methods for obscured quasars recover only "the tip of the iceberg" of the obscured quasar population.

As we've described above, the origin of the radio emission in radio-quiet obscured quasars is unknown, but it appears that the amount of this emission in AGN and

quasars is positively correlated with the kinematics of the forbidden emission lines such as [OIII]λ5007Å (Mullaney et al., 2013; Zakamska & Greene, 2014), implying that there is a connection between radio emission and the ionized gas winds driven by the quasar. The best-fit quadratic relationship is

$$\begin{aligned} \log(\nu L_{\nu}[1.4\ \mathrm{GHz}], \mathrm{erg\ s^{-1}}) = \\ 2 \times \log(\mathrm{FWHM,\ km\ s^{-1}}) + 34.47 = \\ 2 \times \log(\mathrm{FWQM,\ km\ s^{-1}}) + 34.07, \end{aligned} \tag{3.2}$$

with a standard deviation of around 0.5 dex around this relationship when the radio-loud quasars are removed. Here FWHM and FWQM are the full width at half maximum and at quarter maximum of the [OIII]λ5007Å emission line.

The strongest forbidden line [OIII]λ5007Å is redshifted out of the optical spectrum at the redshifts of our targets and therefore is not directly accessible with the SDSS spectra. To probe where our candidates lie in relation to this correlation, we use [OIII] kinematics analysis from Greene et al. (2014) who followed up 25 candidate obscured quasars with near-infrared observations, including four of the objects with VLA observations (SDSS J0913+0342, SDSS J0951+4504, SDSS J1032+3736, and SDSS J2229+0055). The median FWHM([OIII]) in that sample is 475 km s^{-1}, which would imply the median radio luminosity of $\nu L_{\nu}[1.4\ \mathrm{GHz}] = 10^{39.8}$ erg s^{-1}, entirely consistent with the observed value ($10^{40.0}$ erg s^{-1}). The objects in our sample are

selected in a manner similar to the optical selection of low redshift ($z \sim 0.5$) obscured quasars (Zakamska et al., 2003; Reyes et al., 2008): on the basis of strong narrow rest-frame ultra-violet emission lines and the absence of a detectable quasar continuum. When they are observed in the rest-frame optical they tend to show relatively quiescent [OIII] kinematics (Greene et al., 2014) in addition to their small radio luminosities.

We now compare these results with the properties seen in a population of extremely red quasars which are selected from BOSS and WISE based on their high infrared-to-optical ratios and high equivalent widths of the CIVλ1549Å emission (Ross et al., 2015). Although these objects do not conform to all the classical characteristics of type 2 quasars, their multi-wavelength properties are indicative of large amounts of obscuration (Ross et al., 2015; Hamann et al., 2017). In follow-up near-infrared spectroscopy, four of these objects show [OIII]λ5007Å with extremely high velocity widths, FWHM([OIII])=2800$-$5000 km s^{-1} (Zakamska et al., 2016a). Radio stacking of a sample of 81 extremely red quasars using FIRST observations shows a mean flux density of 0.13 mJy (Hamann et al. in prep.) which we estimate is about 0.18 mJy when corrected for the Snapshot bias (White et al., 2007). Because this sample is of similar size to our type 2 sample which showed no detection, we conclude that there is a clear difference in the average radio properties of these two samples.

This flux density at the median redshift ($\langle z \rangle = 2.48$) of the stacked sample of extremely red quasars corresponds to $\nu L_\nu[1.4\ \mathrm{GHz}] = 8 \times 10^{40}$ erg s^{-1}. With a median

FWHM([OIII])= 2930 km s^{-1} (Zakamska et al., 2016a), we would expect a somewhat higher radio luminosity, $10^{41.4}$ erg s^{-1}. However, the objects picked for the near-infrared follow up thus far are the most extreme and therefore likely have a higher than average FWHM([OIII]) compared to the full sample, biasing any calculation of the expected radio luminosity from the radio/kinematics relationship. Overall, the qualitative agreement between the low-redshift kinematics/radio relationship and the two high-redshift samples – type 2 quasar candidates from this paper and extremely red quasars from Hamann et al. (2017) – is remarkable and implies that the relationship observed between [OIII] kinematics and radio luminosity observed at $z \lesssim 0.8$ may also be applicable at higher redshifts. This gives further support to the notion that radio emission in radio-quiet quasars is intimately connected with quasar-driven ionized gas outflows.

Radio emission in nearby radio-quiet AGN is often attributed to star formation (Rosario et al., 2013). However, in quasars with $L_{\rm bol} \gtrsim 10^{45}$ erg s^{-1} at low redshifts ($z \lesssim 1$), radio emission due to star formation (as estimated from infrared measures of star formation) is about an order of magnitude too low to account for the observed radio luminosity (Zakamska et al., 2016b). In high-redshift quasars, hundreds of $M_\odot$ yr^{-1} of star formation would be required to power the observed radio emission at the radio-quiet tail of the quasar distribution (Kimball et al., 2011; Condon et al., 2013). In the two classes of obscured quasars discussed here, with estimated bolometric luminosities in the range $L_{\rm bol} \sim 10^{46-47}$ erg s^{-1} – narrow-line selected type 2 quasar

candidates and extremely red quasars – 360 and 3800 $M_{\odot}$ yr^{-1} respectively would be required to power all of the observed radio emission (our adopted calibration is discussed in § 3.5.6). We do not yet have any additional information to support or rule out this scenario of extremely high star formation accompanying the quasar activity in these objects. Tsai et al. (2015) argue against such high star formation rates for hot dust-obscured galaxies (which are analogs of extremely red quasars) on the basis of the lack of a molecular gas reservoir, although it is not clear if the same argument applies for our less radio-luminous type 2 quasars. Taken together, the improbably high rates of star formation implied by converting νL_{ν}[1.4 GHz] to a star formation rate, and the observed correlation between the quasar powered $L_{[OIII]}$ and νL_{ν}[1.4 GHz] suggests that the radio luminosity is being predominantly fueled by the quasar.

3.4 Low redshift quasars

As was discussed in the previous section, the radio emission of radio-quiet quasars is related to the ionized gas kinematics (Mullaney et al., 2013; Zakamska & Greene, 2014). With this in mind we discuss high-resolution A-array observations of five low-redshift quasars and their ionized gas kinematics in § 3.4.1 and the implications of our observations in § 3.4.2.

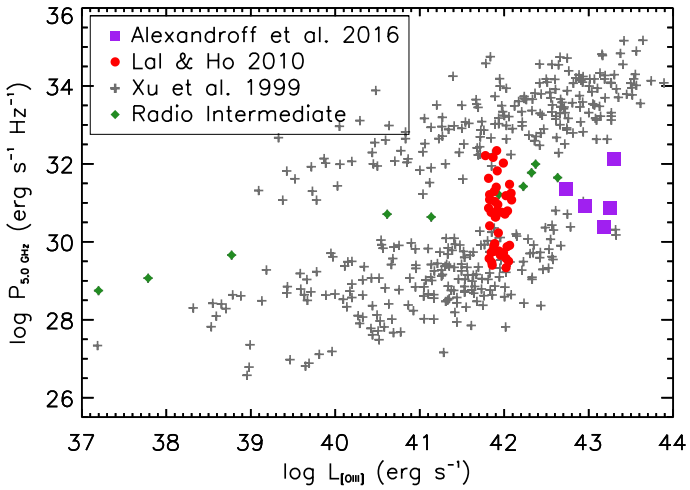

Figure 3.3: Relationship between radio power and [OIII] luminosity for type 1 and type 2 AGN, after Xu et al. (1999) and Lal & Ho (2010). The gray crosses are the sample of Xu et al. (1999) but using a modern cosmology. These objects appear to cover two separate regions of parameter space, and were thus classified as radio-loud (top) and radio-quiet (bottom) AGN respectively. The green points are those of the objects from Xu et al. (1999) that are classified as radio-intermediate based on this diagram. The red circles are from the sample of Lal & Ho (2010). The four low-redshift Type 2 quasars and one low-redshift Type 1 quasar observed in this program are plotted in purple.

3.4.1 FIRST and VLA observations of $z < 1$ quasars

We observed five fields with the A-array at 6 GHz, four centered on type 2 quasars from Reyes et al. (2008) and one centered on a type 1 quasar from Liu et al. (2014). All five are easily detected. All of our objects lie in the radio-quiet or radio-intermediate regime based on the ratio of the [O III] emission to radio flux density (Figure 3.3, after Xu et al. 1999).

We resolve or marginally resolve four of the five sources we observed with the A-array resolution of 0.5″ (Figure 3.4). The remaining source, SDSS J1101+4004, is consistent with being point-like but it is almost certainly the core of a larger radio

structure with lobes seen at ~ 175 kpc from the nucleus on either side (Figure 3.5). This is strikingly different from our previous attempt (Zakamska & Greene, 2014) to spatially resolve radio emission in radio-quiet type 2 quasars on somewhat larger scales: when we examined 19 objects that fell into the "Stripe 82" region covered by $1.8''$ observations by Hodge et al. (2011), none showed resolved structures. Therefore it appears that the typical scale of radio emission in radio-quiet quasars might be well-matched to the sizes of their host galaxies, as $1'' = 5.4$ kpc at the median redshift of our five targets.

For the four objects that were previously detected in the FIRST survey, we can calculate the spectral index between the 1.4 GHz FIRST observations and our 6 GHz observations. The fifth object, SDSS J1144+1043, is below the FIRST catalog threshold, but in the FIRST image centered on the SDSS position we see a 0.69 mJy/beam flux density excess which we correct for CLEAN bias to yield an 0.94 mJy estimate for the 1.4 GHz flux density. There is a significant time delay between the FIRST survey and our observations. Our spectral indices do not take into account the effects of variability on the measured flux densities, but unless much of the radio emission is concentrated in a pc-scale core, the variability on several year time scales is not a concern. To measure spectral indices, we calculate the peak and integrated flux densities of our targets at 6.0 GHz using the CASA task IMFIT to fit a 2D Gaussian to each source. In the case of SDSS J1123+3105 we fit a gaussian to each component and label them left(l), right(r) and center(c) respectively. We use the larger of the peak

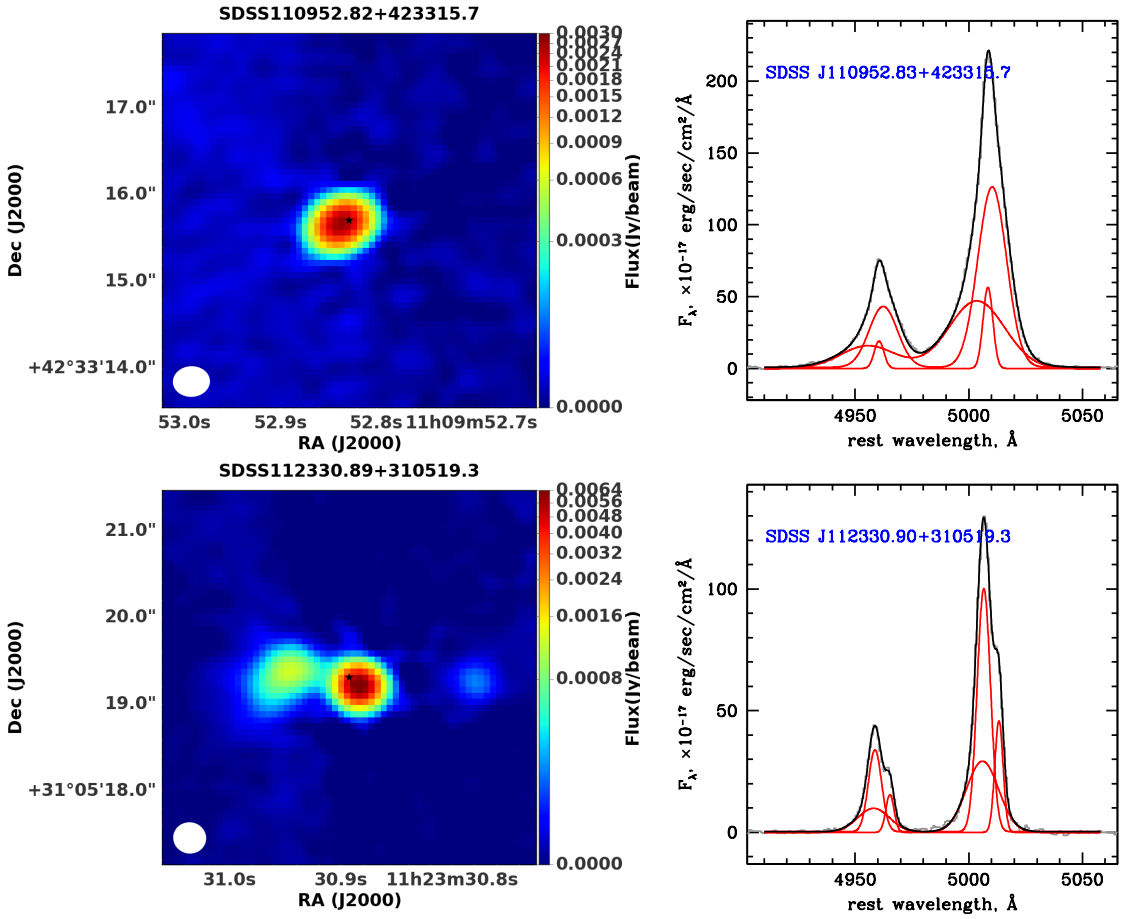

Figure 3.4: Left: Radio maps of four quasars that are spatially resolved in our VLA observations at 0.495″ resolution. The black star shows the optical coordinates of the source. The restoring beam is depicted as an ellipse on the lower left corner. **Right:** Continuum-subtracted SDSS spectra of the [OIII] doublet (in grey) with multi-Gaussian decomposition in red and the total fitted profile in black.

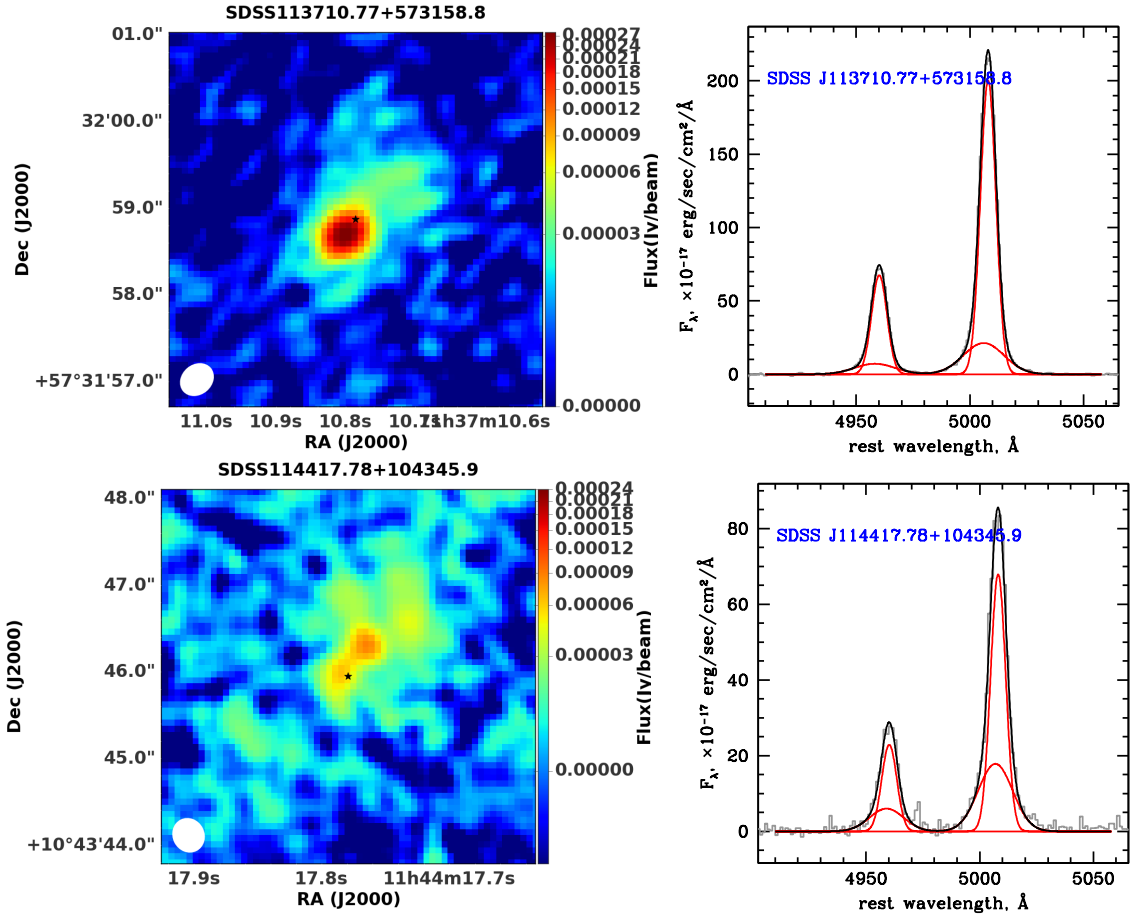

Figure 3.4: continued

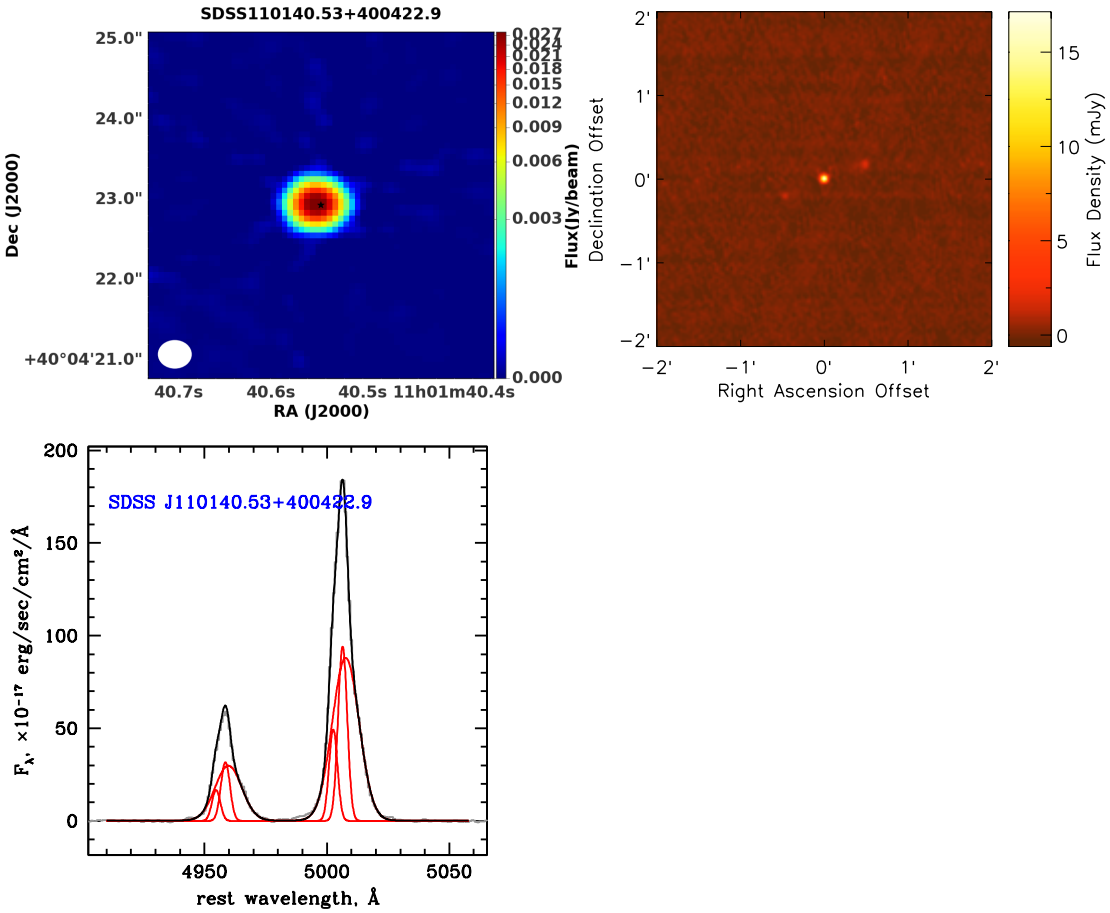

Figure 3.5: Top left: VLA A configuration 6.0 GHz image of the one type 2 quasar SDSS J1101+4004; a point radio source at resolution of 0.495″. **Top right**: the FIRST image on larger scales show that there are faint symmetric double lobes associated with the unresolved core. The projected physical distance between the cored and each of the lobes is ∼175 kpc. **Bottom:** the corresponding SDSS spectrum of [OIII] with the best multi-Gaussian fit.

and integrated flux density as the radio flux density. Spectral indices are determined between the FIRST flux densities and tapered 6.0 GHz flux densities with FWHM = 5″ to match the resolution of the FIRST survey. The resulting spectral indices are listed in Table 3.2.

Four objects show steep spectral indices between −0.5 and −1.0, whereas SDSS J1101+4004 – the only point source in our sample and the only radio core associated with clear large-scale jets – shows a flat spectral index of 0.4. For SDSS J1123+3105, the spectral index is calculated using the total flux density from all three components at 6.0 GHz. We also calculate a "corrected" spectral index for the core assuming that both radio lobes have a steep spectrum of $\alpha = -0.7$. Subtracting the expected lobe radio flux density at 1.4GHz from the FIRST flux density gives a value of $\alpha_{\rm core} = -0.56$. Thus, in this object the core component also appears to have a steep index.

Figures 3.4 and 3.5 also include our kinematic models for the [OIII]λ5007Å emission of each quasar. Each [OIII]λ5007Å emission line is fit with one to three gaussian components depending on the reduced χ^2 value of the fit (for more details see Zakamska & Greene (2014)). Note that in our model we assign no physical significance to each of multiple gaussian components but we find that each [O III] profiles requires at least two components, implying the existence of several structures moving at different velocities (e.g. for SDSS J1123+3105 the reduced χ^2 value for an emission line fit using a single Gaussian component is 14.7 while for an emission line fit using three

Gaussian components the χ^2 value is 0.7). There appears to be no statistical relation between the observed radio properties and the kinematics of the [OIII]λ5007Å emission lines for our sample of five quasars, although with such a small sample size this is unsurprising. We will explore in the next section several possible qualitative connections between the [OIII] kinematics and observed radio properties.

3.4.2 Discussion of low-redshift results

There are several models to explain the radio emission observed in these five objects on kpc scales: (i) compact jets (Leipski et al., 2006; Mullaney et al., 2013), (ii) extended radio coronae (Laor & Behar, 2008; Raginski & Laor, 2016), (iii) radiatively driven winds that produce radio emission as a biproduct (Stocke et al., 1992; Zakamska & Greene, 2014; Nims et al., 2015), and (iv) star formation in the host galaxy (Kimball et al., 2011; Padovani et al., 2011; Condon et al., 2013).

We can rule out possibilities (ii) and (iv) in our sample. Since four of the five targets are resolved on a few kpc scales and these four objects also show steep spectral indices, this most likely rules out a radio corona as the dominant contributor to the radio emission: a putative radio corona would have scales of $\sim 10^5$ Schwarzschild radii – i.e., parsec scales – and because of its compactness would also be expected to have a flat spectral index. The only object with both a compact radio source and a flat spectral index is SDSS J1101+4004, but this is also the one object that shows large-scale jets, so we can be quite confident that we are seeing the core of a

collimated jet in this source (Blandford & Königl, 1979).

In addition, we have the infrared measures of star formation for the four type 2 quasars in the literature (Zakamska et al., 2016b). In all four cases the radio emission due to star formation is $0.6-1.7$ dex below the observed emission, so although the objects are radio-quiet / radio-intermediate, star formation makes a negligible contribution, and the radio emission must be associated with the quasar activity. This leaves us with the possibility that the remaining four objects (excluding our large-scale radio jet in SDSS J1101+4040) have radio emission powered either by compact jets or radiatively driven quasar winds.

3.4.2.1 Implications from radio morphology and [OIII] kinematics

In three of our targets the spatially resolved emission is clearly directional. It is therefore tempting to classify them all as jets (Leipski et al., 2006). This assumption was recently called into question by Harrison et al. (2015) in a detailed observation of a nearby AGN called the "Teacup". In this object, both the ionized gas emission and the radio emission are well resolved into a core and two lobe-like components. The lobe components are further identified in high-resolution observations as shells that are likely caused by an AGN-driven outflow. Although the source demonstrates a classical 'core+lobes' morphology typically associated with collimated jets, Harrison et al. (2015) demonstrate that despite exquisite observations available for this source,

what drives the outflow – radiatively powered wind or collimated jet – remains an unanswered question.

This observation is particularly relevant for our study because the double-lobed morphology of our targets SDSS J1123+3105 and SDSS J1144+1043 is reminiscent of the "Teacup", and the double-peaked kinematics of the [OIII] emission line we observe in these objects would also be a natural consequence of the two plowed shells, each with relatively small internal velocity dispersion, but each expanding with a significant overall velocity relative to the nucleus. Exactly this situation is seen in the "Teacup" object where the two plowed shells are offset in velocity by about 330 km s^{-1}, while the two [OIII] components have FWHM of 250 and 325 km s^{-1} respectively. In our source SDSS J1123+3105, the two [OIII] components in our spectral fit are offset from each other by 330 km s^{-1}. If the outflow is propagating close to the plane of the sky – as the radio morphology of our source might suggest – then the physical velocity of the outflow is much higher than the observed velocity splitting because of the projection effects.

In addition, type 1 quasar SDSS J1144+1043 was previously observed using optical integral field unit spectroscopy (Liu et al., 2014). This object shows [OIII] emission with fairly low FWHM$\sim$200 km s^{-1} (also consistent with a plowed shell) extending in the South-East direction (Figure 6 in Liu et al. (2014), which is oriented with South at the top and East to the left). Therefore, we find that the axis of elongation for our radio image is qualitatively similar to the one seen in the ionized gas (see

Figure 3.4). However, the brighter radio lobe extends toward the North-West from the nucleus (and is thus co-spatial with the highest FWHM$\sim$ 900 km s^{-1} [OIII] component), whereas the brightest extended component of ionized gas as imaged in [OIII] is extended toward the South-East, in the direction of the fainter radio lobe. It is remarkable that these details are emerging from radio and integral-field unit observations of a quasar at $z = 0.678$; for comparison, the "Teacup" is at $z = 0.085$.

3.4.2.2 Implications from radio spectral indices

It is possible that the three most extended sources – SDSS J1123+3105, SDSS J1144+1043 and SDSS J1137+5731 – are similar to compact steep spectrum (CSS) or Gigahertz-peaked spectrum (GPS) objects (O'Dea, 1998) in that they show compact radio emission and steep spectral indices. CSS and GPS objects are produced by powerful jets which strongly interact with the surrounding gas and produce very luminous radio lobes. While CSS and GPS sources are compact ($\lesssim$ kpc) by the standards of radio galaxies ($\gg$ kpc), the lobe emission is extended enough that self-absorption is not important and thus as long as the lobe emission dominates over the cores, the indices are steep. Recent research at very high resolution needed to differentiate the morphology of GPS sources (e.g. Snellen et al., 2000; Taylor et al., 2000; Polatidis et al., 2002; Orienti & Dallacasa, 2012, 2014), finds that many of them look morphologically similar to SDSS J1123+3105 and SDSS J1144+1043. The difference, however, is that GPS sources still have flat radio spectra in their core

because on small scales the flux density is dominated by the self-absorbed jet core (e.g. Snellen et al., 2000; Polatidis et al., 2002; Orienti & Dallacasa, 2012, 2014). This contrasts with our observations of SDSS J1123+3105 and SDSS J1137+5731 where the central radio source is both dominant and has a steep spectrum.

Therefore, the brightest compact parts of our targets are inconsistent with pure jet core emission. This implies that our objects either have unresolved steep-spectrum hotspots dominating the observed spectral index of their core component, or that we must seek an alternative explanation, such as quasar winds, for their radio flux. The presence both of extended radio lobes on several kpc scales and of young hot spots within the unresolved central component would imply that the quasar has had several episodes of strong interaction between the putative jet and the host interstellar medium – the older episode resulting in the extended lobe emission and the newer episode resulting in the more compact emission in the unresolved core. Because the extended lobes expand with velocities $500-1000$ km s^{-1} as seen in their [OIII] emission over $5-10$ kpc, their age must be about 10^7 years. Thus in order to explain our observations with hot spots from multiple episodes of AGN activity and jet / gas interactions, our quasars must have active episodes every 10^7 years and sufficient gas available to interact with the jet. Evidence for such episodes is also seen in a nearby quasar with a powerful outflow (Sun et al., 2014, 2017) and in large samples of FR IIs with no core emission (van Velzen et al., 2015).

Alternatively, there is no jet at all on any scale, and the radio emission is domi-

nated by particles accelerated in shocks which arise when a radiatively driven wind propagates through the galaxy. Because this emission is extended on scales $\gg 1$ pc, it is not affected by self-absorption the way the jet core is and its spectrum would be steep. In this scenario, the most extended double-lobed sources such as SDSS J1123+3105 are produced when the wind "breaks out" of the galaxy and plows through the circumgalactic medium resulting in shells of ionized gas and radio emission. Such extended morphology can be produced by jet-driven and radiatively-driven outflows alike (Harrison et al., 2015). It is the characteristics of the central unresolved emission that might make it possible to distinguish between the two.

SDSS J1109+4231 is both a steep spectrum source and is marginally resolved but symmetric in our radio map. It also shows the most extreme [O III] kinematics from SDSS optical spectroscopy. Thus, this object may be the best candidate for quasar-wind driven radio emission which could produce the observed spherically-symmetric outflow observed in the radio. In this scenario the wind is in the early stages of development and has not yet engulfed the entire galaxy and thus the radio emission is relatively compact. The wind has also not yet slowed down due to interactions with the galactic interstellar medium and therefore shows very high velocity components in [O III]. This scenario fits well, qualitatively, with what we observe in SDSS J1109+4231. Spatial mapping of the [O III] emission on galactic scales and VLBI observations of the radio emission would help to confirm this scenario.

3.4.2.3 Equipartition and Pressure Balance

If the observed radio lobes are indeed evidence for quasar-driven winds, we can ask if the inferred energy density of highly relativistic particles is comparable to that needed to drive an outflow. Assuming equipartition of energy we can make an order of magnitude calculation of the energy density due to highly relativistic particles in the lobes of SDSS J1123+3105 (Burbidge, 1956). Assuming that the radio lobe is spherically symmetric, the minimum energy density in relativistic particles is (Pacholczyk, 1970):

$$u_{Emin} = c_{13} \left[(1+\eta)L\right]^{4/7} R^{3/7} \tag{3.3}$$

Using a total luminosity integrated from 10^7-10^{11}Hz assuming a power-law flux density with $\alpha = -0.7$ and a radius for the lobe of R$\sim$ 0.5kpc, we find a minimum energy density of $\sim 10^{-9}$ dynes cm^{-2}. This value is in very good agreement with predictions of the pressure needed to drive a starburst-driven outflow and seen in local starbursts $\sim 2 - 4 \times 10^{-9}$ dynes cm^{-2} (Heckman et al., 1990). We would expect a larger value for a quasar-driven wind, as the Heckman et al. (1990) calculation is for a starburst but nevertheless this is good evidence that the energy density we measure would be enough to drive an outflow.

3.4.3 Conclusions

Lal & Ho (2010) found that 64% of a sample of $z \sim 0.5$ Type 2 quasars from Zakamska et al. (2003) were flat-spectrum sources, with only 10% being extended at 0.8″ resolution. Therefore, our results are quite different from those of Lal & Ho (2010). As far as we know, the only difference in the selection of the two samples is the [OIII]λ5007Å luminosity, with Lal & Ho (2010) objects being about an order of magnitude less [OIII]-luminous than the ones discussed here (Figure 3.3).

If high bolometric luminosity (and with it, stronger [O III]) is a necessary condition for the existence of powerful quasar winds (Zakamska et al., 2016a), the difference between our observations and those of Lal & Ho (2010) may in fact indicate that we are probing the transition between the low luminosity regime where large-scale winds and associated radio emission do not exist and the high luminosity regime where such an effect is prevalent. Some evidence for such a luminosity threshold is found in observations of molecular outflows (Veilleux et al., 2013). In theoretical models (Zubovas & King, 2012), the threshold quasar luminosity might arise because a more powerful quasar-driven wind is necessary to push a given amount of material out of a galactic potential. Our assessments are currently speculative with such a small number of objects but hopefully a future program at a similar resolution and sensitivity would allow us to perform a more thorough investigation into the connection between the radio emission in radio-quiet quasars and [OIII]λ5007Å kinematics. In addition, VLBI observations of our objects with higher radio flux would allow us to probe to

even higher resolution and perhaps differentiate these scenarios. Even from our small sample, it can be seen that the combination of radio morphology, power and spectral index can be a powerful tool to differentiate the origin of the radio emission in radio-quiet quasars.

Table 3.2: Low Redshift Sample Properties. Peak flux densities and rms values are in mJy/beam and integrated flux densities are in mJy. [OIII] luminosities are given as $\log(L[\mathrm{OIII}]/L_{\odot})$. Designation as radio-loud (RL), radio-intermediate (RI) or radio-quiet (RQ) is based on the position of the object in the L[OIII] vs 6 GHz luminosity space (Xu et al., 1999).

Source name SDSS coordinates	z	F_ν^{peak} 6	F_ν^{int} 6	F_ν^{rms} 6	F_ν^{peak} 1.4	F_ν^{int} 1.4	F_ν^{rms} 1.4	spectral index α	L[OIII]	RL?
SDSS J110140.53+400422.9	0.4569	32.3	32.2	0.015	17.85	17.38	0.142	0.40	9.71	RI
SDSS J110952.82+423315.7	0.2612	2.8	3.6	0.0157	16.21	16.96	0.135	-0.75	9.37	RQ
SDSS J112330.90+310519.3(c)	0.3097	6.9	6.9	0.00938	17.27	19.89	0.122	-0.73	9.15	RI
SDSS J112330.90+310519.3(l)		1.3	2.9	0.00938						
SDSS J112330.90+310519.3(r)		0.22	0.43	0.00938						
SDSS J113710.77+573158.8	0.3953	0.29	0.36	0.00696	2.35	2.14	0.143	-1.0	9.6	RQ
SDSS J114417.78+104345.9	0.6783	0.052	0.45	0.00836	0.94		0.154	-0.51	9.67	RQ

3.5 Source Populations

In this section we describe our efforts to determine the nature of the field sources identified in our radio fields using publicly available multi-wavelength surveys. We compare our results to those of recent deep radio surveys. Automatic source identification is accomplished using *Aegean* (Hancock et al., 2012). This source finding algorithm assumes a compact source structure allowing it to fit multiple components (as determined by a curvature map) to each island of pixels identified in the algorithm. This enables *Aegean* to identify both faint sources close to the detection limit and sources within an island of pixels containing multiple components. According to Hancock et al. (2012), when matching with a synthetic catalog, *Aegean* is 93.87% complete for 5σ detections with a reliability of 98.69%. We ran *Aegean* on each of our fields to produce a catalog of all sources present at a detection limit of 6σ. This limit is chosen because there appeared to be a significant percentage (42%) of false positives around 5σ as seen by an excess of sources around this detection threshold relative to the expected value when extrapolating linearly from higher S/N. All sources from this catalog are included in the analysis unless it is clear that the program had mis-identified residual flux as a source. We excluded such sources by eye. Our ability to match theoretical source counts (see section 3.5.2) gives us confidence that the remaining sources are correctly identified with accurate fluxes by Aegean.

In total we identify 179 sources in our fields using *Aegean*, with flux densities between $\sim$ 40 μJy and $\sim$ 40 mJy and a median flux density of 0.23 mJy. The

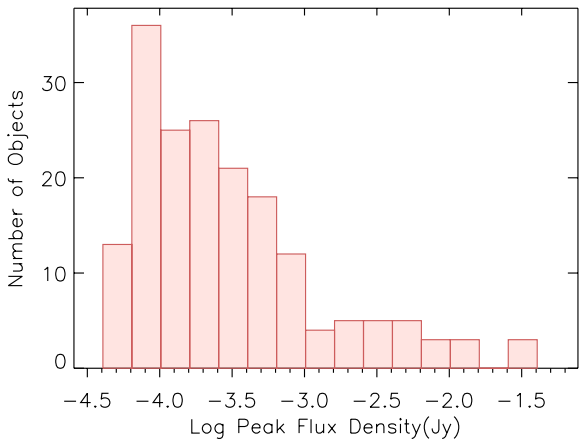

Figure 3.6: Distribution of 6 GHz radio flux densities for all sources identified in our twenty radio fields by *Aegean*.

distribution of peak flux densities are shown in Figure 3.6. The full table of all sources is available online with the first 20 rows included here as Table 3.3. With the 6 GHz-selected source catalog in hand, we use *Aegean* in forced measurement mode to calculate the flux density at our source locations in matching 1.4GHz data for fields in Program 13B-382 (see § 3.5.3).

Aegean returns both a point source flux density and an integrated flux density for all islands and for each component within a given island. Unfortunately, the current version, as of February 14 2016, does not correctly calculate the integrated flux density of identified islands, though the integrated flux density of components is correct. Thus, unless otherwise indicated, we choose as our sources *Aegean* islands, but only report and use their peak flux density in our measurements. This means we may be underestimating the true radio flux density in our resolved sources. Six of our sources identified with *Aegean*, two of which are our targets, upon visual inspection

are clearly multiple components of an extended source with lobes or other features. All six sources are identified as single sources in FIRST.

We cross-matched all of our sources identified using *Aegean* with the FIRST catalog. In the case of our B-configuration fields we have L-band (central frequency $\sim$ 1.4GHz) data at a similar resolution to FIRST which provides a direct check on our measured flux densities. We create a test catalog using *Aegean* to identify sources in our L-band fields and then cross-match this catalog with FIRST using a matching radius of $< 4''$. For sources where FIRST matches existed, typically 97% of sources above 2 mJy and 25% of sources below 2 mJy, we found a mean flux density ratio of $\mathrm{flux_{Aegean}/flux_{FIRST}} = 0.83$ and a standard deviation of 0.21. We are thus confident that *Aegean* is capturing most of the radio flux density in our fields; the remaining discrepancy is accounted for by the CLEAN bias (taken into account in the FIRST catalog but not in our images) and the missed flux density in spatially resolved objects.

To verify that the faint sources we detect using *Aegean* are real, we stack FIRST cut-outs of all of sources not individually detected in FIRST (121 sources). The resulting FIRST stack at 1.4 GHz has a median flux density of 0.16 mJy, 6 times below the FIRST detection limit, and a mean flux density of 0.18 mJy. (0.25 mJy when accounting for Snapshot bias). For comparison, the mean and the median flux density of the same sources measured by *Aegean* at 6 GHz is 0.22 mJy and 0.14 mJy respectively. Assuming a spectral index of $\alpha = -0.7$ our extrapolated 1.4 GHz flux

density is a factor of two greater than the FIRST flux density measured in our stacked image. The combination of the 1.4 GHz and 6 GHz results implies a spectral index of $\alpha = -0.1$, a flat value consistent with our results below (see § 3.5.3).

3.5.1 Resolved Sources

There are several accepted methods in the literature to determine the percentage of resolved sources in a survey. In particular, the obvious definition is to check if a source's FWHM is greater than the beamsize taking into account the effects of bandwidth smearing as a function of position and depth. Using this technique, the FIRST survey found that $\sim 20\%$ of their sources are resolved with a beam FWHM of $5.4''$ and Hodge et al. (2011) found that $\sim 60\%$ of their sources are resolved in their survey of Stripe 82 with a beam FWHM of $\sim 2.3''$. We find, for the gaussian components that make up our source islands, not taking into account the effects of beam smearing, that 50% of the components we observed with the highest resolution (A-array) had a FWHM $> 0.495''$, which is the approximate beamsize at the center of the image given natural weighting.

Alternatively, surveys such as VLA-COSMOS (Schinnerer et al., 2004) and E-CDFS (Miller et al., 2013) compared the ratio of total integrated flux density/peak flux density to peak flux density/rms noise. They take the definition of "resolved" to be:

$$\frac{S_{\rm int}}{S_{\rm peak}} > 1 + \frac{A}{(S_{\rm peak}/{\rm rms})^3} \tag{3.4}$$

where A is some constant set such that some large percentage of sources ($\gtrsim 95\%$) fall above the function mirrored over the axis total/peak = 1. In good agreement with our previous value, we find that 52.4% of the components that make up our sources in our fields observed with the highest resolution A-array are resolved according to this definition, when we set $A = 100$ (which bounds 98% of our sources). In addition, according to this definition we find that 52.2% of the components that make up our sources observed in the B-array configuration (approximate beamsize of 1.3″ with natural weighting) are resolved. In comparison, the VLA-COSMOS survey found that 44% of their sources are resolved with a beam FWHM of $\sim$ 1.5″ and the E-CDFS survey found 14% of their sources are resolved with a beam FWHM of $\sim$ 2.2″. Thus, our observations seem consistent with the overall trend, unlike for our smaller sample of low redshift type 2s where we appear to see a large increase in the fraction of resolved sources at a specific resolution.

3.5.2 Source Counts

Our first task is to verify that we recover the faint radio sources at source number densities comparable to those found in other deep radio surveys. We use the 6 GHz catalog from both the A-array and B-array observations. The effective area of our

observations varies as a function of flux density because of primary beam attenuation. For every source flux density, we use the primary beam shape to estimate the distance from the center of the field at which this source flux density would fall below the detection limit and use this distance to calculate the effective area of the survey at this flux density. We then calculate the number of sources detected per unit flux density and per unit effective area of the survey, which is well fit by a power-law between 0.1 and 10 mJy:

$$\log\left(F_\nu^{5/2}\frac{\mathrm{d}N}{\mathrm{d}F_\nu}, \mathrm{Jy}^{3/2}\ \mathrm{sr}^{-1}\right) = (3.0 \pm 0.2) + (0.8 \pm 0.1)\log\left(F_\nu, \mathrm{Jy}\right). \quad (3.5)$$

(The errors include only the error in the fit, but not the cosmic variance. This should be considered only an estimate as the same sensitivity curve is assumed for all the fields.)

This is in excellent agreement with the compilation of source counts presented by Massardi et al. (2010) at 5 GHz (which we correct to 6 GHz using a spectral index of -0.7). According to their population synthesis models, 0.1 mJy at 5 GHz is precisely the flux density above which AGN should dominate the radio population and below which star-forming galaxies are expected to dominate. Unfortunately, our survey becomes incomplete below 0.1 mJy where the source counts would start arising predominantly from star forming galaxies (e.g. Padovani et al., 2011, 2015), but in

what follows we attempt to elucidate the nature of the bulk of our detections between 0.1 and 10 mJy for comparison with such population synthesis models.

3.5.3 Spectral Indices

For our high-redshift fields in Program 13B-382, spectral indices are determined using our 6.0GHz (C-band) and 1.4GHz (L-band) data. For a proper comparison, new 6.0GHz maps are created at the resolution of the 1.4GHz data using *CLEAN* with a uv-taper FWHM of 6.45″ (the approximate resolution of the L-band in B-configuration if imaged with natural weighting). We then force *Aegean* to calculate the peak flux density in our L-band maps and tapered C-band maps using locations provided from our full resolution C-band maps. A spectral index is then calculated using our L-band data at 1.4 GHz (whenever the flux density from forced photometry is positive) and our tapered C-band data at 6.0 GHz. We compare the measured C-band flux density at full resolution to the calculated flux density using our uv-tapered map and identify a sample of point sources for which the measured fluxes in the full resolution map and lower resolution map are within a factor of five though we note that the median spectral index of our full sample is actually steeper by only -0.04 with a similar standard deviation. We find a flat median slope of $\alpha_{med} = -0.19$ with a standard deviation of 0.66.

Although there are some hints of spectral index flattening toward lower radio flux densities (Gralla et al., 2014; Huynh et al., 2015), such values are surprising.

To understand this observation we conduct a simulation which closely mimics our observations. We draw sources from the radio flux density distribution of Massardi et al. (2010) and "observe" them including the effects of the primary beam on the detection sensitivity both at 1.4 and 6 GHz. In addition, we include CLEAN bias, typical observational errors and our catalog strategy, in which the sources are selected at 6 GHz and then forced photometry is obtained at 1.4 GHz to produce the mock catalog. Our simulation uses a Gaussian distribution of real spectral indices with mean $\alpha_{\rm im} = -0.7$ and standard deviation $\sigma_\alpha = 0.5$, and then we use the generated mock catalog to determine the mean and the standard deviation of the recovered spectral index as a function of 6.0 GHz flux density for our survey.

We find much flatter output spectral indices, $\alpha_{\rm out} \simeq -0.2$, similar to what we observe, with overall trend $\alpha_{\rm out} \simeq 1.4\sigma_\alpha - 0.9$. The most important reason for this strong spectral index bias is that our catalog is selected at 6 GHz and we dig well into the noise at 1.4 GHz to recover objects with the flattest spectral indices, whereas the objects with the steepest indices and faint (but detectable) 1.4 GHz flux densities would never make it into our catalog as they are not detected at 6 GHz. Additional complications include the difference in the shape of the primary beam, whose size is $\propto 1/\nu$. As a result the 1.4 GHz data is not as sensitive as our 6.0 GHz data in the center of the field, so we would have difficulty identifying flat spectrum objects among the faint sources which can only be identified near the field center. As we step away from the center of the field, the shape of the primary beam makes 1.4 GHz

data more sensitive than the 6 GHz data, but the flux density limit for the detection is now much higher. As a result, there is a slight steepening of the observed indices at the faintest flux densities in the simulation which is also seen in the data. These effects are a result of the fact that our survey is not a mosaic of a particular field and so our sensitivity varies across each field. These effects swamp much of the intrinsic effects we would hope to observe as trends in our spectral index as it evolves with the changing distribution of source type.

3.5.4 Cross-matching with the SDSS data

We cross-match our 179 sources with the SDSS data release 12 (Alam et al., 2015) photometric and the spectroscopic catalogs, within $1''$. We find 47 photometric matches and 24 spectroscopic matches (excluding our original targets), for a total recovery fraction of 41%. To estimate the chance background rate we displace our source RA positions by +5' are re-match to the SDSS catalog. We find a total background match rate within 1" of 2 sources, implying 97% of our sources are likely to be physical matches. Out of the sources matched in SDSS, 91% have either a photometric redshift estimate (Csabai et al., 2007) or a clear measurement from SDSS spectroscopy (Table 3.3). The matching rate as a function of radio flux density is shown in Figure 3.7.

We examine the 24 spectra as well as their classifications from the Portsmouth group (Thomas et al., 2013). We use the spectroscopic classifications from the

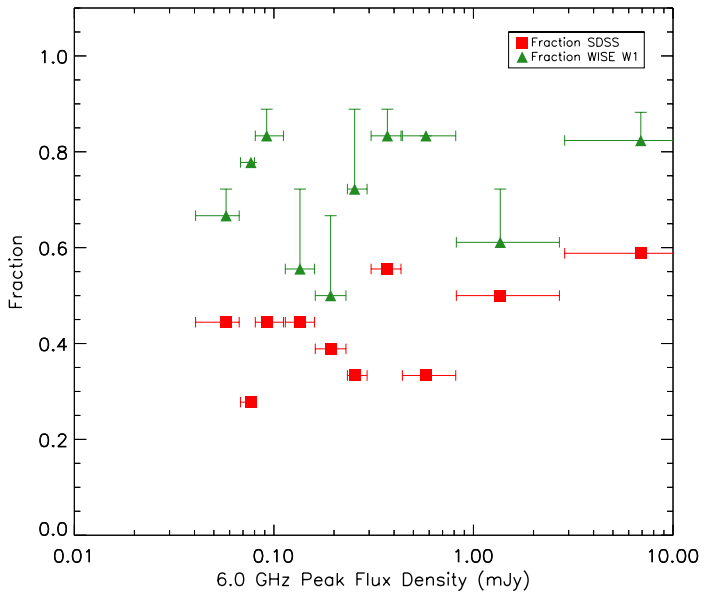

Figure 3.7: Fraction of detections as a function of 6.0 GHz peak flux density. We divided the sample into 10 bins with an equal number of sources in each bin and placed the data point at the median flux density in each bin. The range of flux densities in each bin is represented by the horizontal error bars. The green triangles show the fraction of sources in each bin with a WISE detection within 3″ and a S/N ratio > 3 in W1. We plot an upper limit for each bin by including all WISE sources detected within 6″ with a S/N ratio > 3 in W1. The red squares show the fraction of sources in each bin with an SDSS detection within 1″.

Portsmouth group in all cases except two for which both human classifiers agreed with each other but disagreed with the pipeline. Our spectroscopic identifications include seven AGN (including low-redshift Seyferts, high-redshift quasars, one serendipitous $z = 0.44$ type 2 quasar and one blazar), two star-forming galaxies with redshifts 0.088 and 0.073 respectively, and ten absorption-line galaxies. In addition, there are four LINERs and one composite object which is an absorption line galaxy that shows signs of AGN activity. The median radio flux density at 6 GHz of this sample is 0.39 mJy, while the mean flux density is 3.4 mJy, dominated by the seven brighter sources with flux densities $>$ 1mJy. Of the spectroscopic matches identified as AGN, 33% are above the median radio flux density of our full sample. One of our spectroscopic SF galaxies falls above the median peak flux density of our total radio sample while one falls below.

The photometric redshift estimator of Csabai et al. (2007) also provides optical classification based on the best fit to the spectroscopic templates of Dobos et al. (2012). We create three categories for optical classifications: AGN, SF galaxies, and passive galaxies. We categorize any object showing signs of AGN activity in the optical (including LINERs from the spectroscopic sample) as AGN. Only objects without any sign of AGN activity are placed in the SF category. Our final category, passive galaxies, showed no sign of either AGN or star-formation activity in spectroscopy or in the photometric template used in optical classification.

Using this classification scheme, of the 77 sources with SDSS spectroscopy or

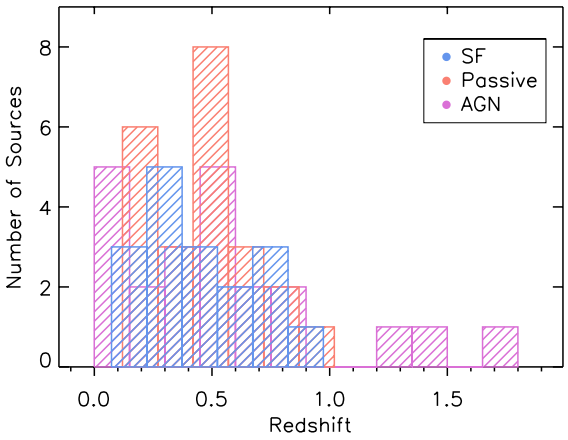

Figure 3.8: Redshift distribution of all of our objects with either a photometric or spectroscopic redshift in SDSS. The different subsamples are classified according to § 3.5.4.

photometry, 22% of our sources are classified as SF galaxies, 29% are classified as AGN and 30% are classified as passive galaxies. The remainder are either target sources (8%), or did not have a photo-z (11%) so remain unclassified in all future analysis. We show the full redshift distribution of our sources in figure 3.8. The mean redshift of the sample is $z = 0.48$ though this represents only those sources which had a match in SDSS – the missing sources with no counterparts in the optical are likely to be at a higher redshift. In addition, in Figure 3.9 we show the radio flux density distribution of our samples, including an additional category for both unclassified objects (no detection in SDSS or WISE, or an SDSS detection without a redshift and classification) as well as IR-bright objects (those detected in WISE W1 but not SDSS, see Section 3.5.5).

Interestingly, a significant fraction of our sources are identified as passive or ab-

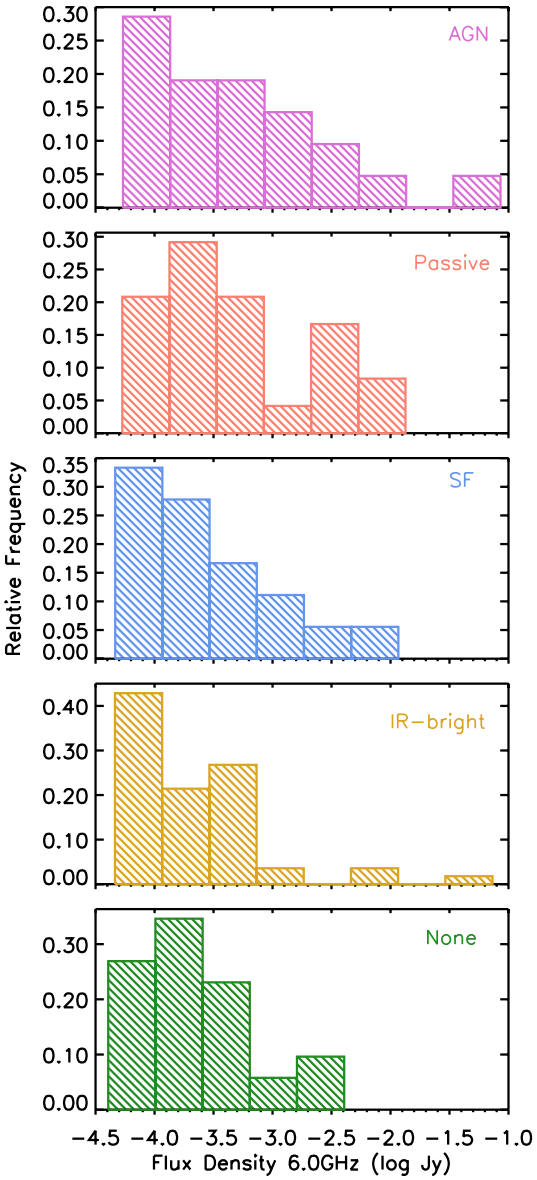

Figure 3.9: Distribution of radio flux densities at 6.0 GHz of all of our objects with WISE and / or SDSS counterparts. The different subsamples are classified according to § 3.5.5 and § 3.5.4.

sorption line galaxies – showing neither star formation or AGN activity in the optical. This population is most plausibly identified with the "low-excitation" or "radio-mode" AGN of Best & Heckman (2012). Such a population would be mis-identified as star-forming galaxies in surveys that assume all objects not classified as AGN are star-forming galaxies and require optical, infrared or X-ray signatures for AGN classification. For example, Bonzini et al. (2013) require X-ray or mid-infrared signatures of AGN activity to be present in order to classify their sources as AGN. Similarly, Smolčić et al. (2008) require either emission line activity or X-ray activity to classify sources as AGN candidates, and it is not clear how passive galaxies would be classified in their scheme. Such classification schemes would overestimate the contribution of SF galaxies to the radio flux at small flux densities.

3.5.5 Cross-matching with WISE data

We use the All-WISE catalog of the Wide-Field Infrared Survey Explorer (WISE; Wright et al., 2010a) to investigate the mid-infrared properties of the faint radio population detected in our observations. Of the 179 sources individually detected in all 20 fields in the C-band, we find 128 WISE matches within $3''$ and 143 matches within $6''$. Because there is not a well-pronounced minimum in the distribution of the matching distance, it is not clear what matching radius is more appropriate. We consider the matches within $3''$ to be robust (listed in Table 3.3) and the other ones to be tentative. Using the same technique as mentioned in section 3.5.4, we estimate

that only 4% of our sources are spurious within a 3" matching radius.

In Figure 3.7 we show the fraction of sources with robust WISE matches as a function of the measured radio flux density. The upper limit shows how the fraction of detections in each bin would change if we instead used a matching radius of 6″. The overall detection rate remains high even down to our flux density limit, with a detection rate of 67% of sources in W1 with flux densities between 40.5 and 67 μJy. Essentially all SDSS matches are also matched in WISE, but the reverse is not true: we define a category of objects, henceforth referred to as "IR-bright", for which there is a WISE detection in W1 but no SDSS detection.

Interestingly, the median W1−W2 colour for these objects has a value 0.25 mag higher than the SDSS-detected sample (Figure 3.10). Of particular interest is the condition W1−W2$>$ 0.8 mag, which is often used to identify infrared-luminous AGN (Assef et al., 2010; Stern et al., 2012). While this condition does not select all AGN (an obscured AGN spectral energy distribution can be dominated by the host galaxy with W1−W2$<$ 0.8 mag if the warm dust is not visible from the observer's direction, Mateos et al. 2013), samples selected by this cut have low contamination rates. 29% of objects in our IR-bright sample lie above this threshold, compared to only 18% of SDSS-detected objects. Combined with non-detection in the SDSS, this observation likely indicates that the IR-bright sample may be dominated by obscured AGN.

Using the IPAC Infrared Science Archive, we extract and stack WISE exposures of individually non-detected faint radio sources, centered on the *Aegean*-derived po-

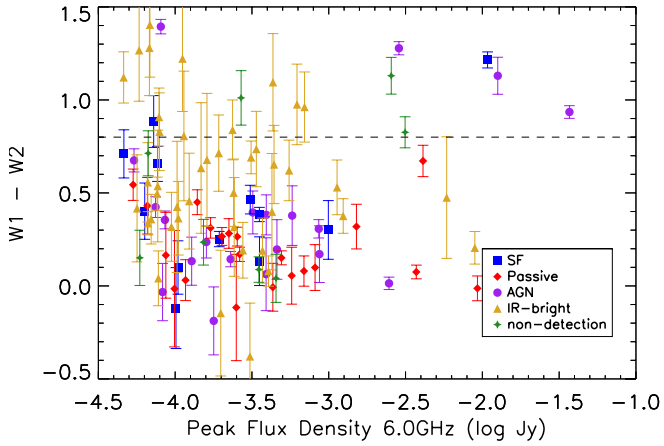

Figure 3.10: WISE colors of the infrared-detected counterparts to radio sources, classified as described in § 3.5.5 and § 3.5.4. The Rayleigh-Jeans tail of a stellar population has W1−W2≃ 0 mag because the WISE photometric system is Vega-based. Objects with significant hot dust contribution (such as luminous AGN) typically have W1−W2> 0.8 mag. While this is a sufficient condition for AGN selection, it is not a necessary one, as the spectral energy distribution of dust can start rising at much longer wavelengths depending on the geometry of obscuration, and such sources will appear to have W1−W2 colors typical of a normal stellar population.

sitions. We find no detection in any of our stacks. The 2-σ brightness upper limit in our W1 stack corresponds to a flux density of ≈ 6 μJy.

3.5.6 Star Formation Rates

We use the 6.0 GHz radio flux density and SDSS redshift of our sources, where available, to estimate a star formation rate (SFR). SFRs are estimated using equation (6) of Bell (2003), where we can calculate the rest-frame 1.4 GHz luminosity by k-correcting as in our equation (3.1), with the resulting star formation rate:

$$\psi(\mathrm{M}_\odot\ \mathrm{yr}^{-1}) = 3.94 \times 10^{-38} \left(\frac{\nu \mathrm{L}_\nu[1.4\,\mathrm{GHz}]}{\mathrm{erg\ s}^{-1}} \right). \tag{3.6}$$

Calculated SFRs are shown in figure 3.11, where we have assumed $\alpha = -0.7$ (radio luminosities and SFRs smaller by a factor of 2 would be inferred if $\alpha = -0.2$ is assumed instead). A star-formation rate greater than 1000 $M_\odot$ yr^{-1} would be comparable to some of the most active sub-mm galaxies in the universe (Casey et al., 2014) making our calculated SFRs, especially for most objects identified as AGN, improbable.

We can test whether our radio SFR estimates agree with the observed WISE fluxes. At a redshift of ~ 0.5, the strong polycyclic aromatic hydrocarbon emission feature at 7.7μm falls into the center of the W3 band, so W3 fluxes would be a sensitive measure of extreme star formation at those redshifts. We take seven objects with measured W3 fluxes (the rest are upper limits) and use SF templates from Mullaney et al. (2011), placed at the redshift of each object, convolved with a W3 filter curve and scaled to the observed W3 flux to calculate the total infrared luminosity (8-1000 μm) which we then convert to a star-formation rate (Bell, 2003). Our key assumption is that the total W3 flux is contributing to star formation, so there is no contamination in the W3 band from AGN activity. Thus, the calculated SFR represents an upper limit on the actual SFRs of our objects. We find star formation rates ranging between 2 and 25 $M_\odot$ yr^{-1} (with good agreement between the W3-based and the radio-based star formation rates for the two spectroscopic SF galaxies), with only one object

(photometric redshift $z \approx 0.7$) at 200 $M_\odot$ yr^{-1}. We find no star formation rates as high as would be necessary to explain the radio flux density we see in this subsample.

This leads us to conclude that the majority of the objects classified by the SDSS photometric pipeline as SF galaxies in our sample are in fact AGN. With only five optical bands and often at the limit of the optical survey, distinguishing between an SF galaxy and an AGN is very difficult. Both types of objects show emission lines and blue continua of varying strength. We add additional information with our radio detection, namely the implied radio-derived SFR, that allows us to distinguish between SF galaxies and AGN. The two spectroscopically confirmed SF galaxies (both at $z < 0.1$ and with SF rates of $2-5$ $M_\odot$ yr^{-1}) are robust classifications and consistent with all observations.

For objects with SDSS spectroscopy we can also cross-check our radio-derived SFRs with those calculated from Hα using equation 1 from Overzier et al. (2009). We make no effort to correct for AGN contamination in the Hα emission line for objects classified as AGN so these measurements represent upper limits on the SFR. We find, with the exception of our star forming galaxies and a single AGN, that the radio-derived SFRs also massively over-predict the Hα-derived SFRs, which range from 1.0×10^{-3} $M_\odot$ yr^{-1} to 40 $M_\odot$ yr^{-1}. This provides further confirmation, for a small subset of our total sample, that the majority of the observed radio flux density is not due to star formation alone.

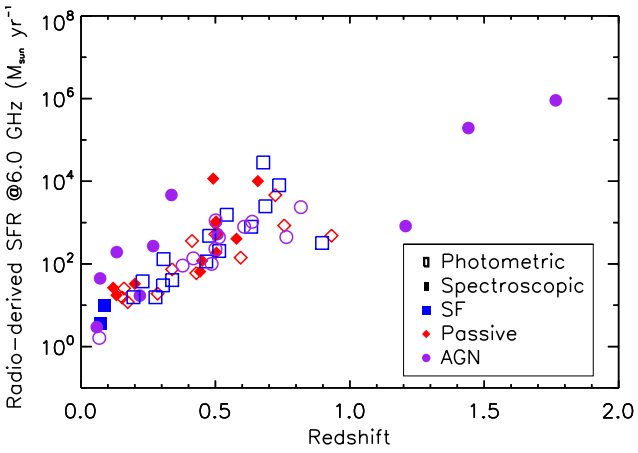

Figure 3.11: SFR as a function of redshift for all of our sources with a match in the SDSS spectroscopic or photometric sample. Sources are identified as AGN, SF or passive galaxies based on either spectroscopy or templates used in photometric redshift determinations. SFRs of $> 10^4$ $M_\odot$ yr^{-1} are unlikely even in the high redshift universe implying that some of the measured radio flux density must be due to AGN activity.

3.5.7 Summary and discussion of the study of faint radio sources

We identify 179 radio sources in the C-band observations. 41% of these have optical matches in the SDSS (magnitude limit of $i_{AB} = 21.3$) , and an additional 33% have matches in the WISE survey, but not in the SDSS. Our matching fraction is somewhat dependent on the radio flux density, with a higher matching fraction at higher flux densities. Smolčić et al. (2008) investigate the nature of the radio sources in the VLA-COSMOS survey using follow-up optical data down to a depth of $i_{AB} = 26$ mag. They find optical counterparts to 65% of their sources. Because we are sensitive to faint radio sources only over a small fraction of our observing area,

the flux density distributions of radio sources in our mini-survey are biased toward higher values than that of Smolčić et al. (2008), and therefore our optical detection fraction of 40% is higher than what would be naively predicted from the flux density distribution of matches in their survey.

We classify our detected counterparts into four roughly equal categories based on their optical and infrared properties: AGN, passive galaxies (which have no signs of AGN activity other than the radio source), star-forming galaxies and IR-bright sources. Star-forming galaxies are primarily identified as such by the SDSS photometric redshifts pipeline (Csabai et al., 2007), with only two star-forming galaxies spectroscopically confirmed. Estimating star formation rates from the measured radio flux densities and the nominal photometric redshifts, we find that 73% of our star-forming galaxy classifications have radio flux densities that imply star formation rates > 100 $M_{\odot}yr^{-1}$ while 33% of our star-forming galaxies have radio flux densities that imply star formation rates > 500 $M_{\odot}yr^{-1}$. These values are implausibly high especially given the star formation rate estimated from the W3 flux which covers the 7.7μm PAH feature at these redshifts. Thus, these objects are probably mis-identified AGN which are difficult to distinguish from star-forming galaxies on the basis of five photometric measurements of the SDSS, especially close to the magnitude limit of the survey.

Because we have a set of pointed observations rather than a mosaic, our survey depth is not uniform and is strongly affected by the frequency-dependent primary

beam. Correcting for this effect, we estimate that our number counts in the C-band are consistent with the previous compilations by Massardi et al. (2010). These authors predict from the population synthesis models that the < 0.1 mJy population should be dominated by star-forming galaxies. The vast majority of the optical and infrared counterparts that we find are not star-forming galaxies. Thus either star-forming galaxies dominate at even lower flux densities than our survey probes or they all fall below the flux limit of the SDSS survey (Smolčić et al., 2008; Padovani et al., 2011, 2015).

3.6 Interesting sources

3.6.1 Dual AGN

In the A-array observation of type 1 quasar SDSS J114417.78+104345.9 (which is at redshift $z = 0.678$) we found two objects with SDSS optical spectroscopy unrelated to our target (Figure 3.12). Both sources are at $z = 0.444$, separated by about $4''$, or 23 kpc. The northern source is an absorption line galaxy with no optical or IR signs of AGN activity (it is detected in WISE with W1$-$W2 = 0.34 mag), and it is also a 63.2 μJy radio source, with a corresponding luminosity νL_ν[1.4 GHz]$= 1.57 \times 10^{39}$ erg s^{-1}. Its estimated mass from SDSS is $10^{10.9}$ M$_\odot$. The southern source is an optically identified type 2 quasar, but without a radio counterpart and an estimated mass of $10^{11.5}$ M$_\odot$. The measured FWHM([OIII]) from SDSS of the type 2 quasar implies

an expected radio luminosity of $\nu L_\nu[1.4\ \mathrm{GHz}] = 8.5 \times 10^{39}$ erg s^{-1} according to our equation (3.2), which should be easily detectable by our survey. It is not possible to tell whether the two galaxies are in fact physically interacting.

3.6.2 Objects with interesting structure in radio images

We show two particularly pretty objects from our radio fields (at 6 GHz) in Figure 3.13. The source on the left of Figure 3.13 is a beautiful example of a scaled-down radio core/lobe structure with a clear jet. This source has an SDSS photometric counterpart but no photo-z which prevents an optical classification. There is a WISE detection $< 1''$ from the SDSS optical position with W1−W2=0.83 mag implying it is an AGN and so it is classified as an "IR-bright" source in our catalog. We measure a total 6.0 GHz flux density of 10.4 mJy and it is detected at 1.4 GHz in FIRST at 31.52 mJy. While we cannot determine the spectral index of the seperate components as it appears as only a single extended source in FIRST, the total spectral index of the entire extended source is $\alpha = -0.76$, suggesting that the source flux is dominated by the extended lobes.

The source on the right of Figure 3.13 has no close optical counterpart in the SDSS catalog, though there does appear to be a faint source at the radio location in the SDSS images. The leftmost lobe has a radio flux density of 1.10 mJy and the

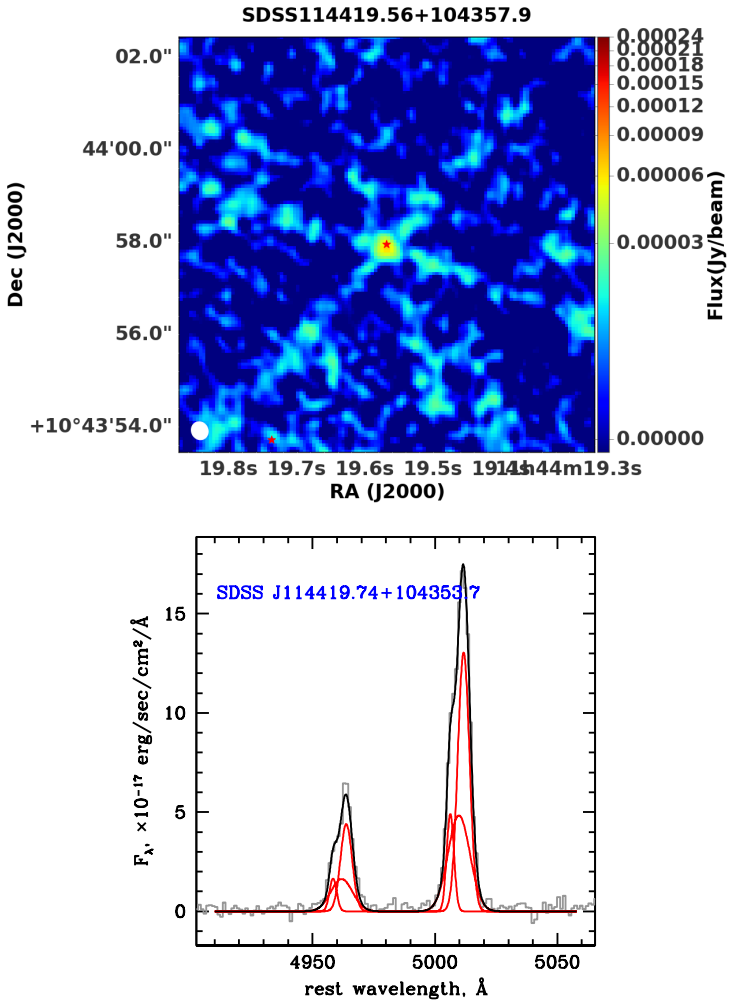

Figure 3.12: VLA (6 GHz) image of the pair of active galaxies SDSS J114419.74+104353.7 (left bottom red star marks optical position) and SDSS J114419.56+104357.9 (center, detected radio source, optical position marked with red star). The first object is an optically identified type 2 quasar which is not detected in the radio, whose [OIII]$\lambda\lambda$4959,5007ÅÅ emission is shown in the right panel. The second object is detected in the radio, but shows a pure absorption-line spectrum in the SDSS with no optical signs of AGN activity.

rightmost lobe of 1.24 mJy. In FIRST at 1.4 GHz it appears that only the right lobe is strongly detected with an integrated flux density of 11.06 mJy. The leftmost lobe is visible at a peak flux density of 0.69 mJy, a 4.6σ detection. This would imply a steep spectral index of $\alpha = -1.5$ in the rightmost lobe, typical of jet-driven radio hotspots, and an unusual flat spectral index of $\alpha = 0.32$ in the left lobe. This source is detected in WISE near the position of the radio center and shows W1−W2=0.27 mag. It would thus be placed in the "IR-bright" category in our analysis in section § 3.5.

3.7 Discussion and conclusions

In this paper we present a sensitive follow up with VLA of five low-redshift ($z \sim 0.5$) and eleven high-redshift ($z = 2 - 3$) obscured radio-quiet quasar candidates.

Radio properties of the high-redshift type 2 population: Our high-redshift candidates are selected on the basis of their emission line properties in the SDSS spectroscopy (Alexandroff et al., 2013) and in their rest-frame spectra they show moderate levels of obscuration ($\lesssim$ a few mag, Greene et al. 2014). The eleven high-redshift quasar candidates that we observed with VLA are radio-quiet, with typical luminosities derived from stacking of $\nu L_\nu[1.4\ \mathrm{GHz}] = 9.1 \times 10^{39}$ erg s^{-1}. At redshifts $2 - 3$, individual radio detections of optically-selected type 2 quasars remain elusive. These objects are radio-quiet and would not be picked up by selection methods which

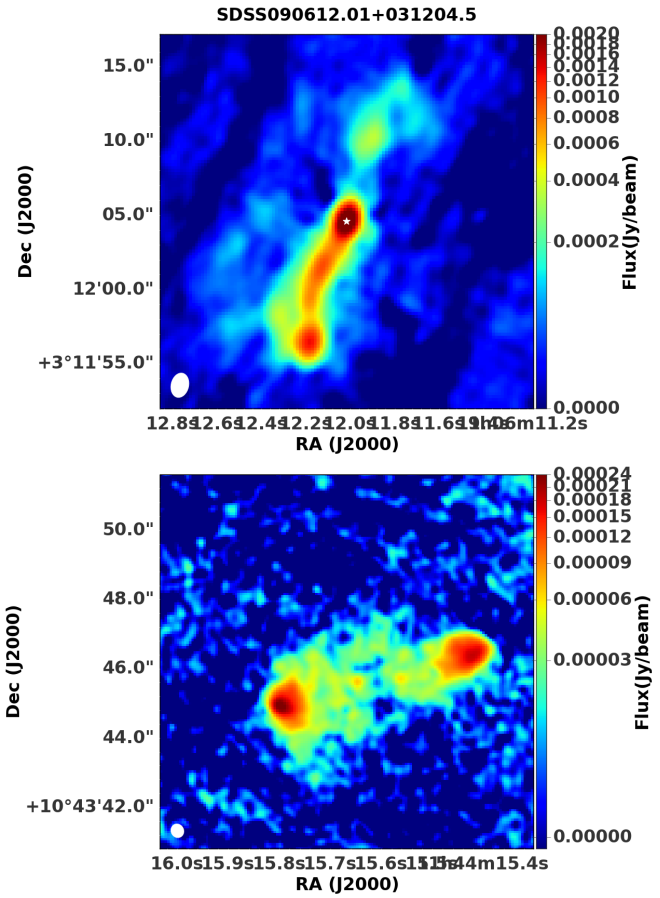

Figure 3.13: Top: VLA (6 GHz) image of an AGN, SDSS J090612.01+031204.5. The beautiful core+lobe structure has a spectral index of $\alpha = -0.76$. It is detected in SDSS with no photo-z measurement and in WISE with a W1−W2 colour of 0.83 which confirms its designation as an AGN. **Bottom:** VLA (6 GHz) image of a radio lobe source which is undetected in SDSS but detected in WISE.

require radio detections to distinguish these objects from dusty star-forming galaxies. Such methods would likely identify only a small fraction of the obscured quasar population.

The radio and emission line properties of type 2 quasar candidates and extremely red quasar candidates lie on opposite ends of the correlation between radio luminosities and velocity widths of [O III] (Mullaney et al., 2013; Zakamska & Greene, 2014). Type 2 quasar candidates are radio-faint and have modest emission line widths (median FWHM[OIII]= 530 km s^{-1}), whereas extremely red quasar candidates which show signatures of fast outflows in their [OIII] emission (FWHM[OIII]= 2930 km s^{-1}) are also significantly brighter in the radio (νL_{ν}[1.4 GHz]= 10^{41} erg s^{-1}). Despite the low fraction of radio detected quasar candidates, we found the stacked radio luminosity to be in agreement with that expected from the measured [O III] luminosity using the relationship defined for $z < 1$ AGN, which suggests that this relationship also holds at high redshift ($z \sim 2.5$) and in a wide range of velocity widths.

Radio properties of the low-redshift type 2 population. The mechanics of the radio / gas kinematics relationship and the origin of radio emission in radio-quiet quasars can be difficult to untangle (Mullaney et al., 2013; Zakamska & Greene, 2014). The relationship could be due to either compact jets driving outflows of ionized gas or to radiatively driven winds which produce radio emission as they shock the interstellar medium of the host galaxy. We attempt to address this issue using high-resolution A-array observations of a small exploratory sample of 5 $z < 0.8$ radio-quiet and radio-

intermediate quasars (four type 2s and one type 1). Few (if any) radio-quiet sources are spatially resolved at the resolution of $\sim$ 10 kpc (Hodge et al., 2011), whereas 4 out of 5 are resolved with a resolution of $\sim$ 2.5 kpc. Thus, galaxy scales might be the key scale to probe in understanding the origin of radio emission in radio-quiet quasars. Future observations of a larger sample of redshift $z < 0.8$ type 2 quasars using the VLA A-array would test this hypothesis.

Of the five sources observed, one is most likely powered by a jet, and in the VLA images we are seeing the self-absorbed, compact jet core. Four more objects are spatially resolved and have steep radio spectra in what would be otherwise considered their radio "core". In a jet scenario, a steep spectrum core in combination with extended emission requires multiple radio jet cycles every $\sim 10^7$ yr of strong interaction between the jet and the surrounding interstellar medium. Alternatively, we could be seeing radio emission associated with radiatively-driven quasar winds.

Study of the faint radio population. We have observed 16 fields with the A-array and the B-array of VLA in a frequency range centered at $\sim$6.0GHz. Eleven of these fields are also observed at a frequency range centered at $\sim 1.4GHz$. Because of the high sensitivity of our observations (typical field center rms of 15 μJy and 80 μJy at 6.0GHz and 1.4GHz, correspondingly), we take the opportunity to investigate the properties of the 179 faint radio sources detected in these observations.

The nature of the sub-mJy population remains poorly understood. We find SDSS counterparts to 41% of our radio sources and an additional 33% are only matched in

WISE. Using spectroscopic and photometric diagnostics we classify the counterparts into optical AGN, passive galaxies (with no signs of AGN activity other than the radio source), star-forming galaxies and IR-bright sources (most likely obscured AGN). Although the four classes of counterparts have roughly equal numbers of sources, we suspect that most of the star-forming galaxies in our sample are mis-identified AGN because the required star formation rate would be implausibly high to account for the observed radio emission. Although population models (Massardi et al., 2010) predict that the 6 GHz sky below 0.1 mJy should be dominated by star-forming galaxies, we find only a small number of such sources. While our small survey limits the number of objects and is only able to probe to our highest sensitivity over a very small area, nevertheless we show the fraction of passive galaxies (most likely identifiable with the low-Eddington ratio sources of Best & Heckman 2012) and IR-bright sources is under-appreciated in studies of the faint radio sky.

In the future, the Very Large Array Sky Survey (VLASS[3]) will likely share many properties with our study of the sub-mJy radio population. Current plans for the VLASS will use the B-array at 3.0 GHz down to a co-added sensitivity of 69 μJy. Similarly, while sensitive data will be available in some regions, large-scale optical and infrared identification will be accomplished with SDSS and WISE with supplemental data from e.g. PANStarrs, the Dark Energy Survey and Hyper Suprime-Cam. Thus, it is clear from our analysis that it will be challenging to identify optical and

[3]https://science.nrao.edu/science/surveys/vlass

infrared counterparts for many of the new faint sources we can expect to detect with the VLASS. For example, E-CDFS matched only 74% of their sources with optical counterparts when their optical data had a 5σ limit of 28.0 magnitudes (Bonzini et al., 2013). In addition, care must be taken to classify sources based on all available multiwavelength data so as to correctly identify all AGN. While in-band spectral indices will be possible with the VLASS, spectral indices with FIRST will be necessary to probe a large frequency range. In this paper we have raised concerns regarding the statistical analysis of spectral indices for populations in which the flux density limit at one frequency is different from the flux density limit at the second frequency or in which the sensitivity strongly varies across the mosaics. Accurately measuring indices in large surveys will require uniform coverage and careful examination of possible biases. Much remains to be discovered about the sub-mJy radio population and a large all-sky survey, especially one that allows for the calculation of spectral indices, will allow us to start definitively identifying the composition of sources contributing in the radio-quiet regime.

Acknowledgements

The authors are very grateful to the astronomers at the National Radio Astronomy Observatory for their technical assistance with proposal submission, verification, and subsequent data analysis. Additionally, the authors would like to acknowledge the

constructive comments of the referee as well as the scientific editor of MNRAS both of whom improved this article. R. A. would also like to acknowledge the assistance of Dr. Ron Allen who provided technical assistance during data analysis.

The National Radio Astronomy Observatory is a facility of the National Science Foundation operated under cooperative agreement by Associated Universities, Inc.

Funding for the Sloan Digital Sky Survey IV has been provided by the Alfred P. Sloan Foundation, the U.S. Department of Energy Office of Science, and the Participating Institutions. SDSS-IV acknowledges support and resources from the Center for High-Performance Computing at the University of Utah. The SDSS web site is www.sdss.org.

SDSS-IV is managed by the Astrophysical Research Consortium for the Participating Institutions of the SDSS Collaboration including the Brazilian Participation Group, the Carnegie Institution for Science, Carnegie Mellon University, the Chilean Participation Group, the French Participation Group, Harvard-Smithsonian Center for Astrophysics, Instituto de Astrofísica de Canarias, The Johns Hopkins University, Kavli Institute for the Physics and Mathematics of the Universe (IPMU) / University of Tokyo, Lawrence Berkeley National Laboratory, Leibniz Institut für Astrophysik Potsdam (AIP), Max-Planck-Institut für Astronomie (MPIA Heidelberg), Max-Planck-Institut für Astrophysik (MPA Garching), Max-Planck-Institut für Extraterrestrische Physik (MPE), National Astronomical Observatory of China, New Mexico State University, New York University, University of Notre Dame, Obser-

vatário Nacional / MCTI, The Ohio State University, Pennsylvania State University, Shanghai Astronomical Observatory, United Kingdom Participation Group, Universidad Nacional Autónoma de México, University of Arizona, University of Colorado Boulder, University of Oxford, University of Portsmouth, University of Utah, University of Virginia, University of Washington, University of Wisconsin, Vanderbilt University, and Yale University.

This publication makes use of data products from the Wide-field Infrared Survey Explorer, which is a joint project of the University of California, Los Angeles, and the Jet Propulsion Laboratory/California Institute of Technology, funded by the National Aeronautics and Space Administration.

Table 3.3: Full Sample Properties.
[1]Original Target Field for the source
[2]Full SDSS J2000 right ascension coordinates
[3]Full SDSS J2000 declination coordinates
[4]Peak Flux Density measured at 6 GHz (mJy/beam)
[5]Local RMS at 6 GHz (mJy/beam)
[6]Peak Flux Density at 1.5 GHz (forced measurement at the location of the brightest component) if available (mJy/beam)
[7]Local RMS at 1.5 GHz (forced measurement at the location of the brightest component) if available (mJy/beam)
[8]Spectral Index using tapered 6 GHz peak flux density of the brightest component and forced flux density measurement at 1.5 GHz
[9]SDSS i−band flux if a source match is identified within 1“ (AB mag)
[10]WISE W1 flux (3.6 μm) if a source match is identified within 3“(Vega mag)
[11]FIRST peak flux density at 1.4 GHz if a source match is identified (mJy/beam).

Field[1]	RA[2]	Dec[3]	$F^4_{P,6GHz}$	rms^5_{6GHz}	$F^6_{P,1.5GHz}$	$rms^7_{1.5GHz}$	α^8	i[9]	W1[10]	FIRST[11]
SDSS J0046	11.5355	0.093513	1.26E−02	3.75E−05	6.26E−02	2.80E−04	−0.55	20.013	16.019	86.48
SDSS J0046	11.55222	0.001347	3.72E−03	2.41E−04	2.51E−02	5.34E−04	−0.24		12.977	29.12
SDSS J0046	11.54333	0.182291	5.74E−04	7.12E−05	1.66E−03	5.80E−04	−0.11		15.689	1.41
SDSS J0046	11.54244	0.046513	2.77E−04	2.35E−05	1.09E−03	3.00E−04	−0.64		17.532	1.07
SDSS J0046	11.58750	0.123513	2.40E−04	3.18E−05	7.51E−05	1.81E−04	1.08		17.379	
SDSS J0046	11.54933	0.116291	1.53E−04	2.49E−05	−1.65E−04	1.93E−04	NaN	21.734	15.65	
SDSS J0047	11.87120	0.742138	1.10E−02	9.25E−05	5.28E−02	1.05E−04	−0.59			58.68
SDSS J0047	11.86126	0.575138	8.94E−03	5.77E−05	1.65E−02	8.70E−05	−0.22	18.559	15.05	19.61
SDSS J0047	11.86915	0.739750	4.22E−03	9.25E−05	1.85E−02	1.47E−04	−0.46			22.42
SDSS J0047	11.92282	0.69152	2.86E−03	1.76E−05	4.09E−03	6.90E−05	−0.08	16.558	13.553	3.97
SDSS J0047	11.88143	0.56719	7.05E−04	5.51E−05	1.40E−03	8.55E−05	−0.66		17.441	0.99
SDSS J0047	11.94349	0.72463	3.91E−04	2.87E−05	6.81E−04	7.08E−05	−0.06	20.932	15.901	
SDSS J0047	11.8659	0.605249	3.10E−04	1.93E−05	5.76E−04	7.64E−05	−0.53			

SDSS J0047	11.96738	0.724860	2.84E−04	4.59E−05	3.69E−04	6.71E−05	0.54			
SDSS J0047	11.81370	0.695360	2.50E−04	1.46E−05	2.95E−04	7.35E−05	0.10	20.843	16.288	
SDSS J0047	11.93143	0.669082	2.24E−04	1.54E−05	4.27E−04	6.70E−05	−0.46	19.244	14.992	
SDSS J0047	11.86776	0.682527	1.01E−04	1.28E−05	2.67E−04	1.06E−04	−0.48	19.793	15.901	
SDSS J0047	11.83165	0.674694	6.96E−05	8.87E−06	−2.92E−04	7.28E−05	NaN		17.257	
SDSS J0047	11.84659	0.619527	6.70E−05	1.03E−05	6.12E−04	1.06E−04	−3.12			
SDSS J0133	23.4072	0.254058	1.36E−03	2.32E−05	4.83E−03	7.29E−04	−0.73			

Chapter 4

Spectropolarimetry of High Redshift Obscured and Red Quasars

Spectropolarimetry is a powerful technique that has provided critical support for the geometric unification model of local active galactic nuclei. In this paper, we present optical (rest-frame UV) Keck spectropolarimetry of five luminous obscured (Type 2) and extremely red quasars (ERQs) at $z \cong 2.5$. Three objects reach polarization fractions of $\gtrsim 10\%$ in the continuum. Though this is close to the theoretical maximum polarization fraction achievable from dust scattering at this wavelength range with typical dust distributions, this mechanism is still preferred because of the known scales of obscuration in these targets. Emission lines are polarized at a lower

level than the continuum. This suggest that the emission-line region is on similar spatial scales as the scattering region. In three objects we detect an intriguing 90 degree swing in the polarization position angle as a function of line-of-sight velocity in the emission lines of Lyα, C IV and N V. We interpret this phenomenon using a conical emission line region and equatorial scattering model in which the scattering material is outflowing at several thousand km sec^{-1}. Our observations provide a tantalizing view of the inner region geometry and kinematics of high-redshift obscured and extremely red quasars and lend strong support for toroidal obscuration and powerful outflows on the scale of the emission line region, as previously indicated by near-infrared data.

4.1 Introduction

The classical unification model of Active Galactic Nuclei (AGN; Antonucci, 1993; Urry & Padovani, 1995) explains the difference between unobscured or "Type 1" AGN and obscured or "Type 2" AGN as the result of differences in viewing angle. In this model, a geometrically and optically thick torus of gas and dust surrounds the AGN accretion disk and broad-line region (BLR). Therefore, if the viewer's line of sight points through the torus, the majority of quasar emission from the accretion disk and the BLR in the optical, ultraviolet (UV) and soft X-rays is obscured. Such an obscured AGN is classified as a "Type 2" and is characterized at optical and

ultraviolet wavelengths by little to no continuum emission and an absence of broad lines (e.g. Kauffmann et al., 2003; Hao et al., 2005). Quasars are high-luminosity AGN (typical bolometric luminosities $\gtrsim 10^{45}$ erg s^{-1}) and it was only in the last fifteen years or so that we have been able to identify appreciable numbers of Type 2 quasars and extend the unification model to all AGN luminosities (Norman et al., 2002; Stern et al., 2002; Zakamska et al., 2003; Stern et al., 2005; Reyes et al., 2008; Treister et al., 2009a; Donley et al., 2012; Alexandroff et al., 2013; Yuan et al., 2016).

In the local universe, a convincing case for the geometric unification model was first made using optical spectropolarimetry of nearby Type 2 AGN (e.g. Antonucci & Miller, 1985; Miller et al., 1991). Though the line of sight in Type 2 AGN is blocked by the obscuring torus, in this geometry optical AGN emission can still escape along the unobscured direction perpendicular to the torus and scatter off of free electrons or dust particles in the quasar host galaxy and into the observer's line of sight. This scattering causes the emission to become linearly polarized, making optical polarimetry and spectropolarimetry the best way to view this scattered emission from the nucleus (Miller & Goodrich, 1990; Tran, 1995a).

This process is also presumably occurring in unobscured or Type 1 AGN, but linearly polarized optical emission represents a much smaller fraction of the total light in these objects and the geometry is less favourable (e.g. Borguet et al., 2008). In fact, typical levels of polarization in unobscured AGN are only 0.5% (Berriman et al., 1990). In contrast, optical polarization levels in Type 2 quasars at low redshift can

reach values of at least a few percent (Smith et al., 2002, 2003; Zakamska et al., 2005) and occasionally as high as $\gtrsim 20\%$ (Hines et al., 1995; Smith et al., 2000; Zakamska et al., 2005). In addition, light from the BLR scatters into our line of sight by the same process so the spectrum of a Type 2 AGN in polarized light possesses broad emission lines (e.g. Antonucci & Miller, 1985; Zakamska et al., 2005). Thus, high measured levels of polarization and broad emission lines seen only in polarization are a tell-tale sign of obscured active nuclei in the classical orientation model. Indeed, it was imaging polarimetry and later deep spectropolarimetry that confirmed the presence of hidden AGN at the centers of radio galaxies– demonstrating that these objects were in fact radio loud Type 2 AGN (see Tadhunter, 2005, and references therein).

Few, if any, spectropolarimetric observations of radio-quiet obscured quasars at the peak of galaxy formation ($z \sim 2.5$) are available because until recently, such objects could not be readily identified. Furthermore, obscured quasars are by definition very faint at rest-frame optical and UV wavelengths, whereas spectropolarimetry requires high signal-to-noise ratio observations to detect polarized flux at the level of a few percent. Therefore, we can only perform polarimetry and especially spectropolarimetry of high-redshift obscured quasars with large telescopes and / or long integration times. Alexandroff et al. (2013) reported the results of spectropolarimetry performed on two high redshift ($z \sim 2.5$) rest-frame UV-selected Type 2 quasar candidates using the CCD spectropolarimeter (SPOL; Schmidt et al., 1992b) at the

6.5m MMT telescope. They demonstrated the presence of a polarization signature at the level of a few percent but low S/N and data on only two objects made further interpretation difficult.

While it is clear what the polarization signal is expected from a quasar obscured by a classical torus (Type 2), perhaps not all quasars possess a classical obscuring region. For example, Sanders et al. (1988) and Hopkins et al. (2006) argue that some obscured quasars may be a particular phase in quasar evolution after a merger or some other instability enshrouds the object in gas and dust. In this mode, obscuration exists on galaxy-wide scales. We then might expect a population of objects with nearly 4π steradians of obscuring material, where the openings in the obscured material are not well-organized in a conical structure. Red quasars at both low (e.g. Smith et al., 2000; Glikman et al., 2007; Urrutia et al., 2009; Glikman et al., 2012, 2013) and high (Eisenhardt et al., 2012; Wu et al., 2012; Tsai et al., 2015; Banerji et al., 2015; Ross et al., 2015; Hamann et al., 2017) redshift may be undergoing a phase of quasar evolution where the obscuring region exists on galaxy-wide scales as evidenced by the presence of galaxy-wide outflows (Zakamska et al., 2016a) and merger signatures (Glikman et al., 2015). Such objects, would not have the same axial scattering regions, and thus would have a lower polarization fraction than classical Type 2 quasars. This work represents an attempt to identify such differences.

In this paper we present observations of five high redshift obscured and extremely red quasars (ERQs) with the Low Resolution Imaging Spectrometer (LRIS; Oke et al.,

1995) in polarimetry mode (Goodrich et al., 1995). We describe our sample selection as well as observations and data reduction in Section § 5.2. Then Section § 4.3 describes our data analysis and results followed by a discussion of those results in Section § 4.4. We introduce our proposed model in Section § 4.4.1 and summarize our conclusions in Section § 4.5.

Throughout this paper, we adopt a cosmology with $h = 0.7$, $\Omega_m = 0.3$ and $\Omega_\Lambda = 0.7$. We use SDSS Jhhmm+ddmm notation throughout the text (full coordinates are listed in Table 5.1) with an additional marker letter to represent how the source was originally identified (see section 4.2.1 for more details). Throughout, u and q refer to Stokes flux densities while U and Q refer to percentages.

4.2 Sample Selection, Observations and Data Reduction

4.2.1 Parent Sample

Our sample includes five reddened and obscured quasars selected by a variety of methods at redshift ($z \sim 2.5$) described in detail in Alexandroff et al. (2013), Ross et al. (2015) and Hamann et al. (2017). We briefly describe the original parent sample selection methods below. General information on these five quasars may be found in Table 5.1. The full sample was chosen to search for evidence of differences in the

covering factor of obscuration (as traced by the polarization fraction) between these two populations.

Two of our sources, which we mark with a 'T' at the end of the designation, SDSSJ1515+1757T and SDSSJ1623+3122TE, were originally selected from the Sloan Digital Sky Survey (SDSS) Baryon Oscillation Spectroscopic Survey (BOSS; Dawson et al., 2013) by their narrow line widths (FWHM < 2000 km s^{-1} in both C IV and Lyman α) and weak continuum in the rest-frame UV, in an attempt to form an optically-selected sample of high redshift Type 2 quasars (for more details see Alexandroff et al., 2013). Only objects from Data Release 9 (Ahn et al., 2012) or earlier were included in this search, which yielded a sample of 145 Type 2 quasar candidates.

An additional three sources, labeled with an 'E', SDSSJ1232+0912E, SDSS1652+1728E and SDSSJ2215−0056E were selected based upon a combination of data from the SDSS and the Wide-Field Infrared Survey Explorer (WISE; Wright et al., 2010b) AllWISE data release[1] to search for objects with red infrared-to-optical colours (Ross et al., 2015; Hamann et al., 2017). This selection method was used to search for obscured quasars at high redshift based on expected high infrared-to-optical ratios. A sub-sample of these very red objects show unusual spectroscopic properties including large rest equivalent width (REW) emission lines ($\gtrsim$ 100 Å), unusually high N V/Lyα ratios and emission lines with high kurtosis (lacking the typical broad wings of gaussian emission lines). These objects were labelled Extremely Red Quasars

[1] http://irsa.ipac.caltech.edu/

(ERQ). We separately selected objects with a required colour between the SDSS i-band and the WISE W3 band (12 μm) ≥ 4.6 and a measured REW of CIV > 100 Å, producing a final sample of 97 ERQs in a redshift range of $2.0 < z < 3.4$ (Hamann et al., 2017).

There is also some overlap between the two samples. While SDSSJ1652+1728E does not meet the strict cutoff required of the Alexandroff et al. (2013) sample of Type 2 candidates, its relatively narrow FWHM in C IV (< 2500 km s^{-1}) should be noted. Additionally, SDSSJ1623+3122TE is considered to be a part of the "expanded" sample of ERQs, defined to have "ERQ-like" line properties even if they are less red than the principal sample in $i - W3$ colours Hamann et al. (2017). We have labelled it as TE in table 5.1 to denote this joint classification. Both the Alexandroff et al. (2013) and the Ross et al. (2015), and Hamann et al. (2017) methods aim to select obscured quasars at high redshifts. While we still do not fully understand the physical properties of each of these populations, SDSSJ1623+3122TE and SDSSJ1652+1728E demonstrate that there can be some overlap between the methods.

Table 4.1: Basic properties of our obscured and highly reddened quasar targets for observation. Our targets span a range of properties in their line widths and colours. Position and redshift information from the SDSS Skyserver Data Release 12. C IV FWHM, REW and kt_{80} were measured by Hamann et al. (2017) for four objects. Measurements for SDSS1515+1757T are taken from the SDSS Skyserver Data Release 12. [[O III]] FWHM and luminosity are either from Zakamska et al. (2016a) or derived from as yet unpublished data from Gemini North.

Short Name	RA	Dec	z	CIV FWHM	[OIII] FWHM	log $L_{[OIII]}$	i − W3	designation
	hh:mm:ss	dd:mm:ss		km s^{-1}	km s^{-1}	erg s^{-1}	AB	
SDSSJ1232+0912E	12:32:41.73	+09:12:09.37	2.374	4787 ± 52	5627	43.92	6.8	ERQ
SDSSJ1515+1757T	15:15:44.00	+17:57:53.06	2.402	1118	856.4	43.98	2.0	T2
SDSSJ1623+3122TE	16:23:27.66	+31:22:04.29	2.344	1572±68	658.3	44.08	4.5	T2E
SDSSJ1652+1728E	16:52:02.64	+17:28:52.38	2.942	2403 ± 45	1461	44.87	5.4	ERQ
SDSSJ2215−0056E	22:15:24.00	−00:56:43.80	2.493	4280 ± 112	3057	43.64	6.2	ERQ

4.2.2 Rest-frame Optical Properties

SDSS covers the rest-frame UV at the redshift of our objects and so follow-up near-infrared (NIR) spectroscopy is necessary to probe the rest-frame optical. We will study the rest-frame optical properties of our targets in more detail in forthcoming papers. For the purposes of the current study, we use the near-infrared (rest-frame optical) spectra primarily to distinguish between classical Type 1 and Type 2 objects, as well as ERQs.

The [O III]λ5007Å+Hβ spectra for all five targets in this Keck program are shown in Figure 4.1, with three objects on top from our new program on the Gemini Near-Infrared Spectrograph (GNIRS) on Gemini-North and two objects on the bottom from the previously published XShooter program (Zakamska et al., 2016a). Our new GNIRS data was obtained in semester 15A in queue mode (PI Alexandroff). The instrument was operated in cross-dispersed mode using the 1/32 mm grating and with a slit width of 0.45″ to provide full wavelength coverage from 0.9 - 2.5 μm, which covers Hα, Hβ and [O III] in the rest-frame of our objects. Each object was observed in queue mode for a total of 60 minutes in a series of nodded 300s exposures along the slit. Data reduction was performed using the XDGNIRS package v2.0 (described in more detail in Mason et al., 2015), a wrapper script for the various PyRAF tasks in the Gemini IRAF package. The script was run in interactive mode and the data were examined at each step in the process to ensure that the pipeline was giving sensible results. As these objects are relatively faint point sources we manually

set the position of the aperture for the trace of each order rather than having the program find it automatically.

Using the calibrated 1D spectra, we performed emission-line fits as in Zakamska et al. (2016a). Briefly, [O III]λ4959Å and [O III]λ5007Å are always assumed to have the same velocity structure and a fixed flux density amplitude ratio of 0.337. Beyond this assumption, our fits are either "kinematically tied" – i.e., the same velocity structure is assumed for [O III], and Hβ – or "kinematically untied", in which Hβ has velocity structure which is different from [O III]. Our null hypothesis is that in Type 2 quasars, [O III] and Hβ are kinematically tied and their typical ratio is 10:1, with the caveat that both of these characteristics can be affected by strong outflows (Zakamska & Greene, 2014; Zakamska et al., 2016a).

Unlike low-redshift Type 2 quasars selected to have narrow Balmer lines, follow-up observations in the rest-frame optical (Greene et al., 2014) of twenty-five objects from our parent sample of Type 2 quasar candidates showed that $\sim 90\%$ of objects displayed a broad Hα or Hβ line and all had intermediate values of extinction (0 mag $< A_{\rm v} <$ 2.2 mag) akin to Type 1.8/1.9 quasars. Yet, both SDSSJ1515+1757T and SDSSJ1623+3122TE – selected based on their narrow high-equivalent-width ultraviolet lines (Alexandroff et al., 2013) – show classical Type 2 quasar features in the optical: they have weak continua, narrow Hβ that has the same velocity structure as [O III], and [O III]/Hβ ratios of 9.9 and 6.9, respectively. These specific objects were chosen for spectropolarimetry follow-up because they are unambiguously high-

redshift Type 2 quasars. SDSSJ1515+1757T shows no sign of [O III] outflows, whereas SDSSJ1623+3122T has a noticeable blue-shifted component in its [O III] emission.

SDSSJ1652+1728E has a mix of features. While it is best fit with a kinematically tied model with [O III]/Hβ=7.7, the rest-frame optical continuum is relatively stronger and marginally inconsistent with a Type 2 classification. In addition, the rest equivalent width of [O III]λ5007Å of 213Å is intermediate between Type 1s and Type 2s at these luminosities, Greene et al. 2014. This object shows very kinematically disturbed [O III], with the width containing 80% of line power of $w_{80} = 1760$ km sec^{-1}, which is in the upper $\sim 5\%$ of [O III] velocity width in the $z < 1$ Type 2 population (Zakamska & Greene, 2014). The remaining two targets, SDSSJ1232+0912E and SDSSJ2215−0056E, are ERQs. In the rest-frame optical, they have a mix of Type 2 and Type 1 characteristics as described in detail in Zakamska et al. (2016a). Primarily, the rest-frame optical spectra is not best fit with a kinematically tied model (in the case of SDSSJ2215−0056E there is no preference between kinematically tied and untied) with REW of [O III]λ5007Å intermediate between expected Type 1 and Type 2 values. Both objects have extremely fast [O III] outflows– FWHM measured as 5630 and 3060 km s^{-1} respectively. Such velocities are too large to be contained by any reasonable galaxy potential and perhaps indicate that these quasars are in the predicted "blowout" phase of quasar activity (Hopkins et al., 2006).

The sample of five objects was selected for follow-up with Keck LRISp to be either Type 2 objects in the rest-frame UV and optical or to be ERQs with signs of outflows.

Thus, this sample allows us to probe the obscuring geometry and scattering efficiency over a variety of obscuring properties in quasars at high redshift.

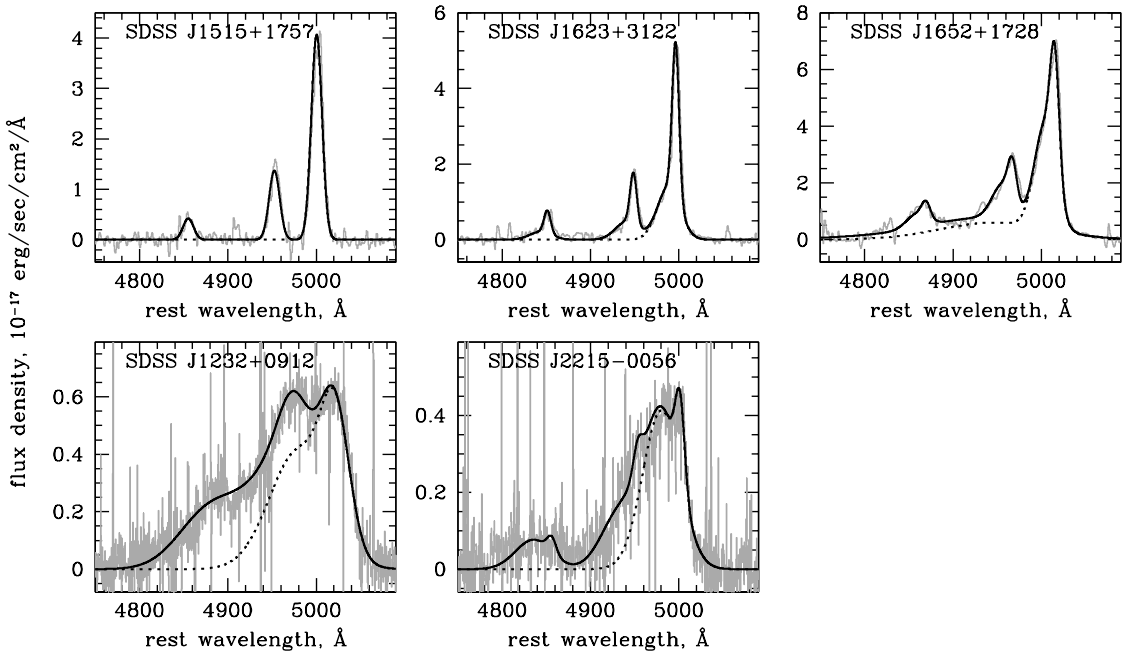

Figure 4.1: The continuum-subtracted [O III]+Hβ complex and best fits for the five objects studied in this paper. Data was obtained for the top three objects with Gemini GNIRS and has not previously been published. Data for the bottom two objects was obtained with the VLT XShooter and was previously published in Zakamska et al. (2016a). The grey histograms show the data, the solid black line shows the best overall fit and the dotted black line shows the [O III]λ5007Å fitted profile separately. In SDSSJ1515+1757T, SDSSJ1623+3122TE and SDSSJ1652+1728E the best fits are kinematically tied (i.e., [O III] and Hβ have the same velocity structure), and the best velocity fit is comprised of one, two and three Gaussian components, respectively. The best fits for SDSSJ1232+0913E and SDSSJ2215−0056E were previously presented in Zakamska et al. (2016a) and are reproduced here. In SDSSJ1232+0913E, the best fit is kinematically untied; in SDSSJ2215−0056E it is kinematically tied; in both cases, two Gaussian components are used for [O III].

4.2.3 Observations and Data Reduction

Data for this project were obtained as part of a NASA time allocation on the Keck Telescope in semester 2015A. All observations were conducted over the course of a single night (UT 2015-05-22) on Keck I from Keck Headquarters in Waimea in clear conditions with seeing around 0.6″. The observational setup was chosen to maximize S/N over resolution for our faint targets and to put the relevant emission lines of Lyα and C IV on the blue side CCD where cosmic ray (CR) effects could be minimized. We used a 1.0″ slit width and the D68 dichroic to separate light into blue and red beams. The blue side spectrograph used a 300 grooves mm^{-1} grism giving a dispersion of 1.43Å pixel^{-1} while the red side used a 400 grooves mm^{-1} grating which gave a dispersion of 1.16Å pixel^{-1}. This blue side grism provides some level of contamination on the red end due to second order light at $\lambda \gtrsim 6400$ Å. No binning either spatially or spectrally was applied during observations. Combined wavelength coverage from both the blue and red sides stretched from 3100-10,300 Å, with a small overlap around $\sim 6500 - 6800$ Å. Calibration darks, dome flats and arcs were taken the afternoon before the start of observations, with additional dome flats taken at the end of the evening.

All of our science targets were observed in a standard sequence of four rotatable half-waveplate exposures (0°, 45°, 22.5°, and 67.5°) lasting 600 seconds on the blue side and 520 seconds on the red side to synchronize read-out times for the ends of the exposures. Four of the quasars were observed for two full observation se-

quences for a total observed time of 4800.0/4160.0 seconds on the blue and red sides respectively. SDSSJ2215−0056E was observed for a single full sequence– half the time of the other objects due to timing constraints. In addition, we observed the flux standard star Feige 34, the null (unpolarized) standard stars HD 109055 and BD+28°4211 (also a flux standard) and the polarized standards HD 155528 and HD 204827. All observations were done at the parallactic angle except for the special case of SDSS1652+1728E described further below.

Cosmic rays for the blue detectors are removed from the unreduced science images using the IRAF imaging version of L.A. cosmic (van Dokkum, 2001). The red detectors, 300μm thick LBNL CCDs (Rockosi et al., 2010) have a much higher detection rate of CRs than the blue CCDs. Because each Stokes parameter is measured using four separate beam spectra and differencing pairs of spectra, any error in cleaning cosmic rays is multiplied four-fold for a single Stokes parameter, and eight-fold for the polarization fraction or polarization position angle. Thus, the red side CCDs suffer so acutely from cosmic ray contamination that the data were unusable.

Data reduction and calibration were conducted following the methods of Miller et al. (1988) and Barth et al. (1999). In brief, bias subtraction, flat fielding, spectral extraction, wavelength and flux calibration were first performed using IRAF, and polarization measurements were performed using routines written in IDL. Uncertainties due to photon-counting statistics and detector readout noise were propagated at every step of the reduction process, yielding error spectra for the Stokes parameters

q and u. Extraction regions were 24 pixels (corresponding to 3.24″) wide except for SDSS1652+1728E which had a different spatial profile (described below). The background region was calculated over 10 pixels (corresponding to 1.35″) above and below the extraction region and additional 10 pixels away from the extraction region. A wide extraction region was used because the science targets were very faint.

SDSS1652+1728E is point-like in the SDSS images. There is another point-like source 1.6″ away which doesn't have SDSS spectroscopy. During the observations, we placed the slit to cover both objects with the thought that the second object might be physically related. The spectra of this companion showed no features in the rest-frame UV and upon further inspection its SDSS photometric colours ($u - g = 0.97$, $g - i = 0.58$) place it firmly in the stellar locus for SDSS point-like objects (Yèche et al., 2010). The presence of this source on the slit makes proper extraction of SDSS1652+1728E complicated as the sources are so close as to be blended in the 2D spectra. We moved the background region an additional ten pixels away and made the extraction region only 20 pixels to avoid the additional source.

The extracted spectra were rebinned to 2Å bin^{-1} prior to polarimetry analysis. Then very fine wavelength alignment (to within 0.1Å) was done using the cross-correlation of all eight available extracted spectra for a single object. The zero point of the polarization angle was calibrated by normalizing to the published value for HD15528 (Clemens & Tapia, 1990) of 105.13°. We find that calculated polarization values and angles for our polarized standards agreed well with published values. For

HD15528 we measure a polarization of $4.979 \pm 0.003\%$ in the V-band (mean $\lambda \sim$ 5388Å and $\Delta\lambda \sim$ 352Å) which differs by 2.61% from the original published value (Clemens & Tapia, 1990). For HD204827, we measure a polarization of $5.760 \pm 0.003\%$ with a polarization position angle of $\theta = 59.48 \pm 0.02$ degrees in the B -band (4000-5000 Å). This is only 0.5% from the published values in Schmidt et al. (1992a). In addition, observations of unpolarized standard stars show well-behaved, flat response over the entire observed wavelength range and give a calculated polarization of 0.08%. Though this measurement is some combination of the stellar and instrumental polarization it is small enough that we conclude we can disregard the effects of instrumental polarization.

We conduct a variety of consistency checks with our data to convince us of the accuracy of our results. We measure the polarization for each sequence of exposures separately to make sure they were consistent before we combined them using a simple algorithm which weights each half equally. We also checked that the normal and optimal weighting algorithms (Horne, 1986) for the source extraction gave similar results. We used the optimal weighting algorithm except for when measuring the line polarization for SDSS1515+1757T and SDSS1623+3122TE where the results did not agree well. It is also encouraging that clear detections of polarization in the continuum show consistent values of the observed polarization angle except in cases where the polarization angle can clearly be seen to physically vary as a function of wavelength (see section 4.3 for more information).

All polarization measurements were then made in the q and u spectra and converted to a debiased polarization and position angle, following the steps outlined in Miller et al. (1988). To increase S/N in the continuum we binned over several hundred Angstroms for each measurement. We are careful not to include wavelengths on the very red edge of the blue CCD to avoid the second order light due to the blue side grism. Polarization fractions and angles as well as the wavelength range over which each was calculated are listed in Tables **??** and 4.3. The usual polarization is a positive-definite value, $p = \sqrt{q^2 + u^2}$ which becomes problematic in our regime of low S/N so instead we report the debiased polarization which has a better behaved error distribution, $p = \sqrt{q^2 + u^2 - \sigma_q^2 - \sigma_u^2}$. In the cases where measured error is larger than the measured signal we report a debiased polarization fraction of zero. The total flux spectra as well as continuum polarization and position angle measurements are shown in figure 4.2.

All our candidates lie at relatively high Galactic latitudes ($|b| > 30°$) with a range of $34.0° < |b| < 71.5°$, and thus the contribution to the polarization from interstellar dust is expected to be quite low. In fact, Serkowski et al. (1975) demonstrated that the Galactic interstellar polarization is measured to be $\lesssim 9\%$ E(B-V). We check the measured values of E(B-V) along the sightlines to our targets from both Schlegel et al. (1998) and Schlafly & Finkbeiner (2011) and find a range of values $0.0206 <$ E(B-V) < 0.1179 mag implying polarizations of $\lesssim 1\%$, much smaller than any of the values we are measuring in our targets. Thus we conclude that interstellar polarization has

a negligible effect on our measured polarization values.

4.3 Results

Our sample spans a range of rest-frame optical properties as described in Section 4.2.2, from classical Type 2 spectra with quiescent [O III] kinematics to extreme [O III] outflow activity. Here, we discuss the results of our spectropolarimetry analysis and connect them to other known multi-wavelength properties of our targets.

In Figure 4.2 we present the Keck LRISp data for each of our objects. We display the high sensitivity total UV spectrum followed by the binned polarization fraction and polarization position angle. We also display the full polarization position angle as a function of wavelength in the emission lines (smoothed using a least-squares polynomial smoothing filter with a window of five pixels) to allow variations to be apparent. In the following sections we discuss the observed trends in our spectra which we will attempt to connect to the relevant physics in section 4.4.

4.3.1 Level of Continuum Polarization

In Table 4.2 and Figure 4.2, we present continuum polarization measurements in several continuum regions, chosen in the rest-frame of the quasar to avoid contamination by UV emission lines. The level of continuum polarization just blueward of C IV (rest frame 1425Å-1525Å) spans from $15.7 \pm 0.4\%$ in SDSSJ1652+1728E to consistent

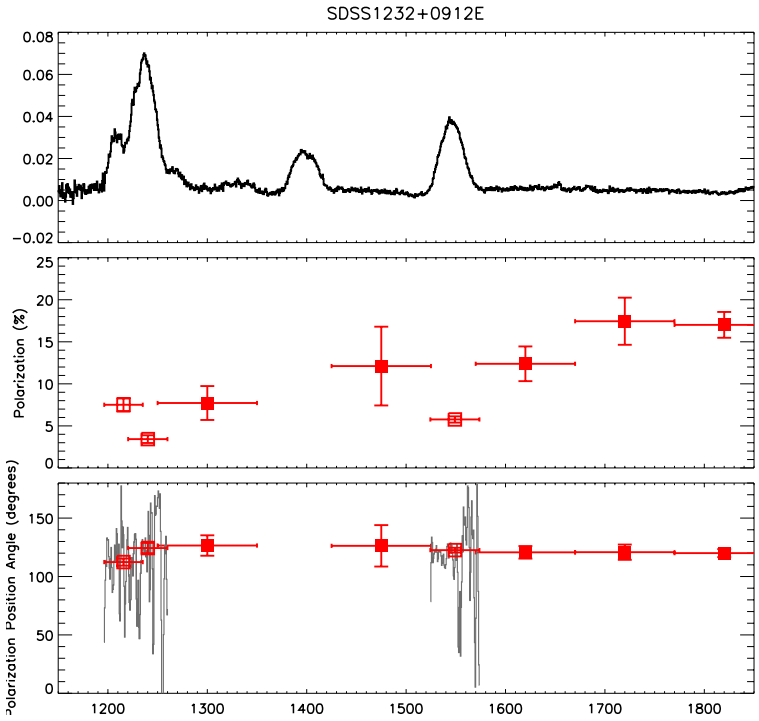

Figure 4.2: LRISp spectra of our targets. The top panel shows the total flux spectrum while the middle panel shows the continuum polarization and statistical error in that measurement over the binned wavelength range indicated by the x-axis error bars (same as Table 4.2) and the bottom panel shows the same for polarization angle (also given in Table 4.3). The filled squares represent continuum measurements while the open squares represent emission line measurements. In grey, we include the unbinned polarization position angle in the emission lines to highlight the wavelength dependence. See section 4.3.4 for a discussion.

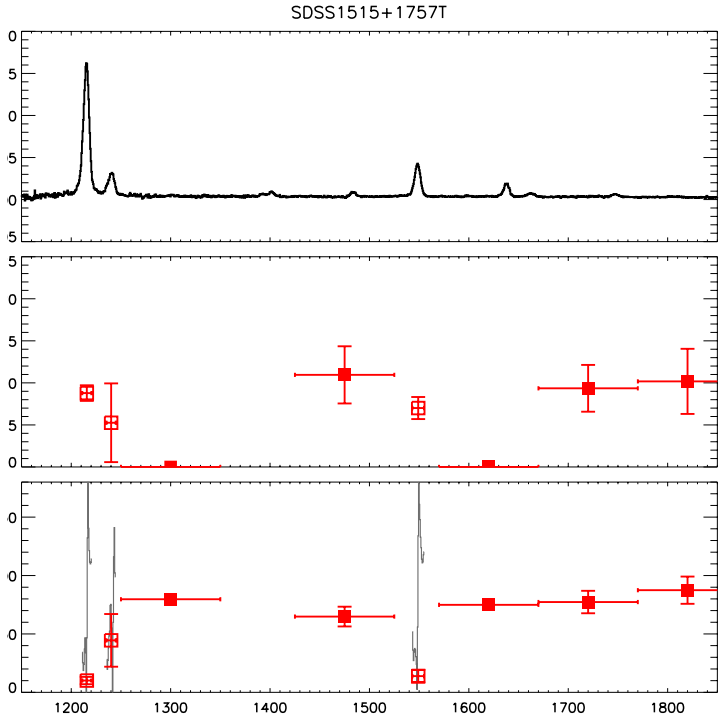

Figure 4.2: continued

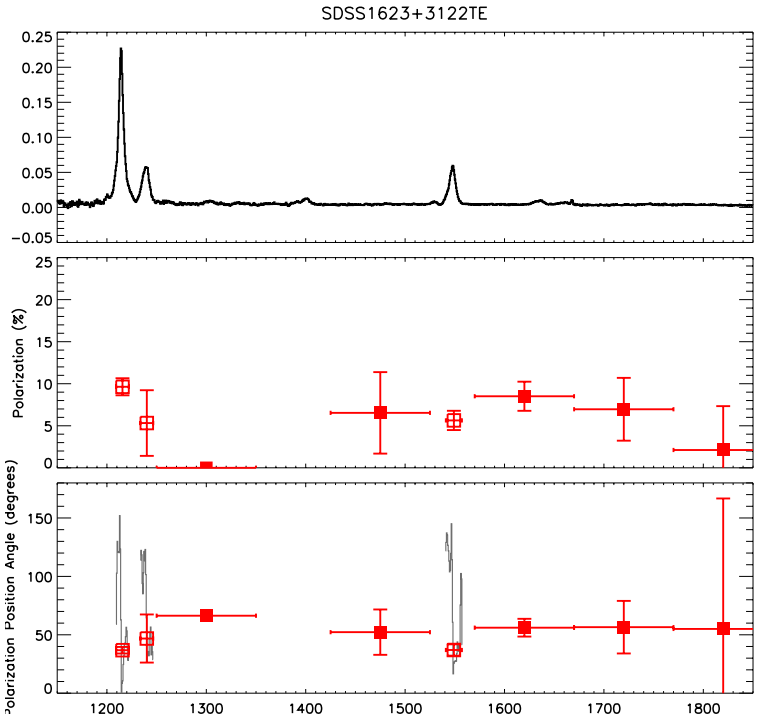

Figure 4.2: continued

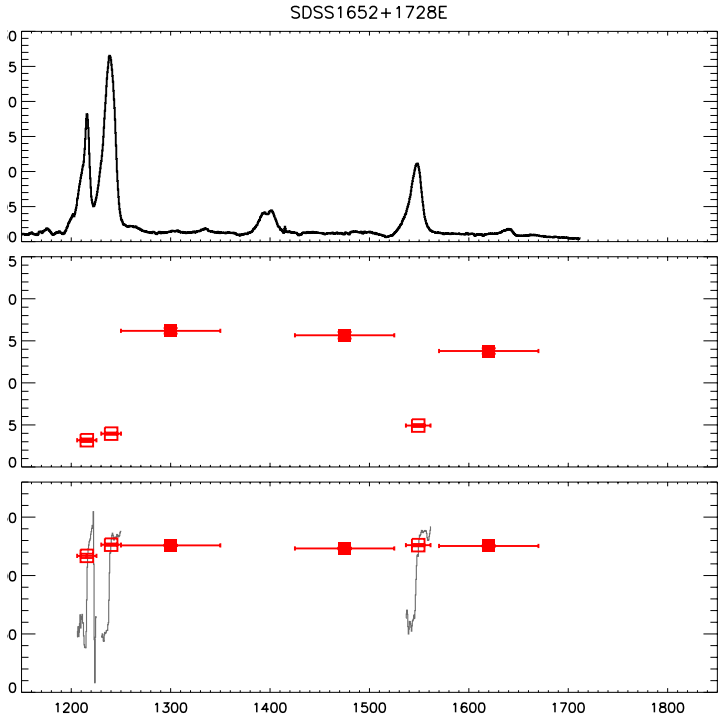

Figure 4.2: continued

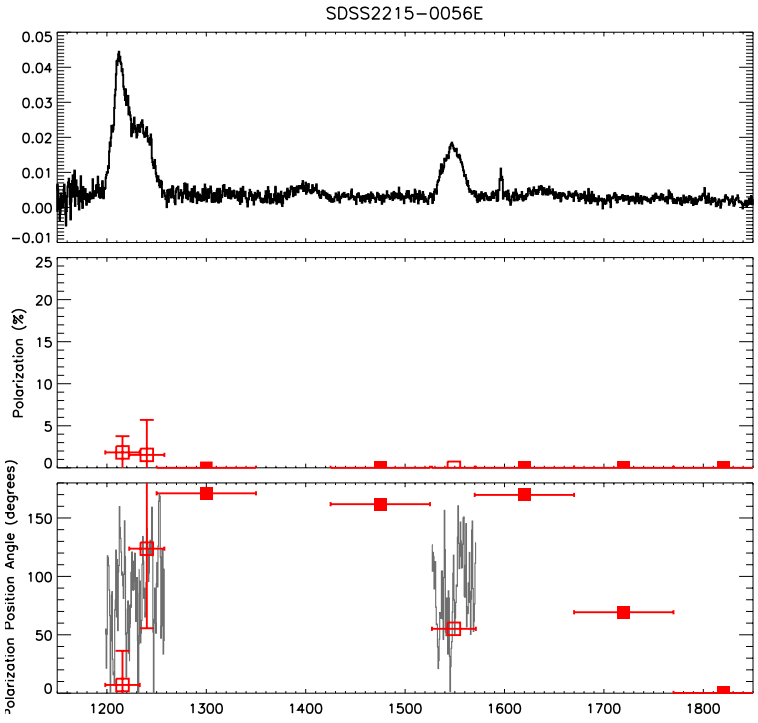

Figure 4.2: continued

with zero in SDSSJ2215−0056E.

These values of continuum polarization are very high for non-synchrotron emitting sources. The notable exception is SDSSJ2215−0056E, where we observe low levels of polarization with large uncertainty consistent with zero polarization in most wavelength ranges covered. Overall, the polarization values measured are much higher than that observed in Type 1 AGN where, for example, Berriman et al. (1990) found an average polarization of 0.5% for all 114 quasars from the Palomar-Green Bright Quasar Survey with a maximum polarization of 2.5%. These values are even on the extreme end of Type 2 AGN, radio galaxies and BAL quasars (Hines et al., 1995; Smith et al., 2000, 2002, 2003; Zakamska et al., 2005). For example, Smith et al. (2002) found no Type 2 quasars with polarization values $> 3\%$ but their continua were contaminated by host galaxy light. Zakamska et al. (2005) measure a polarization $> 3\%$ in nine of twelve Type 2 quasars and a mean polarization of 5.7% for all twelve objects with a maximum polarization of 15.4%. They contend all but one object are uncontaminated by the host galaxy though this is for the rest-frame optical (between ~ 2800 and ~ 6500Å). Smith et al. (2000) studied two Two Micron All-Sky Survey (2MASS)-selected obscured AGN and found continuum polarization values of $\sim 15\%$ in their optical continuum and BLR, in line with our measurements.

In Alexandroff et al. (2013), we found levels of polarization $> 5\%$ in the blue continuum of one object, SDSSJ220126.11+001231.5, and an overall average polarization of $1.9 \pm 0.3\%$, higher than could be accounted for by a typical unobscured

quasar combined with instrumental systematics ($\lesssim 0.1\%$) and galactic polarization ($< 0.8\%$). The second object observed in that paper, SDSSJ004728.77+004020.3 had an average polarization of only $0.91 \pm 0.35\%$ making our interpretation of the nature of the source less clear. These objects however were not pre-selected to be unambiguous Type 2 quasars based on their rest-frame optical spectra unlike the objects designated with a 'T' in this work.

We argued in Alexandroff et al. (2013) that the continuum luminosity detected in our sample of high-redshift Type 2 candidates from SDSS was too high to be explained by the host galaxy alone. Instead, because the rest-frame UV slope was relatively flat or blue some sort of "patchy" geometry allowing some direct sightlines to the quasar or scattered light were required to make up a significant fraction of the observed continuum. Similarly, the high optical continuum in ERQs and other red quasars also suggests patchy obscuration or scattering (Assef et al., 2016; Zakamska et al., 2016a; Hamann et al., 2017) though if the obscuring/scattering region is more or less spherically symmetric on galaxy scales then it would not lead to strong polarization. Detecting such high values of continuum polarization in these sources is unambiguous confirmation that most of the continuum emission is due to anisotropic scattered light.

In figure 4.3 we plot the mean continuum polarization fraction as a function of outflow velocity as measured by the [O III] w_{80} parameter. Type 2 and ERQ objects lie in different regions of this parameter space– the two Type 2s have the smallest outflow velocities. Though admittedly a small sample, we find no relationship between the

rest-frame optical type (Type 2, ERQ) or the presence of [O III] outflows and the continuum polarization level.

Table 4.2: Polarization percentages for each of our targets as a function of rest wavelength. All measurements are listed as percentage of the total flux.

Short Name	1250Å-1350Å	1425Å-1525Å	1550Å-1650Å	1650Å-1750Å	1750Å-1850Å
SDSSJ1232+0912E	7.7±2.0	12.1±4.7	12.4±2.1	17.4±2.8	17.0±1.5
SDSSJ1515+1757T	0.0	11.0±3.4	0.0	9.4±2.8	10.2±3.9
SDSSJ1623+3122TE	0.0	6.5±4.8	8.5±1.7	7.0±3.7	2.1±5.2
SDSSJ1652+1728E	16.2±0.3	15.7±0.4	13.8±0.3		
SDSSJ2215−0056E	0.0	0.0	0.0	0.0	0.0

Table 4.3: Polarization percentages for each of our targets as a function of rest wavelength. All measurements are listed as percentage of the total flux. For emission lines the polarization was measured over the FWHM of C IV for each object.

Short Name	Lyα	N V	C IV
SDSSJ1232+0912E	7.5±0.8	3.4±0.5	5.8±0.4
SDSSJ1515+1757T	8.8±0.9	5.3±4.7	7.0±1.3
SDSSJ1623+3122TE	9.6±1.0	5.3±3.9	5.6±1.1
SDSSJ1652+1728E	3.2±0.2	4.0±0.1	4.9±0.2
SDSSJ2215−0056E	1.8±1.9	1.5±4.2	0.0

4.3.2 Wavelength Dependence of Continuum Polarization

Scattering of the continuum can be due to dust or free electrons in the ionized gas. The expected polarization fraction due to electron scattering is described by the Thomson formula and is independent of wavelength. For dust scatting, the polarization fraction may vary as a function of wavelength depending on the dust composition and size distribution. Of course there are many complicating factors (see section 4.4.4), but it is still important to establish whether the polarization fraction varies in order to help determine the polarization mechanism.

There is marginal evidence for a wavelength-dependence in the polarization fraction in the continuum of our objects, with the polarization fraction appearing to rise at longer wavelengths. Such a trend is particularly evident in SDSSJ1232+0912E. Unfortunately, our achievable sensitivity makes it difficult to determine if this trend is real as most of the variation is within the observed error bars.

Alexandroff et al. (2013) also concluded for a single object that there was evidence for wavelength-dependent polarization fraction that was strongest at bluer wavelengths, the opposite of what we observe. A decreasing polarization fraction at redder wavelengths suggests either that the polarization is wavelength-dependent and therefore likely caused by dust, or that the continuum is contaminated in this region by red unpolarized light that dilutes our polarization signal.

4.3.3 Overall Polarization of Emission Lines

The observed level of polarization in emission lines relative to the continuum is a good indicator of the geometry and polarization mechanism of the emission lines. In particular, the polarizing fraction of the emission lines relative to the continuum can indicate the scale of the scatterer. If the emitting region and the scattering region are on the same scale then this will dilute the polarization signature as there is no single, coherent scattering direction. Higher values of the ratio of emission line to continuum polarization imply scattering on large scales, beyond the line emitting regions, so that the lines remain as polarized as the continuum while lower values of this ratio imply that the scattering is on scales closer to or within the emission line region and thus the line emission is only marginally polarized. This geometric dilution in emission line regions relative to the continuum is found in many AGN sources (e.g. Stockman et al., 1981; Glenn et al., 1994; Goodrich & Miller, 1995; Tran, 1995b) and implies that the scattering region is on a similar, or slightly larger scale, than the emission

region.

We consider the UV emission lines of Lyα, N v and C iv, integrating over the FWHM of C iv (see Table 5.1). In all cases the observed polarization fractions are lower than the continuum polarization with the possible exception of the quasar SDSSJ1623+3122TE. Nevertheless, polarization values can still reach levels of $> 8\%$ in the Lyman α emission line, most notably in SDSSJ1515+1728T and SDSSJ1623+3122TE.

In figure 4.3 we plot the ratio of the line polarization fraction to the continuum polarization fraction just blueward of C iv between 1425Å and 1525Å. There is some evidence that those objects designated as classical Type 2s in our sample (left side of the plot, also with smaller outflow velocities), may show higher values of this ratio. In fact, the mean ratio over all lines is 0.36 for ERQs, while the mean ratio for Type 2 objects is 0.85. In a scenario where resonant scattering has little effect on the measured polarization fraction this ratio measures the geometric mixing of each emission region and the scattering medium. This implies that the scattering regions for classical Type 2s may be on larger scales than the scattering regions in ERQs. This scenario is complicated if resonant scattering has a strong effect on the measured emission line polarization fractions but, in section § 4.4.4 we consider and reject the possibility of resonant scattering as the source of polarization in the emission lines of our objects.

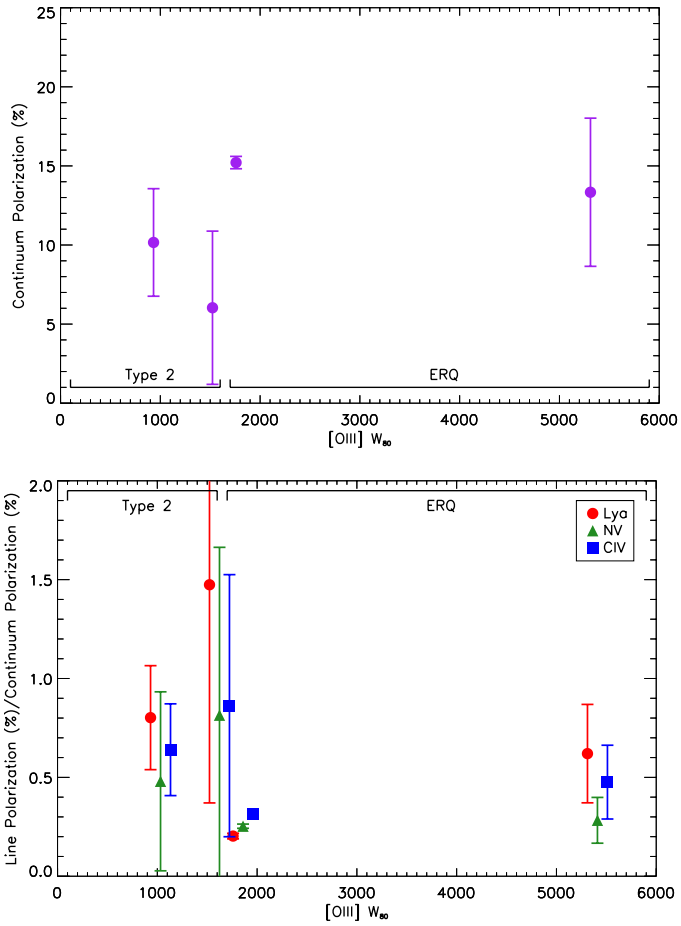

Figure 4.3: Top: Continuum polarization levels (percent) averaged over the continuum regions as a function of outflow speed as measured by the w_{80} parameter of [O III]. We see no trend between this measure of the outflow speed and the polarization fraction in the continuum. **Bottom:** Ratio of line polarization for the three prominent lines in the observable range of our objects to continuum polarization levels measured blueward of C IV between 1425Å and 1525Å (percent) as a function of outflow speed as measured by the w_{80} parameter of [O III]. There is some evidence that the Type 2 objects are in a different regime with higher line polarizations. In a scenario where this ratio is a measure of the geometric mixing of the emission and scattering regions this would imply that the scattering regions in classical Type 2s are on larger scales than the scattering regions of ERQs.

4.3.4 Kinematics of Line Polarization

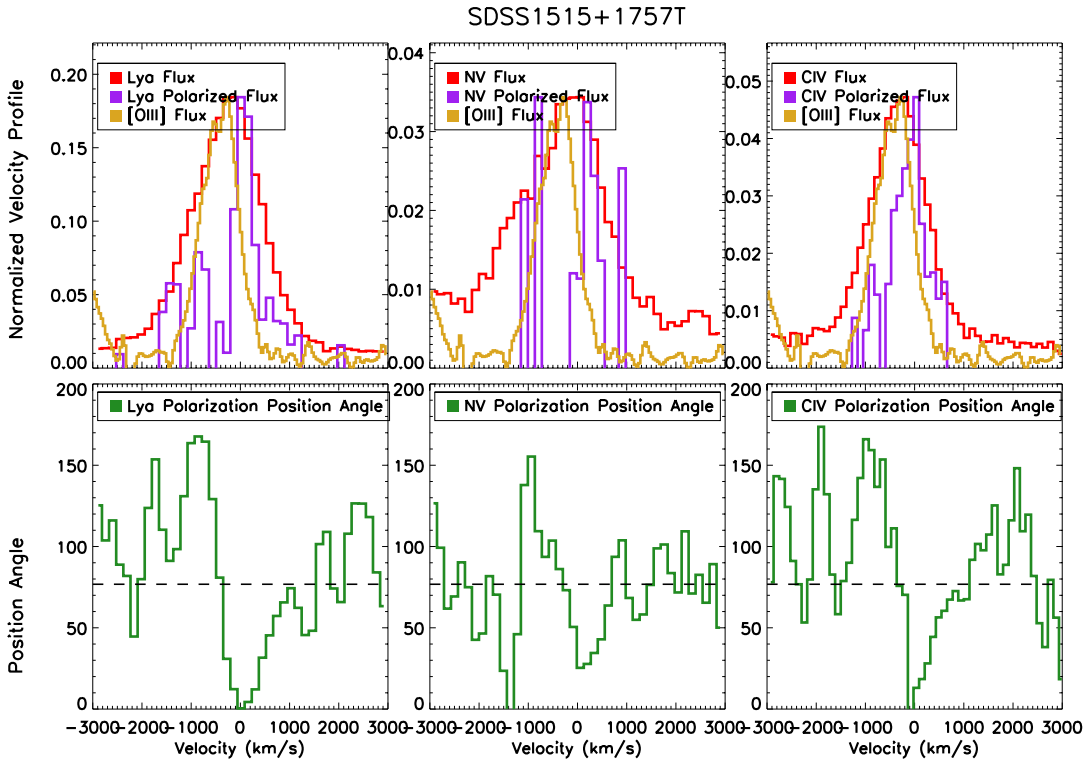

Figure 4.4: LRISp spectrum of SDSSJ1515+1757T, SDSSJ1623+3122TE, and SDSSJ1652+1728E over various important emission line regions in velocity space. We overplot the total flux of the line (red), the polarized flux (polarization fraction × flux; purple), and the [OIII] flux (yellow), all scaled to arbitrary units to illustrate how the different quantities exhibit various structures in velocity space. We also show the polarization position angle (green) below.

There is also a significant amount of variation in the polarization fraction across emission lines. The polarization fraction tends to reach a minimum around the line centroid and a maximum at a redshift between $+1000 < v_{max} + 2000\text{km s}^{-1}$. This pattern is perhaps most pronounced in SDSSJ1652+1728E (Fig. 4.4). Such wavelength-dependent polarization in emission lines is present in several objects in our sample and may provide a unique window in to our understanding of the scattering geometry.

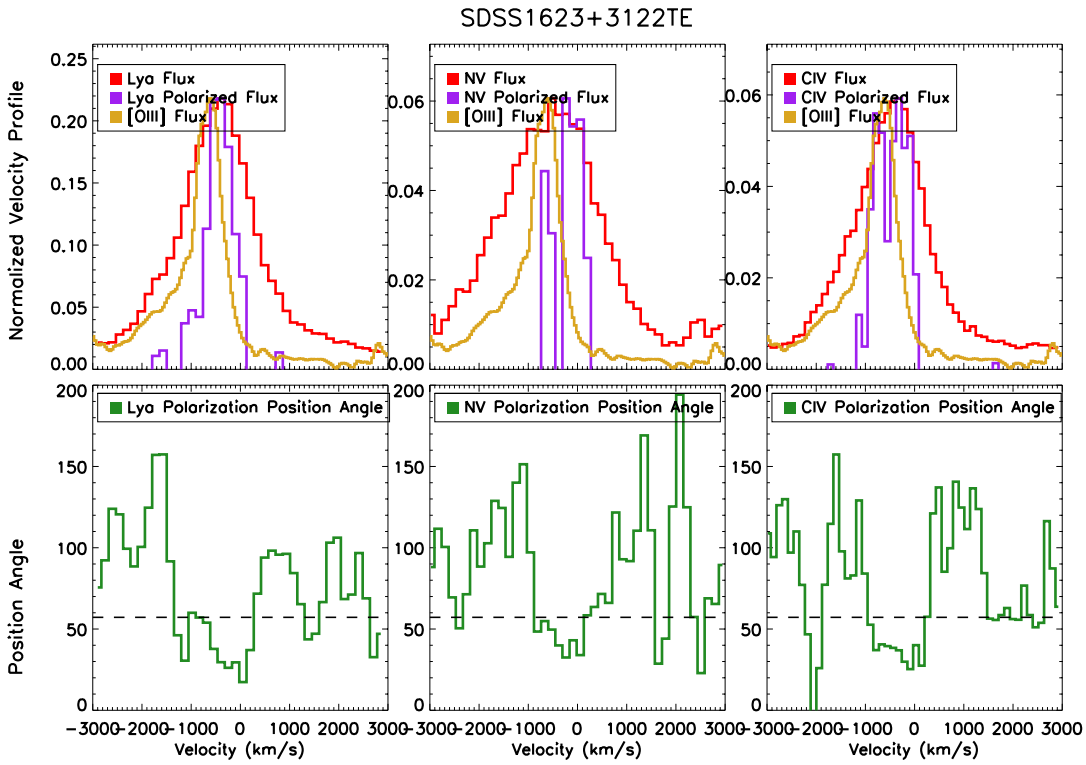

Figure 4.4: continued

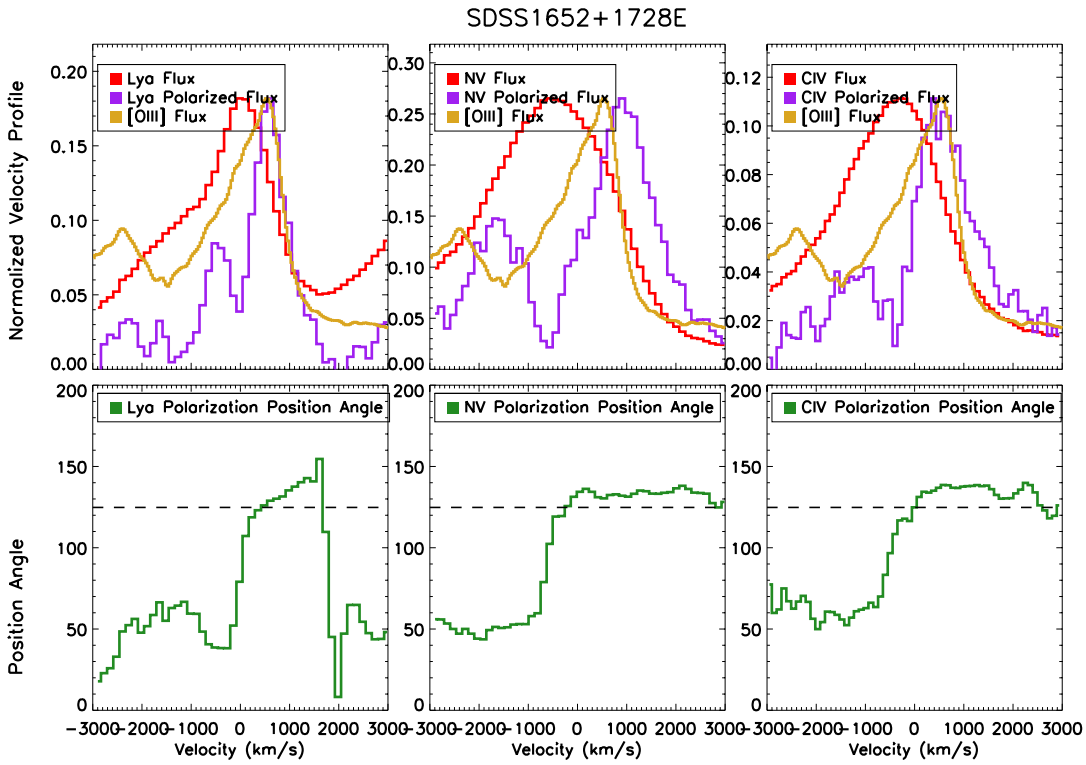

Figure 4.4: continued

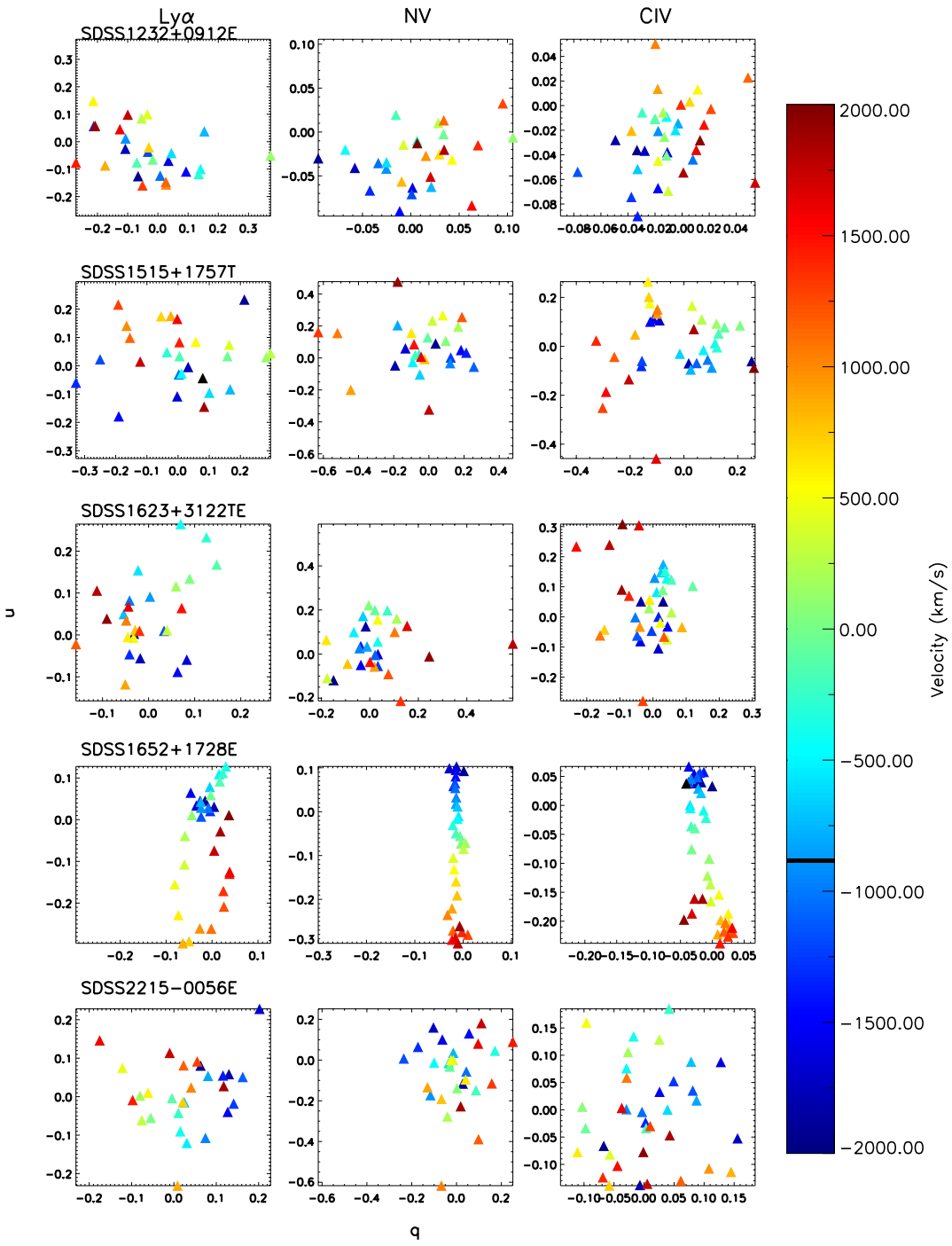

Figure 4.5: Plot of q and u Stokes parameters for each of the key emission lines in our targets. Each point represents a spectroscopic pixel. We show over $\pm$2000 km s^{-1} in velocity space with the colour scale. Notice, especially in SDSSJ1652+1728E, the clear presence of loops in q vs. u space.

We discuss further in section § 4.4.

Perhaps the most intriguing trend we observe is the wavelength-dependence of the polarization position angle across all emission lines in many of our objects. This trend can be observed in SDSSJ1515+1728T, SDSSJ1623+3122T and most dramatically in SDSSJ1652+1728E. This observed trend has several key features. First, the polarization position angle appears to vary by almost exactly $\pi/2$ radians across the emission line (again, see Fig. 4.4). Most notably for our analysis, the polarization position angle of the continuum is the same as the polarization position angle of the emission line gas at the reddest wavelengths. This trend can easily be observed in Figure 4.4 but we also present the observation as a change in the ratio of the u and q Stokes parameters in Figure 4.5. This format is inspired by similar figures for the study of polarization in supernovae (SNe; for a thorough review see Wang & Wheeler, 2008).

If there were a single, smooth and axisymmetric scattering region where the polarization was independent of wavelength, we would find a consistent polarization fraction which would result in a clustering of all data points in the q/u plane. If, instead, there is some form of homologous expansion of the scattering material ($v \propto r$), then at each wavelength the viewer is seeing a different slice or shell in the expanding scattering material. Each slice will have a different optical depth which would introduce a wavelength dependence to the polarization and thus cause the data points to spread out in a line in the q/u plane, also known as the "dominant axis" (Hoeflich

et al., 1996; Wang et al., 2001). Deviations from this straight line in the q/u plane then represent deviations from the assumptions of smoothness or axisymmetry in the scattering geometry. These deviations must be finite to maintain the presence of a single dominant axis in the plane (e.g. the presence of clumpy material). This model ignores scattering in the interstellar medium of our galaxy which can cause a rotation in the polarization position angle. It also does not include scattering of continuum photons in to resonance with emission lines which can change the polarization position angle if the geometry of the continuum scattering region is different from that of the emission line scattering region. One common feature both in our data, best seen in SDSSJ1652+1728E, as well as many SNe (Wang & Wheeler, 2008) is the presence of loops in the q/u plane where both the amount of polarization and the polarization position angle varies across the emission line, representing a large physical deviation from axial symmetry. Possible explanations for loops in the q/u plane include an overall asymmetry to the scattering structure, an additional expanding shell with a different geometry, or the breakup of an axially-symmetric scattering structure into clumps (Kasen et al., 2003; Wang & Wheeler, 2008).

Loops in the q/u plane as a function of wavelength across emission lines has been widely observed among a number of AGN observed with spectropolarimetry. Smith et al. (1995) argued that structure in the polarization fraction of the emission lines in Mrk 231 requires several scattering components. Smith et al. (2000) further argued that structure in the polarization fraction and polarization position angle across broad

emission lines coupled with larger values of polarization in the continuum than the emission lines implies that the the BLR of the 2MASS quasars contains multiple scattering components. In contrast, Young (2000), Smith et al. (2005), and Young et al. (2007) have argued that such swings in the polarization position angle are due to emission and scattering by an equatorial disk wind that is visible in Type 1 quasars but is overwhelmed by polar scattering signatures in Type 2 quasars.

4.4 Discussion

Several trends are visible in our observations as noted in section 4.3:

1. polarization reaching $> 10\%$ in the continuum for three of five sources;

2. a ratio of emission line polarization/ continuum polarization that is close to 1/3 for ERQs and 4/5 in our Type 2 sources;

3. strong evidence for wavelength-dependent polarization fraction in the emission lines; and

4. change in the polarization position angle across emission lines of $\sim \pi/2$ radians, with the redshifted line emission at the same position angle as the continuum.

4.4.1 Proposed Model

To model these trends, we vary a number of parameters. Polarimetry models include both an emission and scattering region (though they can be coincident) which can be either stationary or have some velocity. In addition, we can vary the type of scatterer and scattering mechanism. For example, the classical model that explains the spectropolarimetry of obscured quasars is that of a point-like emitting region with a conical scattering region defined by the opening angle of the torus (Miller et al., 1991).

Combining all of these considerations, we constructed a model of the emission, scattering and resulting polarization expected for simple geometries and polarization mechanisms. The full details of this model are available in Zakamska et al. 2017 (in prep). We find that the model with the best fit to our data is a polar emission region (expanding emission within a filled cone) which is scattered by dust in an equatorial outflow (see Figure 4.6). While there are certainly more complicated geometries that would reproduce all our results, this model has the advantage of being straightforward and physically motivated.

There is both observational evidence and much theoretical work to support an equatorial, dusty outflow from the AGN accretion disk that is supported by radiation pressure (e.g. Wills et al., 1992; Elitzur & Shlosman, 2006; Veilleux et al., 2016; Chan & Krolik, 2016; Elvis, 2017). If the AGN is near or super-Eddington, the creation of a geometrically thick accretion flow also produces polar radiation driven outflows (e.g.

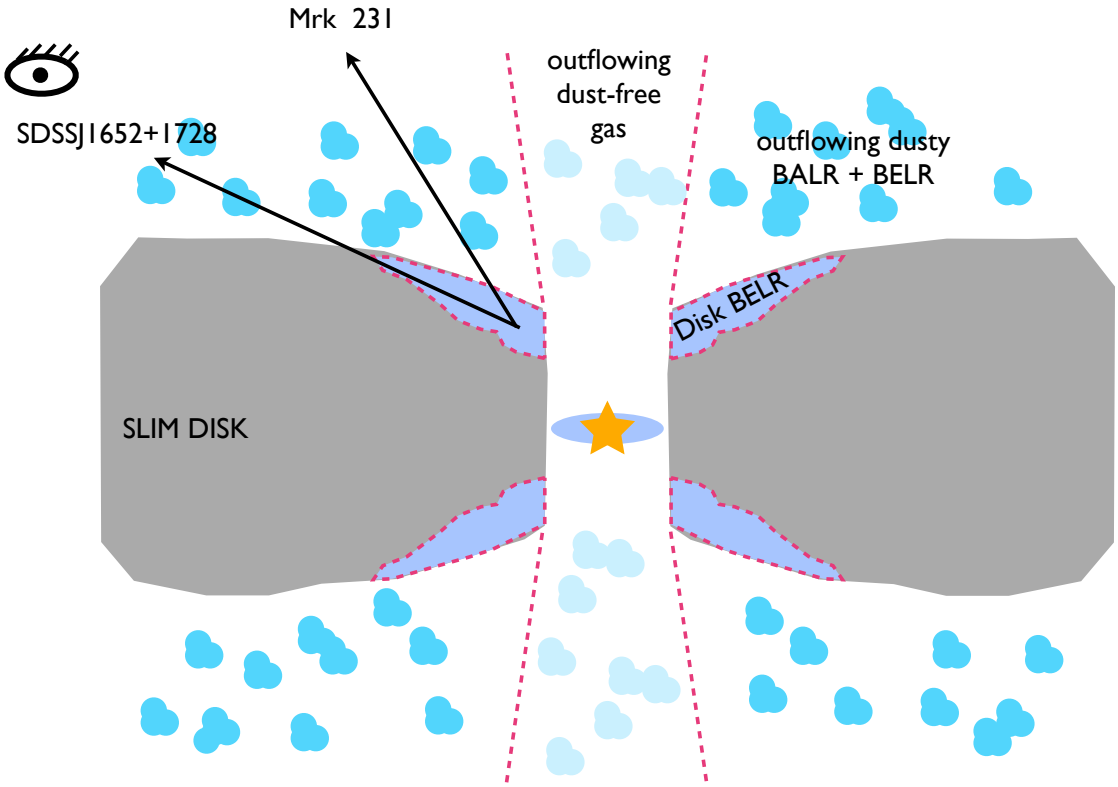

Figure 4.6: Our preferred model for SDSSJ1652+1728 is adapted from Veilleux et al. (2016). It combines a polar outflow which produces the emission lines with a dusty equatorial wind where the scattering occurs. Side-on view of the inner ∼10 pc of our model (not to scale). The inner accretion disk ($\lesssim$ 0.01pc) is responsible for the X-ray emission and is surrounded by a geometrically-thick accretion disk ("slim disk") which, for a near- or super-Eddington quasar produces narrow funnels that drive a polar wind. This polar wind is comprised of both dust-free outflowing gas, responsible for X-ray absorption, as well as dusty clouds that produce FeLoBAL absorption signatures and the blueshifted FUV emission lines of Lyα and C IV. The extended accretion disk is the source of the UV and optical continuum emission as well as the Balmer lines (seen through the screen of the outflowing dusty BALR). Mrk 231 is constrained to have a jet angle of $\theta_{max} = 25.6^{+3.2}_{-2.2}$ degrees from radio observations (Reynolds et al. 2013). This means that the scattered light, though still significant, is unpolarized in the observer's line of sight due to geometric cancellation. In contrast, SDSSJ1652+1728 is seen at a larger angle to the jet or polar axis as inferred from the mean SED of ERQs (see section 4.4.1 for further discussion). The increased column density of obscuration suppresses the FeLoBAL features while the more edge-on sight line reduces geometric cancellation of the polarization signature. Though the original cartoon contains a radio jet we omit this as it is not the subject of this work.

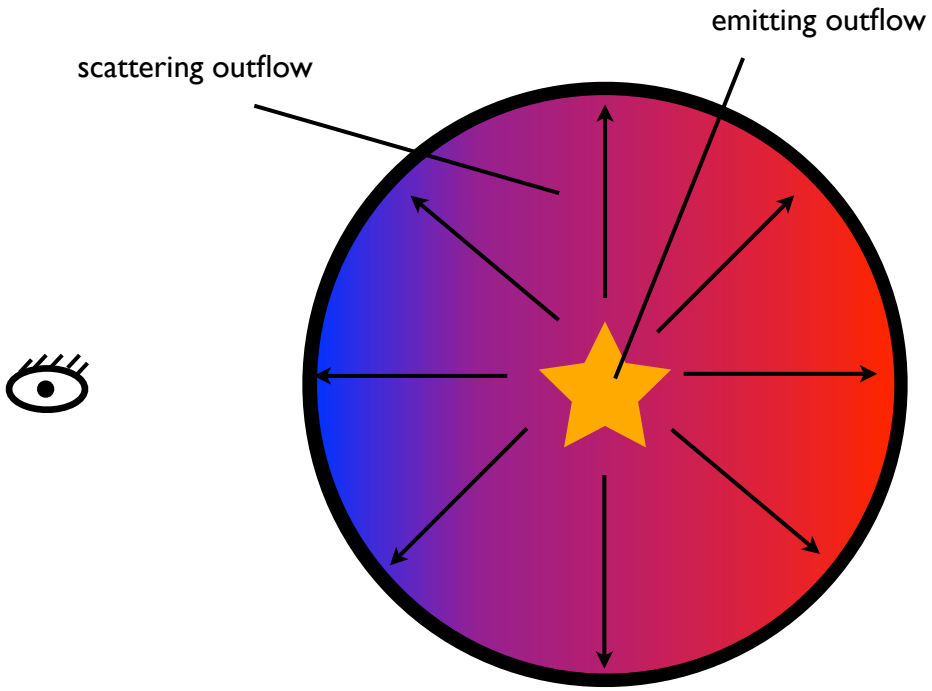

Figure 4.7: Our preferred model for SDSSJ1652+1728 is adapted from Veilleux et al. (2016). It combines a polar outflow which produces the emission lines with a dusty equatorial wind where the scattering occurs. The same model as viewed from above (looking along the polar axis). Here we show how the kinematic features in the polarized emission-line regions are created by the blue and red-shifted scattering emission respectively. The viewer (eye on the left) sees blueshifted emission coming towards them and scattered off of cloudsmoving towards the observer. In contrast, the redshifted wings of the emission lines are dominated by scattering off the "sides" of the outflow (from the observers perspective). Emission from the back of the cone is largely suppressed in polarization because the scattering efficiency is low at angles $\gtrsim$ 90 degrees though this emission does contribute to the overall redshift of polarized emission lines compared to the unpolarized emission lines. These features combined produce the ninety degree rotation in the polarization position angle across the emission lines.

Abramowicz et al., 1988; Sądowski et al., 2015; McKinney et al., 2015). We adapt the cartoon of Veilleux et al. (2016) who model Mrk 231 with a slim disk responsible for the continuum emission. The broad emission line region (BELR) is composed of a polar region, an extended accretion disk atmosphere and the disk itself (see Veilleux et al., 2016, figure 8 and our Figures 4.6, 4.7) whereas the broad absorption line region (BALR) originates only in the polar outflow and disk atmosphere. Using this model, the FeLoBAL features are produced in the BALR, blueshifted FUV emission lines are produced in the outflowing BELR, and the optical and NUV emission lines are produced in the disk BELR. We find that some of the features of this model reproduce well our spectropolarimetry results. In particular, when the FUV lines are produced in the polar region and then are scattered by a dusty, ionized equatorial outflow, the puzzling kinematics of the emission lines can be reproduced.

The main difference between Mrk231 and our objects (ERQs and Type 2s) is that our viewing angle is closer to edge-on than the $\sim$ 25 degrees polar viewing angle inferred for Mrk 231 from radio observations (Reynolds et al., 2013). We make this conclusion on the basis of the shape of the SED of our sources (Zakamska et al., 2016a; Hamann et al., 2017): as a function of wavelength, ERQ SEDs do not rise until 1-2μm, whereas Mrk231 is essentially unobscured at Hα wavelengths in the optical, and the steep rise of the Mrk 231 SED occurs at $\sim$ 3000Å. Therefore, the net line-of-sight column density of obscuration is $\sim$ 10 times higher in ERQs than in Mrk 231, implying the more edge-on viewing angle. For an SMC-like dust curve (Weingartner & Draine,

2001; Draine, 2003) in the "screen of cold dust" approximation, the Mrk231 rise would correspond to $A_V \simeq 0.3$ mag, and the $1-2\mu$m rise for ERQs would correspond to $A_V \simeq 5$ mag. This difference in viewing angle could explain why Mrk 231 exhibits low levels of FUV polarization – at the viewing angle of Mrk 231 the scattering region becomes nearly symmetric and thus geometric cancellation would dilute the polarization fraction (similar polarization fractions with opposite scattering angles will combine to produce a lower total polarization fraction) though the scattered flux is still high.

In subsequent sections we explore how this model matches the observational trends noted in our data. Section § 4.4.2 explains how this model matches our continuum polarization results while Section § 4.4.3 shows how this model produces the expected line polarization features. Finally, in § 4.4.4 we demonstrate that resonant scattering does not have a significant impact on our preferred model.

4.4.2 Continuum Polarization and Scattering Geometry

While scattering off of dust or electrons is the most likely source of polarization in AGN, especially at the high levels we observe in our objects, without some understanding from imaging of the scales on which polarization occurs it is difficult to distinguish between the two. For objects where the scattering cone is visible on ∼kpc

scales (Dey et al., 1996; Kishimoto et al., 2001; Zakamska et al., 2005) the required gas mass for electron scattering is likely prohibitive though it is not always possible to completely rule out. In contrast, on circumnuclear scales the polarization of NGC 1068 is wavelength-independant from the X-ray to the optical, and is therefore likely due to electron scattering (Miller et al., 1991).

The high infrared-to-optical ratios and multiple features of the rest-frame optical spectra of our objects (Alexandroff et al., 2013; Ross et al., 2015; Zakamska et al., 2016a; Hamann et al., 2017) indicate that they are obscured. We also know that the observed UV continuum of our objects is dominated by scattered light, because the net continuum polarization is so high that it cannot be appreciably diluted by the direct (unpolarized) light of the host galaxy. Therefore, scattering must be happening primarily on scales greater than obscuration scales, which in turn must be larger than the dust sublimation region (defined by the radius, $r_{\rm dust}$; Barvainis, 1987, equation 5):

$$r_{\rm dust} = 1.3 \left(\frac{L_{\rm UV}}{10^{46} {\rm erg/sec}} \right)^{1/2} \left(\frac{T}{1500 {\rm K}} \right)^{-2.8} {\rm pc}. \tag{4.1}$$

Here $L_{\rm UV}$ is the UV luminosity and T is the dust sublimation temperature. In the case of our extremely luminous sources ($L_{\rm UV} \approx$ a few $\times 10^{47}$), the sublimation scales might reach a few to 10 pc.

For a normal dust-to-gas ratio, the cross-section of dust scattering is two orders of magnitude higher than the electron scattering cross-section (Draine, 2003), therefore

since scattering must be happening outside of the dust sublimation zone, the presence of dust implies that dust scattering dominates our scattered light. In our proposed model, therefore, the dust scattering occurs somewhere in the BELR/BALR region (see Figure 4.6).

Scattering efficiency, the ratio of scattered flux to the flux that would have been observed directly in the absence of obscuration, is

$$\epsilon = \frac{\mathrm{d}\sigma}{\mathrm{d}\Omega}\Delta\Omega \int n_{\mathrm{H}}(r)\mathrm{d}r. \tag{4.2}$$

Here $\mathrm{d}\sigma/\mathrm{d}\Omega$ is the cross-section of scattering per unit hydrogen atom as calculated in Draine (2003), $\Delta\Omega$ is the solid angle covered by the scatterer as seen from the emitter, and $\int n_{\mathrm{H}}(r)\mathrm{d}r$ is the column density of hydrogen associated with the scattering region. For a constant velocity outflow, $n_{\mathrm{H}}(r) \propto 1/r^2$, and therefore this integral is weighted toward the smallest unobscured sizes, so it is $\sim n_{\mathrm{H,max}} d_{\mathrm{min}}$. We take a fiducial value of $\epsilon = 3\%$, which is obtained by extrapolating the IR emission of ERQs using a type 1 quasar SED (Richards et al., 2006a) toward UV wavelengths to see what fraction of this estimated intrinsic emission is observed (see figure 16 and figure 8 of Zakamska et al. 2016 Hamann et al., 2017, respectively). We take $\Delta\Omega = \frac{4\pi}{3}$ and 90° scattering by SMC dust with $\mathrm{d}\sigma/\mathrm{d}\Omega \simeq 4 \times 10^{-24}$ cm^2/H/Ω at 1500Å(Draine, 2003). We arrive at the constraint in Figure 4.8 and hydrogen densities for scattering material on the order of $10 - 100$ cm^{-3}.

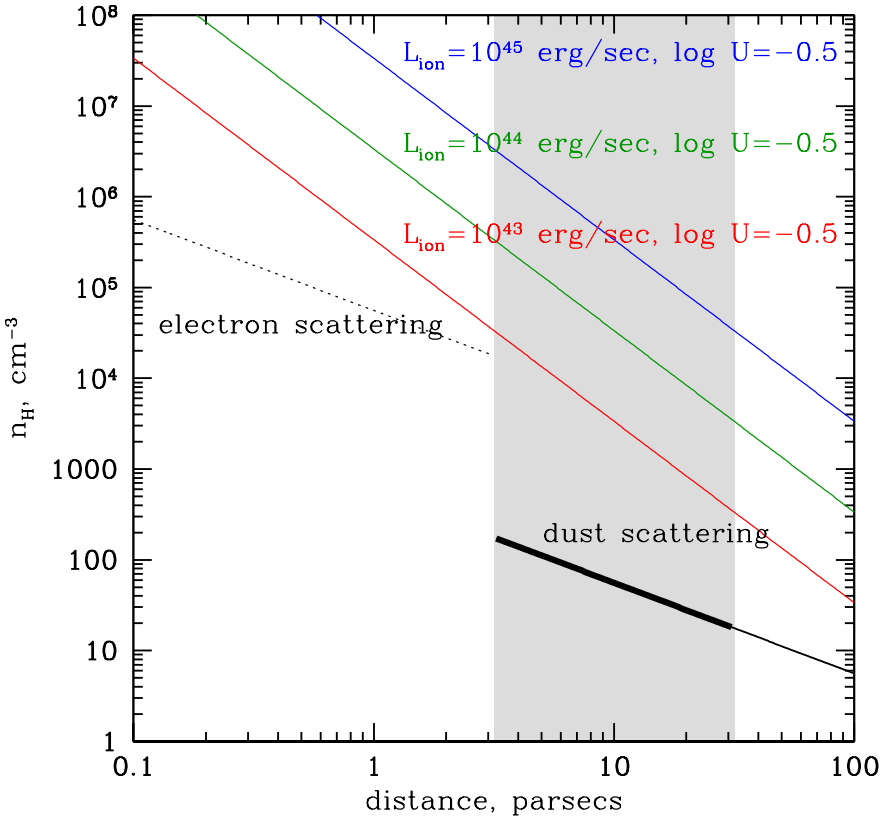

Figure 4.8: The scattering efficiency and ionization parameter allow us to place constraints on the size of the scattering region and the density of scattering material. Assuming a scattering efficiency of 3% and following from equation 4.3, the black lines show the range of densities for reasonable distances to the dust (solid) or electron (dotted) scattering regions respectively. The coloured lines in the upper right show the limits on the density placed at the same distances based on our assumptions of the quasar ionizing luminosity and ionization parameter (see equation 4.4. Our preferred regime is the grey region which covers dust scattering at scales 3-30 pc (around the dust sublimation radius) though we are not able to place strong limits on the actual ionizing luminosity available from our quasars which is likely suppressed by extinction. We hypothesize that these two limits are incompatible because while the line emission is occurring in dense clouds in the quasar BELR, the scattering is occurring on similar scales but in the less dense medium surrounding these clouds.

If this scattering region is too dusty, then no emission from the quasar could escape at all. Therefore, we need to verify that our derived densities and sizes are compatible with the escape of radiation from the quasar in order to be available for scattering into our line of sight. We use equation 4.2 to find the optical depth to dust extinction through the scattering region:

$$\tau = C_{\rm ext} \int n_{\rm H} {\rm d}r = \frac{\epsilon C_{\rm ext}}{\Delta\Omega {\rm d}\sigma/{\rm d}\Omega}, \tag{4.3}$$

where $C_{\rm ext} = 2.9 \times 10^{-22}$ cm^2/H is the total cross-section for extinction (Weingartner & Draine, 2001). With our fiducial values, $\tau \simeq 0.5$ and is therefore just right: a quasar viewed through BELR / BALR would be reddened, as is Mrk 231, but not completely extinguished. We also see from this expression that the scattering efficiency, ϵ, cannot be a lot greater than our fiducial value, because otherwise the extinction becomes prohibitively high. Therefore we conclude that our observed scattered component cannot be appreciably extincted or obscured, either by diffuse or by patchy material.

Assuming an SMC-like dust distribution, the theoretically achievable maximum polarization fraction at 1800 Å is $\sim$ 14.7% for a scattering angle of 90° and the polarization fraction continues to rise towards the blue (Draine, 2003). Thus, some of our targets display such high levels of polarization in the continuum that they come close to reaching this theoretically achievable limit and the geometric cancellation of polarization means that to achieve the observed 15% polarization level, the intrinsic

polarization level of each scattering must be even higher. We know dust can be an efficient polarizer depending on the size distribution of the dust as compared to the wavelength of the scattered light (Weingartner & Draine, 2001). Thus, to achieve the observed polarization fraction in our sources might require some adjustments to the dust size distribution compared to pre-existing models. The same is true for any wavelength-dependence in the polarization fraction of our objects that appears to increase towards redder wavelengths– in contrast to the Draine (2003) predictions. It is also not possible at this time to rule out a wavelength-dependent unpolarized component which dilutes the polarization as the cause of any wavelength-dependent polarization signatures in our continuum data.

4.4.3 Line Polarization

In low-redshift type 2 quasars, scattering occurs on a wide range of scales reaching several kpc (Hines et al., 1999; Zakamska et al., 2005, 2006; Schmidt et al., 2007; Obied et al., 2016) and on the same scales as the optical forbidden lines such as [O III] are produced. The co-spatial distribution of the line-emitting gas and of the scattering medium leads to a geometric cancellation of the polarization of the emission lines and to mixing of direct (unpolarized) emission with scattered light, resulting in the observed low fractional polarization of the narrow emission-line region (Stockman et al., 1981; Glenn et al., 1994; Goodrich & Miller, 1995; Tran, 1995b).

In our objects, we observe a lower net polarization of the UV emission lines than

in the continuum. By analogy to the suppression of polarization of the narrow-line region of type 2 quasars, we hypothesize that the UV emission lines arise on scales similar to those that dominate scattering. In the cartoon shown in Figure 4.6, the low fractional polarization of the emission lines would be achieved if the lines are produced either in the dusty BELR / BALR or in the dust-free cone at scales similar to or greater than the scales of the dusty BELR / BALR. There is also empirical evidence (Czerny & Hryniewicz, 2011) and emission line calculations (Netzer & Laor, 1993) that suggest the broad-liner region and inner edge of the obscuring material should exist on similar scales.

In the simple case of a spherical emitting region of radius R and scattering region of radius D, Cassinelli et al. (1987) show that the polarization is reduced by a factor of $[1-(R/D)^2]^{1/2}$ relative to an emitting point source. If we assume that the continuum emitting region is a point source, and it is roughly $\sim 3\times$ more polarized than the emission line region, this implies that the emission line region is 94% the size of the scattering region, confirming that the emission line region and scattering regions extend to similar scales.

What constraints on the physical conditions do we get from requiring that continuum scattering and UV emission line production occur on similar scales? The ionization parameter is

$$U = \frac{L_{\rm ion}}{4\pi r^2 \phi n_e c}. \tag{4.4}$$

Here $L_{\rm ion}$ is the luminosity of the ionizing radiation, $\phi = 13.6$ eV is the threshold

energy of the ionizing photons, and $n_e \simeq (1 - 1.2) \times n_{\rm H}$ is the electron density which depends slightly on whether helium is fully ionized. As a fiducial value of the ionization parameter in the C IV-emitting region we use $\log U = -0.5$ from Rodríguez Hidalgo et al. (2011).

It is clear from Figure 4.8 that if emission lines are produced on spatial scales that are similar to those of scattering, then either a strong suppression of the ionizing continuum or strong clumping of the emission-line gas or both are required to produce the observed ionization parameter. We will model the UV emission lines of ERQs in a forthcoming photo-ionization analysis of the emission line ratios (Hamann et al., in prep.). In the meanwhile, our qualitative model is that the emission lines are produced in high density clouds either in the joint BELR / BALR or in the dust-free zone. These clouds are ionization-bounded and therefore are by definition optically thick to ionizing radiation, so only the compact surfaces of these clouds will be able to scatter continuum emission in the dusty zone (scattering is much weaker in the dust-free zone and is unlikely to dominate). Thus, scattering is dominated by a lower-density, volume-filling component of the BELR / BALR gas. This allows us to reconcile the densities implied by the scattering efficiency and by the ionization parameter (see Figure 4.8).

The biggest success of our model in Figure 4.7 is that our model naturally explains the change in the polarization fraction and position angle as a function of velocity in the FUV emission lines. The blue-shifted line emission we see in our objects is

from the near-side of the equatorial outflow which gives it the observed velocity shift (see Figure 4.7). In contrast, the observed redshifted emission is dominated not by the back of the outflow (this emission is suppressed because dust back scattering is inefficient) but instead from the sides of the equatorial outflow which are moving away from the observer and thus produce redshifted scattered emission. This results in the swing in polarization position angle as a function of velocity in the emission lines as the two scattering regions are roughly perpendicular to each other as seen in the plane of the sky so the polarization position angle transitions as a function of velocity from being dominated by the near-side of the equatorial outflow in the blue to the sides of the outflow in the red. This also explains the overall redshift in emission line features seen in polarized light as the net redshift of the scattered line is due to the redshift of the scatterer relative to the emitter.

Smith et al. (2004) suggested a similar model of the torus with both polar and equatorial scattering regions to explain the range of properties observed in low redshift Seyfert 1s and 2s. The polar scatterer extends beyond the torus and may be outflowing while the equatorial scatterer lies within the torus and is described by Young (2000) as a rotating disk wind. Other differences between our model and Young (2000) model include the specific emission lines: they consider Balmer lines, which in our cartoon are produced in a more extended region of the disk than the FUV lines which we focus on. Furthermore, in Type 1 objects there is dilution of the scattered light by the direct unpolarized continuum, which may explain the much lower values of polarization and

position angle swings achieved in Seyfert 1s. But the main difference is that Young (2000) explain the rotation in the polarization position angle using a rotating disk wind, where rotation might be difficult to maintain dynamically. In contrast, in our model the polarization position angle swing is achieved naturally by the geometric projection effects, with the blueshifted scattered emission and the redshifted scattered emission having different orientations in projection on the plane of the sky.

4.4.4 Resonant Scattering?

In addition to scattering by either electrons or dust grains, resonant scattering is a possible mechanism for the polarization observed in the emission lines of our objects. Permitted electric dipole transitions in an anisotropic radiation field can produce linearly polarized emission, and thus resonantly polarized scattering becomes important mechanism either if the emission line source region is not spherically symmetric, or if radiation, either from an emission line or the continuum region, is Doppler-shifted into resonance with a permitted transition and is incident on a gas cloud (Lee & Blandford, 1997). For a single $\Delta J = 0 - 1$ scattering viewed at 90 degrees the polarization reaches 100% (Hamilton, 1947). However, the resonant scattering in AGNs might involve multiple scatterings, and if the optical depth to scattering is high enough the net expected polarization signal is low. Lee (1994) showed that standard emission-line clouds emit almost completely unpolarized line radiation unless the optical depth is $\tau \lesssim 1$ which is usually only the case for the semi-forbidden C III] λ1909 transition. For

reflection off of nearby clouds to contribute significantly to the polarized line emission the optical depth must be in a specific regime where only a small number of reflections occur. Lee & Blandford (1997) determine that this happens at a column density of $N \sim 10^{17}$ cm^{-2} for a single reflection which is approximately six orders of magnitude smaller than the regime where electron scattering has a significant effect ($N \sim 10^{23}$ cm^{-2}). We will find that resonant scattering contributes at most only modestly to the polarization fraction in our objects.

We can calculate the expected ratio of the optical depth of resonant scattering compared to the optical depth to dust scattering. The optical depth to dust scattering, τ_{dust} is given by

$$\tau_{dust} = N_H \times C_{ext,H} \tag{4.5}$$

assuming a constant number density of dust grains along the line of sight. Here N_H is the column density of hydrogen nucleons and $C_{ext,H}$ is the extinction cross section of the dust per hydrogen nucleon, taken to be 3.768×10^{-22} cm^2/H for an SMC-like dust distribution at 1200Å from Draine (2003). Similarly, the optical depth to resonant scattering, τ_{res} is given by:

$$\tau_{res} = N_H \times \frac{m_C}{m_H} \frac{\Delta v}{v_{wind}} \sigma_{res} \tag{4.6}$$

where $\frac{m_C}{m_H} \simeq 1.0 \times 10^{-3}$ is the mass ratio of C IV to H nucleons which we estimate

based on the assumption that the number ratio of carbon to hydrogen in the ISM is solar, $\frac{\log N_H}{\log N_C} = 3.57$ (Grevesse et al., 2010), and $\sim 30\%$ of carbon is triply ionized (Proga, personal communication). $\frac{\Delta v}{v_{wind}} \approx 0.1$ is the fraction of photons that lie within a thermal width of the resonance frequency given an estimate of the outflow velocity of $v_{wind} \approx 3000$ km s^{-1} and the gas temperature $T \approx 15,000$K based on the assumption of photo-electric temperature balance with C IV. Finally, the cross section for resonant scattering is taken to be $\sim 1.0 \times 10^{-17}$ cm^2 for a single scattering event as taken from Lee et al. (1994). Combining these quantities gives us a rough estimate for the ratio of the dust scattering to resonant scattering optical depth of $\frac{\tau_{res}}{\tau_{dust}} \approx 0.3$ implying that resonant scattering in the emission lines of our objects is likely present but at most enhances the polarization fraction by $\sim 30\%$. We thus conclude that continuum dust scattering is the dominant scattering mechanism both for the continuum and the emission lines.

4.5 Conclusions

We have obtained rest-frame ultraviolet spectropolarimetry for five $z \sim 2.5$ obscured and highly reddened quasars using LRIS in polarimetry mode on Keck. Our Type 2 targets are classically selected, narrow-line objects (Alexandroff et al., 2013). Extremely red quasars are color-selected and show signs of extreme outflow activity in their rest-frame optical spectra (Ross et al., 2015; Zakamska et al., 2016a; Hamann

et al., 2017). Although our initial expectations were that narrow line-selected Type 2s should be more highly polarized than the extremely red quasars, we find (in this admittedly small sample) no systematic trends between the optical and UV "type" and the levels of continuum polarization.

We do see several interesting trends in our polarization data:

1. We find high levels of polarization in the continuum, higher than 15% in three of our sources, with some signs that the polarization fraction may be increasing to longer wavelengths.

2. We find lower levels of polarization in emission lines with a ratio of continuum polarization/emission line polarization between 1/3 and 4/5.

3. Intriguingly, we see a rotation of almost exactly ninety degrees in the polarization position angle across all strong emission lines, Lyα, CIV, and NV;

4. The polarization position angle of the continuum matches the polarization position angle at the most redshifted part of emission lines.

To explain our data, we prefer a model in which an equatorial dusty disk wind scatters both continuum emission from the disk and line emission from a polar outflow. This model is physically motivated and appears to match the main features of our observations. The high polarization fraction can be explained by dust scattering though it may require a few adjustments to typical dust models. Assuming the emission line region and dusty scattering region exist on similar scales that are larger

than the continuum emission region produces the lower polarization fraction observed in the emission lines of our objects. Finally, this model allows for different outflow components to dominate in the continuum and the red wavelengths of emission lines compared to the blue wavelengths of emission lines and thus produces a ninety degree rotation in the polarization position angle as a function of wavelength across the emission lines as observed.

Absent high resolution imaging, spectropolarimetry can be an important tool to understand the scattering geometry of our high redshift obscured and reddened quasars and can be an important piece of information to evaluate different proposed models of quasar geometry on small scales near the black hole. This allows us a window in to the potential launching mechanism for galaxy-scale quasar winds which are a necessary ingredient for quasar feedback.

4.6 Acknowledgments

The data presented herein were obtained at the W.M. Keck Observatory, which is operated as a scientific partnership among the California Institute of Technology, the University of California and the National Aeronautics and Space Administration. The Observatory was made possible by the generous financial support of the W.M. Keck Foundation. The authors wish to recognize and acknowledge the very significant cultural role and reverence that the summit of Mauna Kea has always had within the

indigenous Hawaiian community. We are most fortunate to have the opportunity to conduct observations from this mountain.

R.A. was supported in part by NASA JPL grant 1520456. Support for this work was provided in part by the National Aeronautics and Space Administration through Chandra Award Number GO6-17100X issued by the Chandra X-ray Observatory Center, which is operated by the Smithsonian Astrophysical Observatory for and on behalf of the National Aeronautics Space Administration under contract NAS8-03060. R.A. would like to acknowledge the assistance of C. Steidel, A. Strom, D. Perley, and H. Tran during observations at Keck I and the assistance of M. Kassis on the evening of LRISp observations. R. A. would also like to thank D. Neufeld for his useful conversations and S. Veilleux for allowing us to adapt figure 8 of Veilleux et al. 2016. N. L. Z. would like to acknowledge the remote observing support of Yale University and support by the Catalyst award of the Johns Hopkins University.

Chapter 5

Molecular Gas in Obscured and Red Quasars at z$\sim$ 2.5

Quasar feedback is a key element of modern galaxy formation theory. During powerful episodes of feedback, quasar-driven winds are suspected of removing large amounts of molecular gas, thus limiting supplies for star formation and ultimately limiting the maximum mass of galaxies. In this paper we present EVLA observations of the CO(1-0) transition in 11 powerful red and obscured quasars, some of which display signatures of powerful quasar-driven winds in their ionized gas. With a combined exposure of over 10 hours, we do not detect any molecular emission, whether kinematically disturbed due to quasar wind or in equilibrium with the host galaxy. This observation is in stark contrast with the previous suggestions that such objects should occupy gas-rich, extremely star-forming galaxies. Possible explanations in-

clude paucity of molecular gas or inverted populations of CO rotational levels, both of which could be the results of quasar feedback. We detect an average point-like (< 5 kpc) radio continuum emission with luminosity $\nu L_{\nu}[33GHz] = 2.2 \times 10^{42}$ erg s^{-1}, consistent with optically-thin ($\alpha \approx -1.0$) synchrotron with some possible contribution from thermal free-free emission. The radio emission of these radio-intermediate objects may be a bi-product of radiatively driven winds or may be due to weak jets confined to the host galaxy.

5.1 Introduction

In order for analytic simulations of galaxy formation to match the observed galactic number density over cosmic time, it is necessary to invoke a process to limit the maximal mass of galaxies in the universe (Springel et al., 2005; Bower et al., 2006; Croton et al., 2006; Silk & Mamon, 2012). At the less massive end, this process is likely feedback from supernovae-driven winds (Heckman et al., 1990; Veilleux et al., 1994, 2005). At the most massive end of the galaxy mass function, this process is believed to be quasar feedback (Hopkins et al., 2006; Fabian, 2012).

Quasar feedback is invoked for several reasons. Firstly, there is an observed empirical correlation between the mass of a galaxy's supermassive blackhole (SMBH) and galaxy bulge properties which seems to imply a causal correlation (Magorrian et al., 1998; Ferrarese & Merritt, 2000; Gebhardt et al., 2000; Gültekin et al., 2009; Wang

et al., 2011; Kormendy & Ho, 2013). In addition, the quasar number density and galaxy number density peak at a similar time in history again implying some form of co-evolution (Boyle & Terlevich, 1998; Hopkins et al., 2008; Madau & Dickinson, 2014).

Theoretical models derive these correlations through the mediating relation of quasar winds– strong, energetic winds that couple the energy of the quasar to the surrounding gas, thereby clearing the surrounding galaxy of gas and shutting off star formation (Sanders et al., 1988; Hopkins et al., 2006). For the most luminous quasars, only $\sim 1\%$ of the energy released by the quasar need couple to the surrounding gas to clear the galaxy of the material necessary for star formation (King, 2010; Zubovas & King, 2012).

Evidence is beginning to point to "red quasars" as the missing "blow-out" phase of quasar feedback where the quasar wind is clearing the host galaxy of material. Samples of red quasars have been identified at both low and high redshifts under different names including red quasars (Glikman et al., 2007, 2012, 2013), hot dust obscured galaxies (hot DOGs; Wu et al., 2012; Tsai et al., 2015) and extremely red quasars (ERQs; Ross et al., 2015; Hamann et al., 2017) using mid- or near-infrared selection often combined with another wavelength such as the optical (Ross et al., 2015; Hamann et al., 2017, selected with a combination of SDSS and WISE) or the radio (Glikman et al., 2007, 2013, selected with a combination of FIRST and 2MASS).

These objects are extremely luminous, and observations of the high ionization

emission line of [O III] in some of the most extreme of these objects show evidence for outflow speeds of $\gtrsim$ 2000 km s^{-1} (Zakamska et al., 2016a), clear evidence for an outflow capable of clearing the host galaxy of high ionization gas as it is too fast to be contained by any reasonable galaxy potential. The question remains however, do the extreme outflows we observe in ionized gas exist in the molecular gas?

It is crucial to understand how quasar-driven outflows are affecting the molecular gas in their hosts galaxies as this is the main material of star formation. Tracing molecular gas is difficult, however, because the bulk of the molecular gas in the interstellar medium (ISM) is in the form of molecular hydrogen (H_2), which has no emission or absorption features at the relatively cool temperatures expected in the ISM (though quasar-driven winds might enhance the emission of warm H_2, Hill & Zakamska 2014). Instead, carbon monoxide (CO) is a common and useful tracer of the molecular gas content, with several rotational transitions at the correct temperature.

The study of many high redshift quasars, due to frequency and sensitivity constraints, is often conducted at higher J transitions (J $\geq$ 3) and so are biased towards more highly excited gas which may or may not be a good tracer of the overall molecular gas distribution. Indeed, for $z \gtrsim 2$ unlensed quasars, the CO(J = 1 $\rightarrow$ 0) transition is redshifted out of the frequency range of Atacama Large Millimeter/submillimeter Array (ALMA) and in to the high frequency range of the Karl A. Jansky Very Large Array (VLA).

In this paper we present the new limits on the CO (1-0) luminosity in a sample

of obscured and red quasars at $z \sim 2.5$ using the VLA which allow us to place stringent limits on the molecular gas reservoirs in these galaxies. We find significant evidence for depletion of the molecular gas reservoirs in these objects which provides the first evidence that these luminous quasars are clearing their host galaxies of star forming material. We present our sample selection in § 5.2 and our observations and data reduction in section § 5.3. We discuss our resulting constraints on the quasar continuum in section § 5.4 and the CO (1-0) emission line in section § 5.5. We offer our conclusions in section § 5.6.

Throughout this paper, we adopt a cosmology with $h = 0.7$, $\Omega_m = 0.3$ and $\Omega_\Lambda = 0.7$. We use SDSS Jhhmm+ddmm notation throughout the text (full coordinates are listed in Table 5.1).

5.2 Sample Selection

Our sample includes eleven red and obscured quasars at redshift $z \sim 2.5$ described in detail in Alexandroff et al. (2013), Ross et al. (2015) and Hamann et al. (2017). We briefly describe the original parent sample selection methods below. General information on these eleven quasars can be found in Table 5.1.

Three of our sources, were originally selected from the Sloan Digital Sky Survey (SDSS) Baryon Oscillation Spectroscopic Survey (BOSS; Dawson et al., 2013) by their narrow line widths (FWHM < 2000 km s^{-1} in both C IV and Lyman α) and weak

continuum in the rest-frame UV in an attempt to form an optically-selected sample of high redshift Type 2 quasars. Only objects from Data Release 9 (Ahn et al., 2012) or earlier were included in this search which yielded a sample of 145 Type 2 quasar candidates (for more details see Alexandroff et al., 2013).

An additional eight sources were selected based upon a combination of data from the SDSS and the Wide-Field Infrared Survey Explorer (WISE; Wright et al., 2010a) AllWISE data release[1] to search for objects with red infrared-to-optical colours (Ross et al., 2015; Hamann et al., 2017). This selection method was used to search for obscured quasars at high redshift based on expected high infrared-to-optical ratios. A sub-sample of these very red objects also possessed unusual spectroscopic properties such as large rest equivalent width (REW) emission lines ($\gtrsim$ 100 Å), unusually high N v/Lyα ratios and emission lines with high kurtosis (lacking the typical broad wings of Gaussian emission lines). These objects were labelled Extremely Red Quasars (ERQ). The final sample selection required a value of i-W3 $\geq$ 4.6 and a measured REW of CIV $>$ 100 Å and produced a sample of 97 objects with a redshift range of $2.0 < z < 3.4$ (Hamann et al., 2017). One source, SDSSJ1623+3122, originally selected as a Type 2 quasar candidate, is also part of the "expanded" ERQ sample which has slightly less red colours but many of the same line properties as ERQs (Hamann et al., 2017).

The eleven objects were selected to span the widest possible range of rest-frame

[1]http://irsa.ipac.caltech.edu/

optical ionized gas properties, as traced by the [O III]λ5007Åẽmission in follow-up rest-frame optical spectroscopy. The [O III] line has been shown to be a good tracer of high-ionization outflows mostly because it is particularly strong and exists on galaxy-scales. Strong signs of galaxy-scale outflows, where the gas velocities are greater than the galaxy escape velocity, demonstrate that the quasar is likely able to clear its host galaxy of gas and affect galactic evolution (Hopkins et al., 2006). In particular, a blueshift in the centroid position of [O III] and/or large measured velocity widths are both strong indicators of outflows (e.g. Whittle, 1985; Greene et al., 2009, 2011; Villar-Martín et al., 2011; Liu et al., 2013). Our sample was chosen to span the range from completely quiescent to those with extreme outflow signatures in their [O III] lines.

Table 5.1: Basic properties of our obscured and highly reddened quasar targets for observation. Our targets span a range of properties in their line widths and colours. Position and redshift information is from the SDSS Skyserver. C IV FWHM, REW & kt_{80} were measured by Hamann et al. (2017) with the exception of SDSS1515+1757 which is not an ERQ where the measurements are taken from the SDSS Skyserver. [O III] FWHM and luminosity are from either Greene et al. (2014), Zakamska et al. (2016a) or as yet unpublished data from Gemini North.

Short Name	RA	Dec	z	CIV FWHM	[OIII] FWHM	log $L_{[OIII]}$	i − W3	designation
	hh:mm:ss	dd:mm:ss		km s^{-1}	erg s^{-1}	AB		
SDSSJ0812+1819	08:12:57.14	+18:19:16.8	2.383	762	420	44.53	–	T2
SDSSJ0826+0542	08:26:53.42	+05:42:47.3	2.570	2434 ± 35			6.0	ERQ
SDSSJ0832+1615	08:32:00.20	+16:15:00.3	2.450	3082 ± 65		6.7	ERQ	
SDSSJ0834+0159	08:34:48.48	+01:59:21.1	2.591	2863 ± 65		6.0	ERQ	
SDSSJ1232+0912	12:32:41.73	+09:12:09.37	2.374	4787 ± 52	5627	43.92	6.8	ERQ
SDSSJ1356+0730	13:56:08.32	+07:30:17.2	2.270	2043 ± 46		5.1	ERQ	
SDSSJ1515+1757	15:15:44.00	+17:57:53.06	2.402	1118	856.4	43.98	2.0	T2
SDSSJ1623+3122	16:23:27.66	+31:22:04.29	2.344	1572±68658.3	44.08	4.5	T2E	
SDSSJ1652+1728	16:52:02.64	+17:28:52.38	2.942	2403 ± 451461	44.87	5.4	ERQ	
SDSSJ2215−0056	22:15:24.00	−00:56:43.80	2.493	4280 ± 112	3057	43.64	6.2	ERQ
SDSSJ2323−0100	23:23:26.17	−01:00:33.1	2.356	3989 ± 62	2625	43.52	7.2	ERQ

5.3 Observations & Data Reduction

5.3.1 Observations

We chose eleven objects for deep observations with the VLA (see Table 1) in semester 16A (Program ID 16A-326) surrounding the rest-frame of the CO (1-0) transition (ν_{rest} =115.2712 GHz). This required us to use the VLA's Ka frequency band (ν_{obs} =26.5-40 GHz) with the central frequency tuned to match the rest frame of the quasar. Without absorption features from the host galaxy to benchmark the host redshift, we used redshifts derived from the centroid of the Hα or Hβ line (e.g. Zakamska et al., 2016a) to determine the host galaxy redshift. Observations were scheduled dynamically. Each object was part of its own scheduling block and so observations were spaced out over the course of the semester.

We observed one flux/bandpass calibrator, either 3C286 or 3C48, at the beginning or end of each observation set. Targets were observed while nodding between a phase/amplitude calibrator which also served as a reference pointing approximately ever seven minutes. Total on-source time was 53 minutes per source. We recorded in full polarization across two bands using the 8-bit samplers with each baseband (spanning 128 MHz) being covered by 64 channels (the lowest possible resolution) to yield a total instantaneous bandwidth of $2 \times 1024 = 2048$ MHz. Due to constraints with the correlators there is a gap between the two contiguous bands.

We observed in the C configuration giving us a resolution of $\sim 0.6''$ which corre-

sponds to approximately $\sim$ 5kpc at a redshift of 2.5 – thus allowing us to probe for the presence of CO emission on galaxy scales.

5.3.2 Data Reduction

We reduced the data using the Common Astronomy Software Applications (CASA) package v4.3.0 (McMullin et al., 2007). Raw visibilities were calibrated using the VLA Calibration pipeline version1.3.14. All solutions were inspected and additional flagging, as necessary, was accomplished by hand using CASA's Plotms task.

We created average images for each source over the full bandwidth range using CASA's clean task in mfs mode with a Briggs weighting scheme of ROBUST = 0.5 to study the continuum emission from our sources. The typical rms at the field center was 1.0×10^{-5} Jy/beam. If initial imaging showed the clear detection of a source (the case for SDSSJ0812+1819T, SDSSJ0826+0542 and SDSSJ1652+1728), we used CASA task uvcontsub to subtract a continuum point source (displayed in Figure 5.1), assuming a linear slope to the flux within the 2 GHz bandwidth and fitting without the three subbands containing or nearest to the expected rest frequency of the CO (1-0) line. Then with the continuum subtracted images for these sources as well as the initial reduced data for our other sources we mapped our data to the velocity of the CO (1-0) line at the quasar redshift using the CASA task cvel to image in 25 km s^{-1} intervals from -5000 to $+5000$ km s^{-1} around the CO (1-0) line center. We created clean maps for these images using the same input as for the full bandwidth

images.

Table 5.2: Radio properties of our obscured and highly reddenned quasars including previous detections with FIRST (if any) and the results of our current survey with the VLA Ka band (observed frame 26.5 - 40 GHz) tuned to center CO (1-0) in the rest frame of the quasar.

Short Name	1.4_{peak} mJy/beam	1.4_{Int} mJy	Ka band mJy/beam	α
SDSSJ0812+1819	2.10	3.31	0.23	-0.8
SDSSJ0826+0542	1.14	0.90	6.5E-02	-0.9
SDSSJ0832+1615	1.00	1.13		
SDSSJ1652+1728	1.64	1.26	6.0E-02	-1.0

With no clear detection in any single source (including those three sources with clear detections in the continuum) we stacked all of our non-detections in 100 km s^{-1} velocity bins and used the idl task aper to calculate the flux in each bin to derive a rough spectrum which is displayed in Figure 5.2. We chose an extraction radius of five pixels as this covers approximately one and a half beamwidths and so captures all of the potential source flux.

5.4 Continuum Measurements

5.4.1 FIRST Detections

Of our eleven sources, four are detected in the Faint Images of the Radio Sky at 20 Centimeters (FIRST; Becker et al., 1995) Survey at 1.4 GHz (for more details see Table 5.2). Their close to marginal detections at this redshift makes them

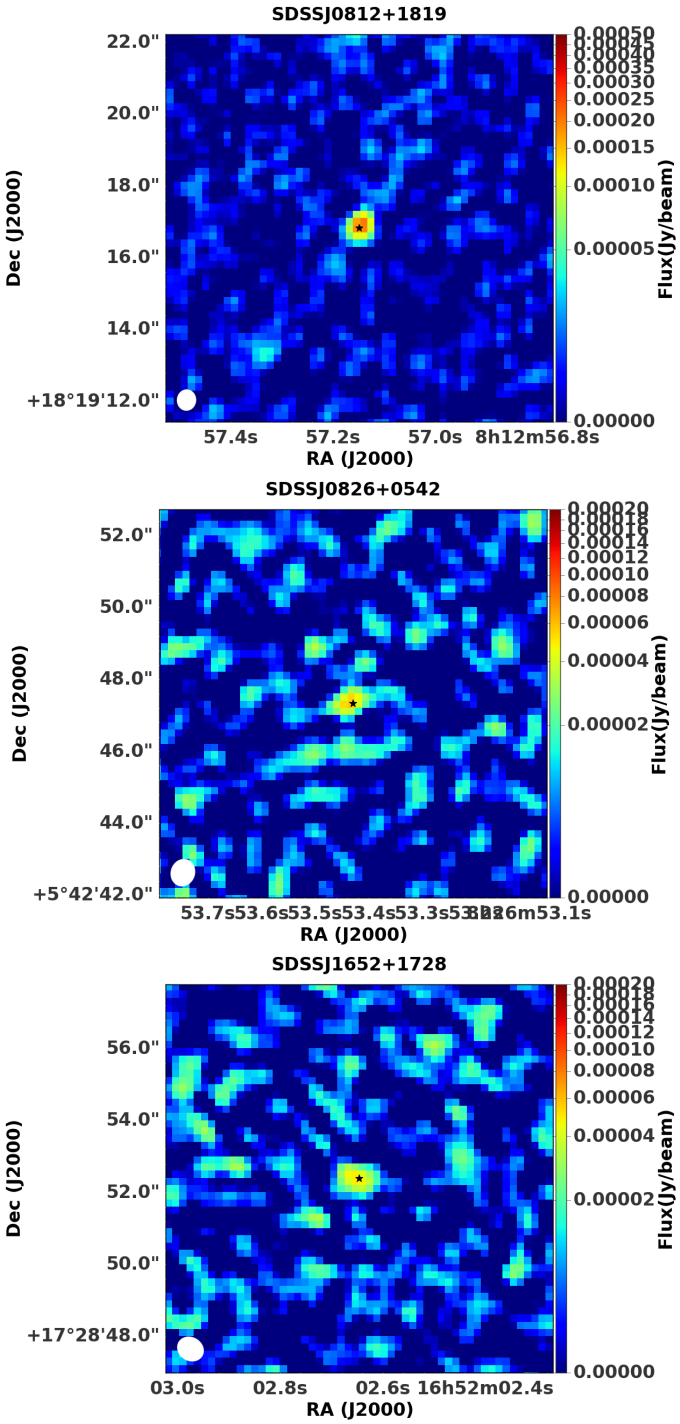

Figure 5.1: VLA C configuration 33.0 GHz images at 0.6″ resolution of our three quasars detected in the continuum. The black star shows the optical coordinate of the source. The restoring beam is depicted as an ellipse on the lower left corner of each map and the scale is given on the right. The detections have a S/N of 24, 6.5 and 6.0 respectively. The top source has been lightly cleaned to a flux level of 0.1 mJy.

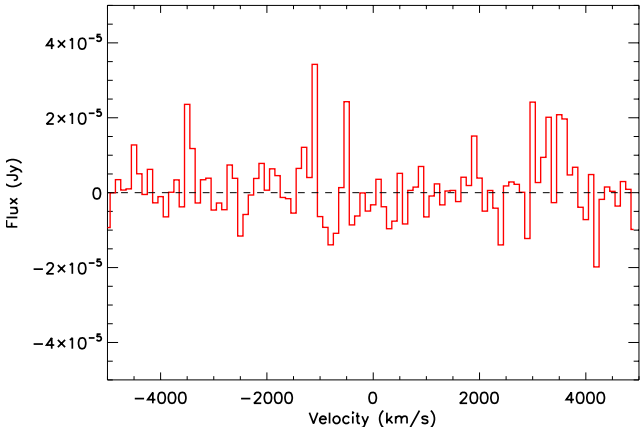

Figure 5.2: Extracted spectra of all eleven stacked sources at 33GHz. We used an extraction radius approximately 1.5× the beamsize and used data that had been re-binned in 100 km s^{-1} bins covering the range ±5000 km s^{-1} around the line center (for more information see Section 5.3).

radio intermediate under the definition of Xu et al. (1999). Stacking the remaining seven images produces a mean image with no detection but a standard deviation of $57\mu Jy$. Assuming a 3σ threshold for detection this places an upper limit on the flux of the undetected sources at $\sim$ 0.17mJy which corresponds to a radio luminosity of $\log\nu L_\nu$[1.4GHz]= 40.95 at the median redshift of the undetected sources ($z \sim 2.4$). Thus we can conclude that all of the sources which are not detected in FIRST are either radio intermediate or radio quiet.

At this frequency range this detection is most likely that of synchrotron emission from the source though without additional information it is difficult to discern if the synchrotron emission is from small-scale jets, winds, star-formation or nuclear coronae (For a more detailed discussion see Alexandroff et al., 2016).

5.4.2 VLA 33 GHz Detections

Three of our sources are directly detected at $\sim$ 33GHz. We measure their flux using the CASA task imfit and list the results in table 5.2. We have three detections and with a conservative estimate of the rms noise in each image as 1.0×10^{-5}Jy, they have a SNR of 24, 6.5 and 6.0 respectively.

For the remaining eight sources we create a mean stack of the images excluding the region within $\pm$500 km s^{-1} from the CO(1-0) line center and find a detection with a peak flux of 1.9×10^{-2} mJy/beam. Given the standard deviation of the stacked image this represents a $\gtrsim 3.5\sigma$ detection of the stacked sources. At the median redshift of these eight sources this corresponds to a radio luminosity of $\nu L_{\nu}[33GHz] \approx 2.9 \times 10^{41}$ erg s^{-1}.

There is the possibility at our rest-frame frequency of $\sim$ 115 GHz that the observed radio emission is due not to synchrotron emission, but to free-free emission. There is some evidence from Hwang et al. 2017 (in prep) that the average spectral index for ERQs from synchrotron emission, measured from 5.0-7.0 GHz in the observed frame, is actually significantly steeper than $\alpha = -0.7$ with $\alpha_{mean} = -1.3 \pm 0.3$ for the seven ERQs detected with enough signal to noise to derive in-band spectral indices. In addition, of these seven ERQ detections at 6.0 GHz, only one has the flat spectral index expected of a nuclear core. This provides some evidence to suspect that the spectral index for synchrotron emission in these sources is likely fairly steep. As a result, the spectral index we calculate between 1.4GHz and 33GHz (listed in Table 5.2)

may be disguising a broken power law with steeper spectral index due to synchrotron emission at lower frequencies and an additional component due to free-free emission at higher frequencies (with spectral index of $\alpha = 0.1$). Assuming an intrinsic power-law for the synchrotron emission of $\alpha = -1.3$ for our sources, we can calculate the expected contribution to the rest-frame 115 GHz flux from free-free emission. While it cannot be ruled out that the AGN is providing the ionizing flux to generate the free-free emission, we can estimate an upper limit on the star formation rate using the free-free emission and the prescription in Murphy et al. (2012)

$$\left(\frac{\mathrm{SFR}^T}{M_\odot \mathrm{yr}^{-1}}\right) = 4.6 \times 10^{-28} \left(\frac{T_e}{10^4 \mathrm{K}}\right)^{-0.45} \left(\frac{\nu}{\mathrm{GHz}}\right)^{0.1} \left(\frac{L_\nu^T}{\mathrm{erg\ s^{-1} Hz^{-1}}}\right) \tag{5.1}$$

Where the star-formation rate is a function of the electron temperature, T_e, here assumed to be 10^4K, the rest frequency ($\nu_{rest} = 115$ GHz) and the contribution to the thermal (free-free) luminosity at that frequency (L_ν^T). Any flattening in the actual spectral index from synchroton emission would increase the contribution from synchrotron emission at these frequencies and thus reduce the calculated star formation rate. Alternatively, any contribution by the AGN to the free-free emission would also reduce the true SFR. The calculated SFRs are extremely high– if true, it would make these sources both some of the most luminous quasars in the universe and some of the most heavily star-forming galaxies. We estimate an upper limit on the star-formation

rate of SFR $\approx 6.6 \times 10^4$ $M_\odot$ yr^{-1} for SDSSJ0812+1819 and SFR $\approx 1.8 \times 10^4$ $M_\odot$ yr^{-1} for both SDSSJ0826+0542 and SDSSJ1615+1728. Without knowing the real spectral index or AGN contribution to free-free emission in these objects it is likely that the true star formation rate is far smaller than this though there is some evidence to suggest that the SFRs in other samples of red and dust obscured quasars are extremely high (e.g. Tsai et al., 2015). This calculation also does not account for any contribution to the continuum at this wavelength from thermal emission from dust, though at 115GHz this contribution should also be negligible (Gralla et al., 2014).

Some evidence to support a contribution from free-free emission at a rest-frame of 115GHz comes from comparing the detection of our eight sources in our VLA data with the non-detection in FIRST. Assuming the steep spectral index of ERQs ($\alpha = -1.3$) we would expect only a negligible contribution at rest-frame 115 GHz from synchrotron emission. It is only when assuming a typical spectral index of ($\alpha = -0.7$) that we can account for the observed emission at 33GHz with only synchrotron emission.

5.5 Line Measurements

We find no detection of CO (1-0) in any of our individual z $\sim$ 2.5 quasars nor in the stacked quasars binned at the rest frequency of the line within $\pm$500 km s^{-1} (see Figure 5.2). This does allow us to place a strict upper limit on the velocity-integrated line

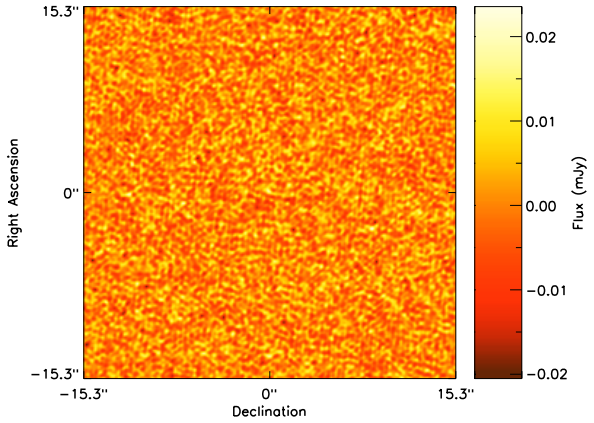

Figure 5.3: VLA C configuration 33.0 GHz stacked image at 0.6″ resolution of eight quasars undetected individually in the continuum. We binned within ±5000 km s^{-1} of the CO(1-0) transition, excluding the region within ±500 km s^{-1} of the line center. There is a 3σ detection at the location of the stacked sources with a flux of 0.19 mJy.

flux of CO (1-0) emission in these sources. The upper limit on the velocity-integrated line flux, S_{CO}, was calculated according to the equation: $S_{CO} = 3\sigma(\delta v \Delta v_{FWHM})^{1/2}$ (e.g. Seaquist et al., 1995; Greve et al., 2005) where σ is the channel-to-channel rms noise measured to be 1.2×10^{-5} Jy, δv is the velocity resolution (here 100 km s^{-1}) and Δv_{FWHM} is the linewidth. We take a conservative value for the FWHM of 500 km s^{-1} (similar to Greve et al., 2005; Coppin et al., 2008). This gives us a velocity-integrated line flux of $S_{CO} \cong 8$ mJy km s^{-1}. To convert to a CO line luminosity we use the standard conversion from Solomon & Vanden Bout (2005):

$$L_{CO} = 1.04 \times 10^{-3} S_{CO} \Delta v \nu_{rest} (1+z)^{-1} D_L^2 \tag{5.2}$$

where the final result is in units of $L_\odot$, ν_{rest} is the rest frequency of the observations (here 115 GHz), and the luminosity distance is in units of Mpc. We calculate a line luminosity of $L_{CO} = 1.2 \times 10^5 L_\odot$. We also calculate the line luminosity in units of K km s^{-1} pc^2 using the correspond equation in Solomon & Vanden Bout (2005):

$$L'_{CO} = 3.25 \times 10^7 S_{CO} \Delta v \nu_{obs}^{-2} (1+z)^{-3} D_L^2 \tag{5.3}$$

which for our sources gives us an upper limit of $L'_{CO} = 2.4 \times 10^9$ K km s^{-1} pc^2.

To translate this in to a gas mass requires the use of the conversion factor $\alpha_{CO} = \frac{M_{gas}}{L'_{CO}}$ usually taken to be 0.8 for starbursts and 4 for normal star forming galaxies such as our Milky Way assuming that the CO emission is optically thick (Bolatto et al., 2013). It is common practice to adopt the starburst conversion factor for quasars (e.g. Coppin et al., 2008; Wu et al., 2014; Banerji et al., 2017) so we do the same. Our assumption of optically thick CO emission may also be incorrect for our objects (see Section 5.5.1). Nevertheless, adopting the give value for α_{CO} gives us an upper limit on the gas mass in our quasars of $M_{gas} = 1.9 \times 10^9$ M$_\odot$. This value, though a stringent limit, is not unheard of in sub-millimeter galaxies (SMGs) at a similar redshift though it is low compared to quasars selected in similar ways (see Figure 5.4). It should be noted that most samples of SMGs and quasars chosen for follow-up with the VLA, ALMA or other sub-mm facilities are highly biased as they are often pre-selected by a detection in the far-infrared (e.g. Coppin et al., 2008) thus biasing previous attempts to detect molecular gas in quasar hosts. This is not true, however,

for some of the samples we show in Figure 5.4 including Banerji et al. (2017) which was selected based only on NIR colour.

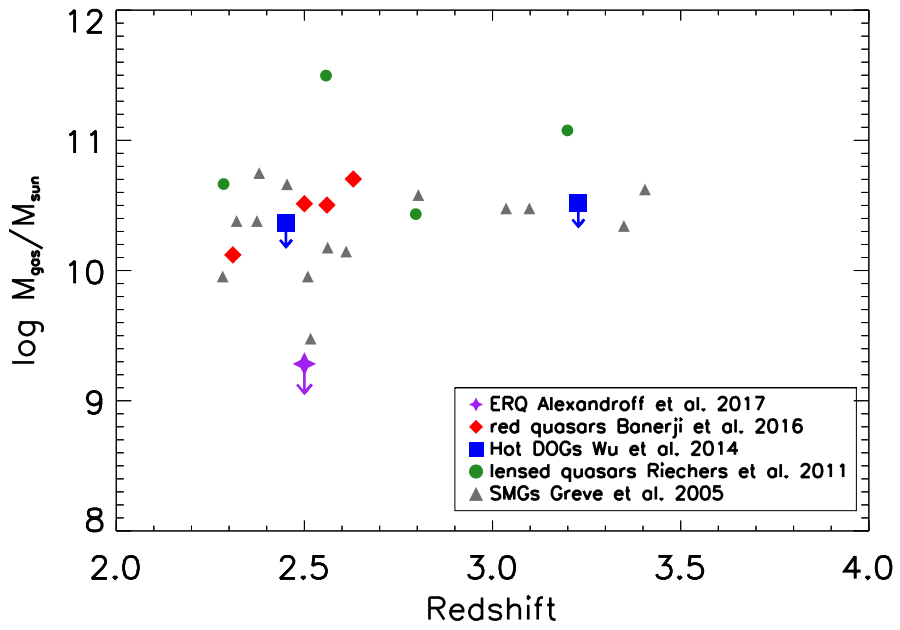

Figure 5.4: Gas mass as a function of redshift in our stacked quasars as compared to samples of quasars and SMGs at similar redshifts. We re-calculate every gas mass assuming, $r_{3-2/1-0} = 0.97$, $r_{4-3/1-0} = 0.87$ and $\alpha_{CO} = 0.8$ These samples, unlike ours, are often pre-selected based on past detections in the sub-mm or FIR so it is difficult to construct an unbiased comparison sample.

5.5.1 Evidence for suppression of low-J transitions?

There is emerging evidence to suggest that quasars may have more highly excited molecular gas than SMGs or main sequence galaxies. Riechers et al. (2011) find evidence for a single, highly excited gas component in a sample of five redshift $z \sim 2.5$ lensed quasars. Both objects modeled are best fit with optically thick CO(1-

0). Evidence suggests that all of the molecular gas is associated with star formation. In addition, it is possible that either wind- or jet-mediated quasar feedback would introduce a second more excited component of molecular gas. For example, citet-Dasyra2016 found that the ratio of CO(4-3)/CO(2-1) in IC 5063 was ≈ 1 for the disk but closer to 5 in regions near the AGN-driven jet (necessitating that the gas be optically thin).

This is contrast to SMGs where there appears to be an excess of cold, low-excitation gas (Ivison et al., 2011). For example, Ivison et al. (2011) find a typical brightness temperature ratio of $r_{3-2/1-0} \sim 0.4$ in a sample of four submillimeter galaxies at $z = 2.2 - 2.5$ (though this may be high as the sample was pre-selected by a detection in CO(3-2)). Thus, we may be missing a significant component of the molecular gas in our objects by our choice to probe a low-J transition. Follow-up ALMA observations would help to confirm this.

Nevertheless, should it be the case that the molecular gas in our targets is highly excited, and thus not visible given our sensitivity in CO(1-0), this supports the theory that SMGs and quasars are at different stages in galaxy evolution with quasar feedback clearing the host galaxy of low-excitation molecular gas in quasar hosts but not SMGs.

5.5.2 Evidence of gas depletion?

The evidence for luminous quasars driving power outflows of high ionization gas (Greene et al., 2011; Villar-Martín et al., 2011; Harrison et al., 2012; Cano-Díaz et al., 2012; Liu et al., 2013; Harrison et al., 2014; Villar Martín et al., 2014; Brusa et al., 2015; Perna et al., 2015; Kakkad et al., 2016; Zakamska et al., 2016a) as well as other components of the hot wind (Rupke & Veilleux, 2013; Greene et al., 2014; Nardini et al., 2015) is increasing. However, observations of molecular gas content of powerful quasars using sub-millimeter continuum and molecular line emission provide some conflicting results. Some objects appear gas-rich and strongly star-forming (Beelen et al., 2004; Coppin et al., 2008; Husemann et al., 2017; Banerji et al., 2017) and others depleted of gas (Cicone et al., 2014; Kakkad et al., 2016; Carniani et al., 2017).

Our observation, which places the gas mass in our objects at a level significantly below other transition objects at a similar redshift (see Figure 5.4), implies that our objects exist at a later evolutionary stage. Red quasars are often considered to be transition objects but still possess high levels of star formation ($> 1000 M_{\odot}$ yr^{-1}) and significant molecular gas reservoirs (Wu et al., 2014; Banerji et al., 2017). Our objects would be part of the "blowout" phase of quasar feedback when instead the quasar is actively clearing its host galaxy of star forming material but has not yet removed enough dust to be an unobscured blue quasar. This provides an interesting contrast to our calculation in Section 5.4 and suggests either that we overestimated the contribution from free-free emission to our observed fluxes or perhaps that a

starburst phase has also contributed to the depletion of the molecular gas reservoir in these sources.

5.6 Conclusions

Quasar feedback is a key ingredient in galaxy evolution and it is crucial to explore the ability of quasar winds to clear their host galaxy of star forming material (molecular gas).

We report a non-detection in a stack of eleven high redshift obscured and red quasars at the frequency of the CO(1-0) transition. This places a strict upper limit on the line luminosity of $L_{CO} = 1.2 \times 10^5 L_{\odot}$. This is almost an order of magnitude smaller than other "transition" quasars at a similar redshift. Whether due to a lack of cold, low excitation gas as observed by the J=1-0 transition, or because the molecular gas reservoir has been significantly depleted, this points to the effects of quasar feedback on the molecular gas in these sources. More sensitive observations with ALMA at higher J transitions will allow us to confirm our hypothesis.

We also report a detection of continuum emission at rest-frame 115GHz in three individual objects as well as a stack of the remaining eight sources. Pending a confirmation of the spectral index from synchrotron emission in our sources, we can only place an upper limit on the contribution from free-free emission at this frequency in our sources and use that to derive a star formation rate. With an upper limit

$> 1.0 \times 10^4 M_\odot$ yr^{-1} in all cases, we see some evidence for a recent starburst that may have accompanied or preceded the "blowout" phase of quasar feedback though it is possible that there is a quasar contribution to the measured free-free emission. Additional radio observations at different frequencies will allow for full SED modeling of the different contributions at 115 GHz.

Bibliography

Abazajian, K. N., Adelman-McCarthy, J. K., Agüeros, M. A., Allam, S. S., Allende Prieto, C., An, D., Anderson, K. S. J., Anderson, S. F., Annis, J., Bahcall, N. A., & et al. 2009, ApJS, 182, 543

Abramowicz, M. A., Czerny, B., Lasota, J. P., & Szuszkiewicz, E. 1988, ApJ, 332, 646

Ahn, C. P., Alexandroff, R., Allende Prieto, C., Anderson, S. F., Anderton, T., Andrews, B. H., Aubourg, É., Bailey, S., Balbinot, E., Barnes, R., & et al. 2012, ApJS, 203, 21

Alam, S., Albareti, F. D., Allende Prieto, C., Anders, F., Anderson, S. F., Anderton, T., Andrews, B. H., Armengaud, E., Aubourg, É., Bailey, S., & et al. 2015, ApJS, 219, 12

Alexander, D. M., Bauer, F. E., Brandt, W. N., Daddi, E., Hickox, R. C., Lehmer, B. D., Luo, B., Xue, Y. Q., Young, M., Comastri, A., Del Moro, A., Fabian, A. C.,

BIBLIOGRAPHY

Gilli, R., Goulding, A. D., Mainieri, V., Mullaney, J. R., Paolillo, M., Rafferty, D. A., Schneider, D. P., Shemmer, O., & Vignali, C. 2011, ApJ, 738, 44

Alexander, D. M., Smail, I., Bauer, F. E., Chapman, S. C., Blain, A. W., Brandt, W. N., & Ivison, R. J. 2005, Nature, 434, 738

Alexandroff, R., Strauss, M. A., Greene, J. E., Zakamska, N. L., Ross, N. P., Brandt, W. N., Liu, G., Smith, P. S., Ge, J., Hamann, F., Myers, A. D., Petitjean, P., Schneider, D. P., Yesuf, H., & York, D. G. 2013, MNRAS, 435, 3306

Alexandroff, R. M., Zakamska, N. L., van Velzen, S., Greene, J. E., & Strauss, M. A. 2016, MNRAS, 463, 3056

Anderson, L., Aubourg, E., Bailey, S., Bizyaev, D., Blanton, M., Bolton, A. S., Brinkmann, J., Brownstein, J. R., Burden, A., Cuesta, A. J., & et al. 2012, MNRAS, 427, 3435

Antonucci, R. 1993, ARA&A, 31, 473

Antonucci, R. R. J. & Miller, J. S. 1985, ApJ, 297, 621

Assef, R. J., Eisenhardt, P. R. M., Stern, D., Tsai, C.-W., Wu, J., Wylezalek, D., Blain, A. W., Bridge, C. R., Donoso, E., Gonzales, A., Griffith, R. L., & Jarrett, T. H. 2015, ApJ, 804, 27

BIBLIOGRAPHY

Assef, R. J., Kochanek, C. S., Brodwin, M., Cool, R., Forman, W., Gonzalez, A. H., Hickox, R. C., Jones, C., Le Floc'h, E., Moustakas, J., Murray, S. S., & Stern, D. 2010, ApJ, 713, 970

Assef, R. J., Stern, D., Kochanek, C. S., Blain, A. W., Brodwin, M., Brown, M. J. I., Donoso, E., Eisenhardt, P. R. M., Jannuzi, B. T., Jarrett, T. H., Stanford, S. A., Tsai, C.-W., Wu, J., & Yan, L. 2013, ApJ, 772, 26

Assef, R. J., Walton, D. J., Brightman, M., Stern, D., Alexander, D., Bauer, F., Blain, A. W., Diaz-Santos, T., Eisenhardt, P. R. M., Finkelstein, S. L., Hickox, R. C., Tsai, C.-W., & Wu, J. W. 2016, ApJ, 819, 111

Ballantyne, D. R., Draper, A. R., Madsen, K. K., Rigby, J. R., & Treister, E. 2011, ApJ, 736, 56

Banerji, M., Alaghband-Zadeh, S., Hewett, P. C., & McMahon, R. G. 2015, MNRAS, 447, 3368

Banerji, M., Carilli, C. L., Jones, G., Wagg, J., McMahon, R. G., Hewett, P. C., Alaghband-Zadeh, S., & Feruglio, C. 2017, MNRAS, 465, 4390

Barger, A. J., Cowie, L. L., Mushotzky, R. F., Yang, Y., Wang, W.-H., Steffen, A. T., & Capak, P. 2005, AJ, 129, 578

Barth, A. J., Filippenko, A. V., & Moran, E. C. 1999, ApJ, 525, 673

Barvainis, R. 1987, ApJ, 320, 537

BIBLIOGRAPHY

Becker, R. H., White, R. L., & Helfand, D. J. 1995, ApJ, 450, 559

Beelen, A., Cox, P., Pety, J., Carilli, C. L., Bertoldi, F., Momjian, E., Omont, A., Petitjean, P., & Petric, A. O. 2004, A&A, 423, 441

Bell, E. F. 2003, ApJ, 586, 794

Bentz, M. C., Hall, P. B., & Osmer, P. S. 2004, AJ, 128, 561

Berriman, G., Schmidt, G. D., West, S. C., & Stockman, H. S. 1990, ApJS, 74, 869

Best, P. N. & Heckman, T. M. 2012, MNRAS, 421, 1569

Blandford, R. D. & Königl, A. 1979, ApJ, 232, 34

Bolatto, A. D., Wolfire, M., & Leroy, A. K. 2013, ARA&A, 51, 207

Bolton, A. S., Schlegel, D. J., Aubourg, É., Bailey, S., Bhardwaj, V., Brownstein, J. R., Burles, S., Chen, Y.-M., Dawson, K., Eisenstein, D. J., & et al. 2012, AJ, 144, 144

Bonchi, A., La Franca, F., Melini, G., Bongiorno, A., & Fiore, F. 2013, MNRAS, 429, 1970

Bonzini, M., Padovani, P., Mainieri, V., Kellermann, K. I., Miller, N., Rosati, P., Tozzi, P., & Vattakunnel, S. 2013, MNRAS, 436, 3759

Borguet, B., Hutsemékers, D., Letawe, G., Letawe, Y., & Magain, P. 2008, A&A, 478, 321

BIBLIOGRAPHY

Bovy, J., Hennawi, J. F., Hogg, D. W., Myers, A. D., Kirkpatrick, J. A., Schlegel, D. J., Ross, N. P., Sheldon, E. S., McGreer, I. D., Schneider, D. P., & Weaver, B. A. 2011, ApJ, 729, 141

Bower, R. G., Benson, A. J., Malbon, R., Helly, J. C., Frenk, C. S., Baugh, C. M., Cole, S., & Lacey, C. G. 2006, MNRAS, 370, 645

Boyle, B. J. & Terlevich, R. J. 1998, MNRAS, 293, L49

Brandt, W. N. & Hasinger, G. 2005, ARA&A, 43, 827

Brusa, M., Bongiorno, A., Cresci, G., Perna, M., Marconi, A., Mainieri, V., Maiolino, R., Salvato, M., Lusso, E., Santini, P., Comastri, A., Fiore, F., Gilli, R., La Franca, F., Lanzuisi, G., Lutz, D., Merloni, A., Mignoli, M., Onori, F., Piconcelli, E., Rosario, D., Vignali, C., & Zamorani, G. 2015, MNRAS, 446, 2394

Burbidge, G. R. 1956, ApJ, 124, 416

Busca, N. G., Delubac, T., Rich, J., Bailey, S., Font-Ribera, A., Kirkby, D., Le Goff, J.-M., Pieri, M. M., Slosar, A., Aubourg, É., & et al. 2013, A&A, 552, A96

Canalizo, G. & Stockton, A. 2001, ApJ, 555, 719

Cano-Díaz, M., Maiolino, R., Marconi, A., Netzer, H., Shemmer, O., & Cresci, G. 2012, A&A, 537, L8

Cappelluti, N., Brusa, M., Hasinger, G., Comastri, A., Zamorani, G., Finoguenov, A., Gilli, R., Puccetti, S., Miyaji, T., Salvato, M., & et al. 2009, A&A, 497, 635

BIBLIOGRAPHY

Carniani, S., Marconi, A., Maiolino, R., Feruglio, C., Brusa, M., Cresci, G., Cano-Díaz, M., Cicone, C., Balmaverde, B., Fiore, F., Ferrara, A., Gallerani, S., La Franca, F., Mainieri, V., Mannucci, F., Netzer, H., Piconcelli, E., Sani, E., Schneider, R., Shemmer, O., & Testi, L. 2017, ArXiv e-prints

Casey, C. M., Narayanan, D., & Cooray, A. 2014, Physics Reports, 541, 45

Cassinelli, J. P., Nordsieck, K. H., & Murison, M. A. 1987, ApJ, 317, 290

Chan, C.-H. & Krolik, J. H. 2016, ApJ, 825, 67

Cicone, C., Maiolino, R., Sturm, E., Graciá-Carpio, J., Feruglio, C., Neri, R., Aalto, S., Davies, R., Fiore, F., Fischer, J., García-Burillo, S., González-Alfonso, E., Hailey-Dunsheath, S., Piconcelli, E., & Veilleux, S. 2014, A&A, 562, A21

Civano, F., Elvis, M., Brusa, M., Comastri, A., Salvato, M., Zamorani, G., Aldcroft, T., Bongiorno, A., Capak, P., Cappelluti, N., & et al. 2012, ApJS, 201, 30

Clemens, D. P. & Tapia, S. 1990, PASP, 102, 179

Comastri, A., Ranalli, P., Iwasawa, K., Vignali, C., Gilli, R., Georgantopoulos, I., Barcons, X., Brandt, W. N., Brunner, H., Brusa, M., Cappelluti, N., Carrera, F. J., Civano, F., Fiore, F., Hasinger, G., Mainieri, V., Merloni, A., Nicastro, F., Paolillo, M., Puccetti, S., Rosati, P., Silverman, J. D., Tozzi, P., Zamorani, G., Balestra, I., Bauer, F. E., Luo, B., & Xue, Y. Q. 2011, A&A, 526, L9

BIBLIOGRAPHY

Comerford, J. M., Gerke, B. F., Stern, D., Cooper, M. C., Weiner, B. J., Newman, J. A., Madsen, K., & Barrows, R. S. 2012, ApJ, 753, 42

Condon, J. J., Cotton, W. D., Greisen, E. W., Yin, Q. F., Perley, R. A., Taylor, G. B., & Broderick, J. J. 1998, AJ, 115, 1693

Condon, J. J., Kellermann, K. I., Kimball, A. E., Ivezić, Ž., & Perley, R. A. 2013, ApJ, 768, 37

Constantin, A. & Shields, J. C. 2003, PASP, 115, 592

Coppin, K., Pope, A., Menéndez-Delmestre, K., Alexander, D. M., Dunlop, J. S., Egami, E., Gabor, J., Ibar, E., Ivison, R. J., Austermann, J. E., & et al. 2010, ApJ, 713, 503

Coppin, K. E. K., Swinbank, A. M., Neri, R., Cox, P., Alexander, D. M., Smail, I., Page, M. J., Stevens, J. A., Knudsen, K. K., Ivison, R. J., Beelen, A., Bertoldi, F., & Omont, A. 2008, MNRAS, 389, 45

Croton, D. J., Springel, V., White, S. D. M., De Lucia, G., Frenk, C. S., Gao, L., Jenkins, A., Kauffmann, G., Navarro, J. F., & Yoshida, N. 2006, MNRAS, 365, 11

Csabai, I., Dobos, L., Trencséni, M., Herczegh, G., Józsa, P., Purger, N., Budavári, T., & Szalay, A. S. 2007, Astronomische Nachrichten, 328, 852

Czerny, B. & Hryniewicz, K. 2011, A&A, 525, L8

BIBLIOGRAPHY

Dawson, K. S., Schlegel, D. J., Ahn, C. P., Anderson, S. F., Aubourg, É., Bailey, S., Barkhouser, R. H., Bautista, J. E., Beifiori, A., Berlind, A. A., & et al. 2013, AJ, 145, 10

De Breuck, C., Röttgering, H., Miley, G., van Breugel, W., & Best, P. 2000, A&A, 362, 519

Dey, A., Cimatti, A., van Breugel, W., Antonucci, R., & Spinrad, H. 1996, ApJ, 465, 157

Dey, A., Soifer, B. T., Desai, V., Brand, K., Le Floc'h, E., Brown, M. J. I., Jannuzi, B. T., Armus, L., Bussmann, S., Brodwin, M., Bian, C., Eisenhardt, P., Higdon, S. J., Weedman, D., & Willner, S. P. 2008, ApJ, 677, 943

DiPompeo, M. A., Brotherton, M. S., & De Breuck, C. 2011, ApJS, 193, 9

Dobos, L., Csabai, I., Yip, C.-W., Budavári, T., Wild, V., & Szalay, A. S. 2012, MNRAS, 420, 1217

Donley, J. L., Koekemoer, A. M., Brusa, M., Capak, P., Cardamone, C. N., Civano, F., Ilbert, O., Impey, C. D., Kartaltepe, J. S., Miyaji, T., Salvato, M., Sanders, D. B., Trump, J. R., & Zamorani, G. 2012, ApJ, 748, 142

Draine, B. T. 2003, ApJ, 598, 1017

Dunlop, J. S., McLure, R. J., Kukula, M. J., Baum, S. A., O'Dea, C. P., & Hughes, D. H. 2003, MNRAS, 340, 1095

BIBLIOGRAPHY

Eisenhardt, P. R. M., Wu, J., Tsai, C.-W., Assef, R., Benford, D., Blain, A., Bridge, C., Condon, J. J., Cushing, M. C., Cutri, R., Evans, II, N. J., Gelino, C., Griffith, R. L., Grillmair, C. J., Jarrett, T., Lonsdale, C. J., Masci, F. J., Mason, B. S., Petty, S., Sayers, J., Stanford, S. A., Stern, D., Wright, E. L., & Yan, L. 2012, ApJ, 755, 173

Eisenstein, D. J., Weinberg, D. H., Agol, E., Aihara, H., Allende Prieto, C., Anderson, S. F., Arns, J. A., Aubourg, É., Bailey, S., Balbinot, E., & et al. 2011, AJ, 142, 72

Elitzur, M. & Shlosman, I. 2006, ApJL, 648, L101

Elvis, M. 2017, ArXiv e-prints

Erb, D. K., Pettini, M., Shapley, A. E., Steidel, C. C., Law, D. R., & Reddy, N. A. 2010, ApJ, 719, 1168

Fabian, A. C. 2012, ARA&A, 50, 455

Fan, X. 1999, AJ, 117, 2528

Faucher-Giguère, C.-A. & Quataert, E. 2012, MNRAS, 425, 605

Ferrarese, L. & Merritt, D. 2000, ApJL, 539, L9

Fukugita, M., Ichikawa, T., Gunn, J. E., Doi, M., Shimasaku, K., & Schneider, D. P. 1996, AJ, 111, 1748

BIBLIOGRAPHY

Gebhardt, K., Bender, R., Bower, G., Dressler, A., Faber, S. M., Filippenko, A. V., Green, R., Grillmair, C., Ho, L. C., Kormendy, J., Lauer, T. R., Magorrian, J., Pinkney, J., Richstone, D., & Tremaine, S. 2000, ApJL, 539, L13

Gibson, R. R., Brandt, W. N., & Schneider, D. P. 2008, ApJ, 685, 773

Gilli, R., Comastri, A., & Hasinger, G. 2007, A&A, 463, 79

Gilli, R., Vignali, C., Mignoli, M., Iwasawa, K., Comastri, A., & Zamorani, G. 2010, A&A, 519, A92

Giroletti, M. & Panessa, F. 2009, ApJL, 706, L260

Glenn, J., Schmidt, G. D., & Foltz, C. B. 1994, ApJL, 434, L47

Glikman, E., Helfand, D. J., White, R. L., Becker, R. H., Gregg, M. D., & Lacy, M. 2007, ApJ, 667, 673

Glikman, E., Simmons, B., Mailly, M., Schawinski, K., Urry, C. M., & Lacy, M. 2015, ApJ, 806, 218

Glikman, E., Urrutia, T., Lacy, M., Djorgovski, S. G., Mahabal, A., Myers, A. D., Ross, N. P., Petitjean, P., Ge, J., Schneider, D. P., & York, D. G. 2012, ApJ, 757, 51

Glikman, E., Urrutia, T., Lacy, M., Djorgovski, S. G., Urry, M., Croom, S., Schneider, D. P., Mahabal, A., Graham, M., & Ge, J. 2013, ApJ, 778, 127

BIBLIOGRAPHY

Goad, M. & Koratkar, A. 1998, ApJ, 495, 718

Goodrich, R. W., Cohen, M. H., & Putney, A. 1995, PASP, 107, 179

Goodrich, R. W. & Miller, J. S. 1995, ApJL, 448, L73

Gralla, M. B., Crichton, D., Marriage, T. A., Mo, W., Aguirre, P., Addison, G. E., Asboth, V., Battaglia, N., Bock, J., Bond, J. R., Devlin, M. J., Dünner, R., Hajian, A., Halpern, M., Hilton, M., Hincks, A. D., Hlozek, R. A., Huffenberger, K. M., Hughes, J. P., Ivison, R. J., Kosowsky, A., Lin, Y.-T., Marsden, D., Menanteau, F., Moodley, K., Morales, G., Niemack, M. D., Oliver, S., Page, L. A., Partridge, B., Reese, E. D., Rojas, F., Sehgal, N., Sievers, J., Sifón, C., Spergel, D. N., Staggs, S. T., Switzer, E. R., Viero, M. P., Wollack, E. J., & Zemcov, M. B. 2014, MNRAS, 445, 460

Green, R. F., Schmidt, M., & Liebert, J. 1986, ApJS, 61, 305

Greene, J. E., Alexandroff, R., Strauss, M. A., Zakamska, N. L., Lang, D., Liu, G., Pattarakijwanich, P., Hamann, F., Ross, N. P., Myers, A. D., Brandt, W. N., York, D., & Schneider, D. P. 2014, ApJ, 788, 91

Greene, J. E., Zakamska, N. L., Ho, L. C., & Barth, A. J. 2011, ApJ, 732, 9

Greene, J. E., Zakamska, N. L., Liu, X., Barth, A. J., & Ho, L. C. 2009, ApJ, 702, 441

Greene, J. E., Zakamska, N. L., & Smith, P. S. 2012, ApJ, 746, 86

BIBLIOGRAPHY

Greve, T. R., Bertoldi, F., Smail, I., Neri, R., Chapman, S. C., Blain, A. W., Ivison, R. J., Genzel, R., Omont, A., Cox, P., Tacconi, L., & Kneib, J.-P. 2005, MNRAS, 359, 1165

Grevesse, N., Asplund, M., Sauval, A. J., & Scott, P. 2010, Astrophysics and Space Science, 328, 179

Groves, B. A., Dopita, M. A., & Sutherland, R. S. 2004, ApJS, 153, 75

Gültekin, K., Richstone, D. O., Gebhardt, K., Lauer, T. R., Tremaine, S., Aller, M. C., Bender, R., Dressler, A., Faber, S. M., Filippenko, A. V., Green, R., Ho, L. C., Kormendy, J., Magorrian, J., Pinkney, J., & Siopis, C. 2009, ApJ, 698, 198

Gunn, J. E., Carr, M., Rockosi, C., Sekiguchi, M., Berry, K., Elms, B., de Haas, E., Ivezić, Ž., Knapp, G., Lupton, R., & et al. 1998, AJ, 116, 3040

Gunn, J. E., Siegmund, W. A., Mannery, E. J., Owen, R. E., Hull, C. L., Leger, R. F., Carey, L. N., Knapp, G. R., York, D. G., Boroski, W. N., Kent, S. M., Lupton, R. H., Rockosi, C. M., Evans, M. L., Waddell, P., Anderson, J. E., Annis, J., Barentine, J. C., Bartoszek, L. M., Bastian, S., Bracker, S. B., Brewington, H. J., Briegel, C. I., Brinkmann, J., Brown, Y. J., Carr, M. A., Czarapata, P. C., Drennan, C. C., Dombeck, T., Federwitz, G. R., Gillespie, B. A., Gonzales, C., Hansen, S. U., Harvanek, M., Hayes, J., Jordan, W., Kinney, E., Klaene, M., Kleinman, S. J., Kron, R. G., Kresinski, J., Lee, G., Limmongkol, S., Lindenmeyer, C. W., Long, D. C., Loomis, C. L., McGehee, P. M., Mantsch, P. M., Neilsen, Jr.,

E. H., Neswold, R. M., Newman, P. R., Nitta, A., Peoples, Jr., J., Pier, J. R., Prieto, P. S., Prosapio, A., Rivetta, C., Schneider, D. P., Snedden, S., & Wang, S.-i. 2006, AJ, 131, 2332

Hainline, K. N., Shapley, A. E., Greene, J. E., & Steidel, C. C. 2011, ApJ, 733, 31

Hainline, K. N., Shapley, A. E., Greene, J. E., Steidel, C. C., Reddy, N. A., & Erb, D. K. 2012, ApJ, 760, 74

Hall, P. B., Hoversten, E. A., Tremonti, C. A., Vanden Berk, D. E., Schneider, D. P., Strauss, M. A., Knapp, G. R., York, D. G., Hutsemékers, D., Newman, P. R., & et al. 2004, AJ, 127, 3146

Hamann, F., Zakamska, N. L., Ross, N., Paris, I., Alexandroff, R. M., Villforth, C., Richards, G. T., Herbst, H., Brandt, W. N., Cook, B., Denney, K. D., Greene, J. E., Schneider, D. P., & Strauss, M. A. 2017, MNRAS, 464, 3431

Hamilton, D. R. 1947, ApJ, 106, 457

Hancock, P. J., Murphy, T., Gaensler, B. M., Hopkins, A., & Curran, J. R. 2012, MNRAS, 422, 1812

Hao, L., Strauss, M. A., Tremonti, C. A., Schlegel, D. J., Heckman, T. M., Kauffmann, G., Blanton, M. R., Fan, X., Gunn, J. E., Hall, P. B., Ivezić, Ž., Knapp, G. R., Krolik, J. H., Lupton, R. H., Richards, G. T., Schneider, D. P., Strateva, I. V.,

Zakamska, N. L., Brinkmann, J., Brunner, R. J., & Szokoly, G. P. 2005, AJ, 129, 1783

Harrison, C. M., Alexander, D. M., Mullaney, J. R., & Swinbank, A. M. 2014, MNRAS, 441, 3306

Harrison, C. M., Alexander, D. M., Swinbank, A. M., Smail, I., Alaghband-Zadeh, S., Bauer, F. E., Chapman, S. C., Del Moro, A., Hickox, R. C., Ivison, R. J., Menéndez-Delmestre, K., Mullaney, J. R., & Nesvadba, N. P. H. 2012, MNRAS, 426, 1073

Harrison, C. M., Thomson, A. P., Alexander, D. M., Bauer, F. E., Edge, A. C., Hogan, M. T., Mullaney, J. R., & Swinbank, A. M. 2015, ApJ, 800, 45

Hasinger, G. 2008, A&A, 490, 905

Hasinger, G., Cappelluti, N., Brunner, H., Brusa, M., Comastri, A., Elvis, M., Finoguenov, A., Fiore, F., Franceschini, A., Gilli, R., Griffiths, R. E., Lehmann, I., Mainieri, V., Matt, G., Matute, I., Miyaji, T., Molendi, S., Paltani, S., Sanders, D. B., Scoville, N., Tresse, L., Urry, C. M., Vettolani, P., & Zamorani, G. 2007, ApJS, 172, 29

Hatziminaoglou, E., Pérez-Fournon, I., Polletta, M., Afonso-Luis, A., Hernán-Caballero, A., Montenegro-Montes, F. M., Lonsdale, C., Xu, C. K., Franceschini, A., & et al., R. 2005, AJ, 129, 1198

BIBLIOGRAPHY

Heckman, T. M., Armus, L., & Miley, G. K. 1990, ApJS, 74, 833

Heckman, T. M., Ptak, A., Hornschemeier, A., & Kauffmann, G. 2005, ApJ, 634, 161

Hewett, P. C. & Wild, V. 2010, MNRAS, 405, 2302

Hickox, R. C. & Markevitch, M. 2006, ApJ, 645, 95

Hill, M. J. & Zakamska, N. L. 2014, MNRAS, 439, 2701

Hines, D. C., Schmidt, G. D., Gordon, K. D., Smith, P. S., Wills, B. J., Allen, R. G., & Sitko, M. L. 2001, ApJ, 563, 512

Hines, D. C., Schmidt, G. D., Smith, P. S., Cutri, R. M., & Low, F. J. 1995, ApJL, 450, L1

Hines, D. C., Schmidt, G. D., Wills, B. J., Smith, P. S., & Sowinski, L. G. 1999, ApJ, 512, 145

Hodge, J. A., Becker, R. H., White, R. L., Richards, G. T., & Zeimann, G. R. 2011, AJ, 142, 3

Hoeflich, P., Wheeler, J. C., Hines, D. C., & Trammell, S. R. 1996, ApJ, 459, 307

Hopkins, P. F., Hernquist, L., Cox, T. J., Di Matteo, T., Robertson, B., & Springel, V. 2006, ApJS, 163, 1

Hopkins, P. F., Hernquist, L., Cox, T. J., & Kereš, D. 2008, ApJS, 175, 356

BIBLIOGRAPHY

Horne, K. 1986, PASP, 98, 609

Humphrey, A., Villar-Martín, M., Vernet, J., Fosbury, R., di Serego Alighieri, S., & Binette, L. 2008, MNRAS, 383, 11

Husemann, B., Davis, T. A., Jahnke, K., Dannerbauer, H., Urrutia, T., & Hodge, J. 2017, ArXiv e-prints

Huynh, M. T., Bell, M. E., Hopkins, A. M., Norris, R. P., & Seymour, N. 2015, MNRAS, 454, 952

Ivezić, Ž., Menou, K., Knapp, G. R., Strauss, M. A., Lupton, R. H., Vanden Berk, D. E., Richards, G. T., Tremonti, C., Weinstein, M. A., Anderson, S., Bahcall, N. A., Becker, R. H., Bernardi, M., Blanton, M., Eisenstein, D., Fan, X., Finkbeiner, D., Finlator, K., Frieman, J., Gunn, J. E., Hall, P. B., Kim, R. S. J., Kinkhabwala, A., Narayanan, V. K., Rockosi, C. M., Schlegel, D., Schneider, D. P., Strateva, I., SubbaRao, M., Thakar, A. R., Voges, W., White, R. L., Yanny, B., Brinkmann, J., Doi, M., Fukugita, M., Hennessy, G. S., Munn, J. A., Nichol, R. C., & York, D. G. 2002, AJ, 124, 2364

Ivison, R. J., Papadopoulos, P. P., Smail, I., Greve, T. R., Thomson, A. P., Xilouris, E. M., & Chapman, S. C. 2011, MNRAS, 412, 1913

Jarvis, M. J. & Rawlings, S. 2004, New Astronomy Reviews, 48, 1173

Jia, J., Ptak, A., Heckman, T., & Zakamska, N. L. 2013, ApJ, 777, 27

Jiang, L., Fan, X., Ivezić, Ž., Richards, G. T., Schneider, D. P., Strauss, M. A., & Kelly, B. C. 2007, ApJ, 656, 680

Jiang, L., Fan, X., & Vestergaard, M. 2008, ApJ, 679, 962

Kakkad, D., Mainieri, V., Padovani, P., Cresci, G., Husemann, B., Carniani, S., Brusa, M., Lamastra, A., Lanzuisi, G., Piconcelli, E., & Schramm, M. 2016, A&A, 592, A148

Kasen, D., Nugent, P., Wang, L., Howell, D. A., Wheeler, J. C., Höflich, P., Baade, D., Baron, E., & Hauschildt, P. H. 2003, ApJ, 593, 788

Kauffmann, G., Heckman, T. M., Tremonti, C., Brinchmann, J., Charlot, S., White, S. D. M., Ridgway, S. E., Brinkmann, J., Fukugita, M., Hall, P. B., Ivezić, Ž., Richards, G. T., & Schneider, D. P. 2003, MNRAS, 346, 1055

Kellermann, K. I., Sramek, R., Schmidt, M., Shaffer, D. B., & Green, R. 1989, AJ, 98, 1195

Khachikyan, É. Y. & Weedman, D. W. 1971, Astrophysics, 7, 231

Kimball, A. E., Kellermann, K. I., Condon, J. J., Ivezić, Ž., & Perley, R. A. 2011, ApJL, 739, L29

King, A. R. 2010, MNRAS, 402, 1516

Kirkpatrick, J. A., Schlegel, D. J., Ross, N. P., Myers, A. D., Hennawi, J. F., Sheldon, E. S., Schneider, D. P., & Weaver, B. A. 2011, ApJ, 743, 125

BIBLIOGRAPHY

Kishimoto, M., Antonucci, R., Cimatti, A., Hurt, T., Dey, A., van Breugel, W., & Spinrad, H. 2001, ApJ, 547, 667

Koekemoer, A. M., Aussel, H., Calzetti, D., Capak, P., Giavalisco, M., Kneib, J.-P., Leauthaud, A., Le Fèvre, O., McCracken, H. J., Massey, R., Mobasher, B., Rhodes, J., Scoville, N., & Shopbell, P. L. 2007, ApJS, 172, 196

Korista, K. T. & Goad, M. R. 2000, ApJ, 536, 284

Kormendy, J. & Ho, L. C. 2013, ARA&A, 51, 511

Kraemer, S. B. & Crenshaw, D. M. 2000, ApJ, 532, 256

Kratzer, R. M. & Richards, G. T. 2015, AJ, 149, 61

Kukula, M. J., Dunlop, J. S., Hughes, D. H., & Rawlings, S. 1998, MNRAS, 297, 366

Lal, D. V. & Ho, L. C. 2010, AJ, 139, 1089

Laor, A. & Behar, E. 2008, MNRAS, 390, 847

Lawrence, A. & Elvis, M. 2010, ApJ, 714, 561

Lee, H. W. 1994, MNRAS, 268, 49

Lee, H.-W. & Blandford, R. D. 1997, MNRAS, 288, 19

Lee, H.-W., Blandford, R. D., & Western, L. 1994, MNRAS, 267, 303

BIBLIOGRAPHY

Lehmer, B. D., Xue, Y. Q., Brandt, W. N., Alexander, D. M., Bauer, F. E., Brusa, M., Comastri, A., Gilli, R., Hornschemeier, A. E., Luo, B., Paolillo, M., Ptak, A., Shemmer, O., Schneider, D. P., Tozzi, P., & Vignali, C. 2012, ApJ, 752, 46

Leipski, C., Falcke, H., Bennert, N., & Hüttemeister, S. 2006, A&A, 455, 161

Liu, G., Zakamska, N. L., & Greene, J. E. 2014, MNRAS, 442, 1303

Liu, G., Zakamska, N. L., Greene, J. E., Nesvadba, N. P. H., & Liu, X. 2013, MNRAS, 436, 2576

Liu, X., Shen, Y., Strauss, M. A., & Greene, J. E. 2010, ApJ, 708, 427

Madau, P. & Dickinson, M. 2014, ARA&A, 52, 415

Magorrian, J., Tremaine, S., Richstone, D., Bender, R., Bower, G., Dressler, A., Faber, S. M., Gebhardt, K., Green, R., Grillmair, C., Kormendy, J., & Lauer, T. 1998, AJ, 115, 2285

Marconi, A., Risaliti, G., Gilli, R., Hunt, L. K., Maiolino, R., & Salvati, M. 2004, MNRAS, 351, 169

Markwardt, C. B. 2009, in Astronomical Society of the Pacific Conference Series, Vol. 411, Astronomical Data Analysis Software and Systems XVIII, ed. D. A. Bohlender, D. Durand, & P. Dowler, 251

Martínez-Sansigre, A., Rawlings, S., Lacy, M., Fadda, D., Jarvis, M. J., Marleau, F. R., Simpson, C., & Willott, C. J. 2006, MNRAS, 370, 1479

Mason, R. E., Rodríguez-Ardila, A., Martins, L., Riffel, R., González Martín, O., Ramos Almeida, C., Ruschel Dutra, D., Ho, L. C., Thanjavur, K., Flohic, H., Alonso-Herrero, A., Lira, P., McDermid, R., Riffel, R. A., Schiavon, R. P., Winge, C., Hoenig, M. D., & Perlman, E. 2015, ApJS, 217, 13

Massardi, M., Bonaldi, A., Negrello, M., Ricciardi, S., Raccanelli, A., & de Zotti, G. 2010, MNRAS, 404, 532

Mateos, S., Alonso-Herrero, A., Carrera, F. J., Blain, A., Severgnini, P., Caccianiga, A., & Ruiz, A. 2013, MNRAS, 434, 941

McCarthy, P. J. 1993, ARA&A, 31, 639

McKinney, J. C., Dai, L., & Avara, M. J. 2015, MNRAS, 454, L6

McMullin, J. P., Waters, B., Schiebel, D., Young, W., & Golap, K. 2007, in Astronomical Society of the Pacific Conference Series, Vol. 376, Astronomical Data Analysis Software and Systems XVI, ed. R. A. Shaw, F. Hill, & D. J. Bell, 127

Mignoli, M., Vignali, C., Gilli, R., Comastri, A., Zamorani, G., Bolzonella, M., Bongiorno, A., Lamareille, F., Nair, P., Pozzetti, L., Lilly, S. J., Carollo, C. M., Contini, T., Kneib, J.-P., Le Fèvre, O., Mainieri, V., Renzini, A., Scodeggio, M., Bardelli, S., Caputi, K., Cucciati, O., de la Torre, S., de Ravel, L., Franzetti, P., Garilli, B., Iovino, A., Kampczyk, P., Knobel, C., Kovač, K., Le Borgne, J.-F., Le Brun, V., Maier, C., Pellò, R., Peng, Y., Perez Montero, E., Presotto, V., Silverman, J. D.,

Tanaka, M., Tasca, L., Tresse, L., Vergani, D., Zucca, E., Bordoloi, R., Cappi, A., Cimatti, A., Koekemoer, A. M., McCracken, H. J., Moresco, M., & Welikala, N. 2013, A&A, 556, A29

Miller, J. S. & Goodrich, R. W. 1990, ApJ, 355, 456

Miller, J. S., Goodrich, R. W., & Mathews, W. G. 1991, ApJ, 378, 47

Miller, J. S., Robinson, L. B., & Goodrich, R. W. 1988, in Instrumentation for Ground-Based Optical Astronomy, ed. L. B. Robinson, 157

Miller, N. A., Bonzini, M., Fomalont, E. B., Kellermann, K. I., Mainieri, V., Padovani, P., Rosati, P., Tozzi, P., & Vattakunnel, S. 2013, ApJS, 205, 13

Mullaney, J. R., Alexander, D. M., Fine, S., Goulding, A. D., Harrison, C. M., & Hickox, R. C. 2013, MNRAS, 433, 622

Mullaney, J. R., Alexander, D. M., Goulding, A. D., & Hickox, R. C. 2011, MNRAS, 414, 1082

Murphy, E. J., Bremseth, J., Mason, B. S., Condon, J. J., Schinnerer, E., Aniano, G., Armus, L., Helou, G., Turner, J. L., & Jarrett, T. H. 2012, ApJ, 761, 97

Mushotzky, R. 2004, in Astrophysics and Space Science Library, Vol. 308, Supermassive Black Holes in the Distant Universe, ed. A. J. Barger, 53

Mushotzky, R. F., Cowie, L. L., Barger, A. J., & Arnaud, K. A. 2000, Nature, 404, 459

Nagao, T., Maiolino, R., & Marconi, A. 2006, A&A, 447, 863

Nardini, E., Reeves, J. N., Gofford, J., Harrison, F. A., Risaliti, G., Braito, V., Costa, M. T., Matzeu, G. A., Walton, D. J., Behar, E., Boggs, S. E., Christensen, F. E., Craig, W. W., Hailey, C. J., Matt, G., Miller, J. M., O'Brien, P. T., Stern, D., Turner, T. J., & Ward, M. J. 2015, Science, 347, 860

Nestor, D., Hamann, F., & Rodriguez Hidalgo, P. 2008, MNRAS, 386, 2055

Netzer, H. & Laor, A. 1993, ApJL, 404, L51

Nims, J., Quataert, E., & Faucher-Giguère, C.-A. 2015, MNRAS, 447, 3612

Norman, C., Hasinger, G., Giacconi, R., Gilli, R., Kewley, L., Nonino, M., Rosati, P., Szokoly, G., Tozzi, P., Wang, J., Zheng, W., Zirm, A., Bergeron, J., Gilmozzi, R., Grogin, N., Koekemoer, A., & Schreier, E. 2002, ApJ, 571, 218

Obied, G., Zakamska, N. L., Wylezalek, D., & Liu, G. 2016, MNRAS, 456, 2861

O'Dea, C. P. 1998, PASP, 110, 493

Oke, J. B., Cohen, J. G., Carr, M., Cromer, J., Dingizian, A., Harris, F. H., Labrecque, S., Lucinio, R., Schaal, W., Epps, H., & Miller, J. 1995, PASP, 107, 375

Oke, J. B. & Gunn, J. E. 1983, ApJ, 266, 713

Orienti, M. & Dallacasa, D. 2012, MNRAS, 424, 532

—. 2014, MNRAS, 438, 463

BIBLIOGRAPHY

Osterbrock, D. E. & Pogge, R. W. 1985, ApJ, 297, 166

Overzier, R. A., Heckman, T. M., Tremonti, C., Armus, L., Basu-Zych, A., Gonçalves, T., Rich, R. M., Martin, D. C., Ptak, A., Schiminovich, D., Ford, H. C., Madore, B., & Seibert, M. 2009, ApJ, 706, 203

Pacholczyk, A. G. 1970, Radio astrophysics. Nonthermal processes in galactic and extragalactic sources

Padovani, P., Bonzini, M., Kellermann, K. I., Miller, N., Mainieri, V., & Tozzi, P. 2015, MNRAS, 452, 1263

Padovani, P., Miller, N., Kellermann, K. I., Mainieri, V., Rosati, P., & Tozzi, P. 2011, ApJ, 740, 20

Pâris, I., Petitjean, P., Aubourg, É., Bailey, S., Ross, N. P., Myers, A. D., Strauss, M. A., Anderson, S. F., Arnau, E., Bautista, J., & et al. 2012, A&A, 548, A66

Perna, M., Brusa, M., Cresci, G., Comastri, A., Lanzuisi, G., Lusso, E., Marconi, A., Salvato, M., Zamorani, G., Bongiorno, A., Mainieri, V., Maiolino, R., & Mignoli, M. 2015, A&A, 574, A82

Pier, J. R., Munn, J. A., Hindsley, R. B., Hennessy, G. S., Kent, S. M., Lupton, R. H., & Ivezić, Ž. 2003, AJ, 125, 1559

Polatidis, A. G., Conway, J. E., & Owsianik, I. 2002, in Proceedings of the 6th EVN Symposium, ed. E. Ros, R. W. Porcas, A. P. Lobanov, & J. A. Zensus, 139

Raginski, I. & Laor, A. 2016, MNRAS, 459, 2082

Reyes, R., Zakamska, N. L., Strauss, M. A., Green, J., Krolik, J. H., Shen, Y., Richards, G. T., Anderson, S. F., & Schneider, D. P. 2008, AJ, 136, 2373

Reynolds, C., Punsly, B., O'Dea, C. P., & Hurley-Walker, N. 2013, ApJL, 776, L21

Richards, G. T., Fan, X., Newberg, H. J., Strauss, M. A., Vanden Berk, D. E., Schneider, D. P., Yanny, B., Boucher, A., Burles, S., Frieman, J. A., Gunn, J. E., Hall, P. B., Ivezić, Ž., Kent, S., Loveday, J., Lupton, R. H., Rockosi, C. M., Schlegel, D. J., Stoughton, C., SubbaRao, M., & York, D. G. 2002, AJ, 123, 2945

Richards, G. T., Hall, P. B., Vanden Berk, D. E., Strauss, M. A., Schneider, D. P., Weinstein, M. A., Reichard, T. A., York, D. G., Knapp, G. R., Fan, X., Ivezić, Ž., Brinkmann, J., Budavári, T., Csabai, I., & Nichol, R. C. 2003, AJ, 126, 1131

Richards, G. T., Kruczek, N. E., Gallagher, S. C., Hall, P. B., Hewett, P. C., Leighly, K. M., Deo, R. P., Kratzer, R. M., & Shen, Y. 2011, AJ, 141, 167

Richards, G. T., Lacy, M., Storrie-Lombardi, L. J., Hall, P. B., Gallagher, S. C., Hines, D. C., Fan, X., Papovich, C., Vanden Berk, D. E., Trammell, G. B., Schneider, D. P., Vestergaard, M., York, D. G., Jester, S., Anderson, S. F., Budavári, T., & Szalay, A. S. 2006a, ApJS, 166, 470

Richards, G. T., Strauss, M. A., Fan, X., Hall, P. B., Jester, S., Schneider, D. P., Vanden Berk, D. E., Stoughton, C., Anderson, S. F., Brunner, R. J., Gray, J.,

Gunn, J. E., Ivezić, Ž., Kirkland, M. K., Knapp, G. R., Loveday, J., Meiksin, A., Pope, A., Szalay, A. S., Thakar, A. R., Yanny, B., York, D. G., Barentine, J. C., Brewington, H. J., Brinkmann, J., Fukugita, M., Harvanek, M., Kent, S. M., Kleinman, S. J., Krzesiński, J., Long, D. C., Lupton, R. H., Nash, T., Neilsen, Jr., E. H., Nitta, A., Schlegel, D. J., & Snedden, S. A. 2006b, AJ, 131, 2766

Riechers, D. A., Carilli, C. L., Maddalena, R. J., Hodge, J., Harris, A. I., Baker, A. J., Walter, F., Wagg, J., Vanden Bout, P. A., Weiß, A., & Sharon, C. E. 2011, ApJL, 739, L32

Rieke, G. H., Young, E. T., Engelbracht, C. W., Kelly, D. M., Low, F. J., Haller, E. E., Beeman, J. W., Gordon, K. D., Stansberry, J. A., Misselt, K. A., Cadien, J., Morrison, J. E., Rivlis, G., Latter, W. B., Noriega-Crespo, A., Padgett, D. L., Stapelfeldt, K. R., Hines, D. C., Egami, E., Muzerolle, J., Alonso-Herrero, A., Blaylock, M., Dole, H., Hinz, J. L., Le Floc'h, E., Papovich, C., Pérez-González, P. G., Smith, P. S., Su, K. Y. L., Bennett, L., Frayer, D. T., Henderson, D., Lu, N., Masci, F., Pesenson, M., Rebull, L., Rho, J., Keene, J., Stolovy, S., Wachter, S., Wheaton, W., Werner, M. W., & Richards, P. L. 2004, ApJS, 154, 25

Rockosi, C., Stover, R., Kibrick, R., Lockwood, C., Peck, M., Cowley, D., Bolte, M., Adkins, S., Alcott, B., Allen, S. L., Brown, B., Cabak, G., Deich, W., Hilyard, D., Kassis, M., Lanclos, K., Lewis, J., Pfister, T., Phillips, A., Robinson, L., Saylor, M., Thompson, M., Ward, J., Wei, M., & Wright, C. 2010, in Proceedings of

the International Society for Optical Engineering, Vol. 7735, Ground-based and Airborne Instrumentation for Astronomy III, 77350R

Rodríguez Hidalgo, P., Hamann, F., & Hall, P. 2011, MNRAS, 411, 247

Rosario, D. J., Burtscher, L., Davies, R., Genzel, R., Lutz, D., & Tacconi, L. J. 2013, ApJ, 778, 94

Ross, N. P., Hamann, F., Zakamska, N. L., Richards, G. T., Villforth, C., Strauss, M. A., Greene, J. E., Alexandroff, R., Brandt, W. N., Liu, G., Myers, A. D., Pâris, I., & Schneider, D. P. 2015, MNRAS, 453, 3932

Ross, N. P., McGreer, I. D., White, M., Richards, G. T., Myers, A. D., Palanque-Delabrouille, N., Strauss, M. A., Anderson, S. F., Shen, Y., Brandt, W. N., Yèche, C., Swanson, M. E. C., Aubourg, É., Bailey, S., Bizyaev, D., Bovy, J., Brewington, H., Brinkmann, J., DeGraf, C., Di Matteo, T., Ebelke, G., Fan, X., Ge, J., Malanushenko, E., Malanushenko, V., Mandelbaum, R., Maraston, C., Muna, D., Oravetz, D., Pan, K., Pâris, I., Petitjean, P., Schawinski, K., Schlegel, D. J., Schneider, D. P., Silverman, J. D., Simmons, A., Snedden, S., Streblyanska, A., Suzuki, N., Weinberg, D. H., & York, D. 2013, ApJ, 773, 14

Ross, N. P., Myers, A. D., Sheldon, E. S., Yèche, C., Strauss, M. A., Bovy, J., Kirkpatrick, J. A., Richards, G. T., Aubourg, É., Blanton, M. R., Brandt, W. N., Carithers, W. C., Croft, R. A. C., da Silva, R., Dawson, K., Eisenstein, D. J., Hennawi, J. F., Ho, S., Hogg, D. W., Lee, K.-G., Lundgren, B., McMahon, R. G.,

Miralda-Escudé, J., Palanque-Delabrouille, N., Pâris, I., Petitjean, P., Pieri, M. M., Rich, J., Roe, N. A., Schiminovich, D., Schlegel, D. J., Schneider, D. P., Slosar, A., Suzuki, N., Tinker, J. L., Weinberg, D. H., Weyant, A., White, M., & Wood-Vasey, W. M. 2012, ApJS, 199, 3

Rupke, D. S. N. & Veilleux, S. 2013, ApJ, 768, 75

Sandage, A. 1965, ApJ, 141, 1560

Sanders, D. B., Salvato, M., Aussel, H., Ilbert, O., Scoville, N., Surace, J. A., Frayer, D. T., Sheth, K., Helou, G., Brooke, T., & et al. 2007, ApJS, 172, 86

Sanders, D. B., Soifer, B. T., Elias, J. H., Madore, B. F., Matthews, K., Neugebauer, G., & Scoville, N. Z. 1988, ApJ, 325, 74

Sądowski, A., Narayan, R., Tchekhovskoy, A., Abarca, D., Zhu, Y., & McKinney, J. C. 2015, MNRAS, 447, 49

Schinnerer, E., Carilli, C. L., Scoville, N. Z., Bondi, M., Ciliegi, P., Vettolani, P., Le Fèvre, O., Koekemoer, A. M., Bertoldi, F., & Impey, C. D. 2004, AJ, 128, 1974

Schlafly, E. F. & Finkbeiner, D. P. 2011, ApJ, 737, 103

Schlegel, D. J., Finkbeiner, D. P., & Davis, M. 1998, ApJ, 500, 525

Schmidt, G. D., Elston, R., & Lupie, O. L. 1992a, AJ, 104, 1563

BIBLIOGRAPHY

Schmidt, G. D., Smith, P. S., Hines, D. C., Tremonti, C. A., & Low, F. J. 2007, ApJ, 666, 784

Schmidt, G. D., Stockman, H. S., & Smith, P. S. 1992b, ApJL, 398, L57

Schmidt, M., Schneider, D. P., & Gunn, J. E. 1995, AJ, 110, 68

Schneider, D. P., Richards, G. T., Hall, P. B., Strauss, M. A., Anderson, S. F., Boroson, T. A., Ross, N. P., Shen, Y., Brandt, W. N., Fan, X., Inada, N., & et al. 2010, AJ, 139, 2360

Scoville, N., Aussel, H., Brusa, M., Capak, P., Carollo, C. M., Elvis, M., Giavalisco, M., Guzzo, L., Hasinger, G., Impey, C., & et al. 2007, ApJS, 172, 1

Seaquist, E. R., Ivison, R. J., & Hall, P. J. 1995, MNRAS, 276, 867

Serkowski, K., Mathewson, D. S., & Ford, V. L. 1975, ApJ, 196, 261

Shapley, A. E. 2011, ARA&A, 49, 525

Shapley, A. E., Steidel, C. C., Pettini, M., & Adelberger, K. L. 2003, ApJ, 588, 65

Silk, J. & Mamon, G. A. 2012, Research in Astronomy and Astrophysics, 12, 917

Smee, S. A., Gunn, J. E., Uomoto, A., Roe, N., Schlegel, D., Rockosi, C. M., Carr, M. A., Leger, F., Dawson, K. S., Olmstead, M. D., Brinkmann, J., Owen, R., Barkhouser, R. H., Honscheid, K., Harding, P., Long, D., Lupton, R. H., Loomis, C., Anderson, L., Annis, J., Bernardi, M., Bhardwaj, V., Bizyaev, D., Bolton, A. S.,

BIBLIOGRAPHY

Brewington, H., Briggs, J. W., Burles, S., Burns, J. G., Castander, F. J., Connolly, A., Davenport, J. R. A., Ebelke, G., Epps, H., Feldman, P. D., Friedman, S. D., Frieman, J., Heckman, T., Hull, C. L., Knapp, G. R., Lawrence, D. M., Loveday, J., Mannery, E. J., Malanushenko, E., Malanushenko, V., Merrelli, A. J., Muna, D., Newman, P. R., Nichol, R. C., Oravetz, D., Pan, K., Pope, A. C., Ricketts, P. G., Shelden, A., Sandford, D., Siegmund, W., Simmons, A., Smith, D. S., Snedden, S., Schneider, D. P., SubbaRao, M., Tremonti, C., Waddell, P., & York, D. G. 2013, AJ, 146, 32

Smith, J. E., Robinson, A., Alexander, D. M., Young, S., Axon, D. J., & Corbett, E. A. 2004, MNRAS, 350, 140

Smith, J. E., Robinson, A., Young, S., Axon, D. J., & Corbett, E. A. 2005, MNRAS, 359, 846

Smith, P. S., Schmidt, G. D., Allen, R. G., & Angel, J. R. P. 1995, ApJ, 444, 146

Smith, P. S., Schmidt, G. D., Hines, D. C., Cutri, R. M., & Nelson, B. O. 2000, ApJL, 545, L19

—. 2002, ApJ, 569, 23

Smith, P. S., Schmidt, G. D., Hines, D. C., & Foltz, C. B. 2003, ApJ, 593, 676

Smolčić, V., Schinnerer, E., Scodeggio, M., Franzetti, P., Aussel, H., Bondi, M., Brusa, M., Carilli, C. L., Capak, P., Charlot, S., Ciliegi, P., Ilbert, O., Ivezić, Ž.,

Jahnke, K., McCracken, H. J., Obrić, M., Salvato, M., Sanders, D. B., Scoville, N., Trump, J. R., Tremonti, C., Tasca, L., Walcher, C. J., & Zamorani, G. 2008, ApJS, 177, 14

Snellen, I. A. G., Schilizzi, R. T., & van Langevelde, H. J. 2000, MNRAS, 319, 429

Solomon, P. M. & Vanden Bout, P. A. 2005, ARA&A, 43, 677

Soltan, A. 1982, MNRAS, 200, 115

Spergel, D. N., Bean, R., Doré, O., Nolta, M. R., Bennett, C. L., Dunkley, J., Hinshaw, G., Jarosik, N., Komatsu, E., Page, L., & et al. 2007, ApJS, 170, 377

Springel, V., Di Matteo, T., & Hernquist, L. 2005, MNRAS, 361, 776

Steidel, C. C., Hunt, M. P., Shapley, A. E., Adelberger, K. L., Pettini, M., Dickinson, M., & Giavalisco, M. 2002, ApJ, 576, 653

Stern, D., Assef, R. J., Benford, D. J., Blain, A., Cutri, R., Dey, A., Eisenhardt, P., Griffith, R. L., Jarrett, T. H., Lake, S., Masci, F., Petty, S., Stanford, S. A., Tsai, C.-W., Wright, E. L., Yan, L., Harrison, F., & Madsen, K. 2012, ApJ, 753, 30

Stern, D., Eisenhardt, P., Gorjian, V., Kochanek, C. S., Caldwell, N., Eisenstein, D., Brodwin, M., Brown, M. J. I., Cool, R., Dey, A., Green, P., Jannuzi, B. T., Murray, S. S., Pahre, M. A., & Willner, S. P. 2005, ApJ, 631, 163

Stern, D., Moran, E. C., Coil, A. L., Connolly, A., Davis, M., Dawson, S., Dey, A., Eisenhardt, P., Elston, R., Graham, J. R., Harrison, F., Helfand, D. J., Holden,

B., Mao, P., Rosati, P., Spinrad, H., Stanford, S. A., Tozzi, P., & Wu, K. L. 2002, ApJ, 568, 71

Stocke, J. T., Morris, S. L., Weymann, R. J., & Foltz, C. B. 1992, ApJ, 396, 487

Stockman, H. S., Hier, R. G., & Angel, J. R. P. 1981, ApJ, 243, 404

Strauss, M. A., Weinberg, D. H., Lupton, R. H., Narayanan, V. K., Annis, J., Bernardi, M., Blanton, M., Burles, S., Connolly, A. J., Dalcanton, J., & et al. 2002, AJ, 124, 1810

Sulentic, J. W., Bachev, R., Marziani, P., Negrete, C. A., & Dultzin, D. 2007, ApJ, 666, 757

Sun, A.-L., Greene, J. E., & Zakamska, N. L. 2017, ApJ, 835, 222

Sun, A.-L., Greene, J. E., Zakamska, N. L., & Nesvadba, N. P. H. 2014, ApJ, 790, 160

Tadhunter, C. 2005, in Astronomical Society of the Pacific Conference Series, Vol. 343, Astronomical Polarimetry: Current Status and Future Directions, ed. A. Adamson, C. Aspin, C. Davis, & T. Fujiyoshi, 457

Takada, M., Ellis, R. S., Chiba, M., Greene, J. E., Aihara, H., Arimoto, N., Bundy, K., Cohen, J., Doré, O., Graves, G., Gunn, J. E., Heckman, T., Hirata, C. M., Ho, P., Kneib, J.-P., Fèvre, O. L., Lin, L., More, S., Murayama, H., Nagao, T., Ouchi,

M., Seiffert, M., Silverman, J. D., Sodré, L., Spergel, D. N., Strauss, M. A., Sugai, H., Suto, Y., Takami, H., & Wyse, R. 2014, PASJ, 66, R1

Taylor, G. B., Marr, J. M., Pearson, T. J., & Readhead, A. C. S. 2000, ApJ, 541, 112

Thomas, D., Steele, O., Maraston, C., Johansson, J., Beifiori, A., Pforr, J., Strömbäck, G., Tremonti, C. A., Wake, D., Bizyaev, D., & et. al. 2013, MNRAS, 431, 1383

Tran, H. D. 1995a, ApJ, 440, 565

—. 1995b, ApJ, 440, 597

Treister, E. & Urry, C. M. 2012, Advances in Astronomy, 2012, 21

Treister, E., Urry, C. M., & Virani, S. 2009a, ApJ, 696, 110

Treister, E., Virani, S., Gawiser, E., Urry, C. M., Lira, P., Francke, H., Blanc, G. A., Cardamone, C. N., Damen, M., Taylor, E. N., & Schawinski, K. 2009b, ApJ, 693, 1713

Tsai, C.-W., Eisenhardt, P. R. M., Wu, J., Stern, D., Assef, R. J., Blain, A. W., Bridge, C. R., Benford, D. J., Cutri, R. M., Griffith, R. L., Jarrett, T. H., Lonsdale, C. J., Masci, F. J., Moustakas, L. A., Petty, S. M., Sayers, J., Stanford, S. A., Wright, E. L., Yan, L., Leisawitz, D. T., Liu, F., Mainzer, A. K., McLean, I. S., Padgett, D. L., Skrutskie, M. F., Gelino, C. R., Beichman, C. A., & Juneau, S. 2015, ApJ, 805, 90

Ueda, Y., Akiyama, M., Ohta, K., & Miyaji, T. 2003, ApJ, 598, 886

Ulvestad, J. S., Antonucci, R. R. J., & Barvainis, R. 2005, ApJ, 621, 123

Urrutia, T., Becker, R. H., White, R. L., Glikman, E., Lacy, M., Hodge, J., & Gregg, M. D. 2009, ApJ, 698, 1095

Urry, C. M. & Padovani, P. 1995, PASP, 107, 803

van Dokkum, P. G. 2001, PASP, 113, 1420

van Velzen, S., Falcke, H., & Körding, E. 2015, MNRAS, 446, 2985

Vanden Berk, D. E., Richards, G. T., Bauer, A., Strauss, M. A., Schneider, D. P., Heckman, T. M., York, D. G., Hall, P. B., Fan, X., Knapp, G. R., & et al. 2001, AJ, 122, 549

Vasudevan, R. V., Brandt, W. N., Mushotzky, R. F., Winter, L. M., Baumgartner, W. H., Shimizu, T. T., Schneider, D. P., & Nousek, J. 2013, ApJ, 763, 111

Vasudevan, R. V., Fabian, A. C., Gandhi, P., Winter, L. M., & Mushotzky, R. F. 2010, MNRAS, 402, 1081

Vasudevan, R. V., Mushotzky, R. F., Winter, L. M., & Fabian, A. C. 2009, MNRAS, 399, 1553

Veilleux, S., Cecil, G., & Bland-Hawthorn, J. 2005, ARA&A, 43, 769

Veilleux, S., Cecil, G., Bland-Hawthorn, J., Tully, R. B., Filippenko, A. V., & Sargent, W. L. W. 1994, ApJ, 433, 48

Veilleux, S., Meléndez, M., Sturm, E., Gracia-Carpio, J., Fischer, J., González-Alfonso, E., Contursi, A., Lutz, D., Poglitsch, A., Davies, R., Genzel, R., Tacconi, L., de Jong, J. A., Sternberg, A., Netzer, H., Hailey-Dunsheath, S., Verma, A., Rupke, D. S. N., Maiolino, R., Teng, S. H., & Polisensky, E. 2013, ApJ, 776, 27

Veilleux, S., Melendez, M., Tripp, T. M., Hamann, F., & Rupke, D. S. N. 2016, ArXiv e-prints

Vignali, C., Alexander, D. M., Gilli, R., & Pozzi, F. 2010, MNRAS, 404, 48

Villar Martín, M., Emonts, B., Humphrey, A., Cabrera Lavers, A., & Binette, L. 2014, MNRAS, 440, 3202

Villar-Martín, M., Humphrey, A., Delgado, R. G., Colina, L., & Arribas, S. 2011, MNRAS, 418, 2032

Villar-Martín, M., Tadhunter, C., & Clark, N. 1997, A&A, 323, 21

Wang, J., Fabbiano, G., Elvis, M., Risaliti, G., Karovska, M., Zezas, A., Mundell, C. G., Dumas, G., & Schinnerer, E. 2011, ApJ, 742, 23

Wang, L., Howell, D. A., Höflich, P., & Wheeler, J. C. 2001, ApJ, 550, 1030

Wang, L. & Wheeler, J. C. 2008, ARA&A, 46, 433

Watson, M. G., Schröder, A. C., Fyfe, D., Page, C. G., Lamer, G., Mateos, S., Pye, J., Sakano, M., Rosen, S., Ballet, J., & et al.. 2009, A&A, 493, 339

Weingartner, J. C. & Draine, B. T. 2001, ApJ, 548, 296

White, R. L., Becker, R. H., Helfand, D. J., & Gregg, M. D. 1997, ApJ, 475, 479

White, R. L., Helfand, D. J., Becker, R. H., Glikman, E., & de Vries, W. 2007, ApJ, 654, 99

Whittle, M. 1985, MNRAS, 213, 1

Williams, R. J., Pogge, R. W., & Mathur, S. 2002, AJ, 124, 3042

Wills, B. J., Wills, D., Evans, II, N. J., Natta, A., Thompson, K. L., Breger, M., & Sitko, M. L. 1992, ApJ, 400, 96

Wright, E. L., Eisenhardt, P. R. M., Mainzer, A. K., Ressler, M. E., Cutri, R. M., Jarrett, T., Kirkpatrick, J. D., Padgett, D., McMillan, R. S., Skrutskie, M., & et al. 2010a, AJ, 140, 1868

—. 2010b, AJ, 140, 1868

Wu, J., Bussmann, R. S., Tsai, C.-W., Petric, A., Blain, A., Eisenhardt, P. R. M., Bridge, C. R., Benford, D. J., Stern, D., Assef, R. J., Gelino, C. R., Moustakas, L., & Wright, E. L. 2014, ApJ, 793, 8

Wu, X.-B., Hao, G., Jia, Z., Zhang, Y., & Peng, N. 2012, AJ, 144, 49

Wuyts, S., Cox, T. J., Hayward, C. C., Franx, M., Hernquist, L., Hopkins, P. F., Jonsson, P., & van Dokkum, P. G. 2010, ApJ, 722, 1666

Xu, C., Livio, M., & Baum, S. 1999, AJ, 118, 1169

Xue, Y. Q., Wang, S. X., Brandt, W. N., Luo, B., Alexander, D. M., Bauer, F. E., Comastri, A., Fabian, A. C., Gilli, R., Lehmer, B. D., Schneider, D. P., Vignali, C., & Young, M. 2012, ApJ, 758, 129

Yèche, C., Petitjean, P., Rich, J., Aubourg, E., Busca, N., Hamilton, J.-C., Le Goff, J.-M., Paris, I., Peirani, S., Pichon, C., Rollinde, E., & Vargas-Magaña, M. 2010, A&A, 523, A14

York, D. G., Adelman, J., Anderson, J. J. E., Anderson, S. F., Annis, J., Bahcall, N. A., Bakken, J. A., Barkhouser, R., Bastian, S., Berman, E., & SDSS Collaboration. 2000, AJ, 120, 1579

Young, S. 2000, MNRAS, 312, 567

Young, S., Axon, D. J., Robinson, A., Hough, J. H., & Smith, J. E. 2007, Nature, 450, 74

Yu, Q. & Tremaine, S. 2002, MNRAS, 335, 965

Yuan, S., Strauss, M. A., & Zakamska, N. L. 2016, MNRAS, 462, 1603

Zakamska, N. L., Gómez, L., Strauss, M. A., & Krolik, J. H. 2008, AJ, 136, 1607

Zakamska, N. L. & Greene, J. E. 2014, MNRAS, 442, 784

Zakamska, N. L., Hamann, F., Pâris, I., Brandt, W. N., Greene, J. E., Strauss, M. A., Villforth, C., Wylezalek, D., Alexandroff, R. M., & Ross, N. P. 2016a, MNRAS, 459, 3144

Zakamska, N. L., Lampayan, K., Petric, A., Dicken, D., Greene, J. E., Heckman, T. M., Hickox, R. C., Ho, L. C., Krolik, J. H., Nesvadba, N. P. H., Strauss, M. A., Geach, J. E., Oguri, M., & Strateva, I. V. 2016b, MNRAS, 455, 4191

Zakamska, N. L., Schmidt, G. D., Smith, P. S., Strauss, M. A., Krolik, J. H., Hall, P. B., Richards, G. T., Schneider, D. P., Brinkmann, J., & Szokoly, G. P. 2005, AJ, 129, 1212

Zakamska, N. L., Strauss, M. A., Heckman, T. M., Ivezić, Ž., & Krolik, J. H. 2004, AJ, 128, 1002

Zakamska, N. L., Strauss, M. A., Krolik, J. H., Collinge, M. J., Hall, P. B., Hao, L., Heckman, T. M., Ivezić, Ž., Richards, G. T., Schlegel, D. J., Schneider, D. P., Strateva, I., Vanden Berk, D. E., Anderson, S. F., & Brinkmann, J. 2003, AJ, 126, 2125

Zakamska, N. L., Strauss, M. A., Krolik, J. H., Ridgway, S. E., Schmidt, G. D., Smith, P. S., Heckman, T. M., Schneider, D. P., Hao, L., & Brinkmann, J. 2006, AJ, 132, 1496

BIBLIOGRAPHY

Zubovas, K. & King, A. 2012, ApJL, 745, L34

Vita

Rachael M. Alexandroff was born on July 18, 1990 in Toronto, Canada. She received her A. B. degree in Astrophysical Sciences with a minor in Planets and Life from Princeton University in 2012 graduating magna cum laude. She was inducted in to the Sigma Xi honours society in 2012. She enrolled in the Ph. D. program in Physics and Astronomy at Johns Hopkins University in 2012 with a Rowland first year fellowship. Her research focus is on identifying and studying obscured and red quasars in the early universe to search for the observational signatures of quasar feedback. She is also interested in the escape fraction of ionizing radiation from local Lyman Break Galaxy analogs. She has taught both at the undergraduate and graduate level. She is currently a junior member of the American Astronomical Society.

Starting in September 2017, Rachael will begin a postdoctoral fellowship offered by the National Science and Engineering Research Council of Canada at the Dunlap

VITA

Institute and the Canadian Institute for Theoretical Astrophysics at the University of Toronto. She also looks forward to continuing her science outreach efforts.